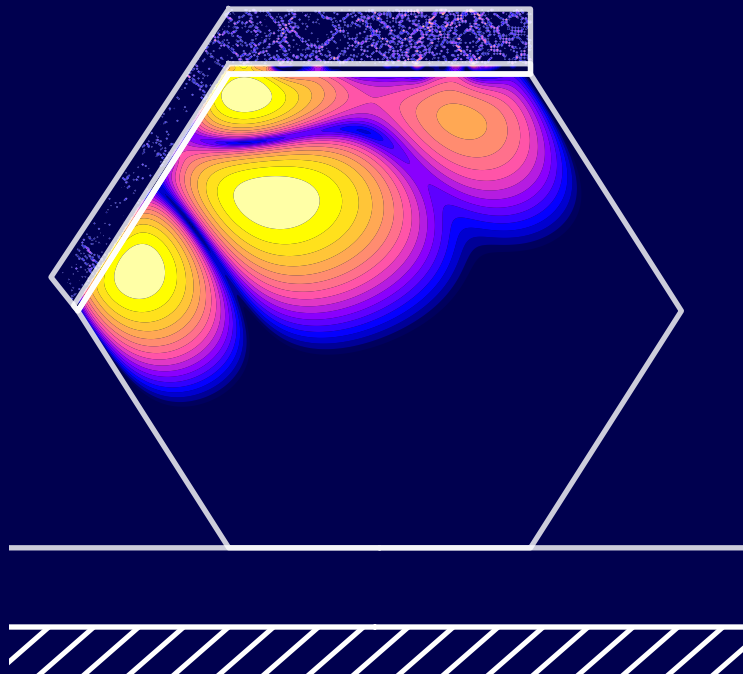# Towards a realistic description of topological hybrid semiconductor, superconductor and ferromagnetic-insulator systems

Majorana nanowires, superlattices and two-dimensional heterostructures

Samuel D. Escribano

TOWARDS A REALISTIC DESCRIPTION OF TOPOLOGICAL HYBRID SEMICONDUCTOR, SUPERCONDUCTOR AND FERROMAGNETIC-INSULATOR SYSTEMS

MAJORANA NANOWIRES, SUPERLATTICES AND TWO-DIMENSIONAL HETEROSTRUCTURES

SAMUEL D. ESCRIBANO

A THESIS SUBMITTED FOR THE DEGREE OF DOCTOR OF PHILOSOPHY

UNIVERSIDAD AUTÓTONOMA DE MADRID

2022

This thesis has been submitted in partial fulfilment for the requirement for the degree of Doctor of Philosophy in Physics. I, **Samuel Díaz Escribano**, hereby declare that this thesis is my original work and all the sources of information have been duly acknowledged.

Advisors
Elsa Prada
Alfredo Levy Yeyati

Comittee
Jelena Klinovaja
Eduardo J. H. Lee
Charles M. Marcus
Gloria Platero
Michael Wimmer

Instituto de Ciencia de los Materiales, Centro Superior de Investigaciones Científicas; Departamento de Física de la Materia Condensada and Departamento de Física Teórica de la Materia Condensada, Universidad Autónoma de Madrid (UAM)

October 2022

A mis padres, Ángel y Celia...

Acknowledgments

I would like to start thanking my PhD advisors, Elsa Prada and Alfredo Levy Yeyati, for their guidance and support along all these years. You've inspired me to have passion for condensed matter physics and you've taught me how to be an excellent scientist. During our time together, I've grown up not only as an independent scientist, but also as a person. This journey has been easy and pleasant thank to you. I'm also deeply grateful to Yuval Oreg for giving me the opportunity to spend some unforgettable months in The Weizmann Institute. I learned a lot about science from you, you made my time there easy and comfortable, and it was an amazing experience to enjoy the fantastic scientific environment of the Weizmann Institute.

I would like to express my gratitude to all my collaborators along these years, Andrea Maiani, Karsten Flensberg, Martin Leijnse and Ramón Aguado. It was a pleasure to learn and discuss about physics with you. I'm specially thankful to Pablo San-Jose for the fruitful discussions, your guidance and for sharing some of your knowledge on computational physics; and also to Rubén Seoane Souto for, apart from our discussions, your support and guidance. Also many thanks to all the experimental groups I've had the opportunity to discuss with, Charlie Marcus', Haim Beidenkopf's and Keiko Takase's groups. I can say that the quality of this thesis is better thanks to all of you.

I'm very grateful to all my colleagues from the department, Antonio, Berta, Emiliano, Guille, Jaime, Jesús, Jose, Mónica, Nerea, Pablo, Yoli, and many others. You've been the only ones understanding all my PhD-related problems, and you've been very kind and helpful. My time in the department has been joyful and pleasant thanks to all of you. I'll never forget our lunches together. I particularly thank Raúl for helping me to manage the computer cluster of our group during the year we didn't have an admin. And of course thank you to our admin, Stefan, for efficiently and competently taking care of it the rest of the years. Also many thanks to the Weizmann people, specially to Omri and Dan, for making me feel like if I were at my own university/home during my time in Israel. I grew up as a person during my stay there, and it was an unforgettable experience in part thanks to you.

Muchísimas gracias a todos mis amigos y familiares que durante todos estos años me han apoyado y animado. Muchas gracias a mi hermano Jorge, por haberme soportado y ayudado en los malos momentos; a mi tía Conchi, por haber confiado en mis capacidades y animado siempre a seguir; a Blanca y Eladio, por haberme dado tanta ayuda, comprensión y cariño; y a mis abuelos, por enseñarme la importancia de la educación y del sacrificio.

i

Y por último, me gustaría agradecérselo a tres personas muy especiales en mi vida. A mis padres, Ángel y Celia, para los que no existen palabras con las que describir toda mi gratitud: me habéis dado todo lo tengo y soy lo que soy gracias a vosotros. Sé todo lo que habéis trabajado y sacrificado por darme la mejor educación posible y que yo pueda dedicarme lo que me gusta. Además, mi vocación por la ciencia nace gracias a vuestra pasión por la lectura. Esta tesis, que os dedico, es absolutamente posible gracias a vosotros. Y a Gonzalo, por quererme incondicionalmente, aguantarme, apoyarme, y hacer este camino lo más llevadero y fácil posible. Sin tu cariño no creo que hubiese tenido la fuerza necesaria para acabar esta tesis. Esto también es gracias a ti.

Abstract

Semiconductor-based heterostructures are suitable platforms to engineer and manipulate exotic quasiparticles that emerge in low dimensions. One example, with promising applications to quantum technologies, is a semiconductor nanowire partially covered by a superconductor layer. These wires support quasi one-dimensional states that acquire superconducting correlations by proximity effect. When applying an external magnetic field, the system may enter a topological superconducting phase giving rise to the so-called Majorana bound states at the ends of the wire. Alternatively, magnetic-free platforms have been proposed in which the hybrid nanowire is additionally covered by a ferromagnetic-insulator layer. Ideally, the ferromagnet induces a proximity-induced spin polarization on the wire that leads to the same kind of topological quasiparticles.

During the last decade, several simplified models have been introduced to predict and explain the features emerging in experimental devices based on these nanostructures. However, the phenomenology arising in these systems seems to be richer and more complex than what these models can capture. In this thesis, we seek to describe this kind of heterostructures in an accurate and realistic way. To this end, we use a microscopic numerical approach in which we consider the three-dimensionality of the heterostructure, the different materials involved, their interaction when they are placed together, as well as the interaction of the hybrid system with the surrounding electrostatic environment.

We apply this formalism to hexagonal nanowires, superlattice nanowires, as well as effective wires in planar stacking geometries. Particularly, we study how the different layers induce their properties into the semiconductor as well as the behavior of the electrostatic potential and the spin-orbit coupling inside the wire. These quantities establish the appearance, extension and robustness of the topological phase and, thus, their understanding is crucial to design topological qubits based on these nanostructures. We find that, in order to acquire topological properties, the wavefunction inside the semiconductor needs to be close to both the superconductor and ferromagnetic insulator layers so that the hybridization among the different materials is enhanced. We show that this can be controlled using external potential gates or by means of a strong confinement if the semiconductor is thin. We furthermore explore the intricate dependence of the spin-orbit coupling on the electrostatic potential profile and strain, showing that it can be strong enough to support a topological phase under certain conditions. We use this knowledge to propose new hybrid wire designs with improved topological performance.

Resumen

Las heteroestructuras basadas en semiconductores son plataformas ideales para crear y manipular las quasipartículas exóticas que emergen en bajas dimensiones. Un ejemplo, con aplicaciones en tecnologías cuánticas, son los hilos semiconductores parcialmente cubiertos por una capa superconductora. Estos hilos albergan estados cuasi-monodimensionales que pueden adquirir correlaciones superconductoras por efecto proximidad. Cuando se aplica un campo magnético externo, el sistema puede entrar en una fase superconductora topológica dando lugar al final del hilo a los llamados *estados ligados de Majorana*. Dado que los campo magnéticos son perjudiciales para la fase superconductora, se han propuesto, como alternativa, plataformas que no necesitan de un campo magnético para alcanzar esta fase. Para ello, el nanohilo híbrido se cubre con una capa adicional de un aislante ferromagnético que idealmente induce una polarización de espín en el hilo por efecto proximidad también.

Durante la última década, diversos modelos simplificados han sido desarrollados para predecir y explicar las observaciones experimentales medidas en este tipo de nanoestructuras. Sin embargo, la fenomenología asociada a estos sistemas es más rica y compleja de la que los modelos pueden predecir. En esta tesis buscamos describir este tipo de heteroestructuras de una forma precisa y realista. Con este fin, utilizamos un modelo microscópico que tiene en cuenta la tridimensionalidad de la heteroestructura, los diferentes materiales involucrados, sus interacciones cuando se juntan, y la interacción entre el sistema híbrido con su entorno electrostático.

Aplicamos este formalismo a hilos hexagonales, hilos en superredes, y a hilos (efectivos) en geometrías planas apiladas por capas. En concreto, estudiamos cómo las diferentes capas inducen sus propiedades en el semiconductor, así como el comportamiento del potencial electrostático y del acoplo espín-órbita dentro del hilo. Estos parámetros establecen la aparición, extensión y robustez de la fase topológica y, por tanto, su compresión es crucial para diseñar cúbits topológicos basados en este tipo de nanoestructuras. Descubrimos que, para que el sistema adquiera una fase topológica, la función de onda dentro del semiconductor tiene que estar cerca de ambos, el superconductor y el aislante ferromagnético, de modo que la hibridización entre los diferentes materiales se vea incrementada. Mostramos que esto se puede controlar usando puertas electrostáticas externas o por medio de un confinamiento fuerte si el semiconductor es fino. Además, exploramos la dependencia compleja que posee el acoplo espín-órbita con el potencial electrostático y la tensión. Hallamos que el acoplo espín-órbita puede ser lo suficientemente fuerte como para que el sistema albergue una fase topológica cuando se satisfacen determinadas condiciones. Por último, usamos todo este conocimiento para proponer nuevos diseños híbridos que presentan un rendimiento toplógico mejorado.

List of Publications

- **Samuel D. Escribano**, Alfredo Levy Yeyati and Elsa Prada, *Interaction-induced zero-energy pinning and quantum dot formation in Majorana nanowires*, Beilstein Journal of Nanotechnology **9**, 2171-2180 (2018). Preprint at arXiv:1712.07625.

- **Samuel D. Escribano**, Alfredo Levy Yeyati, Yuval Oreg and Elsa Prada, *Effects of the electrostatic environment on superlattice Majorana nanowires*, Physical Review B **100**, 045301 (2019). Preprint at arXiv:1904.10289.

- **Samuel D. Escribano**, Alfredo Levy Yeyati and Elsa Prada, *Improved effective equation for the Rashba spin-orbit coupling in semiconductor nanowires*, Physical Review Research **2**, 033264 (2020). Preprint at arXiv:2001.04375.

- **Samuel D. Escribano**, Elsa Prada, Yuval Oreg and Alfredo Levy Yeyati, *Tunable proximity effects and topological superconductivity in ferromagnetic hybrid nanowires*, Physical review B **104**, L041404 (2021). Preprint at arXiv:2011.06566.

- **Samuel D. Escribano**, Alfredo Levy Yeyati, Ramón Aguado, Elsa Prada and Pablo San-Jose, *Fluxoid-induced pairing suppression and near-zero modes in quantum dots coupled to full-shell nanowires*, Physical review B **105**, 045418 (2022). Preprint at arXiv:2107.13011.

- **Samuel D. Escribano**, Andrea Maiani, Martin Leijnse, Karsten Flensberg, Yuval Oreg, Alfredo Levy Yeyati, Elsa Prada and Rubén Seoane Souto, *Semiconductor-ferromagnet-superconductor planar heterostructures for 1D topological superconductivity*, Npj Quantum Materials **7**, 81 (2022). Preprint at arXiv:2203.06644.

- **Samuel D. Escribano**, Alfredo Levy Yeyati, Elsa Prada, Keiko Takase, *et al.*, *Enhancement of spin-orbit coupling in InAs-InP core-shell nanowires due to strain*, manuscript in preparation.

All my publications can be found in my Google Scholar and ResearchGate profiles, as well as my personal webpage www.samueldescribano.com.

CONTENTS

CHAPTER 1

INTRODUCTION

1.1 Preface

Symmetry is perhaps the most important and powerful concept in physics. Many properties that a system exhibits can be understood by direct inspection of the symmetries it possesses. The most paradigmatic (and elegant) example is Noether's theorem [1], which states that, when the action describing a system has some symmetry, a certain physical quantity must be conserved. Another example is Landau's theory [2] that establishes that phase transitions of matter can be understood through a symmetry breaking process. This phenomenological theory was very useful to predict and study phases of matter characterized by an order parameter, and it was long believed to explain every kind of phase transition. However, during the last few decades, another type of phases of matter has been discovered that cannot be explained within Landau's theory. These are the *topological* phases of matter, and they are characterized by a topological invariant, that reflects a kind of global order of the system, rather than by an order parameter, which encodes the degree of local order.

In mathematics, topology studies the properties of geometrical objects that are conserved under continuous deformations. Or in other words, topology allows to classify objects depending on whether or not they can be continuously transformed into each other. This classification is characterized by a *topological invariant*. For instance, the genus, roughly speaking, counts the number of holes on a surface [3]. Two surfaces that can be smoothly transformed into each other without creating or removing a hole have the same genus. Hence, the genus characterizes a certain topology of the surface and, thus, it is a topological invariant.

In condensed matter physics, and in particular in quantum physics, topology is frequently used to classify the band structure of different Hamiltonians. Two Hamiltonians that exhibit a gap and that can be adiabatically transformed into each other without closing the gap or opening a new one, are topologically equivalent. As a consequence, these two Hamiltonians are characterized with the same topological invariant and share the same topological phase. Although continuous symmetries play no role in these topological phases, discrete (global) symmetries do. In fact, A. Atland and M. R. Zirnbauer [4] showed that there exist ten discrete symmetry classes of topological insulators and superconductors depending on three different symmetries of their single-particle Hamiltonian as well as their dimensionality. These three global symmetries, that the system can have or not, are the time-reversal symmetry, particle-hole (or charge conjugation) symmetry, and chiral (or sublattice)

symmetry. This permitted to create a periodic table of the topological invariants. A topological phase transition is therefore signaled by a jump in the corresponding topological invariant, which takes on a discrete set of numbers, as opposed to a conventional (Landau's) phase transition, which is signaled by a discontinuity in the corresponding order parameter (for first-order transitions) or in its derivative (for second-order transitions). Conspicuously, notice that, in the topological case, symmetry plays a role in defining the class of the particular topological phase of matter, whereas in the Landau's case a change of symmetry defines the particular phase transition.

A very important consequence of topology in phases of matter is the bulk-boundary correspondence. As stated above, two gapped Hamiltonians with different topological invariants can only be (adiabatically) connected through a closing and reopening of the gap. This means that if two systems with different topological invariants are attached, edge states must emerge at the interface as the gap must close there. This is the so-called bulk-boundary correspondence, i.e., the bulk is gapped but the boundaries of the topological phase are gapless. This phenomenon is a manifestation of the topological phase of the system and, thus, if one is able to measure this kind of boundary states, one would prove[1] the existence of the different topological phases. Moreover, these boundary states are said to be *topologically protected* as they are robust against any perturbation that do not change the topological invariant of the subsystems.

Several systems have been identified with a non-trivial[2] topological phase during the last decades. The fractional quantum Hall effect, discovered in 1982 [5–7], was one of the first examples that could not be explained in terms of a conventional (Landau's) phase. It was understood latter as a topological phase thanks to the pioneering theoretical works done by J. M. Kosterlitz and D. J. Thouless [8, 9]. Remarkably, the discovery of this new kind of phases of matter led to the Nobel prize for D. J. Thouless, J. M. Kosterlitz and F. D. M. Haldane[3] in 2016 [11]. Around two decades of these works, several solid-state systems were predicted and explained to have a non-trivial topological phase. One example is a system that displays the quantum spin Hall effect, which were understood as a 2D topological insulator in 2005 [12, 13]. This kind of topological insulating phases were experimentally observed in HgTe heterostructures just two years later, in 2007 [14]. Another (more exotic) examples are 3D topological insulators, like some Bismuth binary compounds [15, 16].

Apart from topological insulators, there are also topological superconductors that are characterized by a (topological) superconducting gap and present boundary states as a result of the bulk-boundary correspondence. In order to acquire this kind of topological superconducting phase, the system must exhibit a spinless liquid phase together with p-wave superconducting pairing [17]. Some materials have been observed to naturally exhibit a bulk superconducting topological phase, like

---

[1]Of course, one would need to prove that these boundary states are topologically protected and do not correspond to other kind of boundary states.

[2]A *trivial* phase refers to a phase that has the same topological invariant than the vacuum. Therefore, the interface between a non-trivial topological phase and vacuum also gives rise to (topologically protected) boundary states.

[3]Although the works of F. D. M. Haldane were not related to the fractional quantum Hall effect, he concurrently introduced the notion of topology for the description of some phases of matter [10].

Sr_2RuO_4 [18], but they are rather fragile in nature. However, the seminal work done by L. Fu and C. L. Kane in 2008 [19] proposed to engineer this exotic state by proximitizing a (non-superconducting) topological insulator with a conventional s-wave superconductor. This breakthrough showed that exotic (topological) phases of matter could be realized by combining simpler materials. Two years after this, Y. Oreg and R. Lutchyn [20, 21] proposed to achieve 1D topological superconductivity in a heterostructure made of common widely-used materials, particularly InAs (a well-known III-V binary compound semiconductor) and Al (a conventional s-wave superconductor).

In these 1D hybrid systems, topologically-protected states must appear at the ends of the system by virtue of the topological bulk-boundary correspondence. These states are called Majorana bound states (MBSs), and they do not behave like electrons but they can be understood as a non-local fermion bound to a topological defect of the system (the boundary). Actually, they exhibit non-Abelian anyonic properties [22, 23]. Conventional matter can be divided into fermions or bosons depending on their exchange rules: the wavefunction remains the same when two bosons are exchanged, while it acquires a minus sign for two fermions. Anyons, by contrast, acquire an arbitrary phase after the exchange operation [24]. If they are moreover non-Abelian, then this phase also depends on the order in which several of these anyons are exchanged [24]. These exotic properties make MBSs very appealing for quantum computing tasks as one can define a topological qubit out of them. This is so because a well separated pair of MBSs defines a degenerate two-level system (occupied or empty fermionic state). Moreover, their non-Abelian properties allow to define a set of quantum gates by only performing braiding operations [23]. The key property of this qubit is that the quantum information is stored non-locally. Non-locality leads to an exponentially suppressed susceptibility of the Majorana qubit to arbitrary local electrostatic noise. Therefore, a hypothetical MBS-based qubit would be fault-tolerant as it is topologically protected [25]. As a result, no quantum error correction would be needed (in principle) and the general performance of this *topological qubit* would be outstanding in comparison with a conventional one.

Hence, the understanding of 1D topological superconductivity, or alternatively the MBSs, is not only interesting from a fundamental point of view but also from a technological one. In fact, commercial companies like Microsoft are currently investing important efforts in the development of Majorana qubits based on semiconductor-superconductor heterostructures like the ones studied in this thesis. After a decade of progress, they are now closer to develop the first functional topological qubit [26]. This is the reason why we focus in this thesis on the 1D Oreg-Lutchyn proposal: it is an appealing and promising platform that can be experimentally realized with ordinary materials.

Nonetheless, several works have brought into question the topological origin of the states observed in experimental devices (see Ref. [27] for a review). Notice that typical experimental setups usually involve materials with very different electronic properties (semiconductors, superconductors, ferromagnetic insulators and dielectrics) and other intrinsic ones (crystal structure, quality of the interface, mobility, etc.). In addition to this complexity, external magnetic fields and electrostatic potentials are used to tune the system into the topological phase. The details of all these features have been shown to be crucial to obtain the topological phase. Therefore, it is necessary to perform

a microscopic theoretical model of the experimental device to ascertain whether it can support MBS or not, something that a minimal Hamiltonian cannot accomplish. Numerous groups have tried during the last few years to develop a comprehensive model that could accurately describe most of the properties of the heterostructure. In this regard, our thesis aims to contribute to the development of this model. Furthermore, we use it to give theoretical explanations of the experimental results realized so far and to propose new experimental setups with improved performance that may be useful to create a topological qubit.

In the following sections of this introductory chapter we summarize the properties of the MBSs (Sec. 1.2) and how to realize them in heterostructures (Sec. 1.3). Apart from this, we explain more specifically the particular motivation of this thesis in Sec. 1.4 and we outline its structure and our main results in Sec. 1.5. Additionally, we briefly overview in Sec. 1.6 other contributions of our thesis not included in this manuscript.

1.2 Majorana quasiparticles

Majorana fermions were first proposed by Ettore Majorana [28] as elementary particles in the context of high-energy physics. He hypothesized the existence of a different kind of fermion than the Dirac fermion, described by a real wave function instead of a complex one. This particle, know as the Majorana fermion, is its own antiparticle and therefore it is annihilated by a particle of the same kind. So far, no Majorana particles have been observed as elementary particles in Nature [29–32], but several proposals have been put forward in condensed matter physics to realize them as quasiparticle excitations bound to topological defects in p-wave superconductors [17, 19–21, 33–36] (see Refs. [22, 27, 37–44] for reviews on this subject).

1.2.1 Kitaev chain

Majorana quasiparticles were introduced by Alexei Kitaev in 2001 [17]. He proposed a simple toy model describing a superconducting 1D spinless chain [see Fig. 1.1(a)], whose Hamiltonian can be written as

$$H = -\sum_i^N \mu c_i^\dagger c_i - \sum_i^{N-1} t c_{i+1}^\dagger c_i + \sum_i^{N-1} \Delta c_{i+1}^\dagger c_i^\dagger + \text{h.c.} \tag{1.1}$$

Here, i labels the different sites of the chain (with N sites), μ is the chemical potential, and t and Δ the hopping and superconducting pairing between adjacent sites. Notice that the superconducting term is not a conventional s-wave pairing as it couples next-neighbor sites. When some conditions among the different parameters are met [17], the solutions to this Hamiltonian provides two degenerate zero energy states that are separated from the rest of states by the superconducting gap Δ. The wavefunction ψ related to these modes exhibit a complete localization at each end of the chain: one state, $\psi_{\rm L}$, is completely localized at the leftmost part of the chain; and the other one, $\psi_{\rm R}$, is completely at the rightmost. More surprisingly, these states satisfy that they are their own charge self-conjugate, i.e., $\psi_{\rm L,R}^\dagger = \psi_{\rm L,R}$, and thus, combining spatially two of these Majoranas
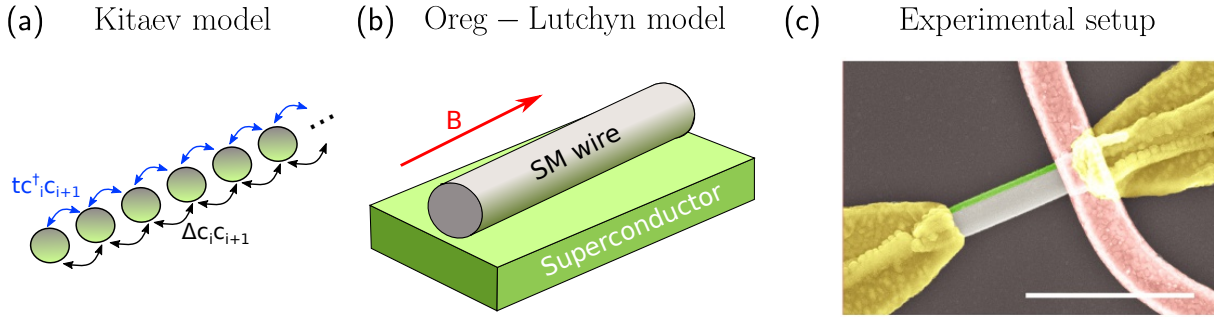
Figure 1.1: Different systems that exhibit 1D *p*-wave superconductivity. (a) The Kitaev chain [17], where different sites of a 1D chain can be occupied by spinless electrons. Adjacent sites are coupled through a hopping parameter *t* and a superconducting paring amplitude Δ. (b) The Oreg-Lutchyn model [20, 21] that consists in a SM nanowire (gray) with strong SO coupling deposited on top of a SC (green). The SC induces, by proximity effect, superconducting correlations to the wire. When a magnetic field *B* is applied, the wire undergoes a topological phase transition to a *p*-wave phase. (c) Electron micrograph of an experimental realization of the Oreg-Lutchyn Hamiltonian extracted from Ref. [45]: an InSb SM nanowire (gray) is partially covered by a thin Al SC layer (green) onto two of its facets. Several gates (yellow and red) surround the wire to control the chemical potential inside the wire and to perform tunneling measurements. Scale bar is $1\,\mu m$. An external magnetic field is also needed in this system to drive the system to a *p*-wave phase.

will annihilate each other. This resembles to the properties of Majorana particles[4], and this is why these states are often called left and right Majorana zero modes (MZMs) in the literature.

The properties of the Kitaev chain have been extensively explored as it gives rise to a rich phenomenology. The origin of these MZMs can be related with a $\mathbb{Z}_2$ [4, 17, 46] topological phase. As the chemical potential μ is varied, the bulk of the chain can undergo a topological phase transition from a trivial (gapped) superconductor (SC) to a topological (gapped) SC. The topological transition is signaled by a closing and reopening of the gap in the bulk, that points to a hybridization between the electron and hole bands. This mixing is key to realize a quasiparticle that could annihilate those of the same kind. Once the topological phase transition is achieved, edge states must emerge at the boundaries of the chain as a result of the transition in the bulk. These states are precisely the left and right Majoranas, and they do not disappear unless the symmetry that gives rise to the non-trivial topology is removed.

This last property is called topological protection, and it makes Majoranas appealing for quantum computing [24, 25, 41, 47, 48]. Actually, several proposals have been made to build quantum topological computers out of these Majorana quasiparticles. A Majorana chain provides a two-level state (the MZMs) whose energies are separated from the rest by the superconducting gap. Therefore, a Majorana chain may constitute a qubit, which would be furthermore immune to

---

[4]We note nevertheless that MZMs behave like anyons, as opposed to Majorana particles which behave like fermions [22].

decoherence processes with the environment due to its topological protection. Hence, no quantum error correction would be needed in principle, reducing the number of qubits necessary to build a functional (topological) quantum computer. In addition to this, the condition $\psi_{\mathrm{L,R}}^{\dagger} = \psi_{\mathrm{L,R}}$ implies that these states have non-Abelian properties [25, 49], and thus the final state after exchanging several MZMs depends on the order of the exchange, what is called braiding operations. This allows to build (some) quantum gates just by performing braiding operations, so that this kind of operations would be topologically protected as well.

1.2.2 1D Oreg-Lutchyn Hamiltonian

Despite its conceptual interest, the Kitaev chain is a toy model with no evident experimental realization. The key ingredient to obtain Majoranas is a superconducting spinless phase, or alternatively, a superconducting p-wave phase where the spin degree of freedom is filtered by some means. Several systems have been proposed to achieve these exotic states, such as in the $\nu = 5/2$ fractional quantum Hall state [50], in vortexes in p-wave SCs [49], or in a combination of a topological insulator with a conventional SC [19]. However, they either rely on exotic materials or in fragile states of matter. But in 2010, the seminal works by Y. Oreg *et al.* [20] and R. Lutchyn *et al.* [21] envisioned a proposal that only requires common materials embedded in a heterostructure. They found that a p-wave phase can be achieved by combining three ingredients: a (topologically trivial) s-wave SC, a helical quasi-1D wire, and a magnetic field. These ingredients can be realized, in principle, by depositing a semiconductor (SM) nanowire with a strong spin-momentum locking (e.g., due to spin-orbit interactions) on top of a SC [see Fig. 1.1(b) for a sketch of this system]. Ideally, the wire would acquire a s-wave superconducting phase by proximity effect to the SC. Then, by applying a magnetic field, the electrons' spin would align with the magnetic field, effectively creating a p-wave phase. The superconducting correlations would not be destroyed inside the wire because the spin-momentum locking would preserve the s-wave phase in the perpendicular direction to the magnetic field. This is, broadly speaking, the underlying mechanism in this proposal but, as usual in physics, details are more subtle. The simplest way to describe the proximitized wire is through the 1D Oreg-Lutchyn Hamiltonian [20, 21]

$$H = \left[\left(\frac{\hbar^2 k_z^2}{2m_{\mathrm{eff}}} - \mu_{\mathrm{eff}} \right) \sigma_0 + V_{\mathrm{Z}}\sigma_z \right] \tau_z + \alpha_{\mathrm{eff}}\sigma_x k_z \tau_z + \Delta_{\mathrm{eff}}\sigma_y \tau_y. \tag{1.2}$$

In this equation, k_z is the momentum along the wire's direction, and $\vec{\sigma} = (\sigma_x, \sigma_y, \sigma_z)$ and $\vec{\tau} = (\tau_x, \tau_y, \tau_z)$ are the Pauli matrices in spin and Nambu space (σ_0 and τ_0 are the identity matrices in their respective spaces). Notice that this Hamiltonian acts on a four-component spinor wavefunction because of the spin and Nambu spaces (the so-called Bogoliubov-de-Gennes formalism). The first term in the Hamiltonian is the kinetic energy of an electron inside the wire. It leads to a (spin-degenerate) parabolic dispersion relation for quasiparticles (with effective mass m_{eff}) that could be shifted in energy by the effective chemical potential of the wire μ_{eff}. The fourth term is the spin-orbit (SO) interaction, and it couples the electron's momentum along one direction with its spin in the perpendicular one. The strength of this coupling is given by α_{eff}, the so-called SO
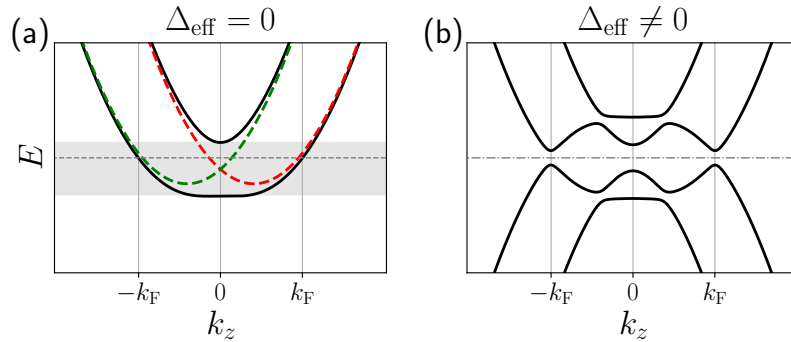
Figure 1.2: Energy vs momentum in the 1D Oreg-Lutchyn Hamiltonian (a) with and (b) without effective superconducting pairing correlations. In (a), we show the bands without any magnetic field (dashed colored lines) and in the presence of an external magnetic field (solid black lines). Notice that the magnetic field opens a gap at $k_z = 0$. If the chemical potential is fixed within the gray area, then the system is topologically non-trivial when the superconducting pairing correlations are turned on. This is the case illustrated on (b).

coupling. This interaction shifts the parabolic dispersion of each spin to opposite momenta [see colored dashed lines in Fig. 1.2(a)]. The third term is the Zeeman field that arises as a response of the wire's electron spin to a magnetic field B. It gives rise to a spin-splitting of the electrons bands breaking the Kramer degeneracy and opening a gap at $k_z = 0$ [see solid lines in Fig. 1.2(a)]. If the chemical potential is fixed adequately at the gap open between both bands (gray colored region), in such a way that the Fermi level (dashed gray line) only cuts one band, then the ground state is given by a state characterized by (approximately) only one spin direction. Finally, the last term is the s-wave pairing amplitude, and it couples the electron and hole bands [see Fig. 1.2(b)]. All the same, the resulting ground state necessarily exhibits in addition a p-wave phase as a result of the (engineered) quasi-spinless nature of the coupled bands.

The Oreg-Lutchyn system undergoes a topological phase transition when the magnetic field is strong enough to drive the ground state to a (dominant) p-wave phase [20, 21]. In parameters space, this happens when

$$V_{\mathrm{Z}} \geq \sqrt{\mu_{\mathrm{eff}}^2 + \Delta_{\mathrm{eff}}^2}. \tag{1.3}$$

This topological phase transition manifests again through a closing and reopening of the bulk gap at $k_z = 0$ when $V_{\mathrm{Z}} = \sqrt{\mu_{\mathrm{eff}}^2 + \Delta_{\mathrm{eff}}^2}$ [see Fig. 1.3(a-c) for the evolution of the energy bands along this topological phase transition]. In fact, it can be shown that when the topological phase is reached, the Oreg-Lutchyn Hamiltonian of Eq. (1.2) can be written in a similar way to the Kitaev one of Eq. (1.2), being the p-wave pairing amplitude [22]

$$\Delta_p = \frac{\pm i \alpha_{\mathrm{eff}} k_z \Delta_{\mathrm{eff}}}{2 \sqrt{V_{\mathrm{Z}}^2 + \alpha_{\mathrm{eff}}^2 k_z^2}}. \tag{1.4}$$

As opposed to the gap at $k_z = 0$, there is always a gap open at $\pm k_{\mathrm{F}}$ [see Fig. 1.3(a-c)]. Well inside
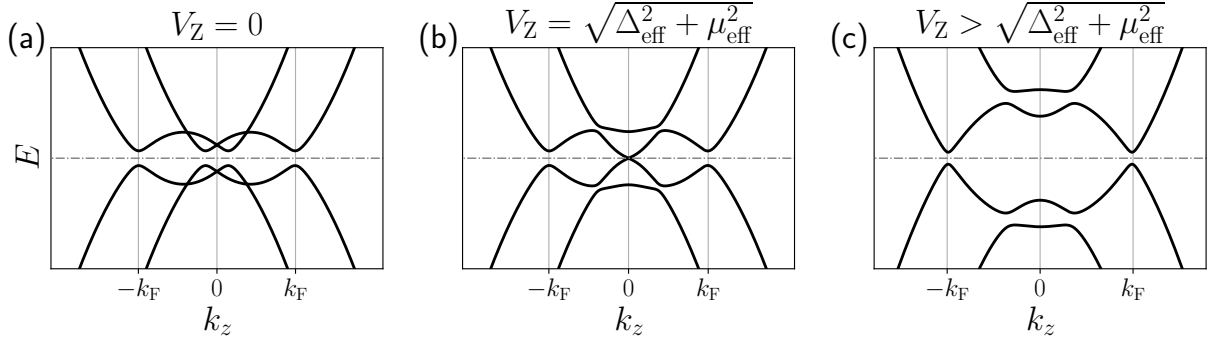
Figure 1.3: Energy bands of the 1D Oreg-Lutchyn Hamiltonian as the system undergoes a topological phase transition. In (a), we show a case before the topological phase transition, in (b) just at the transition, and in (c) well-inside the topological phase. Notice that the topological phase transition is signaled by a gap closing and reopening at $k_z = 0$. Conversely, there is always a gap at $k_z = \pm k_F$ (unless $\Delta_{\text{eff}} = 0$ and/or $\alpha_{\text{eff}} = 0$).

the topological regime ($V_Z \gg \alpha_{\text{eff}} k_F$), it is given by [51]

$$\Delta_{\text{min}} = \frac{\sqrt{2m_{\text{eff}}}\alpha_{\text{eff}}}{\hbar\sqrt{V_Z}}\Delta_{\text{eff}}. \tag{1.5}$$

Notice that this expression is similar to the effective p-wave pairing equation of above, as both are related. Both are proportional to the effective s-wave pairing Δ_{eff} and the SO coupling α_{eff}, while the Zeeman field diminishes their value. Hence, the gap Δ_{min} is always smaller or equal to the superconducting gap, and it is the smallest gap in the system (except close to the phase transition, where the smallest gap is the one at $k_z = 0$). This is why it is frequently called *minigap* in the literature.

In the same way as in a Kitaev chain, in a finite-length nanowire, two additional states emerge bounded at the end of the wire as a result of the bulk topological transition; namely, the MBSs. But now these bound states decay into the wire with a decay length proportional to $\xi_{\text{MBS}} \sim 1/\Delta_{\text{min}}$ due to the interplay between the magnetic field and SO coupling. If the wire is large enough as compared to ξ_{MBS}, the MBSs lie roughly at zero energy and they can be considered truly MZMs. But if the wire is short, then the left and right Majoranas overlap and acquire a finite charge that results in a finite energy splitting. This is detrimental since their Majorana properties are only satisfied approximately and their topological protection is lost. Hence, for quantum computing applications, it is desirable to design devices with the largest Δ_{min} possible.

1.3   Majorana modes in heterostructures

Most of the experimental realizations of the Oreg-Lutchyn Hamiltonian rely on low-dimensional semiconductor-superconductor heterostructures. These include devices such as partial-shell nanowires [52–55], full-shell nanowires [56–58] or planar heterostructures [59–62]. The most popular platform

so far is the partial-shell nanowire, that consist on a SM wire partially covered by a SC onto some of its facets [see Fig. 1.1(c) for an example]. The wire is usually made of a III-V binary compound SM, like InAs or InSb, and the SC layer is mainly made of Al. All these materials accomplish some important criteria to develop a robust topological phase.

III-V binary compound SM can be grown as single-crystal nanowires with low impurities, disorder and regular facets [63–66]. Its thickness can be controlled during the growing process [65], so thin enough wires can be deployed to define a pristine quasi-1D system [67]; and its doping can be easily tuned with the aid of external gates [68]. Moreover, these materials, and particularly InAs and InSb, present a large SO coupling [69–74] and g-factor [75, 76]. The former its beneficial as it enhances the topological protection of the MBSs [see Eq. (1.5)]. While the later is necessary to obtain the topological phase, since the gap closing in the wire should occur for smaller magnetic fields than the gap closing in the SC layer [53, 54, 77, 78].

With respect to the SC layer, Al is a well-characterized SC. It exhibits a conventional s-wave superconducting pairing, with a large and hard gap [79]. It has a similar lattice constant as III-V compound SMs, so it can be grown epitaxially on the wire. Several experiments have shown that this epitaxy is possible [78, 80–82]. Moreover, they have shown that the SC layer induces, by proximity effect, superconducting pairing correlations in the wire. It manifests through an induced hard gap in the wire that is ~ 0.9 smaller than the parent gap in the SC.

The partial covering of these wires is intended to tune the chemical potential with the aid of external potential gates[5]. The potential on these gates can be electronically tuned, what in turn changes the electrostatic potential inside the wire, and thus, its effective electrochemical energy μ_{eff}. This is important since μ_{eff} is one of the parameters that can drive the system into the topological phase, as Eq. (1.3) shows. The other tunable parameter is the magnetic field, whose intensity and orientation can also be controlled in experiments.

Several experiments on partial-shell nanowires have been conducted over the last decade [52, 53, 77, 83–85] to prove that it is possible to create a topological phase. In most of them, spectroscopic transport measurements are performed from one end of the wire to the SC, providing information about the states at the end. Lately, three-terminal and multi-terminal transport measurements have been carried out too [84, 86–90]. This kind of experiments can additionally provide the probability distribution of the states' wavefunction all along the wire. Unfortunately, experimental measurements have not been conclusive in the demonstration of MBSs so far. As a function of gate voltage and Zeeman field, they show an assortment of states with very different behavior and localization. Some of them have been found to stick at zero energy for a wide range of parameters, as MZMs, but only at one end of the wire or interacting with other states. Moreover, their conductance do not match with the one predicted by theoretical models [91–93]. Thus, their topological nature

---

[5]Notice that the SC screens external electrostatic potentials. Hence, a full-shell nanowire cannot be electrostatically tuned, although there are proposals to find the topological phase also in full-shell wires by only tuning the magnetic field.

has been brought into question.

1.4 Motivation of this thesis

The aim of this thesis is to provide a microscopic description of SM-SC heterostructures by considering the different materials involved in the hybrid system, as well as their interaction when they are placed together, taking into account their specific parameters, their three-dimensionality and their interaction with the surrounding electrostatic environment. We are interested to ascertain whether realistic devices (i.e., experimental setups) can support a superconducting topological phase alongside with the characterization (robustness and extension) of this phase. This understanding may be further useful as it can be applied to design devices with improved performance.

Several theoretical works have shown through simple effective models that some of the features observed in SM-SC experiments, compatible in principle with topologically non-trivial MZMs, can be actually explained as trivial Andreev bound states (ABSs) instead. An inhomogeneous electrochemical potential [91, 94–105], SO coupling [106–108] or superconducting pairing [104, 109, 110] along the wire could induce quantum dot (QD) states or near zero-energy ABSs that exhibit similar spectral properties than those of MZMs. In the same vein, a very strong SM-SC hybridization can induce a metalization into the wire that may give rise to the same features even if the SO coupling is negligible [111, 112]. Strikingly, a poor SM-SC hybridization is also detrimental and leads to the creation of ABSs [113–115]. All this phenomenology depends on the quality of the SM-SC interface as well as the precise geometry of the device. In this sense, the fact that the SC covering of the wire is not completely homogeneous (both, across and along the wire) implies that the parameters describing the system must be spatially-dependent quantities so that one needs to take into-account the three-dimensionality of the wire,

$$H = \left[\vec{k}^T \frac{\hbar^2}{2m^*(\vec{r})} \vec{k} - \mu(\vec{r}) + V_{\mathrm{Z}}(\vec{r}) \sigma_z \right] \tau_z + \frac{1}{2} \left[\vec{\alpha}(\vec{r}) \cdot \left(\vec{\sigma} \times \vec{k} \right) + \left(\vec{\sigma} \times \vec{k} \right) \cdot \vec{\alpha}(\vec{r}) \right] \tau_z + \Delta(\vec{r}) \sigma_y \tau_y, \ (1.6)$$

where now $\vec{r}$ applies both along and across the wire. Although this 3D extension of the Oreg-Lutchyn Hamiltonian is not straightforward and may be more subtle, it is useful to understand why the system exhibits a wider phenomenology than Eq. (1.2) can predict. The reason is quite simple: if these parameters change sharply, as it happens in a heterostructure, then the properties of the system depend strongly on the wavefunction position. What is more, it may happen that different parts of the system could undergo a topological phase transition at different values of the magnetic field or chemical potential. Or even worse, that the system cannot become topologically non-trivial if the wavefunction does not acquire all the necessary ingredients.

As it happens in most of the physical systems, the wavefunction position is mainly determined by the electrochemical potential $\mu(\vec{r})$, which sets the doping across the system. In systems involving different materials, like in SM-SC heterostructures, this doping is influenced by the band alignment among the different materials, which can only be addressed through a microscopic modeling of the heterostructure. Apart from this, the system's wavefunction inside the SM is sensitive to external

potential gates. Hence, the electrostatic potential (created by these gates or other mechanisms) also changes the electrochemical potential inside the SM wire. Thus, a proper description of the electrostatic interactions is also required to give a realistic characterization of the hybrid wire.

Apart from the problems stated above, a high concentration of charge impurities [116, 117], disorder [104, 105, 118–122] and/or orbital effects due to the magnetic field [123, 124] have also been found to be detrimental for the topological phase as they could give rise either to quasi-MBS or other trivial ABS. A new generation of devices have been designed to mitigate these problems. On the one hand, platforms based on two-dimensional electron gases (2DEGs), instead of nanowires, could provide cleaner devices as they are reported to have higher mobilities than their nanowire counterparts [60, 62, 117]. The idea is to define a 1D channel in a 2DEG by elecrostatically confining the electrons close to a SC stripe. This system is further advantageous inasmuch it is easier to create multi-terminal devices in planar heterostructures. However, it is not clear if the electrostatic confinement and the proximity effect can be successfully achieved, something that cannot be predicted by minimal models. On the other hand, the orbital magnetic effects, and, in general, the need of an external magnetic field, can be eliminated by contacting the wire (or 2DEG) to an additional layer of a ferromagnetic insulator (FI) [36]. This layer would induce, also by proximity effect, a magnetic phase into the wire, creating an equivalent Zeeman splitting than a magnetic field, but without weakening the superconductivity of the parent superconductor or inducing orbital effects. Experiments [125–128] have shown that the strength of the induced Zeeman splitting depends on the geometry of the device as well as the gate potential, something that simple 1D models cannot address. This seems to indicate that the three-dimensionality of the device is playing a role here too.

It is thus evident that a more realistic description of SM-SC heterostructures is needed to properly characterize this system and ascertain whether it can support a topological phase. Several works and PhD theses (see, for instance, Refs. [129, 130]) have sought for a this goal. In this thesis, we aim primarily on the following key aspects:

- We seek for an accurate 3D description of the heterostructure, i.e., a model that includes the fact that hybrid nanowires or 2DEGs have a finite cross section. Since the system is made of different materials, this model should describe the heterostructure through spatial-dependent parameters and proper boundary conditions. As exemplified before, this dependence is crucial to understand the phenomena emerging in these heterostructures. However, we mainly focus in this thesis on the bulk properties of hybrid systems, and therefore, we do not analyze how the parameters vary along the wire or 2DEG length, only across their cross section. Fortunately, both kind of inhomogeneties typically give rise to distinct phenomenology, so that they can be considered separately to a good approximation.

- We look for a model that includes all the materials involved in the heterostructure (SM, SC and FI). In this sense, we need to find a realistic description of the relevant bands for each material and how these bands align inside a heterostructure. To this end, we use a unified

numerical approach[6] that treats all the materials on an equal footing.

- In addition, we want to unveil the role of the electrostatic environment in establishing the heterostructure properties. As we will illustrate, the position of the wavefunction inside the wire is completely dominated by its electrochemical potential, which can be tuned with the aid of an external potential gate or with a favorable design of the device geometry (although to a lesser extent). Since the heterostructure is composed by different parts (SM, SC and FI) and the parameters change spatially, the position of the electron's wavefunction inside the heterostructure is key to understand the properties it can acquire. We thus include in our model the electrostatic interactions within the wire and with the electrostatic environment[7] (dielectrics surrounding the wire and potential gates).

In close collaboration with some experimental groups (e.g., C. Marcus', H. Beidenkopf's or K. Takase's groups), we have modeled realistic devices and characterized their properties. We believe our work may be helpful for the design of future hybrid SM-SC devices, as well as for improving the performance of topological qubits (as it has been put forward recently [26]).

1.5   Structure and summary of this thesis

This thesis can be broadly divided into two parts. In the first one (Chapter 2), we describe the methodology used to obtain the electronic properties of low-dimensional heterostructures. In the second part, we apply such methodology to different nanostructures of increasing complexity. We first characterize a (stand-alone) SM wire (Chapter 3), then hybrid SM-SC wires (Chapters 4 and 5), and finally SM-SC-FI heterostructures (Chapter 6). In more details, the structure and main contributions of this thesis are the following:

1.5.1   Chapter 2: Methods in low-dimensional quantum devices

In this chapter, we introduce the Schrödinger-Poisson equation whose solutions provide the electronic properties of an arbitrary system (the heterostructure in our case) in the presence of electrostatic interactions, and we explain in detail the self-consistent numerical methods that we use to solve it. Although these methods are quite standard, there are some subtleties we discuss that must be taken into account when simulating quantum low-dimensional systems. Apart from that, we derive a method to *efficiently* compute the topological invariant of (multiband) low-dimensional systems (see Sec. 2.3.3). This method constitutes our main contribution in this chapter.

1.5.2   Chapter 3: Electronic properties of semiconductor nanowires

This chapter is devoted to the description and characterization of III-V compound SM wires. Some of our main results are:

---

[6]Inspired by the seminal work of G. W. Winkler *et al.* [115].

[7]Also inspired by the seminal work of A. Vuik *et al.* [131].

- Starting from an 8-band k·p model, we derive a single-band Hamiltonian that can reproduce the conduction band of III-V compound SMs for both, bulk and nanowires. We find the spatial-dependence of the effective parameters that describe the conduction band as a function of the (spatial-dependent) electrostatic potential inside the wire.

- We obtain the typical values that these parameters could exhibit in realistic nanowire devices. We focus primarily on the SO coupling, as it is a key ingredient for the topological phase. We derive a simple (heuristic) equation that describes the SO coupling in nanowires [Eq. (3.43)] and we compare it with experimental data, finding an outstanding agreement.

- We include the effect of (possible) strain in the single-band description of the wire and we analyze its impact on its electronic properties. We discover that, when strain is compressive towards the wire facets, the SO coupling is enhanced.

1.5.3   Chapters 4 and 5: Semiconductor-superconductor nanowires

In this chapters we analyze the properties of hybrid SM-SC nanowires. In Chapter 4, we focus on the bulk properties of *standard* partial-shell nanowires:

- We first discuss how to describe the SC layer and how they align with the conduction band of the SM wire in hybrid structures.

- We then analyze the electrostatic potential profile and band alignment for a realistic device, and show how the superconducting proximity effect is achieved. Despite the fact that the results presented in this section are not original, we provide a deeper understanding on the interplay between the electrostatic potential and the induced superconductivity on the SM wire.

- We finally present a simplified model in which the SC is effectively integrated out, and the induced proximity effect is directly included on the SM wire. We illustrate that the full model and this simplified model give the same electrostatic dependence of the superconducting induced gap.

In Chapter 5, we analyze a setup that would allow to measure the Majorana wavefunction probability density along the hybrid wire's length. The idea is to replace the homogeneous SC covering of partial-shell nanowires (along the wire) by an array of SC fingers that creates a *superlattice*. When the fingers are below the wire, a scanning tunneling microscope (STM) could be used to access the states of the wire from the top. On the other hand, if the fingers are on top of the wire, they can be used to perform tunneling spectroscopy between them. More specifically:

- We perform 3D and effective 1D simulations to study how the (periodic) inhomogeneous SC covering affects the induced superconductivity as well as the electrostatic potential profile, which in turn modifies the SO coupling and chemical potential. We elucidate how these periodic parameters affect the energy spectrum of the superlattices.

- We compare the spectrum and MBS wavefunction profiles of the two kind of (top and bottom)

superlattices with those of a homogeneously covered nanowire. We find that the superlattice is in general detrimental for the formation of a topological phase. Despite of that, we look for the optimal geometrical parameters of the superlattice (width and separation of the SC fingers) for which the topological phase is sizable.

- Faced with these results and thanks to our microscopic understanding of superlattice nanowires, we propose an original device with a homogeneous SC covering that is deposited on top of a normal (non-superconducting) superlattice. We find that this setup has an improved performance as compared to the other superlattices devices, with the benefit that it allows to perform STM measurements.

1.5.4 Chapter 6: Semiconductor-ferromagnetic insulator-superconductor heterostructures

Lastly, we explore a SM-FI-SC heterostructure in which the need for a magnetic field is eliminated by proximitizing the hybrid SM-SC wire with an additional layer of a FI:

- We first derive the Hamiltonian that describes the whole heterostructure, including the conduction band of the FI layer and its alignment with the SC and SM's conduction bands.

- We characterize the different mechanisms by which the FI induces an effective Zeeman field in the SM wire: a) directly, by direct contact between the FI and the SM wire; b) indirectly, through a more elaborate process in which it is induced first on the SC layer and then in the SM wire; and c) through a spin-dependent tunneling from the SC to the SM wire through the FI (if it is thin enough).

- Once again, we compute the electrostatic potential profile, SO coupling and induced pairing potential for different setups, and we compare their topological phase diagrams.

- We observe that this kind of devices only support topological superconductivity when the wavefunction is pushed sufficiently close to both the SC and the FI layers with the aid of external potential gates. Moreover, devices in which the SC and the FI layers overlap are advantageous as they benefit from both the direct and indirect induced magnetization mechanisms.

- Finally, we propose an original setup based on a 2DEG inside a planar SM-FI-SC stacking geometry, instead of nanowires. In our stacking geometry, the FI is sandwiched between the SM and SC, so that the SM and the SC layers are not directly in contact. We find that for a certain FI thickness range (few nanometers, depending on the choice of materials), the FI is thin enough to allow electrons to tunnel through from the SC to the SM 2DEG, but thick enough to induce a sufficient magnetization on the system to host a topological phase.

- We find that 2DEG-based devices exhibit a more regular and robust topological phase diagram as compared to the nanowire proposals due to the strong cross-section confinement achieved in the 2DEG. Hence, we believe this platform may be promising for the generation of MBSs.

1.5.5 Chapter 7: Conclusions and outlook

Finally, we present the conclusions of this thesis alongside with the outlook for future works in the field (Chapter 8 is the same translated to Spanish). Our work establishes the importance of the wavefunction position inside the heterostructure to induce a topological phase in hybrid devices, which can be tuned by means of electrostatic confinement or with a favorable design of the device.

1.6 Other contributions of this thesis

Apart from the results summarized above, there are some other findings about SM-SC nanowires not included in this manuscript that are also a product of this thesis. We briefly outline them here:

- In Ref. [99], we study the interaction between the SM wire and the surrounding bound charges that arises in the electrostatic environment. We model a realistic partial-shell nanowire and its environment, and we derive an analytical equation for the electrostatic interactions. We find that for a certain choice of materials and wavefunction localization (across the cross section of the wire), the energies of overlapping MBSs can stick at zero energy. This happens because of the incompressibility of the electron density: when an electron is injected into the wire (by increasing the chemical potential), it may be expelled by the bound charges that itself creates in the electrostatic environment. This is reflected in the energy spectrum as a pinning of the energy states vs chemical potential, as the electron cannot enter into the wire for some potential range. And since overlapping MBSs have finite charge, their energy can suffer from this phenomenon. Together with this, we show that the leads attached at the ends of the wire (to perform transport measurements) electrostatically induce QD states at the end of the wire that interact with the MBSs (when the topological phase is achieved).

- In Ref. [132], we study the lowest-energy spectrum of a QD coupled to a hollow SC cylinder. This system may correspond to a full-shell nanowire that is typically uncapped at one end to allow transport measurements. We derive the analytical Green's function that describes the QD as a function of its position with respect to the cylinder's center. We find that, when the QD is placed just in the center, the superconducting pairing correlations are exactly suppressed, giving as a result a zero-energy mode (in the strong QD-SC coupling regime). We point out that this feature is similar to these of MBSs. In addition, we perform 3D electrostatic simulations for a realistic device, and we discover that this phenomenon may be a realistic scenario in some experimental setups.

CHAPTER 2

SELF-CONSISTENT METHOD IN NANOSTRUCTURES

In this chapter we explain in detail the numerical methods that we have implemented to obtain the eigenspectrum of nanostructures. We introduce the Schrödinger-Poisson equation, we explain the self-consistent numerical routine that we implement to solve it, and then we outline the finite difference method (FDM) and the finite element method (FEM). We use these methods to solve the Schrödinger and Poisson parts, respectively, of the joint equation. Although the methods presented here are standard, we clarify some subtleties that must be taken into account when dealing with nanostructures. Besides, we show how to efficiently compute the topological invariant for low-dimensional heterostructures.

The methods explained in this chapter are used throughout all this thesis and in all of our published works. We have implemented them in Python and published them as a package called `Majorana Nanowires: Quantum Simulation Package` [133], as an outcome of our work.

2.1 The Schrödinger-Poisson equation

The nanostructures studied in this thesis are composed of several materials (SMs, SCs and FIs) and are moreover subject to an electrostatic environment composed of different materials (dielectric and metals) and potential gates. In order to achieve the topological phase in one of such nanostructures, or more ambitiously, in order to realize scalable architectures for topological computing, one needs to acquire and apply a fine electrostatic control over the devices. Thus, it is necessary to understand the effect of electric fields on the low-energy properties of the proximitized heterostructures. From a theoretical point of view, this means that one needs to solve the quantum-mechanical dynamics of the electrons in the nanostructure together with the classical electrostatic potential created by the environment and electron charge density itself, which turns the problem into a self-consistent one. This can be achieved through the Schrödinger-Poisson (SP) equation

$$H\left[\{\lambda(\vec{r})\}, \phi(\vec{r})\right]\Psi(\vec{r}) = E\Psi(\vec{r}), \tag{2.1}$$

$$\vec{\nabla} \cdot \left(\epsilon(\vec{r}) \cdot \vec{\nabla}\phi(\vec{r})\right) = -\rho_{\mathrm{T}}\left[\Psi(\vec{r})\right], \tag{2.2}$$

where $H\left[\{\lambda(\vec{r})\}, \phi(\vec{r})\right]$ is the Hamiltonian that describes the electrons (or quasiparticles) in the system and that depends on a set of arbitrary parameters $\{\lambda(\vec{r})\}$ together with the electrostatic

potential $\phi(\vec{r})$. The first equation, Eq. (2.1), is the Schödinger equation, and its solutions provide the wavefunctions $\phi(\vec{r})$ and energies E of the eigenmodes of the system, i.e., the heterostructure in this thesis. The second equation, Eq. (2.2), is the Poisson equation and its solution gives the electrostatic potential in the system. It depends on the dielectric permittivity across the system $\epsilon(\vec{r})$ and the total charge density spread through the system $\rho_T [\Psi(\vec{r})]$. This charge density may be due to different sources, but it usually includes the mobile charges $\rho_{\mathrm{mobile}}(\vec{r})$ that correspond to the electrons or quasiparticles described by the Hamiltonian $H [\{\lambda(\vec{r})\}, \phi(\vec{r})]$. This charge density can be computed from the eigenstates $\Psi(\vec{r})$ and energy E. Therefore, these two equations must be solved together: in order to solve the Schrödinger equation one needs to know the electrostatic potential $\phi(\vec{r})$ by solving the Poisson equation, but at the same time one needs the solutions $\Psi(\vec{r})$ and E of the Schödinger equation to obtain the charge density $\rho_T [\Psi(\vec{r})]$ and thus solve the Poisson equation.

In this chapter, we explain our approach to solve these two equations together. We first explain in Sec. 2.2 the self-consistent procedure that we follow in order to obtain the joint solution. It relies in an iterative method in which both equations are solved independently using the solutions computed at different steps on the procedure. The methods used to solve (independently) each branch of the SP equation are explained in Sec. 2.3 and 2.4. In Sec. 2.3, we first explain the finite difference method (FDM) that allows us to solve the Schrödinger equation to obtain its eigenmodes. On the other side, we explain the methods that we use to solve the Poisson equation in Sec. 2.4, that relies on the more sophisticated finite element method (FEM). The methods explained in these two chapters are standard and they are widely explained and discussed in the literature (see, for example, Ref. [134]).

2.2 Self-consistent scheme

The SP equation (2.1-2.2) constitutes a non-linear equation inasmuch each branch of the equation depends on the other in a non-linear way. More particularly, Eq. (2.1) defines the functional $\tilde{\rho}_T[\phi(\vec{r})]$ for a given electrostatic potential $\phi(\vec{r})$, while Eq. (2.2) defines in turn the functional $\tilde{\phi}[\rho_T(\vec{r})]$ for a given charge density $\rho_T(\vec{r})$. The solution to the SP equation must be a self-consistent solution to both equations, i.e., the functional provided by one of the equations, such as the charge density, must be consistent with the one provided by the other branch. Hence, it satisfies

$$\tilde{\rho}_T[\tilde{\phi}[\rho_T]] - \rho_T = 0. \tag{2.3}$$

This equation can be understood as a minimization problem, in which one looks for a solution that minimizes the difference between the solutions provided by both equations. Unfortunately, this kind of problems do not have an analytical solution for arbitrary conditions due to the complex dependence of the non-linear equation. Thus, they have to be solved using numerical methods.

The most popular ones are based on iterative procedures, mainly the Newton-Raphson's methods [134]. In these methods, both equations are decoupled, so that one solves two separate linear

equations (that are easy to solve), but at the cost of solving them several times. In each step of the procedure, one checks the self-consistency of the solution, and changes the functional accordingly so that Eq. (2.3) is closer to be satisfied. The key is how to choose this change in an appropriate way so that the solution converges quickly to the correct one. Several sophisticated methods have been developed to this end in the context of quantum mechanics, such as the Broyden [135] or the Anderson mixing [136] methods, as well as their modifications [137]. It has been shown [138] that the simpler Anderson mixing one, although being rather simple, leads to a very fast convergence when compared to others of the same kind. We have thus used this method in this thesis (see Algorithm 2.1 for the pseudo-code).

In this approach, one proposes a trial solution at the first step of the iterative procedure. In an arbitrary case, we use $\rho_{\text{mobile}}^{(0)} = 0$, or, if known, the charge density computed at slightly different parameters (e.g., at a similar gate potential during a potential sweep). We then compute first the electrostatic potential solving the Poisson equation (2.2) (see Sec. 2.4 for the methods) in order to obtain the electrostatic potential; and then we solve the Schrödinger equation (2.1) (see Sec. 2.3 for the methods) to obtain the wavefunctions, and from there, the charge density $\tilde{\rho}_{\text{mobile}}^{(1)}$. For the followings steps, we use the so-called two-step Anderson mixing [136],

$$\rho_{\text{mobile}}^{(n)} = \beta\tilde{\rho}_{\text{mobile}}^{(n)} + (1 - \beta)\rho_{\text{mobile}}^{(n-1)}, \tag{2.4}$$

where n is a certain iteration step in the self-consistent process, and β is the so-called Anderson coefficient, which is a constant in the range $[0, 1]$. With this mixing, one computes the charge density at the n step, $\rho_{\text{mobile}}^{(n)}$, by mixing the charge density computed in the step before, $\rho_{\text{mobile}}^{(n-1)}$, with the one obtained by solving the Schrödinger equation using $\rho_{\text{mobile}}^{(n-1)}$, that is, $\tilde{\rho}_{\text{mobile}}^{(n)} = \tilde{\rho}_{\text{mobile}}^{(n)}[\tilde{\phi}[\rho_{\text{mobile}}^{(n-1)}]]$. This iterative scheme is kept until the cumulative error between the charge density at two consecutive steps, $\rho_{\text{mobile}}^{(n)}$ and $\rho_{\text{mobile}}^{(n-1)}$, is below some threshold. This limit depends on the desired accuracy to solve the problem, and we usually set it between 1%–0.1% in our simulations.

In principle, one can set $\beta = 1$, so that the charge density at the n step, $\rho_{\text{mobile}}^{(n)}$, is directly the charge density obtained by solving the Schrödinger equation using the charge density at the previous step, $\tilde{\rho}_{\text{mobile}}^{(n)}$. Although it could work in some (elementary) problems, e.g., when it turns out to be that there is no mobile charge $\rho_{\text{mobile}} = 0$; it is not in general a good idea since the numerical stability is not guaranteed: the changes in the charge density at different steps could be so large that the procedure does not lead to convergence. By using the mixing of Eq. (2.4), one artificially reduces the possible change of the charge density between consecutive steps, so that the solution is reached in a progressive way. Hence, one has to choose a small enough β so that the convergence is ensured, but not too small so that it takes too much time to converge, what would increase the computational cost of the process. To facilitate an efficient convergence, we choose as Anderson coefficient a self-adaptive one (that depends on the step n) given by,

$$\beta^{(n)} = \beta_{\max} \cdot \exp\left(-\frac{\max\left\{\left||\rho_{\text{mobile}}^{(n)}| - |\rho_{\text{mobile}}^{(n-1)}|\right|\right\}}{\max\left\{|\rho_{\text{mobile}}^{(n)}|, |\rho_{\text{mobile}}^{(n-1)}|\right\}}\right), \tag{2.5}$$

Algorithm 2.1: Pseudo-code of the two-step Anderson mixing method, a self-consistent iterative method that allows to compute the solution to the Schrödinger-Poisson equation.

Set $\rho_{\text{mobile}}^{(0)} = 0$.
repeat
    Compute $\phi(\vec{r})$ from the Poisson equation [Eq. (2.2)] using $\rho_{\text{mobile}}^{(n-1)}$.
    Compute the wavefunctions from the Schrödinger equation [Eq. (2.1)] using the new $\phi(\vec{r})$.
    Compute $\rho_{\text{mobile}}^{(n)}$ from the new wavefunctions.
    if $\left| \rho_{\text{mobile}}^{(n)} - \rho_{\text{mobile}}^{(n-1)} \right| > \left| \rho_{\text{mobile}}^{(n-1)} - \rho_{\text{mobile}}^{(n-2)} \right|$ **then**
        $\beta^{(\text{max})} = \beta^{(\text{max})}/2$.
    end if
    Update $\beta^{(n)}$ through Eq. (2.5).
    Perform the Anderson mixing $\rho_{\text{mobile}}^{(n)} = \beta\rho_{\text{mobile}}^{(n)} + (1 - \beta)\rho_{\text{mobile}}^{(n-1)}$.
until $\left| \rho_{\text{mobile}}^{(n)} - \rho_{\text{mobile}}^{(n-1)} \right| \leq$ Desired accuracy
Compute any desired observable.

---

where β_{max} is the maximum value that we allow the Anderson coefficient to take in order to ensure converge; and $\max\{f(x)\}$ is the maximum of the function or set of functions $f(x)$. With this prescription, if the charge density variation between two steps, $|\rho_{\text{mobile}}^{(n)}| - |\rho_{\text{mobile}}^{(n-1)}|$, is too large, then the exponential decay suppresses the mixing ($\beta \to 0$) and the charge density at the n step is changed only slightly. On the other hand, if the variation is too small, then the Anderson coefficient roughly takes the maximum value it can, $\beta \simeq \beta_{\text{max}}$. We set β_{max} ranging from 0.3–0.05 in our simulations depending on the system. Usually, small systems and/or systems with several boundary conditions allow to take 0.3, providing a fast convergence. On the other hand, large systems and/or systems that strongly depends on the charge density (i.e., ρ_{mobile} changes dramatically with ϕ) need a small β_{max}, like 0.05, leading to a slow convergence. For an arbitrary case, this value has to be set empirically.

Using this technique, the solutions along the self-consistent process steadily reaches a fixed point. We know that this fixed point is the correct solution because there are two theorems that ensure that the SP equation has only one possible solution for $\phi(\vec{r})$ and $\rho_{\text{mobile}}(\vec{r})$. The first one is the uniqueness theorem of the Poisson equation, that states that given an arbitrary source term ρ_{T} and Dirichlet boundary conditions, the solution to the Poisson equation is unique. Therefore, this branch can only contribute with one fixed point. The second theorem is the Hohenberg-Kohn theorem of existence [139], which states that given any arbitrary electronic charge density that gives rise to some electrostatic interactions in the Hamiltonian, the ground state of that Hamiltonian is unique. Since the ground state fixes the charge density distribution in turn (and any other observable), then we conclude that the charge density provided by the Hamiltonian must be unique given an

arbitrary electrostatic potential. Therefore, this brunch also contributes with a single fixed point. And this point necessarily corresponds to the correct solution.

It can nevertheless happen that, after a smooth convergence, the solutions end up oscillating around the fixed point without converging to it, e.g., $\rho_{\text{mobile}}^{(n)} = \rho_{\text{mobile}}^{(n+2)}$ and $\rho_{\text{mobile}}^{(n-1)} = \rho_{\text{mobile}}^{(n+1)}$. There are several ways to overcome this problem. The most obvious one is choosing a smaller $\beta_{\max}$ from the beginning. However, this makes the process slower and could still lead to oscillations, although with smaller amplitude. Another approach, typically chosen in the literature [136, 138], is to expand the mixing of Eq. (2.4) to further previous iterations, i.e., $\rho_{\text{mobile}}^{(n-2)}$, $\rho_{\text{mobile}}^{(n-3)}$,..., until $\rho_{\text{mobile}}^{(n-m)}$. This is usually called the m-step Anderson mixing, and it has been shown that the optimal value is $m = 3$ or $m = 4$ [138]; as the power of the method increases very slowly for $m \geq 3$, and with $m = 3$ one already prevents the oscillations. Despite of its success, we choose another approach as we find difficult to generalize Eqs. (2.4) and (2.5) for an arbitrary m (or even $m = 3$) and it moreover introduces more free parameters to adjust. Within our approach, we simply halve $\beta_{\max}$ during the iterative process whenever the charge density between two consecutive steps grows instead of diminishes. Therefore, the process follows the regular pace imposed by the initial $\beta_{\max}$, until the oscillations are reached (if any). Then the oscillations are artificially reduced by reducing $\beta_{\max}$.

Finally, we note that similarly to Eq. (2.3), one can also state the same for the electrostatic potential, i.e., $\tilde{\phi}[\tilde{\rho}_\text{T}[\phi]] - \phi = 0$. This implies that the Anderson mixing of Eq. (2.4) must be done with the electrostatic potential instead. Mathematically, both corresponds to the same problem, but the numerical stability and accuracy of its solutions could be different [131], depending on the problem.

2.3 Schrödinger equation

Equation (2.1) is the time-independent Schrödinger equation. It constitutes an eigenvalue problem whose eigenvalues and eigenfunctions allow to obtain the energies E and wavefunctions Ψ (correspondingly) of the normal modes of a given Hamiltonian H. This Hamiltonian, in our work, describes the electrons (and holes) inside the heterostructure, but the methods explained here are general for any hermitian Hamiltonian.

The Hamiltonians in this thesis usually posses several terms, such as kinetic, spin-orbit or electrostatic interactions. These terms could have a dependence on momentum $\vec{k}$, and due to the low-dimensionality of the systems that we are interested in, they could also have some spatial dependence $\lambda(\vec{r})$ along the finite directions. This is the case, for instance, of the 3D extension of the Oreg-Lutchyn Hamiltonian [Eq. (1.6)] that we wish to solve. Because of this complex and general dependence on $\vec{r}$ and $\vec{k}$, this Hamiltonian does not have in general an analytical solution, so it has to be solved using numerical methods. Below, we outline the ones that we use in this thesis. We have computationally implemented them in Python programming language, and the resulting code is published as a package called `Majorana Nanowires: Quantum Simulation Package` [133].

2.3.1 Finite low-dimensional systems

Let us focus for the moment in a system that is finite along the three directions, as it happen in real experiments. In this case, for an arbitrary system, one fully transforms the Hamiltonian into position space, performing the transformation $k_j \to -i\partial_j$. Then, the Schrödinger equation transforms into a linear partial differential equation whose solutions, in general, cannot be found analytically. In order to solve it, we use a conventional widely-used method for solving differential partial equations called the finite difference method (FDM). In its simplest form, it consists on discretizing the space into a regular rectangular mesh [see Fig. 2.1(b) for an example], in such a way the position operator is discretized $\vec{r} = (x, y, z) \to r_{i,j,k} = (ih_x, jh_y, kh_z)$, where (i, j, k) labels the position of each mesh point and h_η is the (regular) mesh spacing along the direction η. In this manner, the wavefunction $\Psi(\vec{r}) \to \Psi_{i,j,k}$ only applies to the mesh points, as well as any spatial dependent quantity in the Hamiltonian, $\lambda(\vec{r}) \to \lambda_{i,j,k}$. In the same way, the derivatives in the Hamiltonian are also discretized in the mesh using the finite difference scheme. For each point (i, j, k) that is not located at the boundaries of the system, one can replace the derivative of any spatial-dependent function $\lambda(\vec{r})$ using the first-order *central* differences method

$$\vec{\nabla}\lambda(\vec{r}) = (\partial_x\lambda(\vec{r}), \partial_y\lambda(\vec{r}), \partial_z\lambda(\vec{r})) \to$$
$$\left(\frac{\lambda_{i+1,j,k} - \lambda_{i-1,j,k}}{2h_x}, \frac{\lambda_{i,j+1,k} - \lambda_{i,j-1,k}}{2h_y}, \frac{\lambda_{i,j,k+1} - \lambda_{i,j,k-1}}{2h_z} \right). \tag{2.6}$$

For any point at the boundaries, we use instead the first-order *forward* or *backward* difference method, as λ_{i+1} or λ_{i-1} is not well-defined at the boundaries. The forward difference derivative is given by

$$\vec{\nabla}\lambda(\vec{r}) = (\partial_x\lambda(\vec{r}), \partial_y\lambda(\vec{r}), \partial_z\lambda(\vec{r})) \to$$
$$\left(\frac{\lambda_{i+1,j,k} - \lambda_{i,j,k}}{h_x}, \frac{\lambda_{i,j+1,k} - \lambda_{i,j,k}}{h_y}, \frac{\lambda_{i,j,k+1} - \lambda_{i,j,k}}{h_z} \right), \tag{2.7}$$

and the backward difference is the same but subtracting 1 to the indices affected by the derivative. For the second order derivatives, we use the same central difference scheme

$$\vec{\nabla}^2\lambda(\vec{r}) = \left(\partial_x^2\lambda(\vec{r}), \partial_y^2\lambda(\vec{r}), \partial_z^2\lambda(\vec{r}) \right) \to$$
$$\left(\frac{\lambda_{i+1,j,k} - 2\lambda_{i,j,k} + \lambda_{i-1,j,k}}{h_x^2}, \frac{\lambda_{i,j+1,k} - 2\lambda_{i,j,k} + \lambda_{i-1,j-1,k}}{h_y^2}, \frac{\lambda_{i,j,k+1} - 2\lambda_{i,j,k} + \lambda_{i,j,k-1}}{h_z^2} \right). \tag{2.8}$$

Notice that, since the Hamiltonian is to be applied to the wavefuncion in the Schrödinger equation $H[\{\lambda(\vec{r})\}]\Psi(\vec{r})$, the derivatives must be also applied to the wavefunctions $\Psi(\vec{r})$, applying the chain rule first, if needed. One can actually write the Hamiltonian in the FDM as a matrix, and thus, the Schrödinger equation can be written as a matrix product between the Hamiltonian and the wavefunction (which can be written as a column vector). The Hamiltonian written in this way turns out to be similar to a tight-binding Hamiltonian.
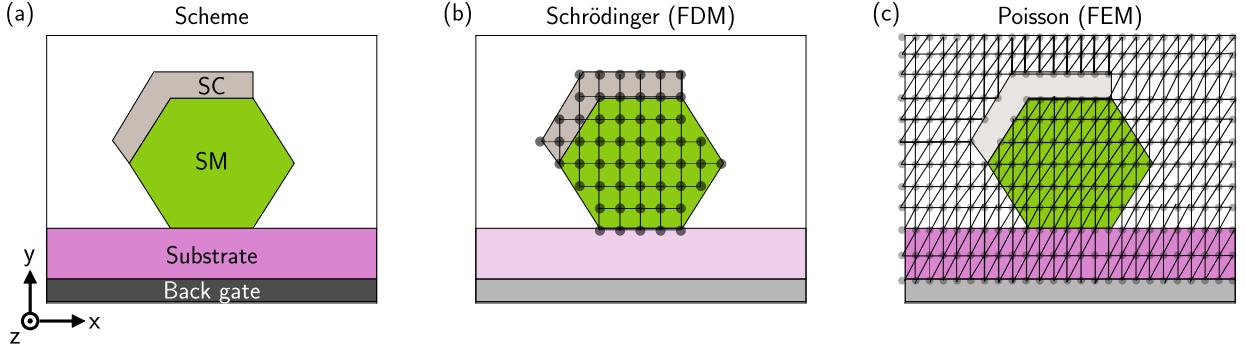
Figure 2.1: (a) Sketch of a prototypical nanostructure simulated in this thesis, a partial-shell SM-SC hybrid nanowire. (b) Sketch of the mesh used to solve the the Schrödinger equation. We use the finite difference method (FDM) with a rectangular grid. Notice that the discretization only applies to non-insulating materials (the SM wire and SC layer in this case). (c) Sketch of the mesh used to solve the Poisson equation. We use the finite element method (FEM) with a self-adaptive Lagrange (type 1) element. In this case, the entire space is discretized.

One has to be careful when writing down the continuum Hamiltonian because the resulting tight-binding Hamiltonian could be non-hermitian[1]. Particularly, any term with both, a spatial dependent parameter and a derivative, must be symmetrized. One example is the SO interaction term $\vec{\alpha}(\vec{r}) \cdot \left(\sigma \times \vec{k} \right)$ that does not give rise to a hermitian Hamiltonian in real space unless it is simetrized as $\frac{1}{2} \left[\vec{\alpha}(\vec{r}) \cdot \left(\sigma \times \vec{k} \right) + \left(\sigma \times \vec{k} \right) \cdot \vec{\alpha}(\vec{r}) \right]$. For the second-order differential terms, like the kinetic energy, it is not necessary to perform the symmetrization if one writes them like $\vec{\nabla} \lambda(\vec{r}) \vec{\nabla}$, as this expression already provides hermitian terms in real space.

Once the Hamiltonian is written in matrix form, we obtain the wavefunctions $\Psi_{i,j,k}^{(n)}$ and energies $E^{(n)}$ for each mode n by diagonalizing it. We perform the diagonalization using the numerical methods implemented in the Python package `Scipy` [140], which basically provides a Python interface to `LAPACK` [141]. Our systems of interest are typically large, meaning that the resulting matrices cannot be stored in the memory RAM of conventional computers. But one can take advantage of the fact that the derivatives only give rise to nearest-neighbors interactions between adjacent sites of the mesh. This is translated to a Hamiltonian matrix that is mainly full with elements that are zero. This allows us to store the matrices in *sparse* form and take advantage of the efficient routines implemented to perform operations with them (also in `Scipy`).

Unfortunately, it is not possible to obtain all the eigenvalues and eigenvectors of a sparse matrix, only a few of them; and the computational resources (RAM memory and execution time) grows with the number of desired eigenmodes one is looking for. Anyway, we do not need all them to describe the main electronic properties of the systems that we are interested in. In non-superconducting

---

[1]Our starting Hamiltonians in this thesis are always hermitian, so are the resulting tight-binding ones. We note that a hermitian Hamiltonian ensures that the energies are always real.

heterostructures, the main electronic properties are either fixed by the states whose energies are close to the Fermi level; or the ground state, which are all the states whose energies are below the Fermi level. In the former, it is clear that it is enough to compute a few states below and above zero energy (the Fermi level). In the later, one has to compute all the eigenvalues below the Fermi level, and a few of them above if temperature is finite. Despite the fact that the number of states below the Fermi level could be huge, we are mainly interested in a low doping limit, since this is the important regime for topological superconductivity, and therefore, this number is always small. In superconducting systems, we are always interested in the subgap states, so it is enough to compute a few eigenstates close to zero energy up to the superconducting gap.

Lastly, we remark that the diagonalization of sparse matrices is never an exact[2] diagonalization, but the eigenstates are found up to some desired accuracy at the cost of increasing the running time of the program. This is important as the wavefunction in each point of the mesh could be given by a small number (i.e., smaller than 10^{-4}, the fourth decimal), and the wavefunction may be not correctly normalized. We set the precision at which the eigenstates are found up to 10^{-8} (i.e., up to the eighth decimal).

The FDM ensures that the numerical solution approaches the correct one as the discretization vanishes, $h \to 0$. Taking a too small spacing increases nevertheless the computational cost, as the number of mesh points increases, so does the size of the Hamiltonian matrix. On the other hand, a too large value of h leads to nonphysical solutions that depends on the spacing, which is not a physical quantity. The best way to choose an appropriate value for the spacing h is to take a small enough one so that it can accommodate the Fermi wavelength of the eigenstates computed. Usually, four times smaller than that is enough. One can check the solutions are not "wrong" by verifying that the solutions barely change with a smaller spacing.

The mobile charge density can be directly computed from the eigenfunctions and energies of the normal modes. In a non-superconducting system, the eigenfunction is described by a two-components spinor because of the spin space structure, $\Psi^{(n)}(\vec{r}) = (\psi_\uparrow^{(n)}(\vec{r}), \psi_\downarrow^{(n)}(\vec{r}))^t$, and the charge density can be computed from them as

$$\rho_{\text{mobile}}(\vec{r}) = -e \sum_n \left\langle \Psi^{(n)}(\vec{r}) \middle| \sigma_0 f_{\text{FD}} \left(E^{(n)} \sigma_0 \right) \middle| \Psi^{(n)}(\vec{r}) \right\rangle$$

$$= -e \sum_n \int \left(\left| \psi_\uparrow^{(n)}(\vec{r}) \right|^2 + \left| \psi_\downarrow^{(n)}(\vec{r}) \right|^2 \right) f_{\text{FD}} \left(E^{(n)} \right) d\vec{r}. \tag{2.9}$$

In the superconducting case, the eigenfunctions have four components due to the Nambu space

---

[2]With "exact", we mean "up to machine precision" in the context of numerical methods.

structure, $\Psi^{(n)}(\vec{r}) = (\psi_{\uparrow,e}^{(n)}(\vec{r}), \psi_{\downarrow,e}^{(n)}(\vec{r}), \psi_{\uparrow,h}^{(n)}(\vec{r}), \psi_{\downarrow,h}^{(n)}(\vec{r}))^t$, and the charge density is given by

$$
\rho_{\text{mobile}}(\vec{r}) = -e \sum_{n\forall E^{(n)} \geq 0} \left\langle \Psi^{(n)}(\vec{r}) \middle| \sigma_0 \tau_0 f_{\text{FD}}\left(E^{(n)} \sigma_0 \tau_z\right) \middle| \Psi^{(n)}(\vec{r}) \right\rangle
$$

$$
= -e \sum_{n\forall E^{(n)} \geq 0} \int \left[\left(\left|\psi_{\uparrow,e}^{(n)}(\vec{r})\right|^2 + \left|\psi_{\downarrow,e}^{(n)}(\vec{r})\right|^2 \right) f_{\text{FD}}\left(E^{(n)}\right) \right.
$$

$$
\left. + \left(\left|\psi_{\uparrow,h}^{(n)}(\vec{r})\right|^2 + \left|\psi_{\downarrow,h}^{(n)}(\vec{r})\right|^2 \right) f_{\text{FD}}\left(-E^{(n)}\right) \right] \mathrm{d}\vec{r}. \tag{2.10}
$$

2.3.2 Bulk low-dimensional systems

In this thesis, we are particularly interested in quasi-1D systems. These systems are strongly confined in two directions (the cross section of the heterostructure) so that they give rise to transverse subbands. Conversely, the other direction is much larger, meaning that the confinement is weaker or even non-existent. Sometimes, we are just interested in the bulk properties of these quasi-1D systems, so that we assume that the system is translational invariant along the weak-confined direction. Even if these simulations do not correspond to a particular experimental setup, they allow to obtain some qualitative predictions that helps to understand the observed/expected behavior in experiments, like a topological phase transition.

Let us assume that the translational invariant direction is the z direction, so that the spatial dependent quantities only depend on the x and y directions, and thus $\vec{r} = (x, y)$. Since our model effectively works at larger scales than the atomic one, which is integrated out inside the parameters as we explain in the following sections, we can take that k_z is conserved. This means that the operator k_z can be directly transformed into a number. This number is called quantum number in the literature, as it also labels the eigenstates of a quantum system. In the other directions, the x and y directions, we nevertheless perform a discretization of the space, and we apply the FDM after transforming the momentum operators by their corresponding partial derivatives, $k_{x,y} \rightarrow -i\partial_{x,y}$. We use the same scheme as explained in the previous subsection along these directions, while keeping k_z as an input number. We diagonalize the resulting Hamiltonian for each k_z using the same methods as before. The eigenvalues and eigenstates of this Hamiltonian correspond to the energy dispersion $E^{(n)}(k_z)$ and wavefunctions $\Psi^{(n)}(\vec{r}, k_z)$, correspondingly, of the normal mode n of the electronic system.

In this case, the mobile charge density for a non-superconducting system can be computed from the eigenfunctions as

$$
\rho_{\text{mobile}}(\vec{r}) = -\frac{e}{2\pi} \sum_n \int \left\langle \Psi^{(n)}(\vec{r}, k_z) \middle| \sigma_0 f_{\text{FD}}\left(E^{(n)}(k_z)\sigma_0\right) \middle| \Psi^{(n)}(\vec{r}, k_z) \right\rangle \mathrm{d}k_z. \tag{2.11}
$$

In close relation to this quantity, we can also compute the density of states (DOS) for each spin as

$$
\text{DOS}_{\uparrow,\downarrow}(E) = \sum_n \int_{\vec{r}} d\vec{r} \int_{k_z} dk_z \cdot \delta(E - E^{(n)}(k_z)) \left|\Psi_{\uparrow,\downarrow}^{(n)}(\vec{r}, k_z)\right|^2. \tag{2.12}
$$

The total DOS can be obtained by summing both spin directions, $\text{DOS}_\text{T} = \text{DOS}_\uparrow + \text{DOS}_\downarrow$.

2.3.3   Topological invariant for low-dimensional systems

The topological phase of a bulk nanowire can be characterized through the topological invariant. We compute the D-class topological invariant [4, 142] (to which the Majorana nanowires belong) by computing the Chern number of the wire

$$C = \frac{1}{2\pi i} \int_{R_{k_z}} dk_z \left\langle \nabla_{k_z} \Phi_{k_z} \left| \times \right| \nabla_{k_z} \Phi_{k_z} \right\rangle, \tag{2.13}$$

where R_{k_z} denotes the first Brillouin zone ($k_z \in (-\pi, \pi]$ in our system), and Φ_{k_z} is the ground state of the system, i.e., the Slater determinant of all the n-th eigenstates whose energies $E^{(n)}$ are below the Fermi energy. To easily compute numerically the Chern number we perform some transformations following the ideas of Refs. [143–145]. First, we apply the Stokes theorem

$$C = \frac{1}{2\pi i} \oint_{\partial R_{k_z}} dk_z \left\langle \Phi_{k_z} | \nabla_{k_z} \Phi_{k_z} \right\rangle, \tag{2.14}$$

in such a way that the (line) integral is now performed through a closed contour around the reciprocal unit cell. Then, we discretize the momentum space $k_z \to k_l$, what allows us to replace the derivatives by finite differences and the integral by a summation over the reciprocal space points

$$C = \frac{1}{2\pi i} \sum_l \frac{\left\langle \Phi_{k_l} | \Phi_{k_{l+1}} \right\rangle - \left\langle \Phi_{k_l} | \Phi_{k_{l-1}} \right\rangle}{2(k_{l+1} - k_l)} = \frac{1}{2\pi} \text{Arg} \left\{ \prod_l \left\langle \Phi_{k_l} | \Phi_{k_{l+1}} \right\rangle \right\}, \tag{2.15}$$

where $\text{Arg}\{z\} \equiv \text{Im}\left\{\log\left(\frac{z}{|z|}\right)\right\}$ is the complex argument function of a complex number z. The product of Slater determinants $\left\langle \Phi_{k_l} | \Phi_{k_{l+1}} \right\rangle$ in the above equation can be rewritten as a determinant of a matrix $\tilde{C}_{k_l, k_{l+1}}$, whose matrix element (i, j) can be directly written in terms of the eigenfunctions of the Hamiltonian,

$$\tilde{C}^{i,j}_{k_l, k_{l+1}} = \left\langle \Psi^{(i)}(k_l) | \Psi^{(j)}(k_{l+1}) \right\rangle. \tag{2.16}$$

From this, the Chern number is simply given by

$$C = \frac{1}{2\pi} \text{Arg} \left\{ \det \left(\prod_l \tilde{C}_{k_l, k_{l+1}} \right) \right\} \equiv \frac{1}{2\pi} \text{Arg} \left\{ \det(\mathcal{W}) \right\}, \tag{2.17}$$

where $\mathcal{W}$ is the so-called Wilson matrix in the literature [146–148]. Finally, we use that the determinant of any square matrix can be written as the product of its eigenvalues to rewrite the expression as

$$C = \frac{1}{2\pi} \sum_l \text{Arg} \left\{ \lambda_l \right\}, \tag{2.18}$$

where λ_l are all the eigenvalues of $\mathcal{W}$. In practice, it is enough to include only the high-symmetry k-points in the product inside the Wilson matrix. In our case, these points are $k_z = \{-\pi, 0, \pi\}$,

which gives as a result the Wilson matrix

$$\mathcal{W} = \tilde{C}_{-\pi,0}\tilde{C}_{0,\pi}\tilde{C}_{\pi,-\pi}. \tag{2.19}$$

Additionally, notice that in principle the matrix $\tilde{C}_{k_l,k_{l+1}}$ involves all the eigenstates of the Hamiltonian (below the Fermi level) at two different k_z points, k_l and k_{l+1}, as shown in Eq. (2.16). But since only the non-trivial topological eigenstates provide a non-zero contribution to the Chern number, and these states can only emerge close to the Fermi level in the studied system, it is thus enough to include the closest states to the Fermi level in the Wilson matrix. This assumption allows to significantly alleviate the computational effort in our calculations.

To summarize this last part, the procedure that we follow in order to compute the topological invariant is the following: We first calculate the eigenstates $\Psi^{(n)}(k_z)$ of the Hamiltonian at $k_z = \{0, \pi, -\pi\}$. We need only those n-th states that are below and close to the Fermi energy. We find that 200 eigenstates are enough in our system to properly characterize the topological phase. We then compute the coupling matrices $\tilde{C}_{k_l,k_{l+1}}$ of Eq. (2.16) and, from them, the Wilson matrix $\mathcal{W}$ using Eq. (2.19). We calculate its eigenvalues λ_i, and from them, we compute the Chern number using Eq. (2.18), which is a positive integer. We finally identify the $\mathbb{Z}_2$ topological invariant with

$$\mathcal{Q} = (-1)^C, \tag{2.20}$$

which is positive $(+1)$ in the trivial topological phase and negative (-1) in the non-trivial one.

2.4 Poisson equation

In principle, it is also possible to solve the Poisson equation [Eq. (2.2)] using the FDM, as Eq. (2.2) constitutes a linear partial differential equation as well. We nevertheless prefer to use a more sophisticated and efficient method, the finite element method (FEM). The FEM is very similar to the FDM, but it takes an integral form instead a differential one. It is easier to implement for arbitrary geometries and inhomogeneous meshes, and it usually has a better accuracy and performance. However, it is not easy to implement for an arbitrary differential equation, and it is not an exact method either. Fortunately, there are several numerical packages that allows for an efficient and stable implementation.

In the FEM, one has to transform the Poisson equation in integral form, also known as weak formulation, that allows for a simpler numerical treatment. This can be done by multiplying both sides of Eq. (2.2) by a test function φ, and then integrating both sides over the whole system Ω

$$\int_\Omega \varphi(\vec{r})\vec{\nabla} \cdot \left(\epsilon(\vec{r}) \cdot \vec{\nabla}\phi(\vec{r})\right)\mathrm{d}\vec{r} = -\int_\Omega \varphi(\vec{r})\rho_\mathrm{T}\mathrm{d}\vec{r}. \tag{2.21}$$

Using the chain rule on the left side and applying the Stokes' theorem[3], we obtain

$$\int_{\partial\Omega} \left(\varphi(\vec{r})\epsilon(\vec{r})\vec{\nabla}\phi(\vec{r})\right) \cdot \vec{n} \mathrm{d}\vec{S} - \int_{\Omega} \vec{\nabla}\varphi(\vec{r}) \cdot \left(\epsilon(\vec{r}) \cdot \vec{\nabla}\phi(\vec{r})\right) \mathrm{d}\vec{r} = -\int_{\Omega} \varphi(\vec{r})\rho_{\mathrm{T}}(\vec{r})\mathrm{d}\vec{r}, \qquad (2.22)$$

where $\partial\Omega$ is the boundary of the system, and $\vec{n}$ and $\mathrm{d}\vec{S}$ is the normal vector and (surface) differential along it, respectively. If there are no Neumann conditions, then it is satisfied that $\vec{\nabla}\phi(\vec{r}) \cdot \vec{n} = 0$ at the boundaries of the the system, so that the first term in the above equation is zero. In this way, we arrive to the expression

$$\int_{\Omega} \vec{\nabla}\varphi(\vec{r}) \cdot \left(\epsilon(\vec{r}) \cdot \vec{\nabla}\phi(\vec{r})\right) \mathrm{d}\vec{r} = \int_{\Omega} \varphi(\vec{r})\rho_{\mathrm{T}}(\vec{r})\mathrm{d}\vec{r}, \qquad (2.23)$$

which is the weak formulation of the Poisson equation (without Neumann conditions). It is called "weak" because it has no second-order partial derivatives, as opposed to the original differential equation, so it needs weaker constraints on its differentiability.

So far we have made use of no approximations. But Eq. (2.23) is still too general to be solved analytically. To solve it numerically, we follow a similar reasoning than for the FDM, and we discretize the space using a mesh (not necessarily regular). But contrary to the FDM, we find the solution over the whole surface among nodes, u_j, called finite element, and not on each node. This can be done since Eq. (2.23) is written in integral form. We moreover allow the solution to vary across the element, $u_j(\vec{r})$, following some *ad hoc* interpolation function that we impose. To do so, we discretize in turn the element in several nodes, that can be placed in the boundaries but also in the surface/volume. This allows to get the solution with better accuracy. Hence, the potential $\phi(\vec{r})$, as well as the test function $\varphi(\vec{r})$, can be written in terms of these element basis as a weighted sum of them

$$\phi(\vec{r}) \rightarrow \sum_i M_i u_i(\vec{r}), \qquad (2.24)$$

$$\varphi(\vec{r}) \rightarrow \sum_i M_i v_i(\vec{r}), \qquad (2.25)$$

where M are the weights for each element that we want to find in order to obtain the solution.

Using this element basis, we can write Eq. (2.23) as

$$\sum_j M_j \int_{\Omega} \vec{\nabla}v_i(\vec{r}) \cdot \left(\epsilon(\vec{r}) \cdot \vec{\nabla}u_j(\vec{r})\right) \mathrm{d}\vec{r} = \int_{\Omega} v_i(\vec{r})\rho_{\mathrm{T}}(\vec{r})\mathrm{d}\vec{r} \leftarrow \forall i \in \text{mesh}, \qquad (2.26)$$

that can be written in matrix form as a linear equation,

$$AM = b, \qquad (2.27)$$

---

[3]Particularly $\int_{\Omega} \vec{\nabla} \cdot \left(\varphi(\vec{r})\epsilon(\vec{r})\vec{\nabla}\phi(\vec{r})\right) \mathrm{d}\vec{r} = \int_{\partial\Omega} \left(\varphi(\vec{r})\epsilon(\vec{r})\vec{\nabla}\phi(\vec{r})\right) \cdot \vec{n}\mathrm{d}\vec{S}$.

where

$$A_{ij} = \int_\Omega \vec{\nabla} v_i(\vec{r}) \cdot \left(\epsilon(\vec{r}) \cdot \vec{\nabla} u_j(\vec{r}) \right) \mathrm{d}\vec{r}, \tag{2.28}$$

$$b_j = \int_\Omega v_i(\vec{r}) \rho_\mathrm{T}(\vec{r}), \tag{2.29}$$

can be numerically computed by performing the integrals. The solutions can be simply found by solving Eq. (2.27) to obtain M. Once again, one can take advantage of the sparsity of the matrix A to solve efficiently the problem. Notice that $\epsilon(\vec{r})$ and $\rho_T(\vec{r})$ must be written in the same element basis to perform the integrals.

The key of the FEM is how to choose appropriately the element (both the shape and the nodes inside) together with the interpolation function. This is problem-dependent, as the interpolation function should capture well-enough the variations of the solution across the element. And this depends on the order of the differential equation and its boundary conditions, among others. But for the linear Poisson equation, it has been shown that a simple Lagrange element with a linear interpolation function is accurate enough [see Fig. 2.1(c) for an example of the mesh]. We discretize the space with this element and solve the Poisson equation using an open-source package for Python called `FEniCS` [149, 150], that solves, in an efficient way, arbitrary differential equations using the FEM.

CHAPTER 3

SEMICONDUCTOR NANOWIRES: ELECTRONIC PROPERTIES

In this chapter we derive the single-band Hamiltonian that *accurately* describes the conduction band of III-V compound SM nanowires starting from a (more accurate) 8-band description. We obtain the dependence of its parameters –the effective mass and SO coupling– with the spatial-dependent electrostatic potential inside the wire. Furthermore, we simulate realistic nanowire devices to show the typical values these parameters can exhibit. In addition, we derive the same Hamiltonian but in the presence of strain and we show that strain at the wire interface enhances the SO coupling of the nanowire.

The contents of this chapter are based mainly on our published article in Phys. Rev. Research **2**, 033264 (2020) [151]; and, to a lower extend (only Sec. 3.4), on a work still in preparation [152].

3.1 Introduction

SM nanowires are ideal platforms for creating quasi-1D quantum devices with potential applications in sensing devices [153–155], spintronics [156, 157] and quantum computing [22, 41, 44]. They are characterized by optical gaps, posses a high mobility [65, 66], and their reduced (transverse) dimensionality imposes furthermore a substantial level spacing between the different sub-bands [67]. Hence, it is possible to tune the chemical potential of these wires in such a way that only a few sub-bands are occupied. Therefore, through transport experiments, one can provide useful information about the properties of the SM itself or other materials that are involved with the SM in a heterostructure.

Among all the SMs, the ones that we are interested in are those with a large SO coupling since they are the ones that can give rise to larger topological gaps, as explained in Chapter 1 [see Eq. (1.5)]. One well-characterized family of SMs with strong SO coupling is the III-V compound SMs [158–160], i.e. alloys made of elements from the group III of the periodic table (typically Al, Ga, In) and the group V (typically P, As and Sb). They can be binary compounds, such as GaAs or InP, or ternary, like InAsSb. However, the former are better characterized and easier to grow, and thus we focus in this thesis on them.

Regardless of the crystallographic orientation, III-V binary compound SMs roughly share the same low-energy band structure [159], see Fig. 3.1. All of them exhibit a direct gap around the Γ-point,
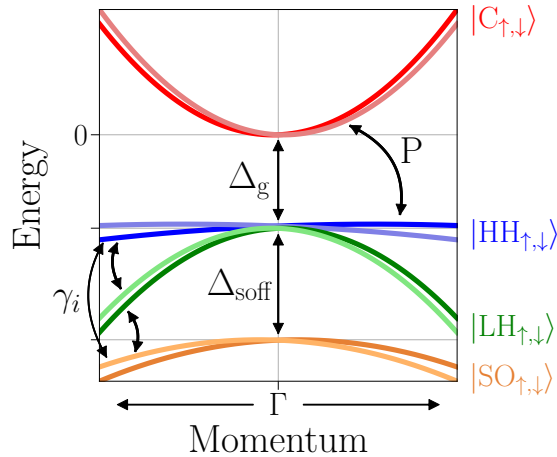
Figure 3.1: Schematic band diagram of III-V compound SMs. The lowest-energy spectrum takes place around the Γ-point, for which the energy bands exhibit a direct band gap $\Delta_{\rm g}$. It comprises the conduction band (in red) and the heavy hole (blue), light hole (green) and split-off (yellow) valence bands. Note all of them are spin-degenerate at the Γ-point. These bands can be analytically described using an 8-band k·p model through effective parameters that account for the conduction-to-valence band coupling P, intravalence band couplings γ_i, and SM and split-off gaps $\Delta_{\rm g}$ and $\Delta_{\rm soff}$, respectively. See Refs. [158, 159] for more details.

with the minimum of the CB and the maximum of the valence bands taking place there. The Fermi level typically falls in the middle of the gap or close to the CB. The lowest-energy spectrum comprises four spinful bands: the topmost three electronic states in the valence band, given by the heavy hole (HHB), light hole (LHB) and split-off (SOB) bands (usually referred as p-like states), and the first CB (referred as s-like state). Note that all these bands are doubly degenerate at the Γ-point, so they are actually eight in total.

This kind of materials can be grown in the form of nanowires with two different crystallographic directions [64, 65], wurtzite [(0001) direction] or zinc-blende [mainly the (111)], with (typically) a regular hexagonal cross section. During the last decade, experimentalists have done a big effort to characterize and improve the performance of these nanowires. Nowadays, these nanowires can be grown as single crystals, with a homogeneous radius and flat facets along the wire's direction. They present low concentration of impurities [65], although still far for their 2DEG counterparts [60, 62, 117]. This may have a tremendous impact for the formation of the topological phase [116, 117]. Their analysis, however, goes beyond the scope of this work.

In this chapter, we study the electronic properties of these SM nanowires. Particularly, we aim to understand the CB behavior under electrostatic interactions. In addition to this, we seek for a single-band Hamiltonian that can describe its lowest-energy properties. This is so because, as we will see in the following chapters, this band (at low energies) is the one of relevance in the heterostructures studied in this thesis. In Sec. 3.1, we start by reviewing its bulk properties, both for bulk crystals and nanowires. We use the standard k·p model that accurately describes the eight

lowest-energy bands of these SMs. From there, it is possible to derive a low-effective Hamiltonian than only applies to the CB. This Hamiltonian has renormalized parameters due to the interactions with the valence bands.

In Sec. 3.2, we study the electrostatic potential profile and charge density distribution of these nanowires by solving the SP equation. As we will see in the next section, Sec. 3.3, this electrostatic potential has a relevant impact on the electronics properties of the nanowires. Primarily, the SO coupling is dominated by this interaction. We provide there simple equations that can accurately describe the SO coupling dependence with the electrostatic potential, and we compare it with other theoretical methods and experiments. We find that these nanowires can support SO couplings ranging from 10 to 50 meV·nm, large enough to support a sizable topological phase.

Finally, in Sec. 3.4, we explore the effect of strain in these wires. We follow the same approach, and we derive a single-band Hamiltonian from an 8-band (8B) model but including possible strain. We find that, when the strain is compressing (like in InAs-InP or InAs-Al interfaces), the SO coupling is enhanced.

3.1.1 Effective conduction-band Hamiltonian for III-V compound semiconductors

We look for an effective Hamiltonian that could accurately describe the CB of a III-V compound SM. Multiband k·p theory is especially suited for this since it retains the symmetries of the lattice, and therefore describes the precise structure of the bands. Moreover, its parameters are extracted from more sophisticated methods, such as DFT or even experiments, giving rise to accurate and realistic predictions. As a drawback, it is not straightforward (or even, not always possible) to extract a effective single-band description from this multiband theory. Fortunately, as we are going to show, it is possible to do that for the CB of III-V compound SMs, although with some degree of approximation.

We start by providing here a general introduction to the multiband k·p extracted from several references [159, 161, 162]. It can be derived starting from the single-electron Hamiltonian

$$H_e = \frac{\vec{p}^2}{2m_e} - e\left(\phi_0(\vec{r}) + \phi(\vec{r})\right) + \frac{\hbar}{4m_e^2 c^2}\left[\vec{\nabla}\phi_0(\vec{r}) \times \vec{p}\right] \cdot \vec{\sigma} \rightarrow H\Psi = E\Psi, \tag{3.1}$$

where $\vec{p} = -i\hbar\vec{\nabla}$ is the momentum operator, m_e the (bare) electron mass, c the speed of light, $\phi_0(\vec{r})$ the (microscopic) electrostatic potential created by the lattice-periodic crystal, $\phi(\vec{r})$ the (slow-varying) one created by an external electric field, and $\vec{\sigma} = (\sigma_x, \sigma_y, \sigma_z)$ the vector of Pauli matrices for the spin degree of freedom. The first term of this Hamiltonian corresponds to the kinetic energy of the electron, the second one corresponds to the effective electrostatic potential energy experienced by the electrons inside some material, and the last one takes into account relativistic SO effects. Notice that we do not include the SO effects generated by $\phi(\vec{r})$, as the dominant contribution to the SO interaction stems from the atomic core potential $\phi_0(\vec{r})$. If the crystal is translational invariant, the potential $\phi_0(\vec{r})$ can be described using a periodic function. As

a consequence, the electron wave function satisfies the Bloch's theorem, i.e.,

$$\Psi_{n,k} = u_{n,k}(\vec{r})e^{i\vec{k}\cdot\vec{r}}, \tag{3.2}$$

where $\vec{k}$ is the wavevector restricted to the first Brillouin zone (and $\hbar\vec{k}$ is the so-called crystal momentum for a periodic system), n the quantum number that labels the different possible energy bands, and $u_{n,k}(\vec{r})$ is the so-called envelope function that encodes the periodic part of the wavefunction. Hence, the electron wave function satisfies the condition $\vec{p}\Psi_{n,k} = e^{i\vec{k}\cdot\vec{r}}(\hbar\vec{k} + \vec{p})u_{n,k}(\vec{r})$ that allows to write a Hamiltonian H_{kp} for the envelope function

$$H_e\Psi_{n,k} = E_{n,k}\Psi_{n,k} \rightarrow H_{\text{kp}}u_{n,k} = E_{n,k}u_{n,k} \rightarrow$$

$$H_{\text{kp}} = \frac{\vec{p}^2}{2m_e} - e\left(\phi_0(\vec{r}) + \phi(\vec{r})\right) + \frac{\hbar}{4m_e^2c^2}\left[\vec{\nabla}\phi_0(\vec{r}) \times \vec{p}\right] \cdot \vec{\sigma} + \hbar\frac{\vec{k}\cdot\vec{p}}{m_e}$$

$$+ \frac{\hbar^2\vec{k}^2}{2m_e} + \frac{\hbar^2}{4m_e^2c^2}\left[\vec{\nabla}\phi_0(\vec{r}) \times \vec{k}\right] \cdot \vec{\sigma}. \tag{3.3}$$

This Hamiltonian is known as the k·p Hamiltonian (because it includes a $\vec{k}\cdot\vec{p}$ term) and it describes the motion of an electron inside a periodic crystal.

In general, the k·p Hamiltonian has no analytical solution, so it is usually solved perturbatively. The most common way to do so is to expand the Hamiltonian around a point $\vec{k}_0$ in reciprocal space, whose solution is known, and then use Löwdin perturbation theory [163] to perform the expansion over a reduced basis set. Within this technique, the states are separated into two classes A and B. Class A includes the truncated basis set elements that describes the main aspects of the crystal. In principle, this basis set could include all the orbitals on each atom of the unit cell, but this would not help to decrease the complexity of the problem. Because of that, the less influential states not included in A are collected in class B. The couplings between class B and A states are the ones treated perturbatively.

In this representation, the envelope function (in Dirac notation) is written as a superposition of both kind of states

$$|n,k\rangle = \sum_{\alpha} c_{\alpha,n}(k)\,|\alpha\rangle + \sum_{\beta} c_{\beta,n}(k)\,|\beta\rangle, \tag{3.4}$$

where $|\alpha\rangle$ and $|\beta\rangle$ are the states in class A and B, respectively. The projection of the Hamiltonian onto the class A basis gives rise in the Löwdin expansion to the matrix elements

$$\langle\alpha|\,H_{\text{kp}}\,|\alpha'\rangle = \left[E_\alpha(\vec{k}_0) + \frac{\hbar^2(\vec{k}^2 - \vec{k}_0^2)}{2m_e}\right]\delta_{\alpha\alpha'} + \langle\alpha|\,\frac{\hbar}{m_e}(\vec{k} - \vec{k}_0)\cdot\vec{p}\,|\alpha'\rangle$$

$$+ \langle\alpha|\,\frac{\hbar}{4m_e^2c^2}\left[\vec{\nabla}\phi(\vec{r}) \times \vec{p}\right]\cdot\vec{\sigma}\,|\alpha'\rangle + \sum_\beta \frac{\langle\alpha|\,\frac{\hbar}{m_e}(\vec{k} - \vec{k}_0)\cdot\vec{p}|\beta\rangle\,\langle\beta|\,\frac{\hbar}{m_e}(\vec{k} - \vec{k}_0)\cdot\vec{p}|\alpha'\rangle}{E_\alpha - E_\beta}. \tag{3.5}$$

Unfortunately, these matrix elements cannot be evaluated analytically in general because one would need to know all the dipole terms $\langle\alpha|\,k\cdot p\,|\beta\rangle$ of all the transitions among the different states, as well

as their corresponding transition energies $E_\alpha - E_\beta$. For this reason, one firstly invokes symmetry arguments (related to the crystal symmetries) to know which matrix elements are forbidden, so they are set to zero; and secondly, one substitutes the remaining expressions by parameters, whose functional forms can be determined using group theory arguments. These parameters are called Luttinger or Kane parameters, and they can be extracted from experimental data or *ab initio* calculations.

In this work, since we are particularly interested on III-V binary compound SMs, we choose as the unperturbed Hamiltonian the one at the Γ-point ($k_0 = 0$) as the lowest-energy spectrum takes place there [see Fig. 3.1]. And for our representation basis, we consider as class A the first four (spinful) lowest-energy bands: the CB, HHB, LHB and SOB. Note that all these bands are doubly degenerate at the Γ-point, so the resulting Hamiltonian can be represented by a 8×8 matrix. For these tetravalence SM materials, it has been shown [164–166] that these eight bands are enough to describe their main electronic properties.

The relation between these band eigenstates and the valence band (*s*-type and *p*-type) atomic orbitals depends on the particular crystal structure of the selected material. Zinc-blende and wurtzite crystals are the most common crystal structures for these kind of semiconductors as they are easy to grow as nanowires and in layered structures. For concreteness, we focus for the moment only on zinc-blende crystals to derive the effective CB Hamiltonian. For these zinc-blende crystals, the bands basis is given by [165, 167].

$$
\begin{cases}
|C_\uparrow\rangle = |S_\uparrow\rangle, & |C_\downarrow\rangle = |S_\downarrow\rangle, \\[4pt]
|LH_\uparrow\rangle = \frac{i}{\sqrt{6}} |(X + iY)_\downarrow - 2Z_\uparrow\rangle, & |LH_\downarrow\rangle = \frac{1}{\sqrt{6}} |(X - iY)_\uparrow + 2Z_\downarrow\rangle, \\[4pt]
|HH_\uparrow\rangle = \frac{1}{\sqrt{2}} |(X + iY)_\uparrow\rangle, & |HH_\downarrow\rangle = \frac{i}{\sqrt{2}} |(X - iY)_\downarrow\rangle, \\[4pt]
|SO_\uparrow\rangle = \frac{1}{\sqrt{3}} |(X + iY)_\downarrow + Z_\uparrow\rangle, & |SO_\downarrow\rangle = \frac{i}{\sqrt{3}} |-(X - iY)_\uparrow + Z_\downarrow\rangle,
\end{cases}
\tag{3.6}
$$

where S, X, Y and Z denote the type of symmetry (*s*-function, or *x*, *y* or *z* *p*-functions) that the orbital has under the tetrahedral group transformation, and $\{\uparrow, \downarrow\}$ denotes the spin projection. In this basis, the z direction corresponds to the (111) crystallographic orientation. The Hamiltonian in the $\Psi = (\Psi_{c,\uparrow}, \Psi_{c,\downarrow}, \Psi_{lh,\uparrow}, \Psi_{hh,\uparrow}, \Psi_{hh,\downarrow}, \Psi_{lh,\downarrow}, \Psi_{soff,\uparrow}, \Psi_{soff,\downarrow})$ basis up to first-order[1] in Löwdin

---

[1]Second-order Löwdin perturbative terms are also included for the k·p term to properly account for the quasi-parabolic dispersion relation.

perturbation theory is given by

$$H_{\text{kp}} = \begin{pmatrix} T_{\text{c}} & 0 & \frac{1}{\sqrt{6}}Pk_+ & 0 & \frac{1}{\sqrt{2}}Pk_- & -\sqrt{\frac{2}{3}}Pk_z & -\frac{1}{\sqrt{3}}Pk_z & \frac{1}{\sqrt{3}}Pk_+ \\ 0 & T_{\text{c}} & -\sqrt{\frac{2}{3}}Pk_z & -\frac{1}{\sqrt{2}}Pk_+ & 0 & -\frac{1}{\sqrt{6}}Pk_- & \frac{1}{\sqrt{3}}Pk_- & \frac{1}{\sqrt{3}}Pk_z \\ \frac{1}{\sqrt{6}}Pk_- & -\sqrt{\frac{2}{3}}Pk_z & T_{\text{lh}} & -\Omega_2^\dagger & \Omega_1 & 0 & \sqrt{\frac{3}{2}}\Omega_2 & -\sqrt{2}\Omega_3 \\ 0 & -\frac{1}{\sqrt{2}}Pk_- & -\Omega_2 & T_{\text{hh}} & 0 & \Omega_1 & -\sqrt{2}\Omega_1^\dagger & \frac{1}{\sqrt{2}}\Omega_2 \\ \frac{1}{\sqrt{2}}Pk_+ & 0 & \Omega_1^\dagger & 0 & T_{\text{hh}} & \Omega_2^\dagger & \frac{1}{\sqrt{2}}\Omega_2^\dagger & \sqrt{2}\Omega_1^\dagger \\ -\sqrt{\frac{2}{3}}Pk_z & -\frac{1}{\sqrt{6}}Pk_+ & 0 & \Omega_1^\dagger & \Omega_2 & T_{\text{lh}} & \sqrt{2}\Omega_3 & \sqrt{\frac{3}{2}}\Omega_2^\dagger \\ -\frac{1}{\sqrt{3}}Pk_z & \frac{1}{\sqrt{3}}Pk_+ & \sqrt{\frac{3}{2}}\Omega_2^\dagger & -\sqrt{2}\Omega_1 & \frac{1}{\sqrt{2}}\Omega_2 & \sqrt{2}\Omega_3 & T_{\text{soff}} & 0 \\ \frac{1}{\sqrt{3}}Pk_- & \frac{1}{\sqrt{3}}Pk_z & -\sqrt{2}\Omega_3 & \frac{1}{\sqrt{2}}\Omega_2^\dagger & \sqrt{2}\Omega_1 & \sqrt{\frac{2}{3}}\Omega_2 & 0 & T_{\text{soff}} \end{pmatrix},$$

(3.7)

where the diagonal terms are

$$T_{\text{c}} = E_{\text{c}} + \frac{\hbar^2 \vec{k}^2}{2m_e} - e\phi(\vec{r}), \tag{3.8}$$

$$T_{\text{lh}} = E_{\text{h}} + \Omega_0^{\text{lh}} - e\phi(\vec{r}), \quad \Omega_0^{\text{lh}} = \frac{\hbar^2}{2m_e}\left[(k_x^2 + k_y^2)(\gamma_3 - \gamma_1) - k_z^2(2\gamma_3 + \gamma_1)\right], \tag{3.9}$$

$$T_{\text{hh}} = E_{\text{h}} + \Omega_0^{\text{hh}} - e\phi(\vec{r}), \quad \Omega_0^{\text{hh}} = \frac{\hbar^2}{2m_e}\left[-(k_x^2 + k_y^2)(\gamma_3 + \gamma_1) + k_z^2(2\gamma_3 - \gamma_1)\right], \tag{3.10}$$

$$T_{\text{soff}} = E_{\text{soff}} + \Omega_0^{\text{soff}} - e\phi(\vec{r}), \quad \Omega_0^{\text{soff}} = -\gamma_1\frac{\hbar^2 \vec{k}^2}{2m_e}, \tag{3.11}$$

and the off-diagonal ones are

$$\Omega_1 = -\frac{1}{\sqrt{3}}\frac{\hbar^2}{2m_e}(\gamma_2 + 2\gamma_3)k_-^2, \tag{3.12}$$

$$\Omega_2 = -\frac{2}{\sqrt{3}}\frac{\hbar^2}{2m_e}(2\gamma_2 + \gamma_3)k_z k_-, \tag{3.13}$$

$$\Omega_3 = \frac{\hbar^2}{2m_e}\gamma_3(k_x^2 + k_y^2 - 2k_z^2). \tag{3.14}$$

Here, E_{c}, $E_{\text{h}} = E_{\text{c}} - \Delta_{\text{g}}$ and $E_{\text{soff}} = E_{\text{c}} - \Delta_{\text{g}} - \Delta_{\text{soff}}$ are the band edges of the conduction, hole and split-off bands, respectively; Δ_{g} and Δ_{soff} are the gaps between the conduction/hole and hole/split-off bands at the Γ point; $\phi(\vec{r})$ is the electrostatic potential; $k_\pm \equiv k_x \pm ik_y$ and $\{\gamma_i\}$ and P are Kane parameters. In this work, we choose the ungated CB edge as the reference energy, i.e., we fix $E_{\text{c}} = 0$. The Hamiltonian elements whose functional form has been substituted by

phenomenological parameters are

$$P \equiv -\frac{i\hbar}{m_e} \langle S| p_x |X\rangle = -\frac{i\hbar}{m_e} \langle S| p_y |Y\rangle = -\frac{i\hbar}{m_e} \langle S| p_z |Z\rangle, \qquad (3.15)$$

$$\Delta_{\mathrm{soff}} \equiv \frac{3\hbar i}{4m_e^2 c^2} \langle X| \frac{\partial \phi_0}{\partial x} p_y - \frac{\partial \phi_0}{\partial y} p_x |Y\rangle = \frac{3\hbar i}{4m_e^2 c^2} \langle Y| \frac{\partial \phi_0}{\partial y} p_z - \frac{\partial \phi_0}{\partial z} p_y |Z\rangle =$$
$$\frac{3\hbar i}{4m_e^2 c^2} \langle Z| \frac{\partial \phi_0}{\partial z} p_x - \frac{\partial \phi_0}{\partial x} p_z |X\rangle. \qquad (3.16)$$

The specific values that we have used for the Kane parameters in this thesis are extracted from Ref. [158] and shown in Appendix B.4. They are extracted from both, experiments and *ab initio* calculations. The 8B k·p Hamiltonian with these parameters perfectly matches the energy bands computed with *ab initio* methods for $\left|\vec{k}\right| \in [-1, 1]$ (nm)$^{-1}$. Outside this range, the agreement is poorer as the modulus of the momentum increases.

The multiband Hamiltonian presented before correctly describe the band shape of III-V zinc-blende SMs around the Γ-point [159, 160, 167–171]. However, dealing with this Hamiltonian in certain situations is a difficult task due to the large number of bands involved [170]. When one is interested only on the properties of one specific band, the CB in our case, it is customary to look for an effective Hamiltonian within that band by integrating out the rest of them. To do this, we write the 8B Hamiltonian of Eq. (3.53) as

$$H_{\mathrm{kp}} = \begin{pmatrix} H_{\mathrm{c}} & H_{\mathrm{cv}} \\ H_{\mathrm{cv}}^\dagger & H_{\mathrm{v}} \end{pmatrix}, \qquad (3.17)$$

where H_{c} is a 2×2 Hamiltonian corresponding to the (spinful) conduction band, H_{v} is a 6×6 Hamiltonian corresponding to the three (spinful) valence bands, and H_{cv} is a 2×6 Hamiltonian that represents the coupling between conduction and valence bands. Following a standard folding-down procedure, we can write an effective 2×2 conduction band Hamiltonian as

$$H_{\mathrm{CB}} = H_{\mathrm{c}} + \Sigma_{\mathrm{v}}, \quad \Sigma_{\mathrm{v}} = H_{\mathrm{cv}} G_{\mathrm{v}} H_{\mathrm{cv}}^\dagger, \quad G_{\mathrm{v}} = (E - H_{\mathrm{v}})^{-1} \quad \rightarrow H_{\mathrm{CB}} \Psi_{\mathrm{c}} = E \Psi_{\mathrm{c}}, \qquad (3.18)$$

where Σ_{v} is the self-energy of the valence bands and G_{v} their corresponding Green's function (or resolvent).

The valence bands self-energy cannot be found exactly, since it is not possible to invert a matrix that has non-commuting terms such as the position-dependent electrostatic potential, $\phi(\vec{r})$, and the momentum operators $\vec{k}$. We can nevertheless expand G_{v} in terms of the small parameter $\sim \Omega_i/\Delta_i$, where $\Omega_i = \gamma_i \hbar^2 \vec{k}^2/(2m_e)$ represents the energy associated to the valence band couplings, and Δ_i are the different band gap energies at the Γ-point. In particular, γ_i represents different combinations of $\gamma_{1,2,3}$, see Eqs. (3.9)–(3.14). On the other hand, Δ_i represents either Δ_{g} or $\Delta_{\mathrm{g}} + \Delta_{\mathrm{soff}}$. Therefore,

defining $H_{\mathrm{v}} = H_{\mathrm{v}}^{(0)} + V$, where

$$
H_{\mathrm{v}}^{(0)} = \begin{pmatrix}
E_{\mathrm{h}} - e\phi(\vec{r}) & 0 & 0 & 0 & 0 & 0 \\
0 & E_{\mathrm{h}} - e\phi(\vec{r}) & 0 & 0 & 0 & 0 \\
0 & 0 & E_{\mathrm{h}} - e\phi(\vec{r}) & 0 & 0 & 0 \\
0 & 0 & 0 & E_{\mathrm{h}} - e\phi(\vec{r}) & 0 & 0 \\
0 & 0 & 0 & 0 & E_{\mathrm{soff}} - e\phi(\vec{r}) & 0 \\
0 & 0 & 0 & 0 & 0 & E_{\mathrm{soff}} - e\phi(\vec{r})
\end{pmatrix},
$$
(3.19)

and

$$
V = \begin{pmatrix}
\Omega_0^{\mathrm{lh}} & -\Omega_2^{\dagger} & \Omega_1 & 0 & \sqrt{\tfrac{3}{2}}\Omega_2 & -\sqrt{2}\Omega_3 \\
-\Omega_2 & \Omega_0^{\mathrm{hh}} & 0 & \Omega_1 & -\sqrt{2}\Omega_1^{\dagger} & \tfrac{1}{\sqrt{2}}\Omega_2 \\
\Omega_1^{\dagger} & 0 & \Omega_0^{\mathrm{hh}} & \Omega_2^{\dagger} & \tfrac{1}{\sqrt{2}}\Omega_2^{\dagger} & \sqrt{2}\Omega_1^{\dagger} \\
0 & \Omega_1^{\dagger} & \Omega_2 & \Omega_0^{\mathrm{lh}} & \sqrt{2}\Omega_3 & \sqrt{\tfrac{3}{2}}\Omega_2^{\dagger} \\
\sqrt{\tfrac{3}{2}}\Omega_2^{\dagger} & -\sqrt{2}\Omega_1 & \tfrac{1}{\sqrt{2}}\Omega_2 & \sqrt{2}\Omega_3 & \Omega_0^{\mathrm{soff}} & 0 \\
-\sqrt{2}\Omega_3 & \tfrac{1}{\sqrt{2}}\Omega_2^{\dagger} & \sqrt{2}\Omega_1 & \sqrt{\tfrac{2}{3}}\Omega_2 & 0 & \Omega_0^{\mathrm{soff}}
\end{pmatrix},
$$
(3.20)

we can write the zeroth-order valence bands Green's function as $G_{\mathrm{v}}^{(0)} = (E - H_{\mathrm{v}}^{(0)})^{-1}$, and the Dyson expansion of the full Green's function as

$$
G_{\mathrm{v}} = G_{\mathrm{v}}^{(0)} + G_{\mathrm{v}}^{(0)} V G_{\mathrm{v}}^{(0)} + G_{\mathrm{v}}^{(0)} V G_{\mathrm{v}}^{(0)} V G_{\mathrm{v}}^{(0)} + \ldots
$$
(3.21)

Ignoring the couplings between the valence bands while still retaining the couplings between the conduction and valence bands, i.e., to zeroth-order in Ω_i/Δ_i, the zeroth-order conduction band Hamiltonian

$$
H_{\mathrm{CB}}^{(0)} = H_{\mathrm{c}} + H_{\mathrm{cv}} G_{\mathrm{v}}^{(0)} H_{\mathrm{cv}}^{\dagger} \rightarrow H_{\mathrm{CB}}^{(0)} \Psi_{\mathrm{c}}^{(0)} = E \Psi_{\mathrm{c}}^{(0)},
$$
(3.22)

has been found [159, 172, 173] to be

$$
H_{\mathrm{CB}}^{(0)} = \left[\frac{\hbar^2 \vec{k}^2}{2m_e} + E_{\mathrm{c}} - e\phi(\vec{r}) \right] \sigma_0 + (\Lambda_0 \sigma_0 + \Lambda_x \sigma_x + \Lambda_y \sigma_y + \Lambda_z \sigma_z),
$$
(3.23)

where σ_i are the spin Pauli matrices (and σ_0 the identity), and

$$
\Lambda_0 = -\sum_{j=\{x,y,z\}} \frac{P^2}{3} k_j \left[\frac{2}{E_h - e\phi(\vec{r}) - E} + \frac{1}{E_{\text{soff}} - e\phi(\vec{r}) - E} \right] k_j, \tag{3.24}
$$

$$
\Lambda_x = i\frac{P^2}{3} \left\{ k_z \left[\frac{1}{E_h - e\phi(\vec{r}) - E} - \frac{1}{E_{\text{soff}} - e\phi(\vec{r}) - E} \right] k_y \right.
$$
$$
\left. -k_y \left[\frac{1}{E_h - e\phi(\vec{r}) - E} - \frac{1}{E_{\text{soff}} - e\phi(\vec{r}) - E} \right] k_z \right\}, \tag{3.25}
$$

$$
\Lambda_y = i\frac{P^2}{3} \left\{ k_x \left[\frac{1}{E_h - e\phi(\vec{r}) - E} - \frac{1}{E_{\text{soff}} - e\phi(\vec{r}) - E} \right] k_z \right.
$$
$$
\left. -k_z \left[\frac{1}{E_h - e\phi(\vec{r}) - E} - \frac{1}{E_{\text{soff}} - e\phi(\vec{r}) - E} \right] k_x \right\}, \tag{3.26}
$$

$$
\Lambda_z = i\frac{P^2}{3} \left\{ k_y \left[\frac{1}{E_h - e\phi(\vec{r}) - E} - \frac{1}{E_{\text{soff}} - e\phi(\vec{r}) - E} \right] k_x \right.
$$
$$
\left. -k_x \left[\frac{1}{E_h - e\phi(\vec{r}) - E} - \frac{1}{E_{\text{soff}} - e\phi(\vec{r}) - E} \right] k_y \right\}. \tag{3.27}
$$

This Hamiltonian can be recast in one of the form

$$
H_{\text{CB}}^{(0)} = \left[\vec{k} \frac{\hbar^2}{2m^{(0)}(\vec{r})} \vec{k} + E_c - e\phi(\vec{r}) \right] \sigma_0 + \frac{1}{2} \left[\vec{\alpha}_R^{(0)}(\vec{r}) \cdot \left(\vec{\sigma} \times \vec{k} \right) + \left(\vec{\sigma} \times \vec{k} \right) \cdot \vec{\alpha}_R^{(0)}(\vec{r}) \right]. \tag{3.28}
$$

The first term corresponds to the kinetic energy, but the electron has now an effective mass given by

$$
\frac{1}{m^{(0)}(\vec{r})} = \frac{1}{m_e} - \frac{2P^2}{3\hbar^2} \left[\frac{2}{E_h - e\phi(\vec{r}) - E} + \frac{1}{E_{\text{soff}} - e\phi(\vec{r}) - E} \right]. \tag{3.29}
$$

Notice that this term has to be written between the two momentum operators $\vec{k}$ in the kinetic energy part of Eq. (3.28) because the effective mass depends in general on position through $\phi(\vec{r})$, and thus, they do not commute. The other term corresponds to the Rashba SO interaction, whose Rashba coefficients $\vec{\alpha}_R^{(0)}(\vec{r})$ are

$$
\vec{\alpha}_R^{(0)}(\vec{r}) = \frac{P^2}{3} \vec{\nabla} \left[\frac{1}{E_h - e\phi(\vec{r}) - E} - \frac{1}{E_{\text{soff}} - e\phi(\vec{r}) - E} \right]. \tag{3.30}
$$

Note that, in this notation, the nabla operator inside $\vec{\alpha}_R^{(0)}(\vec{r})$ only acts on the expression inside the square brackets, i.e., it is not to be applied on the electron wave function.

Equation (3.28) describes the Hamiltonian for an electron in the CB, and therefore, it is only valid as far as conduction and valence bands do not overlap in energy, what means that its applicability range is for $-E_h = \Delta_g - E_c > -e\phi(r) - E$. We have thus reached a Hamiltonian that involves a smaller number of bands (i.e., only one spinful CB), and that allows us to directly introduce additional terms whose functional form we know, as for instance a Zeeman field or a superconducting

pairing term. We note that this simplified Hamiltonian is equivalent to that of the bare electron[2], Eq. (3.1), but with a spatial-dependent effective mass $m^{(0)}(\vec{r})$ and an effective Rashba coupling $\vec{\alpha}_{\mathrm{R}}^{(0)}(\vec{r})$ that depends not only on $\vec{\nabla}\phi(\vec{r})$, but whose prefactor, like that of the effective mass, depends on $E + \phi(\vec{r})$, where E is the quasiparticle energy. Due to the energy dependence of these effective quantities, the CB Hamiltonian has to be solved self-consistently.

To avoid this complication, a further simplification is usually performed in the literature [159, 172, 173]. If Δ_{g} and Δ_{soff} are the largest energies in the conduction band approximation, then it is possible to expand in Taylor series assuming $|E_h| \gg |e\phi(\vec{r}) + E|$,

$$\frac{1}{E_{\mathrm{h}} - e\phi(\vec{r}) - E} = \frac{(-E_{\mathrm{h}})}{1 - \frac{e\phi(\vec{r}) + E}{E_{\mathrm{h}}}} = \sum_{n=0}^{\infty}(-1)^{(n+1)}\frac{(e\phi(\vec{r}) + E)^n}{(E_{\mathrm{h}})^{n+1}}. \tag{3.31}$$

Truncating up to $n = 0$ in the above equation, it is possible to obtain an energy and position-independent effective mass

$$\frac{1}{m^{(0)}} \simeq \frac{1}{m_e} - \frac{2P^2}{3\hbar^2}\left(\frac{2}{E_{\mathrm{h}}} + \frac{1}{E_{\mathrm{soff}}}\right). \tag{3.32}$$

Similarly, truncating up to $n = 1$, we get the Rashba coupling

$$\vec{\alpha}_{\mathrm{R}}^{(0)}(\vec{r}) \simeq -e\frac{P^2}{3}\left(\frac{1}{E_{\mathrm{h}}^2} - \frac{1}{E_{\mathrm{soff}}^2}\right)\vec{\nabla}\phi(\vec{r}), \tag{3.33}$$

which we call *simplified* equations for m and $\vec{\alpha}_{\mathrm{R}}$.

One can proceed in the same way to obtain the effective (zeroth-order) CB Hamiltonian for a wurtzite crystal starting from a wurtzite 8B Hamiltonian. This 8B Hamiltonian has been also derived in previous works [166] [see Appendix B.1, and more particularly, Eq. (B.2) for the Hamiltonian]. However, this derivation would certainly be more involved due to the presence of more coupling parameters that arises due to the anisotropy of the wurtzite unit cell. Actually, as a consequence, we expect the effective mass and the SO coupling to be anisotropic too. However, to avoid this complexity, the zinc-blende zeroth-order results for the effective mass and SO coupling are frequently used in the literature for III-V semiconductor compounds with wurtzite structure as well, but taking the appropriate values of Δ_{g} and Δ_{soff} while keeping the zinc-blende P parameter. In the following sections we discuss the accuracy of this simplification.

3.1.2 Effective conduction-band Hamiltonian for nanowires

If we apply the previous expressions to a III-V compound SM with the form of a nanowire that is translational invariant along the z direction [the (111) direction in zinc-blende crystals], we can take k_z as a good quantum number and thus $\phi(\vec{r})$ depends only on the transverse directions x and y [i.e., $\vec{r} = (x, y)$]. We can then split the Hamiltonian into a transverse part $H_{\mathrm{T}}^{(0)}$ that only depends

---

[2]Using the properties of the triple product, we can equate $(\vec{\nabla}\phi \times \vec{k}) \cdot \vec{\sigma} = -\vec{\nabla}\phi \cdot (\vec{\sigma} \times \vec{k})$.

on $\vec{r}$ and a longitudinal one $H_{\mathrm{L}}^{(0)}$ that also depends on k_z

$$H_{\mathrm{CB}}^{(0)}(\vec{r}, k_z) = H_{\mathrm{T}}^{(0)}(\vec{r}) + H_{\mathrm{L}}^{(0)}(\vec{r}, k_z), \tag{3.34}$$

$$H_{\mathrm{T}}^{(0)}(\vec{r}) = \left[-\partial_x \frac{\hbar^2}{2m^{(0)}(\vec{r})} \partial_x - \partial_y \frac{\hbar^2}{2m^{(0)}(\vec{r})} \partial_y + E_c - e\phi(\vec{r}) \right] \sigma_0$$
$$-i\frac{1}{2} \left[\alpha_{\mathrm{R},y}^{(0)}(\vec{r}) \partial_x - \alpha_{\mathrm{R},x}^{(0)}(\vec{r}) \partial_y + \partial_x \alpha_{\mathrm{R},y}^{(0)}(\vec{r}) - \partial_y \alpha_{\mathrm{R},x}^{(0)}(\vec{r}) \right] \sigma_z, \tag{3.35}$$

$$H_{\mathrm{L}}^{(0)}(\vec{r}, k_z) = \frac{\hbar^2 k_z^2}{2m^{(0)}(\vec{r})} \sigma_0 + \left(\alpha_{\mathrm{R},x}^{(0)} \sigma_y - \alpha_{\mathrm{R},y}^{(0)} \sigma_x \right) k_z. \tag{3.36}$$

Under this situation, if we assume that the inter-subband SO coupling is negligible (i.e., $l_{\mathrm{SO}} \gtrsim W_{\mathrm{wire}}$, being l_{SO} the SO length and W_{wire} the wire's width), different subbands do not mix. This allows us to first diagonalize the transverse Hamiltonian $H_{\mathrm{T}}^{(0)}$ in order to obtain the wavefunctions $\Psi_{\mathrm{T}}^{(j)}(\vec{r})$ for each subband j together with their energies $E_{\mathrm{T}}^{(j)}$. Then, we can write an effective CB Hamiltonian for each subband j

$$H_{\mathrm{eff}}^{(j)}(k_z) = \left(\frac{\hbar^2 k_z^2}{2m_{\mathrm{eff}}^{(j)}} + E_{\mathrm{T}}^{(j)} \right) \sigma_0 + \left(\alpha_{\mathrm{eff},x}^{(j)} \sigma_y - \alpha_{\mathrm{eff},y}^{(j)} \sigma_x \right) k_z, \tag{3.37}$$

where $m_{\mathrm{eff}}^{(j)}$ and $\alpha_{\mathrm{eff}}^{(j)}$ are the effective mass and SO coupling for each subband j. Particularly, they can be computed from the transverse subbands as

$$\frac{1}{m_{\mathrm{eff}}^{(j)}} = \left\langle \frac{1}{m^{(0)}(\vec{r})} \right\rangle_j = \left\langle \Psi_{\mathrm{T}}^{(j)}(\vec{r}) \right| \frac{1}{m^{(0)}(\vec{r})} \left| \Psi_{\mathrm{T}}^{(j)}(\vec{r}) \right\rangle, \tag{3.38}$$

$$\vec{\alpha}_{\mathrm{eff}}^{(j)} = \left\langle \vec{\alpha}_{\mathrm{R}}^{(0)}(\vec{r}) \right\rangle_j = \left\langle \Psi_{\mathrm{T}}^{(j)}(\vec{r}) \right| \vec{\alpha}_{\mathrm{R}}^{(0)}(\vec{r}) \left| \Psi_{\mathrm{T}}^{(j)}(\vec{r}) \right\rangle. \tag{3.39}$$

Notice that, in this particular case $\alpha_{\mathrm{R},z}=0$ (to all orders), and therefore the SO coupling modulus only involves the x and y components: $\left| \vec{\alpha}_{\mathrm{eff}}^{(j)} \right| = \sqrt{ \left(\alpha_{\mathrm{eff},x}^{(j)} \right)^2 + \left(\alpha_{\mathrm{eff},y}^{(j)} \right)^2 }$. The total energy for each subband $E(k_z)$ can be directly evaluated from Eq. (3.37) since k_z is a number, not an operator.

3.2   Electrostatic potential in nanowires

The Rashba SO coupling given in Eq. (3.33) depends on the gradient of the electrostatic potential. This is a direct manifestation that only when there is a structural inversion asymmetry, i.e., an inhomogeneous electrostatic potential, there is a non-zero Rashba SO coupling. Hence, the SO coupling is sensitive to the precise electrostatic environment, as well as to electron-electron interactions inside the wire. To compute the electrostatic potential corresponding to an arbitrary environment we solve the Poisson equation given by Eq. (2.2). The source term, i.e., the total charge inside the wire $\rho_{\mathrm{T}}[\phi(\vec{r})]$ includes two parts [115] in SM nanowires (disregarding charged

impurities),

$$\rho_{\mathrm{T}}\left[\phi(\vec{r})\right] = \rho_{\mathrm{surf}}(\vec{r}) + \rho_{\mathrm{mobile}}\left[\phi(\vec{r})\right]. \tag{3.40}$$

The first one represents a surface charge $\rho_{\mathrm{surf}}(\vec{r})$ that is used to model an accumulation layer of charge typically presented at the facets of these SM wires [174]. This is modeled as a 1 nm layer of positive charge fixed at the wire's surface, so that it creates a band-bending towards the semiconductor-vacuum interface where the electrons tend to accumulate. This surface charge cannot be removed using gates and it thus gives an intrinsic contribution to the electrostatic potential. It depends on the details of the surface chemistry and its precise value is difficult to ascertain, although some works have reported values ranging from $5 \cdot 10^{-3}\left(\frac{e}{\mathrm{nm}^3}\right)$ to $5 \cdot 10^{-2}\left(\frac{e}{\mathrm{nm}^3}\right)$ [175–177]. However, its does not play any fundamental role but it simply results in a small particular contribution to the intrinsic doping of the wire and its SO coupling [178].

The second term in Eq. (3.40), $\rho_{\mathrm{mobile}}\left[\phi(\vec{r})\right]$, represents the mobile charge inside the wire. III-V SM nanowires (not chemically doped) are charge neutral unless the CB is populated with electrons or the valence bands are populated with holes. This can be done by applying an electrostatic potential inside the wire $\phi(\vec{r})$ with the aid of a gate electrode, that effectively modifies the band-bottom level inside the wire [see Eq. (3.28)]. A positive electrostatic potential tends to populate the CB while a negative one tends to deplete the wire. For the range of gate voltages that we are going to explore in this work, we only focus on the mobile charge coming from the CB, as this is the band we are interested in. This charge density can be computed from the eigenstates of the Hamiltonian as explained in Sec. 2.3, together with the numerical methods used to solve the Poisson of Eq. (2.2).

We note that the solution of the coupled SP equation typically possesses a rather demanding numerical problem since it requires the diagonalization of the Hamiltonian in every step of the self-consistent process. It can be nevertheless simplified by relying on the Thomas-Fermi (TF) approximation, as shown in previous works for SM nanowires [113, 173, 178]. This approximation allows to decouple both equations by assuming that the charge density of the wire is indeed very similar to that of a 3D free electron gas,

$$\rho_{\mathrm{mobile}}\left[\phi(\vec{r})\right] \simeq \rho_{\mathrm{mobile}}^{(\mathrm{TF})}\left[\phi(\vec{r})\right] = -\frac{q_e}{3\pi^2}\left[\frac{2m^*|e\phi(\vec{r}) + E_{\mathrm{F}}|f_{\mathrm{FD}}(-(e\phi(\vec{r}) + E_{\mathrm{F}}))}{\hbar^2}\right]^{\frac{3}{2}}, \tag{3.41}$$

where E_{F} is the Fermi energy of the wire and $f_{\mathrm{FD}}(E)$ is the Fermi-Dirac distribution for a given temperature T. Within this approximation, one still has to solve self-consistently the Poisson equation, as $\rho_{\mathrm{mobile}}^{(\mathrm{TF})}\left[\phi(\vec{r})\right]$ depends on $\phi(\vec{r})$. But at least it does not involve the diagonalization of the Hamiltonian, just the evaluation of an analytical expression. In order to solve this self-consistent scheme, we use the same iterative procedure as explained in Chapter 2 but using the charge density obtained through Eq. (3.41) instead of the one provided by the eigenstates.

To illustrate the effect of both charge densities of Eq. (3.40), we show in Fig. 3.2 the electrostatic potential and charge density for a representative device like the one shown in (a): a 80 nm–wide SM nanowire (green) deposited on top of a dielectric substrate (purple) that isolates the wire from

a bottom gate (black). We compute it using the full SP calculations assuming furthermore that the system is translational invariant along the wire's direction (z direction). We first compute the electrostatic potential at $V_{\text{Gate}} = 0$, which provides the intrinsic doping of the wire. We show in Fig. 3.2(b) a cut of the electrostatic potential (red line) along the y direction in the middle of the wire's section (i.e., $x = 0$). The green area corresponds to the electrostatic potential inside the wire, while the violet and white areas correspond to the electrostatic potential in the substrate and vacuum parts, respectively. Overall, the electrostatic potential inside the wire is positive, indicating that the CB is intrinsically populated with electrons. It is roughly minimum at the nanowire center ($y = 0$) and it bends towards the nanowire facets due to the surface charge $\rho_{\text{surf}}(\vec{r})$. As commented above, this surface charge naturally creates an accumulation layer of charge at the nanowire facets as the potential is more positive there. This can be appreciated in Fig. 3.2(b) as the blue line represents the mobile charge density. Besides, the potential is not symmetric along the y direction due to the asymmetry created by both, the gate and the dielectric, which present induced bound charges as a response to the external electric field created by the charge density inside the wire.

In Fig. 3.2(c), we show the electrostatic potential profile across the nanowire section when the gate potential is turned on ($V_{\text{Gate}} = 1$ V). Now the electrostatic potential is much larger at the bottom part of the wire as this part is closer to the potential gate. However, it is still minimum at the nanowire center, and not at the opposite facet to the potential gate. This is because electrons tend to accumulate at the nanowire facets where the electron-electron interactions are minimized: since there are no electrons outside the wire, the repulsive interaction is smaller at the nanowire facets than in the core. An example of the mobile charge density distribution in this situation is shown in Fig. 3.2(d). As predicted, the electron density exhibits a ring-shape structure, with the core of the wire (almost) completely empty. It is nevertheless larger at the bottom part of the wire, as it is closer to the bottom gate; and even more at the bottom corners since electron-electron interactions are further minimized there.

These previous simulations correspond to the full SP ones, where the charge density is computed from the eigenstates of the Hamiltonian. However, as commented above, this is a computationally expensive task that can be surpassed using the TF approximation, where the charge density is simply the one of a free electron gas. To discuss the accuracy of this method, we illustrate in Fig. 3.2(e) the charge density across the wire's section computed using this approximation. For comparison, we show in (f) the charge density difference between both methods [i.e., (f)=(d)-(e)]. The charge density computed using the TF approximation correctly predicts the expected ring-shape structure. In addition, it is also maximum at the bottom part of the wire. Nonetheless, it fails predicting the precise structure of the charge density distribution. For this simulation, the charge density is three times larger just at the nanowire facets in the TF approximation with respect to the full SP calculations. But at the same time, it is three times smaller a few nanometers (~ 5 nm) away from the facets. The reason is that the facets of the wire impose a hard-wall potential, so that the wavefunction must be zero there when solving the Schrödinger equation. Hence, and due to the kinetic energy, the maximum of the electron density cannot be exactly at the nanowire facets, but just a few nanometers inside at most. This fact is completely ignored in the TF approximation,
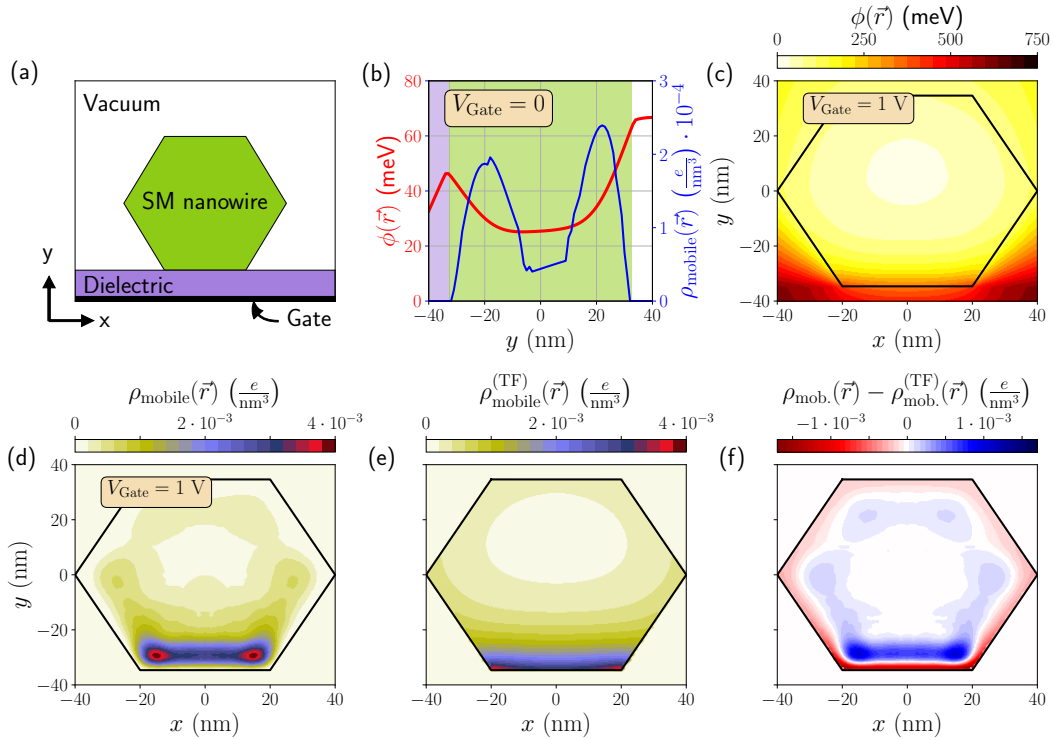
Figure 3.2: (a) Sketch of the simulated device: a 80 nm–wide SM nanowire is deposited on top of a 20 nm–thick dielectric substrate that isolates the wire from the gate at the bottom. The system is translational invariant along the z direction. (b) Electrostatic potential (red line) and mobile charge density (blue line) along the y direction at $x = 0$ and $V_{\mathrm{Gate}} = 0$. The green area corresponds to the nanowire part (and purple and white to the dielectric and vacuum, respectively). (c) Electrostatic profile across the wire cross section at $V_{\mathrm{Gate}} = 1$ V. The black line shows the nanowire surface. (d-f) Mobile charge density distribution across the wire section at $V_{\mathrm{Gate}} = 1$ V using (d) the full Schrödinger-Poisson calculations or (e) the Thomas-Fermi approximation. In (f), we show the difference between both profiles. For all these simulations, we take InAs as the SM nanowire and HfO_2 as the dielectric, although the results are similar for other III-V compound SMs and conventional dielectrics. Temperature is set to $T = 10$ mK. The remaining parameters are provided in Appendix B.4.

as the electrostatic potential is the only input in Eq. (3.41). It should be noticed that the TF approximation is a semiclassical approximation which cannot describe variations of the charge density at subwavelength scales.

Despite of this, the electrostatic potential profile provided by both methods is similar [not shown for the TF approximation as it is similar to Fig. 3.2(c)]. And this is because the difference in the spatial distribution between both methods is small in comparison with the long-range electrostatic interactions. Or in other words, a small change in the spatial distribution of the charge density does not dramatically change the electrostatic potential. Moreover, both methods provide roughly the same occupancy with respect to the gate potential, e.g., the total charge in (d) is $Q_{\mathrm{T}} = 21$ and in (e) is $Q_{\mathrm{T}}^{(\mathrm{TF})} = 21.5$. Although the pace at which electrons enter into the wire as V_{Gate} is increased is different: if temperature is zero or small, electrons can only enter one-by-one into the wire in the full SP calculations, as charge is quantized in a finite-size nanowire. This is not the case in the TF approximation, as Eq. (3.41) varies monotonously with $\phi(\vec{r})$. This difference is in general not important as long as both methods provide (roughly) the same occupation. But it can make a difference when describing some effects, like the pinning effect pointed out in Refs. [99, 179]. This effect relies on the incompressibility of the electron density: when an electron is injected into the wire (by increasing the chemical potential), it may be expelled by the bound charges that itself creates in the electrostatic environment. This is reflected in the energy spectrum as a pinning of the energy states vs chemical potential, as the electron cannot enter into the wire for some potential range. This phenomenon is not well-captured by the TF approximation as it describes a smooth (non-quantized) filling of the CB of the wire.

Baring these limitations in mind, we conclude that the TF approximation is a useful workaround to the full SP calculations when one is only interested in an accurate description of the electrostatic potential and not the charge density. And this is our case inasmuch our main goal is to describe the SO coupling and the effective mass in a realistic way [notice they only depends on $\phi(\vec{r})$, and not on $\rho_{\mathrm{T}}(\vec{r})$].

3.3 Properties of the conduction band in III-V semiconductor nanowires

3.3.1 Spin-orbit coupling

The aim of this section is to find the range of SO couplings that these SM nanowires can typically support. We first compare the SO couplings provided by the 8B model with the CB approximation to know the accuracy of this approximation. As we are going to show, the approximation fails predicting the correct SO coupling in nanowires due to the confinement effects coming from the finite cross section of the wire. We then introduce a correction to the CB approximation in a heuristic way to improve the agreement. We do that for different III-V compound SMs and crystallographic orientations. We lastly compare our theoretical approach with the SO coupling obtained in several experiments, finding an excellent agreement. This will further serve us to illustrate and discuss the

typical values that these SM nanowires can exhibit.

8-band model vs CB approximation

The CB approximation provides a simple and analytical equation for the SO coupling in semiconductors. It is derived in Sec. 3.1.1 from an 8B model performing a zeroth-order Dyson expansion in Ω_i/Δ_i, so that one obtains Eq. (3.30), which only applies to the CB. This equation can be further simplified assuming that $\Delta_{\mathrm{g}} \gg e\phi(\vec{r}) + E$, giving rise to the *simplified* effective SO coupling of Eq. (3.33) that does not require self-consistency to be solved. These equations are easy to implement in a Hamiltonian and have a reduced computational cost in comparison to a 8B model as they only involve the band of interest (the CB). But, since the 8B model is a reliable method to obtain the band structure in semiconductors and in particular the SO coupling, the natural question that arises is how these equations compare to the 8B model.

In order to perform this comparison, we compute the SO coupling using these two equations [zeroth-order Eq. (3.30) and simplified Eq. (3.33)] and the 8B model for the device shown in Fig. 3.3. This device is similar to the one of Fig. 3.2 but it includes a metallic layer on the top facet of the wire. This metallic layer is grounded and it is isolated from the wire by a thin oxide layer (not shown), so that electrons cannot tunnel through. We put this layer simply to increase the asymmetry in the y direction, and thus to enhance the SO coupling. We solve the SP equation in the absence (for the moment) of mobile charges for simplicity. We use the Hamiltonian of Eq. (3.28) for the CB approximation calculations and the Hamiltonian of Eq. (3.7) for the 8B model calculations.

On the one hand, the SO coupling can be extracted from the 8B model calculations once the band structure is obtained by fitting each subband j by the following effective dispersion relation

$$E_{\pm}^{(j)}(k_z) = \frac{\hbar^2 k_z^2}{2m_{\mathrm{eff}}^{(j)}} + E_{\mathrm{T}}^{(j)} \pm \sqrt{(\alpha_{\mathrm{eff}}^{(j)} k_z)^2 + (\beta_{\mathrm{eff}}^{(j)} k_z^2)^2}, \tag{3.42}$$

where j and $\pm$ are the subband and spin indexes, $m_{\mathrm{eff}}^{(j)}$ is the effective mass and $E_{\mathrm{T}}^{(j)}$ is the transverse subband energy at $k_z = 0$. This expression has the same functional form than the zeroth-order CB Hamiltonian for a nanowire [Eq. (3.37)], but including not only a possible Rashba SO coupling $\alpha_{\mathrm{eff}}^{(j)}$ but also a Dresselhaus one $\beta_{\mathrm{eff}}^{(j)}$. While the Rashba contribution to the SO coupling is known to be mainly linear in k_z irrespective of the crystal structure, the Dresselhaus one can be both linear and quadratic for wurtzite crystals, and only linear for zinc-blende (111) crystals [160]. Hence, it is not possible, in principle, to separate the contributions of the Rashba and Dresselhaus coefficients in the linear term of the SO coupling. In practice, the linear Dresselhaus contribution turns out to be zero for zinc-blende (111) crystals and negligible or zero for wurtzite (0001) ones [166, 180] [3]. We

---

[3] Notice that zinc-blende (111) crystals are almost symmetric in the three directions and wurtzite (0001) ones are almost symmetric around the z axis. Therefore, since there is no bulk inversion asymmetry in these directions, there cannot be a SO interaction either. Only higher-order asymmetries, i.e., the ones accounted for by cubic terms in k (although quadratic in k_z), can contribute to Dresselhaus terms. These terms are taken into account through the parameter β_{eff} in Eq. (3.42).

therefore assume that the linear coefficient of the SO coupling $\alpha_{\text{eff}}^{(j)}$ is dominated by the Rashba SO contribution. On the other hand, the SO coupling can be computed in the CB approximation by directly evaluating the expectation value of the SO coupling [either Eq. (3.30) or Eq. (3.33)] for each subband, as shown in Eq. (3.39).

The modulus[4] of the effective Rashba SO coupling obtained using the 8B model is plotted with dots in Fig. 3.3 for the case of a zinc-blende (111) InAs (red) and wurtzite (0001) InAs (blue) nanowires. The first three transverse subbands are considered in (b-d), represented vs the back gate voltage. The SO coupling exhibits a minimum around -0.04V, independently of the transverse mode and the crystal. This is because, at this gate voltage value, the electric field inside the wire is basically zero. It occurs at $V_{\text{Gate}} \neq 0$ due to the surface charge present at the nanowire facets, which introduces a small pinned electrostatic field. Its modulus then increases either for more positive or more negative gate voltages as the electric field inside the wire is increased with the aid of the potential gate. We moreover note that the SO coupling decreases with the number of the transverse mode, i.e., it is larger for the lowest energy subband. This can be understood by directly inspecting the SO coupling expression of Eq. (3.30), that shows that the larger E (which includes the energy of the subband), the smaller $\vec{\alpha}$ is. Moreover, it is remarkable that the SO coupling is smaller for wurtzite crystals than for zinc-blende, something that has been already pointed out in previous works [160].

With a solid (black) green line we show in Fig. 3.3(b-d) the results of the (simplified) zeroth-order CB approximation. Although they are derived for zinc-blende nanowires, it is also frequently used to describe wurtzite crystals. They follow the same trend but they do not numerically agree with any of the full 8B k·p model calculations by a factor of more than two for this device. Lastly, we note that only the zeroth-order SO coupling equation (green line) changes with the transverse subband as the 8B model does. This is not the case of the simplified equation (black line), which is the same for all the subbands, as the dependence with the energy is neglected in Eq. (3.33).

Hence, we conclude that the CB approximation is not quantitatively precise predicting the SO coupling in nanowires, even if Eq. (3.30) provides the qualitative behavior. The reason is that, even if the zeroth-order Dyson expansion is justified, i.e., for this device indeed it is satisfied $\Delta_{\text{g}} = 417$ meV $\gg \Omega_1 = \gamma_1 \hbar^2 \text{k}_{\text{F}}^2 / 2\text{m}_{\text{e}} \simeq 8$ meV; it only means that the total energy $E(k_z)$ provided by the CB approximation should match the one of the 8B model. But the SO coupling is just a small correction to this energy dispersion relation since in general the kinetic energy is much larger than the SO coupling. Therefore, the CB approximation fails capturing a small detail like the SO coupling but still provides a good agreement for the total energy. Actually, as we will show, the CB approximation does provide a good agreement for the effective mass.

---

[4]In our setup, the Rashba SO coupling has only x and y components. The z component is zero due to the translational invariance along that direction.
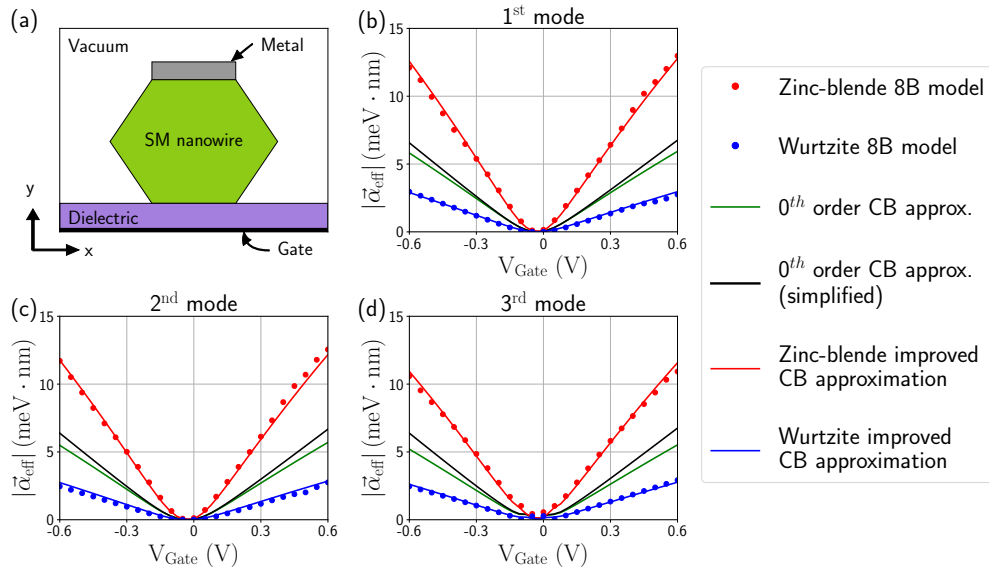
Figure 3.3: (a) Sketch of the simulated device: same as in Fig. 3.2 but with a 10 nm–thick metallic layer on the top facet. There is a thin oxide layer between the SM and the metal (not shown) that prevents electrons to tunnel through. (b-d) Effective SO coupling for the first three subbands computed using different methods: (red/blue dots) extracted from a zinc-blende/wurtzite 8B k·p model or (solid lines) using the zeroth-order CB approximation Eq. (3.30) (green), the simplified equation of Eq. (3.33) (black) or the improved one of Eq. (3.43). The metallic layer is grounded, i.e., we set the electrostatic potential of its boundaries to zero. The mobile charges, ρ_{mobile}, are ignored for simplicity.

Confinement effects and improved equation

Going beyond the zeroth-order in the CB expansion of the SO coupling operator leads to complicated expressions, especially as the order increases, see Appendix B.2. One can check numerically that summation over several terms is needed to approach the correct SO coupling. Since summing up the infinite series is not better than solving the 8B Hamiltonian, and since in this thesis we are looking for a manageable expression for the SO coupling, we resort to the following ansatz. We propose to use an expression for the SO coupling with the same functional form of Eq. (3.30), which is the dominant term in the expansion and it follows the same qualitative trend of the 8B model; but where the parameter P is substituted by an improved one, that we call P_{fit}, chosen so as to reproduce the Rashba SO coupling extracted from the 8B model in nanowires. Moreover, as commented in Sec. 3.1.2, for finite cross-section nanowires, if the SO length is larger than the wire's diameter, i.e., $l_{\mathrm{SO}} \gtrsim W_{\mathrm{wire}}$, we can write the total energy as $E = E_{\mathrm{T}}^{(j)} + E(k_z)$, where $E_{\mathrm{T}}^{(j)}$ is the transverse subband energy and $E(k_z)$ the longitudinal contribution. For the small k_z-range for which the 8B model applies, the condition $|E_{\mathrm{T}}^{(j)}| \gg |E(k_z)|$ is satisfied. Therefore, projecting over the transverse part of the Hamiltonian's eigenstates, we posit that we can write the *improved j*-th

subband effective Rashba SO coupling as

$$\vec{\alpha}_{\text{eff,improved}}^{(j)} = \left\langle \Psi_{\text{T}}^{(j)} \right| \frac{eP_{\text{fit}}^2}{3} \left[\frac{1}{\left(\Delta_{\text{g}} + e\phi(\vec{r}) + E_{\text{T}}^{(j)} \right)^2} - \frac{1}{\left(\Delta_{\text{soff}} + \Delta_{\text{g}} + e\phi(\vec{r}) + E_{\text{T}}^{(j)} \right)^2} \right] \vec{\nabla}\phi(\vec{r}) \left| \Psi_{\text{T}}^{(j)} \right\rangle,$$

(3.43)

where P_{fit} is extracted by fitting this equation to the Rashba SO coupling obtained with the 8B Kane model[5]. In this way, we are conjecturing that the lost information about the intravalence band couplings γ_i, lost when truncating the Dyson expansion can be recovered, at least partially, by one fitting parameter. This parameter is going to depend on the semiconductor compound (InAs, InSb, etc.) and crystallography (zinc-blende or wurtzite). However, we assume that P_{fit} can be taken as independent of $\phi(\vec{r})$ and the electron's energy (or equivalently, W_{wire}). Remarkably, as we will show, these assumptions turn out to be pretty accurate for realistic experimental conditions.

We first discuss how to obtain the improved parameter P_{fit} of Eq. (3.43) for InAs nanowires. To do so, as already mentioned, we fit Eq. (3.43) to the calculations based on the 8B model. To this end, we use the device and simulations of Fig. 3.3. We show in the same figure with a solid red line the SO coupling resulting from the fitting for zinc-blende crystals, and with a solid blue line for wurtzite. As one can appreciate, the improved SO coupling equation perfectly matches the full 8B model calculations for both crystals. We obtain $P_{\text{fit}} = 1252$ meV·nm for zinc-blende, much larger than the original Kane parameter $P = 919.7$ meV·nm; and $P_{\text{fit}} = 723$ meV·nm for wurtzite ones, which is smaller (see Table 3.1 for the parameters). This means that the higher-order effects neglected in the zeroth-order approximation tends to increase the SO coupling in zinc-blende crystals while they tend to decrease the SO coupling in wurtzite ones. The ultimate physical reason for this phenomenon is unknown since our approach is heuristic and therefore it is not transparent in this sense. Notice that we can use the same fitting parameter calculated for the first mode for all the different transverse modes since P_{fit} depends only very slightly on the subband energy. This is not *a priori* obvious since the intravalence band corrections depend, in principle, on the specific subband. Fortunately, as shown in Fig. 3.3, the fit is also good for higher transverse modes.

To carry out the comparison between the different methods described above we needed to consider a specific electrostatic environment. But the value of P_{fit} should be independent of it for the applicability of Eq. (3.43) in arbitrary conditions. We have performed equivalent fittings for very different environments, see Appendix B.3, finding that P_{fit} varies only within a 2% with respect to the value presented in Table 3.1. This means that P_{fit} is reasonably independent of $\phi(\vec{r})$ for typical experimental conditions. The reason is that the main dependence of the SO coupling with the electrostatic potential comes from the gradient of $\phi(\vec{r})$. The prefactor within brackets in Eq. (3.43) [or in Eq. (3.30) for that matter] depends on $\phi(\vec{r})$ through the quantity $E + e\phi(\vec{r})$. Ignoring terms proportional to $(\vec{\nabla}\phi)^2$, $(\vec{\nabla}\phi)^3$, etc., higher order terms in the series expansion of the

---

[5]Note that in the improved SO coupling expression the Rashba z component is zero since the electrostatic potential depends only on the transverse coordinates (x, y). As before, the gradient only acts on ϕ and not on the wave function. This equation has to be solved self-consistently since $E_{\text{T}}^{(j)}$ is the energy associated to the transverse eigenstate $|\Psi_{\text{T}}^{(j)}\rangle$.

Table 3.1: Parameter P_{fit} (in meV·nm units) to be used in the improved equation for the Rashba SO coupling, Eq. (3.43), within the conduction band approximation. This parameter is extracted by fitting Eq. (3.43) to numerical 8B model calculations. For comparison, we show the value of the original Kane parameter P.

|	Zinc-blende (111)	Wurtzite (0001)	Kane P
InAs	1252±12	723.0±0.1	919.7
InSb	1082±7	-	940.2
GaAs	1912±18	-	1047.5
GaSb	1657±35	-	971.3

CB approximation satisfy a similar dependence with $\phi(\vec{r})$ but with more complicated prefactors. For instance, the first-order correction to the SO coupling gives [see Appendix B.2 for the derivation]

$$\vec{\alpha}_{\text{R}}^{(1)} \simeq -2e\frac{P^2}{3}\left[\frac{\gamma_1 - \gamma_3}{(E_{\text{h}} - e\phi(\vec{r}) - E)^3} - \frac{\gamma_1}{(E_{\text{soff}} - e\phi(\vec{r}) - E)^3}\right]\vec{\nabla}\phi(\vec{r})\frac{\hbar^2}{2m_e}(k_x^2 + k_y^2). \qquad (3.44)$$

The key observation is that this prefactor depends on the quantity $E + e\phi(\vec{r})$. On the other hand, the energy is the solution to the eigenvalue problem of the CB Hamiltonian, $E \sim E_{\text{K}} - e\langle\phi(\vec{r})\rangle + E_{\text{SO}}$, where E_{K} stands for the kinetic energy and E_{SO} for the Rashba one. Thus the electrostatic potential gets roughly canceled in all those prefactors. Since P_{fit} is an approximation to the sum of terms like this one, its dependence with $\phi(\vec{r})$ should be small as well.

However, this first-order term (as well as the leading ones) that corrects the zeroth-order Rashba coefficient of Eq. (3.30) in the CB approximation is proportional to the transverse momenta $\frac{\hbar^2}{2m_e}(k_x^2 + k_y^2)$, they produce SO corrections coming from the finite-size of nanowire section. To quantify this effect we consider in Fig. 3.4 wires of different width W_{wire} in an electrostatic environment like the one of Fig. 3.3(a). By using the improved Eq. (3.43) and by fitting it to 8B model calculations, we plot the value of the resulting P_{fit} parameter as a function of W_{wire}. This is done for zinc-blende InAs, InSb, GaAs and GaSb, and for wurtzite InAs. We observe that the fitting parameter for zinc-blende structures increases for small diameters, has a maximum around $100 - 150$ nm (depending on the crystal) and then slowly decreases as $W_{\text{wire}} \to \infty$, approaching the original Kane parameter P (solid line) since confinement effects become negligible. Strikingly, wurtzite nanowires (blue line) exhibit a minimum instead of a maximum for the same range of diameters. The value of P_{fit} is nevertheless pretty constant for a wide range of wire's widths, which correspond to the common experimental values. This justifies our approximation of using a simple width-independent P_{fit} parameter in our ansatz for an improved SO coupling equation. In particular, we consider $P_{\text{fit}}(W_{\text{wire}}) = 80$ nm in Table 3.1, represented with a dashed line in Fig. 3.4, which is a good approximation of $P_{\text{fit}}(W_{\text{wire}})$ for diameters between ~ 50 nm and ~ 200 nm.

To sum up, in finite-width nanowires with non-negligible transverse momenta $k_x, k_y \sim 1/W_{\text{wire}}$, the
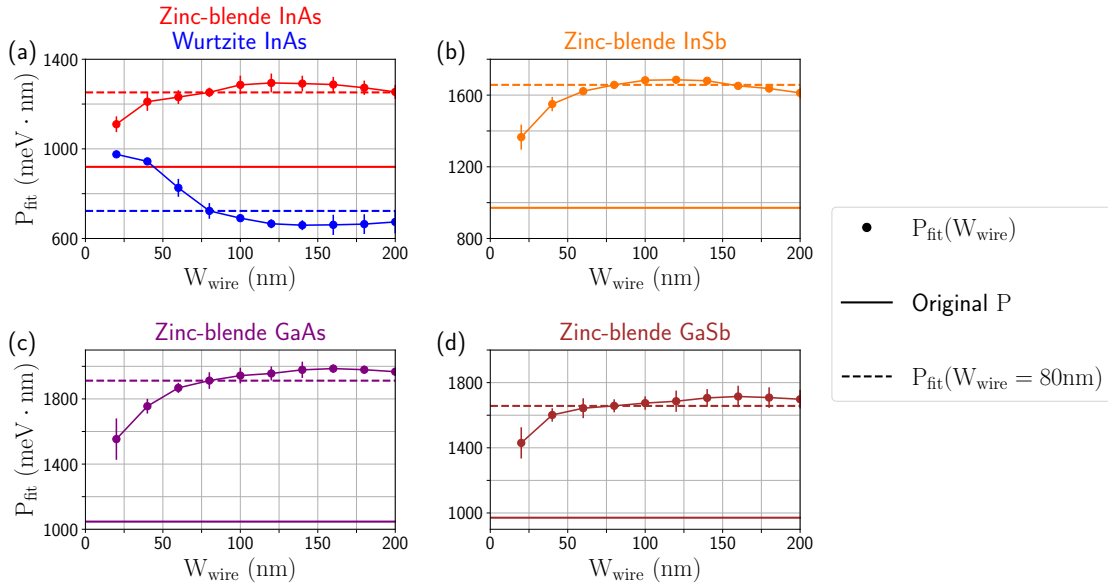
Figure 3.4: (a-d) Calculated P_{fit} parameter vs wire's width (dots) for different zinc-blende/wurtzite III-V compound SMs. For comparison, we show with a solid line the original (nominal) Kane parameter, and with a dashed line the value of P_{fit} for $W_{wire} = 80$ nm. Same simulations as in Fig. 3.3.

higher order terms neglected in the zeroth-order conduction band approximation turn out to be important to predict the correct SO coupling. The reason is that different transverse subbands acquire modified gaps proportional to $\gamma_i \frac{\hbar^2}{2m_e} k^2$ at the Γ-point. Moreover, the dependence with $\gamma_i \frac{\hbar^2}{2m_e} k^2$ produces dramatic differences between distinct crystal structures (zinc-blende vs wurtzite). These confinement effects disappear as $W_{fit} \to \infty$, rendering the zeroth-order approximation correct for bulk crystals. Our parameter P_{fit} allows to include this effect in a direct way while keeping the simplicity of the zeroth-order SO coupling of Eq. (3.30).

SP vs TF approximation

The previous simulations were performed ignoring the charge density of the wire ρ_{mobile}. As justified, since P_{fit} does not depend on the electrostatic potential, the fitting should not be affected by the inclusion of the electron-electron interactions. However, the SO coupling is sensitive to these interactions. To show this, and to prove the validity of the TF approximation for the determination of of the SO coupling, we have performed the same simulations as before (for the *improved* CB approximation) but including ρ_{mobile}. In Fig. 3.5, we show the SO coupling as a function of gate voltage in the absence of mobile charge (dashed line), including it in the TF approximation (solid line) and using the full SP approach (dots). We show the simulations using (a) the zeroth-order SO equation, (b) the simplified one and (c) the improved one. We find that TF provides an excellent approximation that matches the SP results. As we justified, this is because both provide similar electrostatic profiles and the SO coupling only depends on the gradient of this potential. Moreover,
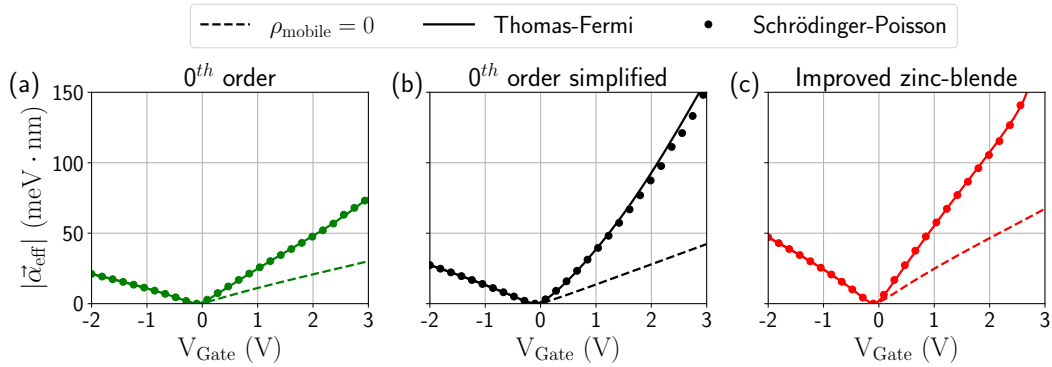
Figure 3.5: Rashba SO coupling modulus vs gate voltage for the lowest-energy subband within the CB approximation. (a) In green the results obtained using the improved Eq. (3.43) but with the original Kane parameter P. (b) In black, using the simplified Eq. (3.33). (c) In red, the results of the improved equation using the corresponding P_{fit} parameter displayed in Table 3.1 for a zinc-blende (111) crystal. Dots are used for full SP simulations, solid lines for the TF approximation and dotted lines for $\rho_{\text{mobile}} = 0$, i.e., ignoring the mobile charge density. Same parameters as the ones of Fig. 3.3 (except ρ_{mobile}). Temperature is $T = 10$ mK.

we realize that taking into account the charge density of the wire is essential to describe the behavior of α_{R} for large positive V_{Gate} values (large doping). This is due to the inhomogeneous electrostatic potential profile created by the charge, which contributes to the structural inversion asymmetry that in turn leads to the Rashba coupling. Once again, we note that the quantitative results predicted by the simplified equation (black curve) deviate considerably from the ones predicted for specific crystal structures (red curve).

Typical SO coupling values and comparison to experiments

In order to test the validity of our approach predicting the SO coupling in realistic situations, we compare the results that it provides with the ones obtained in several recent experiments. During the last decade, there has been an increasing interest in measuring the SO coupling in semiconductor nanowires due to their potential applications as spin-FETs [69, 70, 72, 73, 181, 182] or Majorana qubit devices [183, 184]. In most cases, these nanowires were made of InAs due to its large semiconductor band gap and Rashba coupling, although some of them used InSb nanowires [71, 74] and other mixed heterostructures [185–192] involving type III-V compound SMs. For the comparison, we focus on the works done by S. Dhara *et al.* [69], D. Liang *et al.* [70], K. Takase *et al.* [72], and Z. Scherübl *et al.* [73], carried out on zinc-blende InAs nanowires; and by K. Takase *et al.* [74] on zinc-blende InSb nanowires. We choose these experiments because they measure a representative number of SO coupling points versus a wide range of gate potentials.

In all of these experiments, the SO coupling is determined in an indirect way from magnetotransport measurements [193–195], which permit to access relevant length scales that affect the electron coherence. In particular, the SO coupling can be extracted from the spin-relaxation length l_{SO} as
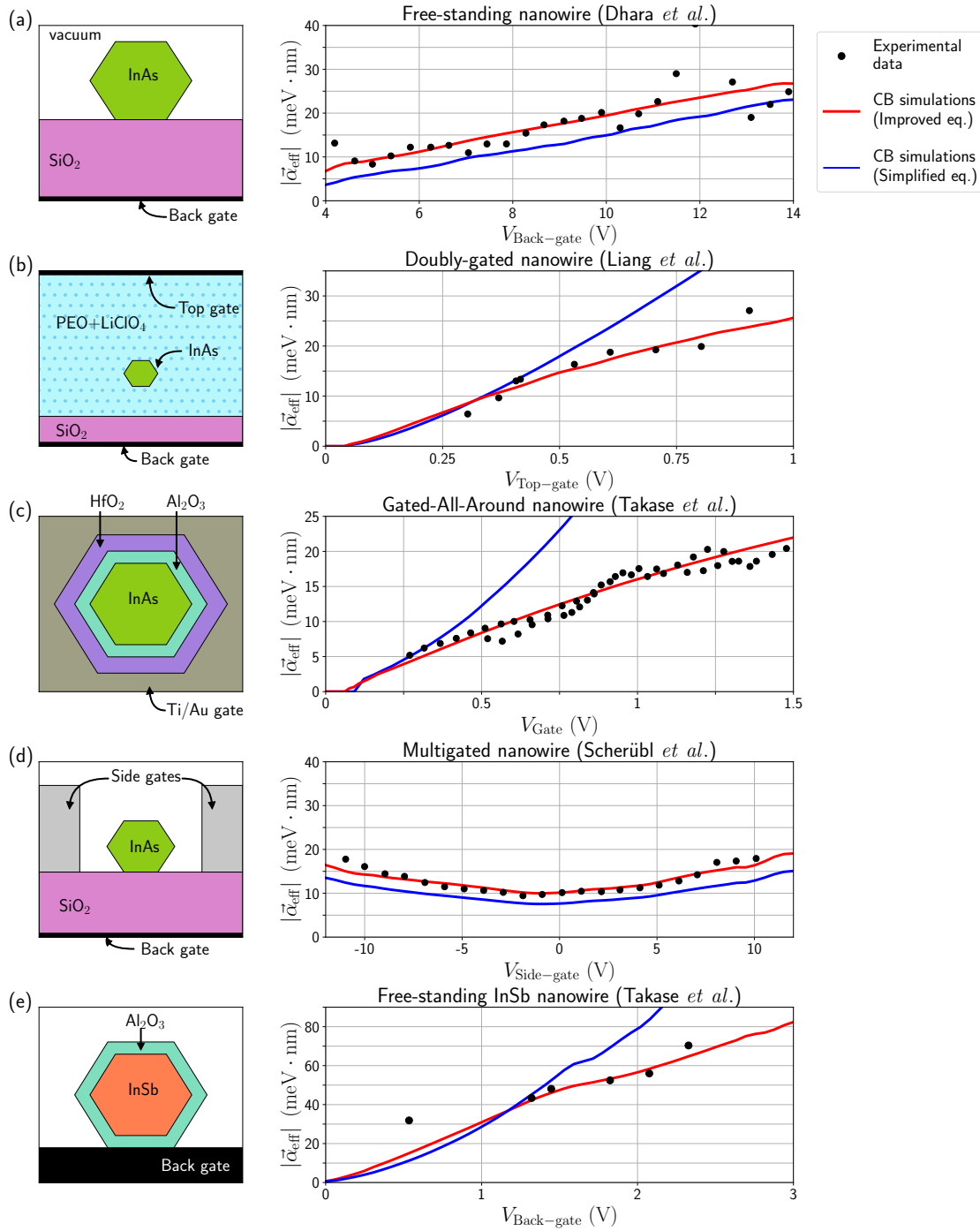
Figure 3.6: Electrostatic environment modelling of some experimental setups (left), and corresponding effective SO couplings (right) obtained in experiments (dots) and with our numerical simulations (solid lines). In red we show the results using the improved Eq. (3.43) and in blue the simplified Eq. (3.33). The experimental data corresponds to (a) Dhara *et al.* [69], (b) Liang *et al.* [70], (c) Takase *et al.* [72], (d) Scherübl *et al.* [73], and (e) Takase *et al.* [74]. The charge density of the wire is taken into account in the TF approximation and the surface charge is $\rho_{\mathrm{surf}} = 5 \cdot 10^{-3} \left(\frac{e}{\mathrm{nm}^3} \right)$. The geometrical parameters used in the simulations can be found in the main text. In agreement with the experiments, in our simulations we fix the temperature to $T = 1.7$ K in (a), $T = 4$ K and the back gate to 0 in (b), $T = 1.5$ K in (c), $T = 4.2$ K and the back gate to 15 V in (d), and $T = 1.7$ K in (e). The rest of the parameters can be found in Appendix B.4.

$\alpha_{\text{eff}} = \frac{\hbar^2}{2m_{\text{eff}} l_{\text{SO}}}$. Hence, to extract the SO coupling, it is necessary to know the electron's effective mass. In all the experiments that we analyze here, the authors use the same values, $m_{\text{eff}} = 0.023 m_e$ for InAs and $m_{\text{eff}} = 0.014 m_e$ for InSb. These are precisely the values one gets from the simplified zeroth-order Eq. (3.32) with the original Kane P parameter. One could argue that, in the same way we need to improve the zeroth-order equation for the SO coupling, one would also need to correct the effective mass $m^{(0)}$ to match the 8B model results. But as we show in the next section, this is indeed not necessary as the zeroth-order is already a very good approximation to the results provided by the 8B model Hamiltonian.

On the other hand, since this kind of measurements involves the collective transport of electrons around the Fermi energy, the SO coupling extracted from l_{SO} does not correspond to one particular subband but it is instead a weighted sum of all the subbands that contribute to the current. To compute numerically this averaged Rashba coupling in the conduction band approximation, we take the expectation value of the SO coefficient

$$\bar{\alpha}_{\text{eff}}^{(\text{EV})} = \frac{\sum_j \left\langle \vec{\alpha}_{\text{eff}}^{(j)}(\vec{r}) \right\rangle n^{(j)}}{\sum_j n^{(j)}}, \tag{3.45}$$

where $n^{(j)}$ is the occupation of transverse subband j. In Fig. 3.6, we compare the experimental data (dots) with the numerical results obtained with the improved Eq. (3.43) and the P_{fit} values of Fig. 3.4. The electrostatic potential is calculated using the TF approximation. For comparison, we also show the results provided by the simplified Eq. (3.33) (blue curves), which has been used in previous theoretical works.

Figure 3.6(a) refers to the experiment performed by Dhara *et al.* [69]. This is one of the first works that used magnetotransport measurements to determine the Rashba coupling in InAs nanowires. The device is quite simple (see sketch on the left): an 80 nm–wide InAs nanowire is placed on top of a SiO$_2$ substrate and 300 nm below the substrate there is a bottom gate that is used to tune the electrostatic potential inside the wire. The large V_{Gate} range explored in this experiment with a relatively small variation of the SO coupling, see right panel, is due to the rather large thickness of the substrate. Both theoretical curves predict the same qualitative behavior but, although they are quantitatively similar, our approach gives a somewhat better agreement with the experimental values. For this particular setup, the simplified equation works reasonably well because the electrostatic potential created by the gate is small. Thus the condition $\Delta_{\text{g}} \gg |e\phi(\vec{r}) + E|$ is almost fulfilled.

Figure 3.6(b) refers to the experiment carried out by Liang *et al.* [70]. They prove that it is possible to enhance the Rashba coupling by using an appropriate electrostatic environment. To do so, a 40 nm–wide InAs nanowire is suspended inside the (ionic) dielectric PEO+LiClO$_4$. At 50 nm below the wire there is a SiO$_2$ substrate of thickness 250 nm sitting on a grounded gate. On top of the device, 500 nm above the wire, there is another gate in contact with the dielectric. The PEO+LiClO$_4$ dielectric is characterized by a large permittivity, which allows to subject the wire

boundaries to almost the same potential as it is applied to the top gate. It is thus possible to significantly increase the wire's doping with a small gate voltage. The origin of the SO coupling in this setup is the inhomogeneous distribution of the charge along the radius of the wire, which is sometimes called pair SO coupling in the literature [196]. In the right panel we can see that the red curve is in good agreement with the experimental data, whereas the blue one deviates, especially at large V_{Gate}, due to the large electrostatic potentials involved.

Figure 3.6(c) deals with the experiment done by Takase *et al.* [72]. This work follows the same spirit than the previous one, but they look for a long-lived device that could be used as a spin-FET for spintronic applications. To this end, they fabricate a gated-all-around (GAA) device in which a 100 nm–wide nanowire is covered with a 2 nm–thick Al_2O_3 dielectric, a 4 nm–thick HfO_2 dielectric and a potential gate (see sketch on the left). Due to the small distance between the gate and the wire, the potential applied to the gate and at the boundary of the wire is almost the same. As in the previous example, the theoretical prediction resulting from our improved equation exhibits an excellent agreement with the experimental data, while the simplified one largely deviates from it. In this case, and motivated by their transport measurements, we have chosen the Fermi level at $E_F = -100$ meV, as if the wire was initially doped with holes.

Figure 3.6(d) shows the last case with InAs. It was performed by Scherübl *et al.* [73] to prove that it is possible to tune the Rashba coupling without changing the electron occupation inside the nanowire. To that end, they use a bottom gate together with two side ones. In this way they can tune two of them to increase the electric field (and thus the Rashba coupling) while keeping constant the total charge of the wire. As shown in the sketch, a 77 nm–wide nanowire is placed over a SiO_2 substrate, a bottom gate is 1 μm below the substrate and the two side gates are placed at 70 nm from the corners of the wire. The main origin of the strong SO coupling in this device is the structural inversion symmetry created by the difference between the gate potentials applied to the side gates. In the right panel, the SO coupling is plotted versus one side gate, while the other side gate is changed accordingly to keep the total charge inside the wire constant (see Ref. [73] for further information). We find here that both theoretical methods give a good match, although our improved equation produces a better agreement with the data. Actually, in order to explain the discrepancy between the prediction of the simplified equation and the experimental data, in Ref. [73] the authors add *ad hoc* a built-in intrinsic SO coupling of ~ 5 meV·nm, which is not necessary using our effective equation.

Finally, Fig. 3.6(e) refers to the experiment realized by Takase *et al.* [74] in InSb nanowires. This work proves that the SO coupling of InSb nanowires is much larger than that of InAs ones. Their device consists of a 182 nm wide wire covered by a 6 nm thick Al_2O_3 dielectric, placed directly over a metallic gate. The small thickness of the dielectric allows to tune (almost) perfectly the wire. In this last case we also find a good agreement between the red curve and the experimental measurements, while the simplified equation fails to predict the proper behavior. Deviations at small V_{Gate} may arise due to the small length of the wire in this experiment (500 nm). This may cause that the leads used for the transport measurements have an impact on the electrostatic potential profile at the

wire edges [99], changing unintentionally the precise SO coupling value.

All these devices exhibit a SO coupling ranging from 5–10 meV·nm in the low-doping regime to 20–40 meV·nm in the high-doping one. The former regime is the important one to create a topological phase in SM-SC heterostructures [20, 21, 115]. The values reported in these experiments, although sufficient to create a topological phase, are not large enough to produce a robust and measurable topological minigap, what is detrimental for the topological phase itself in finite-size nanowires. Particularly, for a $\alpha = 5$ meV·nm, we estimate[6] a small topological minigap of the order of $\Delta_{\min} \simeq 0.035$ meV. However, there are two ingredients missing. First, the SC in the heterostructure can induce a band-bending on the SM towards the interface. This is the case of InAs-Al nanowires, and, as we study in Chapter 4, this enhances the SO coupling. And secondly, strain at the interface is also a source of inversion asymmetry that can further increase the SO coupling. In Sec. 3.4, we provide one example of this in InAs-InP core-shell nanowires, showing that due to the strain at the interface between both materials, the SO coupling is doubled with respect to uncapped InAs wires. We believe that the same kind of strain is present at the interface of InAs-Al nanowires, what would contribute to improve the robustness of the topological phase in Majorana nanowires.

Regarding which III-V compound SM and crystal provides the largest SO coupling, this is something that can be inferred by directly inspecting the value of the prefactors to $\vec{\nabla}\phi(\vec{r})$ in Eq. (3.33). Taking the values of the Kane parameters (see Appendix B.4), one can check that, for the same electrostatic potential, the SO coupling is the largest in InSb nanowires, followed by InAs (4 times smaller to InSb), GaSb (13) and GaAs (49). In InP (287) and GaP (1988) compounds the SO coupling turn out to be completely negligible (their Kane parameters are provided in Ref. [158]). Although, we have only computed the SO coupling of wurtzite crystals for InAs wires, we conclude that in general the SO coupling is smaller in wurtzite than in zinc-blende crystals. This has been deeply investigated in other theoretical works [160, 180].

Together with this, we point out that the strength of the SO coupling also depends on the wire's diameter, since it is affected by confinement effects. In Appendix B.2 [see Fig. B.1(a)], we actually show how the SO coupling changes with the wire's diameter when a constant electrostatic field is fixed inside the wire. We find that the SO coupling is maximum for diameters around 130 nm in zinc-blende InAs wires, although this value may depend on the material and crystal.

3.3.2 Effective mass

In the previous subsection, we have stated that the CB effective mass is properly described using the simplified Eq. (3.32), given in terms of the original Kane parameter P. However, the intravalence band couplings ignored in the CB approximation that are essential for the SO coupling could also have an impact on the effective mass. To demonstrate that this is actually not the case, we

---

[6]We use the equations of a 1D Oreg-Lutchyn nanowire [51], assuming that the SM wire is made of InAs and the SC is Al.

Table 3.2: Parameter P_{mfit} (in meV·nm units) to be used in the improved equation for the effective mass, Eq. (3.46), within the CB approximation. This parameter is extracted by fitting Eq. (3.46) to numerical 8B model calculations. For comparison, we show the value of the original Kane parameter P.

|	P_{mfit}	P
InAs (111)	921±7	919.7
InSb (111)	950±15	940.2
GaAs (111)	1039±5	1047.5
GaSb (111)	977±12	971.3

follow the same reasoning as in Sec. 3.3.1 for the SO coupling, Eq. (3.43), and propose an *improved* equation for the effective mass, where the original P parameter is substituted by an improved one, P_{mfit},

$$
\frac{1}{m_{\mathrm{improved}}^{(j)}} = \frac{1}{m_e} + \left\langle \Psi_{\mathrm{T}}^{(j)} \right| \frac{2P_{\mathrm{mfit}}^2}{3\hbar^2} \left(\frac{2}{\Delta_{\mathrm{g}} + e\phi(\vec{r}) + E_{\mathrm{T}}^{(j)}} + \frac{1}{\Delta_{\mathrm{soff}} + \Delta_{\mathrm{g}} + e\phi(\vec{r}) + E_{\mathrm{T}}^{(j)}} \right) \left| \Psi_{\mathrm{T}}^{(j)} \right\rangle .
$$
(3.46)

Notice that the improved parameter for the effective mass, P_{mfit}, is not the same as the one for the Rashba SO coupling, P_{fit}, in the same way that the quantity between square brackets in Eq. (3.32) is different from the one in Eq. (3.33). This can readily be understood by following the CB approximation in terms of the Green's function Dyson series shown in Sec. 3.1.1.

Following the same procedure as in Sec. 3.3.1 for the Rashba SO coupling, we first compute the 8B model band structure for a particular electrostatic environment. We consider here the same one as in Fig. (3.3). From the conduction band shape, we can extract the value of the effective mass by fitting Eq. (3.42) to the energy subband j. In Fig. 3.7, we show these 8B model results with dots for the first three transverse modes (columns) and for different zinc-blende (111) semiconductor nanowires (rows). For illustration purposes, we only focus here on these three modes but higher modes can be found in Ref. [151]. Secondly, we fit Eq. (3.46) to the 8B model results of the lowest-energy subband (first column) in order to get P_{mfit} for each material. The resulting fitting parameters are shown in Table 3.2. We then use these values to compute the improved effective mass with Eq. (3.46), shown with solid lines in Fig. 3.7.

Note that the P_{mfit} values collected in Table 3.2 turn out to be essentially identical to their corresponding original Kane parameter P. This means that the inter-valence band couplings γ_i ignored in the zeroth-order CB approximation have a minor impact on the effective mass of the CB. Only the coupling between conduction and valence bands, accounted by P, has a significant contribution to the effective mass. This was further confirmed as a function of the wire's diameter W_{wire} in Fig. B.1(b) at the end of Appendix B.2. Therefore, we conclude that, even for low-
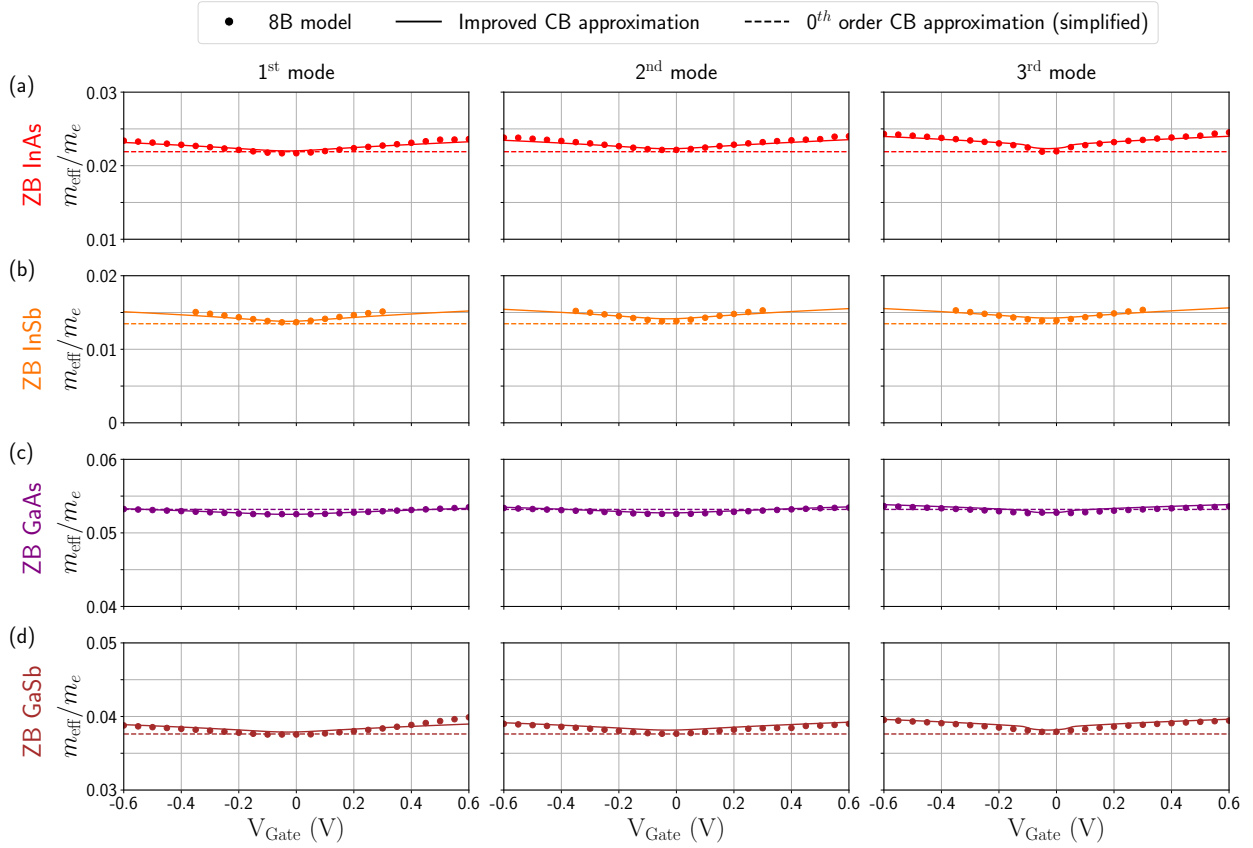
Figure 3.7: CB effective mass m_eff versus gate voltage for different zinc-blende (ZB) (111) semiconductor nanowires (rows) and different transverse modes (columns). Dots correspond to m_eff obtained from the 8B k·p Kane model of Eq. (3.7). Solid lines correspond to m_eff obtained from the improved effective mass Eq. (3.46). The corresponding P_mfit parameters are collected in Table 3.2. Dashed lines correspond to the simplified zeroth-order Eq. (3.32). The simulations have been performed using the same environment and parameters as in Fig. 3.3. Simulations for higher modes can be found in Ref. [151].

dimensional systems like the finite-width nanowires analyzed here, we can use the original Kane parameter P in the zeroth-order effective mass equation, Eq. (3.29), to a very good approximation. This is very different from what happens to the SO coupling. As we argued before, this is because the Dyson expansion does apply for these nanowires, but only to account for the total energy dispersion, which is mainly dominated by the kinetic energy (inversely proportional to the effective mass). The SO interaction is nevertheless a small correction to this energy, and thus, it is not well-captured by the expansion.

Finally, we point out that the values generally used in the literature for the different semiconductor effective masses correspond to those obtained with the simplified version of the zeroth-order CB approximation, Eq. (3.32). In particular, for the experiments analyzed in Sec. 3.3.1 [69, 70, 72–74], these masses are $m_{\text{eff}} = 0.023 m_e$ for InAs and $m_{\text{eff}} = 0.014 m_e$ for InSb. In the simplified equation, the assumption $\Delta_{\text{g}} \gg |e\phi(\vec{r}) + E|$ has been made, and thus the effective mass does not depend on the electrostatic potential. Thus, there could be a deviation between theory and experiments for large gate voltages. To check this, in Fig. 3.7, we show the effective mass provided by the simplified equation with dashed lines. The difference between this approximation and the exact results is always below 5% for the gate voltage range analyzed here. For larger potential values, the effective mass seems to converge to a constant value, being independent of the electrostatic potential, so we expect that the error keeps in the same order of magnitude. Hence, the wide spread use of the previous values for the effective masses, as well as the equivalent ones for other semiconductor compounds, is completely justified.

3.4   Effect of strain

Previous works reported that strain in III-V SM heterostructures change in a non-trivial way the band structure of these materials [197–202]. Its main effect is to change the value of the semiconductor gap, that in turn may modify the SO coupling and the effective mass. Moreover, strain in III-V SM core-shell nanowires, like InAs-InP nanowires, has been reported [203–207] at the interface between both materials. This strain is present along the radial $\vec{r}$ direction even if the shell is grown epitaxially, since there is in general a lattice mismatch between both materials. This situation could also apply at the interface of SM-SC heterostructures that also present a lattice mismatch. In fact, strain at the interface between InAs and Al has been reported in nanowires, being of the same order than that of InAs-InP nanowires [80]. Motivated by these works, we proceed to derive in this section an effective equation for the SO coupling and effective mass as the ones derived at zeroth-order in Dyson expansion but including now the effect of strain. Our goal is to ascertain whether the strain can enhance or being detrimental for the SO coupling, and therefore, for the robustness of the topological phase in SM-SC heterostructures.

3.4.1 Strained conduction-band Hamiltonian for bulk III-V compound semiconductors

We follow the same procedure as in Sec. 3.1.1 when deriving the CB approximation but including in the 8B k·p Hamiltonian the strain as explained in Ref. [198]. The strain can be described as a spatial-dependent tensor $\mathbf{e}(\vec{r})$ that locally changes the lattice constant

$$\vec{a}_\mathrm{s}(\vec{r}) = (\mathbb{I} + \mathbf{e}(\vec{r}))\,\vec{a}_0 \;\leftarrow\; \mathbf{e}(\vec{r}) = \begin{pmatrix} e_x(\vec{r}) & e_{xy}(\vec{r}) & e_{xz}(\vec{r}) \\ e_{yx}(\vec{r}) & e_y(\vec{r}) & e_{yz}(\vec{r}) \\ e_{zx}(\vec{r}) & e_{zy}(\vec{r}) & e_z(\vec{r}) \end{pmatrix}, \tag{3.47}$$

being $\vec{a}_0$ the size of the unperturbed lattice spacing (in each direction) and $\vec{a}_\mathrm{s}(\vec{r})$ the one after the strain is taken into account. Alternatively, one can write the same equation for the coordinate system of the atoms in the lattice, $\vec{r}_\mathrm{s} = (\mathbb{I} + \mathbf{e}(\vec{r}))\,\vec{r}$. Assuming the strain is small, it is possible to expand the electrostatic potential of the deformed crystal to first order

$$\vec{\phi}_{\mathrm{s},0}(\vec{r}, \mathbf{e}) = \vec{\phi}_0(\vec{r}) + \left[\frac{\partial \vec{\phi}_{\mathrm{s},0}(\vec{r}, \mathbf{e})}{\partial \mathbf{e}} \right]_{e=0} \cdot \mathbf{e}. \tag{3.48}$$

This allows us to include directly in the the original (unstrained) k·p Hamiltonian H_kp a perturbative term $\tilde{H}_\mathrm{kp}$ that accounts for the strain, so that the strained k·p Hamiltonian is

$$H_{\mathrm{s,kp}} = H_\mathrm{kp} + \tilde{H}_\mathrm{kp}. \tag{3.49}$$

This perturbation has the same symmetries than the unstrained Hamiltonian, meaning that it just introduces some corrections to the original Kane parameters. Hence, as we did for the unstrained k·p Hamiltonian, we can also separate the perturbation into conduction and valence subspaces

$$\tilde{H}_\mathrm{kp} = \begin{pmatrix} \tilde{H}_\mathrm{c} & \tilde{H}_\mathrm{cv} \\ \tilde{H}_\mathrm{cv}^\dagger & \tilde{H}_\mathrm{v} \end{pmatrix}. \tag{3.50}$$

Assuming that the strain is not position-dependent, no shear or twisting deformations, i.e., $e_{ij} = 0$ $\forall i \neq j$, and no strain along the wire's axis, $e_z = 0$; these Hamiltonians can be written as

$$\tilde{H}_\mathrm{c} = \begin{pmatrix} \tilde{E}_\mathrm{c} & 0 \\ 0 & \tilde{E}_\mathrm{c} \end{pmatrix}, \tag{3.51}$$

$$
\tilde{H}_{\mathrm{v}} =
\begin{pmatrix}
\tilde{E}_{\mathrm{lh}} & 0 & 0 & 0 & 0 & 0 \\
0 & \tilde{E}_{\mathrm{hh}} & 0 & 0 & 0 & 0 \\
0 & 0 & \tilde{E}_{\mathrm{hh}} & 0 & 0 & 0 \\
0 & 0 & 0 & \tilde{E}_{\mathrm{lh}} & 0 & 0 \\
0 & 0 & 0 & 0 & \tilde{E}_{\mathrm{soff}} & 0 \\
0 & 0 & 0 & 0 & 0 & \tilde{E}_{\mathrm{soff}}
\end{pmatrix},
\tag{3.52}
$$

$$
\tilde{H}_{\mathrm{cv}} =
\begin{pmatrix}
-\frac{1}{\sqrt{6}}P(e_x k_x + i e_y k_y) & 0 & -\frac{1}{\sqrt{2}}P(e_x k_x - i e_y k_y) & \cdots \\
0 & \frac{1}{\sqrt{2}}P(e_x k_x + i e_y k_y) & 0 & \cdots \\
\cdots \quad 0 & 0 & -\frac{1}{\sqrt{3}}P(e_x k_x + i e_y k_y) \\
\cdots \quad \frac{1}{\sqrt{6}}P(e_x k_x - i e_y k_y) & -\frac{1}{\sqrt{3}}P(e_x k_x - i e_y k_y) & 0
\end{pmatrix},
\tag{3.53}
$$

where the diagonal terms in the above Hamiltonians are

$$
\tilde{E}_{\mathrm{c}} = a_c(e_x + e_y),
\tag{3.54}
$$

$$
\tilde{E}_{\mathrm{lh}} = -\left(a_v - \frac{b}{2}\right)(e_x + e_y),
\tag{3.55}
$$

$$
\tilde{E}_{\mathrm{hh}} = -\left(a_v + \frac{b}{2}\right)(e_x + e_y),
\tag{3.56}
$$

$$
\tilde{E}_{\mathrm{soff}} = -a_v(e_x + e_y).
\tag{3.57}
$$

As it can be read in these expressions, the main effect of the strain is to change the band edges E_i through the deformation-potential constants a_c, a_v and b (see Ref. [198] for their definitions in term of the first order deformation potential perturbation), together with the coupling between the conduction and valence bands. We note that it does not change the couplings among the valence bands because we have ignored shear or twisting deformations in our system, i.e., $e_{ij} = 0 \ \forall i \neq j$, see Ref. [198].

We proceed to integrate out the valence bands through the folding-down procedure performing again a zeroth-order Dyson expansion but for the strained Hamiltonian $H_{\mathrm{s,kp}}$. Now, the small parameter in which we expand the Hamiltonian is $\sim \Omega_i/(E_i + \tilde{E}_i)$, where $(E_i + \tilde{E}_i)$ are the different *strained* band-gap energies at the Γ-point. This is equivalent to assume that $\gamma_i k_F \ll \Delta_{\mathrm{g}} + \left(a_v \pm \frac{b}{2}\right)(e_x + e_y)$, which implies that the strain e must be a perturbation (since, as we show in the previous section, $\gamma_i k_F \ll \Delta_{\mathrm{g}}$ is already satisfied). Under this approximation, we can perform the folding-down in an

analytical way and obtain the effective *strained* CB Hamiltonian

$$H_{\text{s,CB}}^{(0)} \simeq \left[\frac{\hbar^2 \vec{k}^2}{2m_e} + E_c - e\phi(\vec{r}) \right] \sigma_0 + (\Lambda_{\text{s},0}\sigma_0 + \Lambda_{\text{s},x}\sigma_x + \Lambda_{\text{s},y}\sigma_y + \Lambda_{\text{s},z}\sigma_z), \quad (3.58)$$

where

$$\begin{aligned}
\Lambda_{\text{s},0} = &-\frac{P^2(1-e_x)^2}{3} k_x \left[\frac{3/2}{E_{\text{hh}} - e\phi(\vec{r}) - E} + \frac{1/2}{E_{\text{lh}} - e\phi(\vec{r}) - E} + \frac{1}{E_{\text{soff}} - e\phi(\vec{r}) - E} \right] k_x \\
&-\frac{P^2(1-e_y)^2}{3} k_y \left[\frac{3/2}{E_{\text{hh}} - e\phi(\vec{r}) - E} + \frac{1/2}{E_{\text{lh}} - e\phi(\vec{r}) - E} + \frac{1}{E_{\text{soff}} - e\phi(\vec{r}) - E} \right] k_y \\
&-\frac{P^2}{3} k_z \left[\frac{2}{E_{\text{lh}} - e\phi(\vec{r}) - E} + \frac{1}{E_{\text{soff}} - e\phi(\vec{r}) - E} \right] k_z, \quad (3.59)
\end{aligned}$$

$$\begin{aligned}
\Lambda_{\text{s},x} = i\frac{P^2}{3}(1-e_y) \Bigg\{ &k_z \left[\frac{1}{E_{\text{hh}} - e\phi(\vec{r}) - E} - \frac{1}{E_{\text{soff}} - e\phi(\vec{r}) - E} \right] k_y \\
&-k_y \left[\frac{1}{E_{\text{hh}} - e\phi(\vec{r}) - E} - \frac{1}{E_{\text{soff}} - e\phi(\vec{r}) - E} \right] k_z \Bigg\}, \quad (3.60)
\end{aligned}$$

$$\begin{aligned}
\Lambda_{\text{s},y} = i\frac{P^2}{3}(1-e_x) \Bigg\{ &k_x \left[\frac{1}{E_{\text{hh}} - e\phi(\vec{r}) - E} - \frac{1}{E_{\text{soff}} - e\phi(\vec{r}) - E} \right] k_z \\
&-k_z \left[\frac{1}{E_{\text{hh}} - e\phi(\vec{r}) - E} - \frac{1}{E_{\text{soff}} - e\phi(\vec{r}) - E} \right] k_x \Bigg\}, \quad (3.61)
\end{aligned}$$

$$\begin{aligned}
\Lambda_{\text{s},z} = i\frac{P^2}{3}(1-e_x)(1-e_y) \Bigg\{ &k_y \left[\frac{3/2}{E_{\text{hh}} - e\phi(\vec{r}) - E} - \frac{1/2}{E_{\text{lh}} - e\phi(\vec{r}) - E} - \frac{1}{E_{\text{soff}} - e\phi(\vec{r}) - E} \right] k_x \\
&-k_x \left[\frac{3/2}{E_{\text{hh}} - e\phi(\vec{r}) - E} - \frac{1/2}{E_{\text{lh}} - e\phi(\vec{r}) - E} - \frac{1}{E_{\text{soff}} - e\phi(\vec{r}) - E} \right] k_y \Bigg\}. \quad (3.62)
\end{aligned}$$

This Hamiltonian can be written in a more transparent manner as

$$H_{\text{s,CB}}^{(0)} \simeq \left[\vec{k} \frac{\hbar^2}{2\mathbf{m}_{\text{s}}^{(0)}(\vec{r})} \vec{k} + E_c - e\phi(\vec{r}) \right] \sigma_0 + \vec{\Gamma}_{\text{s}}^{(0)}(\vec{k}) \cdot \vec{\sigma}. \quad (3.63)$$

The first term corresponds to the kinetic energy with $\mathbf{m}_{\text{s}}^{(0)}$ being the strained effective mass. Due to the asymmetry introduced by the strain (it may be different in each direction), the effective mass is now a tensor whose diagonal terms are

$$\begin{aligned}
\left(\frac{1}{\mathbf{m}_{\text{s}}^{(0)}(\vec{r})} \right)_{xx} = \frac{1}{m_e} - \frac{2P^2}{3\hbar^2}(1-e_x)^2 \Bigg[&\frac{3/2}{E_{\text{hh}} - e\phi(\vec{r}) - E} \\
&+ \frac{1/2}{E_{\text{lh}} - e\phi(\vec{r}) - E} + \frac{1}{E_{\text{soff}} - e\phi(\vec{r}) - E} \Bigg], \quad (3.64)
\end{aligned}$$

$$\left(\frac{1}{\mathbf{m}_{\mathrm{s}}^{(0)}(\vec{r})}\right)_{yy} = \frac{1}{m_e} - \frac{2P^2}{3\hbar^2}(1-e_y)^2 \left[\frac{3/2}{E_{\mathrm{hh}} - e\phi(\vec{r}) - E}\right.$$
$$\left. + \frac{1/2}{E_{\mathrm{lh}} - e\phi(\vec{r}) - E} + \frac{1}{E_{\mathrm{soff}} - e\phi(\vec{r}) - E}\right], \tag{3.65}$$

$$\left(\frac{1}{\mathbf{m}_{\mathrm{s}}^{(0)}(\vec{r})}\right)_{zz} = \frac{1}{m_e} - \frac{2P^2}{3\hbar^2}\left[\frac{2}{E_{\mathrm{lh}} - e\phi(\vec{r}) - E} + \frac{1}{E_{\mathrm{soff}} - e\phi(\vec{r}) - E}\right]. \tag{3.66}$$

The non-diagonal terms of the effective mass are always zero unless further terms in the Dyson expansion are taken into account. The other term in Eq. (3.63) corresponds to the Rashba SO interaction, being $\vec{\Gamma}_{\mathrm{s}}^{(0)}(\vec{k})$ the strained SO field. This field can be written as the following matrix product

$$\vec{\Gamma}_{\mathrm{s}}^{(0)}(\vec{k}) = \frac{1}{2}\left[\begin{pmatrix} 0 & \alpha_z^{yy} & -\alpha_y^{yy} \\ -\alpha_z^{xx} & 0 & \alpha_x^{xx} \\ \alpha_y^{xy} & -\alpha_x^{xy} & 0 \end{pmatrix} \cdot \vec{k}^t + \vec{k} \cdot \begin{pmatrix} 0 & \alpha_z^{yy} & -\alpha_y^{yy} \\ -\alpha_z^{xx} & 0 & \alpha_x^{xx} \\ \alpha_y^{xy} & -\alpha_x^{xy} & 0 \end{pmatrix}^t\right]. \tag{3.67}$$

Here α_i^{jk} are the SO couplings that, due to the strain, have an intricate tensor structure as well. These coefficients are given by

$$\alpha_i^{jk} = \frac{P^2}{3}(1-e_j)(1-e_k)\partial_i\left[\frac{3/2}{E_{\mathrm{hh}} - e\phi(\vec{r}) - E}\right.$$
$$\left. - \frac{1/2}{E_{\mathrm{lh}} - e\phi(\vec{r}) - E} - \frac{1}{E_{\mathrm{soff}} - e\phi(\vec{r}) - E}\right] \leftarrow \forall j \neq k, \tag{3.68}$$

$$\alpha_i^{jj} = \frac{P^2}{3}(1-e_j)\partial_i\left[\frac{1}{E_{\mathrm{lh}} - e\phi(\vec{r}) - E} - \frac{1}{E_{\mathrm{soff}} - e\phi(\vec{r}) - E}\right] \leftarrow \forall j = k. \tag{3.69}$$

Notice that if there is no strain, $e_i = 0$, then $\alpha_i^{jk} = \alpha_i^{lm} \equiv \alpha_i \; \forall(j,k,l,m)$ and the matrices in Eq. (3.67) turn out to be antisymmetric. Hence, one can write the dot products as cross-products so that one recovers the conventional SO field term $\frac{1}{2}\left(\vec{\alpha} \times \vec{k} - \vec{k} \times \vec{\alpha}\right)$ of Eq. (3.28). We also note that analogous terms could be derived for the (strained) effective g-factor if there was an external magnetic field.

3.4.2   Strained conduction-band Hamiltonian for nanowires

Following the same reasoning as in Sec. 3.1.2, we look for the Hamiltonian of a nanowire, so we split the strained CB Hamiltonian in transverse (x, y) and longitudinal (z) parts. The finite-size in the transverse direction gives rise to quantized subbands $E_{\mathrm{s,T}}^{(j)}$, while in the z direction the wire is translational invariant so that k_z is a good quantum number. If we assume that the the

inter-subband SO coupling is negligible (i.e., $l_{SO} \gtrsim W_{wire}$), then different subbands do not mix and one can write an effective strained CB Hamiltonian for each of them,

$$H_{s,eff}^{(j)}(k_z) = \left(\frac{\hbar^2 k_z^2}{2m_{s,eff}^{(j)}} + E_{s,T}^{(j)} \right) \sigma_0 + \left(\alpha_{s,eff,x}^{(j)} \sigma_y - \alpha_{s,eff,y}^{(j)} \sigma_x \right) k_z, \qquad (3.70)$$

where $m_{s,eff}^{(j)}$ and $\alpha_{s,eff}^{(j)}$ are the effective strained mass and SO coupling. Particularly, they can be written in their final form as

$$\frac{1}{m_{s,eff}^{(j)}} = \left\langle \left(\frac{1}{\mathbf{m}_s^*(\vec{r})} \right)_{zz} \right\rangle_j \simeq \left\langle \frac{1}{m_e} + \frac{2P^2}{3\hbar^2} \left[\frac{2}{\Delta_g + \left(a_v - \frac{b}{2} \right)(e_x + e_y)} + \frac{1}{\Delta_g + \Delta_{soff} + a_v(e_x + e_y)} \right] \right\rangle_j,$$
$$(3.71)$$

$$\alpha_{s,eff,x}^{(j)} \simeq \left\langle \frac{P^2}{3}(1 - e_y) \left[\frac{1}{\left(\Delta_g + \left(a_v - \frac{b}{2} \right)(e_x + e_y)\right)^2} - \frac{1}{\left(\Delta_g + \Delta_{soff} + a_v(e_x + e_y)\right)^2} \right] \partial_x \phi(\vec{r}) \right\rangle_j,$$
$$(3.72)$$

$$\alpha_{s,eff,y}^{(j)} \simeq \left\langle \frac{P^2}{3}(1 - e_x) \left[\frac{1}{\left(\Delta_g + \left(a_v - \frac{b}{2} \right)(e_x + e_y)\right)^2} - \frac{1}{\left(\Delta_g + \Delta_{soff} + a_v(e_x + e_y)\right)^2} \right] \partial_y \phi(\vec{r}) \right\rangle_j,$$
$$(3.73)$$

where $\langle ... \rangle_j = \left\langle \Psi_T^{(j)} \middle| ... \middle| \Psi_T^{(j)} \right\rangle$ is the expectation value over the transverse subband j. In the above equations, we assume that $\Delta_g + \left(a_v - \frac{b}{2} \right)(e_x + e_y) \gg |e\phi(\vec{r}) + E|$, so that one can neglect $e\phi(\vec{r}) + E$ in the denominators, as we did with the simplified equations in Sec. 3.1.1. In comparison with the unstrained equations, Eqs. (3.33) and (3.32), the only difference with respect to these strained equations is that the gaps have been renormalized, the SM $\Delta_g \to \Delta_g + \left(a_v - \frac{b}{2} \right)(e_x + e_y)$ and the split-off one $\Delta_g + \Delta_{soff} \to \Delta_g + \Delta_{soff} + a_v(e_x + e_y)$, together with the conduction-to-valence coupling $P^2 \to P^2(1 - e_i)$. Notice that a compressive strain, i.e., $e < 0$, tends to reduce the SM gaps[7] and increase the conduction-to-valence couplings. And this in turn enhances the SO coupling and reduces the effective mass of the electrons in the CB.

3.4.3 Spin-orbit coupling in strained heterostructures

To illustrate this phenomenon, we show here one representative example of the enhancement of the SO coupling in strained heterostructures. In Ref. [152], they carry out experiments on InAs-InP core-shell nanowires, showing that they exhibit a larger SO coupling in comparison to an uncapped nanowire [208]. Their STEM measurements together with numerical FEM calculations of the lattice shows that there is some strain at the interface due to the lattice mismatch between both materials. And our simulations prove that this strain is precisely the responsible for the SO coupling enhancement.

A sketch of the experimental device that we simulate is shown in Fig. 3.8(a): a wurtzite (0001) InAs nanowire core (green) of 100 nm–diameter, covered by a 4 nm–thick InP shell (pink), which in turn

---

[7]In general, $a_v/2 > b$ is satisfied for all the III-V compound SM [158].
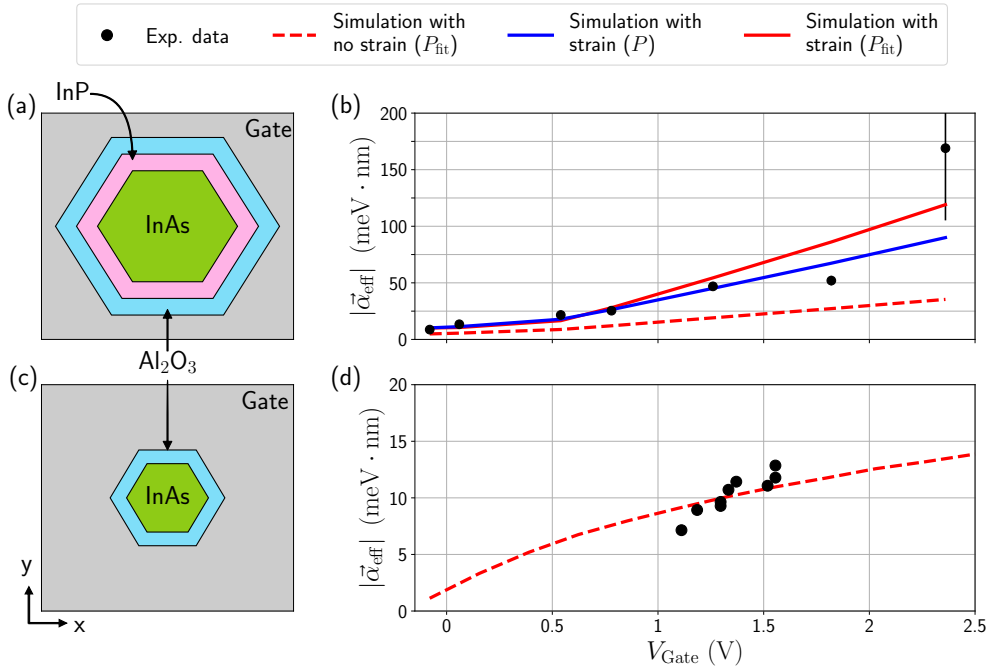
Figure 3.8: (a) Sketch of the experimental device of Ref. [152]: an InAs nanowire (green) is covered by an InP layer (pink), which in turn is covered by an all-around gate (gray). A layer made of Al_2O_3 (cyan) isolates the core-shell InAs-InP nanowire from the gate. A charge density layer ρ_{surf} at the InAs-InP interface models the band-bending towards this interface. (b) Effective SO coupling vs the gate potential measured in the experiments (black dots), and obtained in our simulations without strain (dashed red curve) and including strain in the InAs at the interface (solid red curve). We use for both curves the value of P_{fit}. For comparison, we also include the same simulation with strain but using the original parameter P instead (solid blue line). From the conductance measured in experiments, we estimate $\rho_{surf} = 8 \cdot 10^{-2} \left(\frac{e}{nm^3}\right)$, and from the SO coupling we estimate the strain to be $e \simeq -0.1$ at the interface if we use P_{fit} and $e \simeq -0.045$ if we use P. In (c,d) we show the same as in (a,b) but without the InP shell. This last device was already experimentally analyzed in Ref. [208]. In this case we obtain $\rho_{surf} = 4.5 \cdot 10^{-2} \left(\frac{e}{nm^3}\right)$.

is covered by a $6\,nm$–thick Al_2O_3 dielectric (cyan) used to isolate the wire and the all-around gate (gray). We take that the wire is translationally invariant in the z direction as it is few micrometers long in the experiments. We only model the surface charge at the InAs-InP interface ρ_{surf} and we ignore the one at the InP-Al_2O_3 interface as the InP does not contribute to transport since it is basically an insulator here. Notice that one important parameter to describe the heterostructure is the band alignment between the InAs and the InP. From previous experiments, we know that the center of both semiconductor gaps match [205, 206], so one can infer from there the energy difference between the bottoms of both conduction bands. For comparison, we also compute an uncapped device like the one reported in the experiments of Ref. [208]. A sketch of such device is depicted in Fig. 3.8(c). It is the same device but without the InP shell, and the nanowire diameter is smaller, $65\,nm$.

We first compute naively the SO coupling for both devices without including any kind of strain in the system. We use the same methods as for Sec. 3.3.1, in which we solve the SP equations in the TF approximation using the (unstrained) zeroth-order CB Hamiltonian. We show in Fig. 3.8(b,d) the results of our simulations (dashed red curve) together with the experimental measurements (black dots). The agreement between both curves is poor for the core-shell nanowire, while it is good for the uncapped nanowire. Since the InP acts as an insulating barrier here (with height $0.478\,\mathrm{eV}$), we conclude that the strain at the InP-InAs shell must be the sole responsible of the SO coupling increasing.

The same simulations but including the strain are shown in the same figure with a solid red line. We solve the same equations as before but using the strained zeroth-order CB equation of Eq. (3.63). For the deformation-potential parameters a_v and b, we use values that can be found in the literature [158] (see Appendix B.4). Besides, we assume that the main SO coupling contribution is radial with a negligible angular SO coupling contribution. We only include strain in a narrow region close to the core-shell interface, as the strain decays fast towards the core of the wire [203, 205]. As an educated guess, we take this region as a $4\,\mathrm{nm}$-thick layer inside the InAs from the InAs-InP interface. Since the magnitude of the radial strain is uncertain, we use it as a free parameter, looking for a value that fits the experiments best. Notice that there must also be strain inside the InP layer (also at the InAs-InP interface), but we neglect it as the InP acts here as a mere potential barrier. Now the agreement between theory and simulations is excellent in the InAs-InP device of Fig. 3.8(b). From the fitting, we obtain $\varepsilon \sim -0.1$, that it is quite close to the estimation ~ -0.05 given by the lattice-constant mismatch between both materials. Possible deviations between both values could come from strain along the wire's axis not included in our model, the neglect of the inter-subbands coupling (i.e., in the derivation of the CB Hamiltonian for a nanowire we used $l_{\mathrm{SO}} \gtrsim W_{\mathrm{wire}}$, which is not completely satisfied here), or the uncertainly of some parameters (the deformation-potential parameters a_v and b are not completely well characterized yet). But even if it is not completely accurate, our theory nevertheless proves to give an intuitive and simple explanation of the enhancement of the SO coupling in core-shell nanowires. We have performed the same simulations but using the original Kane parameter P, shown with a solid blue line in Fig. 3.8(b). Although in this case the agreement is poorer, we obtain from the fitting a strain of ~ -0.045, even closer to the estimation. We believe that the strain also introduces some corrections to the confinement effects that modifies P to P_{fit}, meaning that the real P_{fit} value in this strained case should be something in between. This is due to be explored in future works.

To complement our study, we show in Fig. 3.9 several profiles resulting from our simulations (with strain and using P_{fit}). In Fig. 3.9(a), we show the electrostatic potential profile $\phi(\vec{r})$ across the cross section of the heterostructure when the wire is ungated (close to pinch-off). We use a green line as a guide for the InAs-InP interface. As it can be appreciated, even if the gate potential is zero, there is a charge accumulation layer that creates a band-bending towards the interface of $250\,\mathrm{mV}$. This value is compatible with previous InAs-InP nanowire experiments. On the other hand, we obtain that the band-bending is small (smaller than $100\,\mathrm{mV}$) for the uncapped device (not shown). This means that either the work function of InP is larger than that of the dielectric Al_2O_3, or the
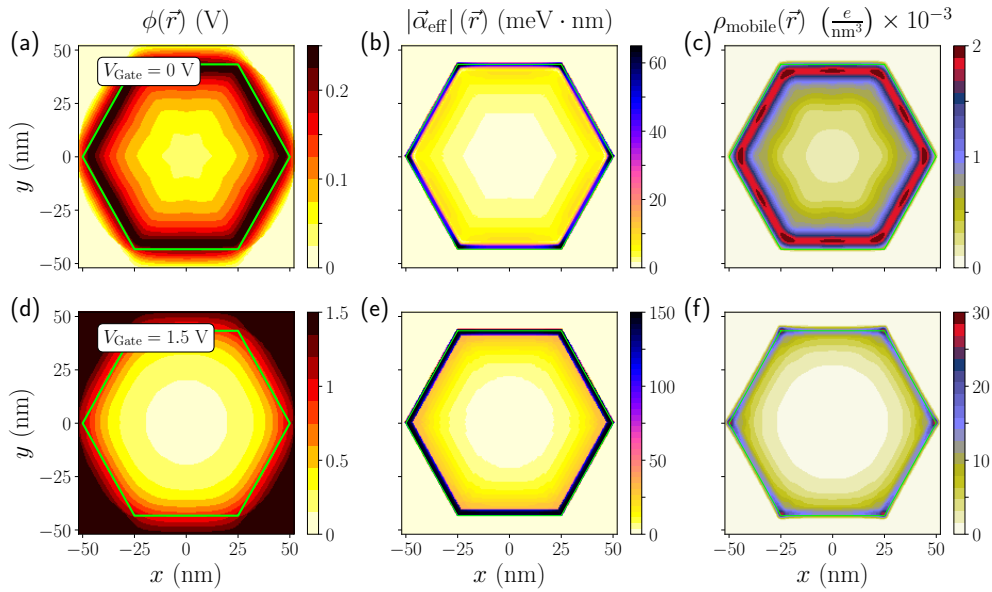
Figure 3.9: (a) Electrostatic potential profile $\phi(\vec{r})$ across the cross section of the InAs-InP core-shell wire at $V_{\text{Gate}} = 0$. (b) Corresponding strained-averaged effective SO coupling profile $\vec{\alpha}_{\text{eff}}^{(\text{EV})}(\vec{r})$ and (c) mobile charge density distribution $\rho_{\text{mobile}}(\vec{r})$. In (d-f) we show the same profiles but for $V_{\text{Gate}} = 1.5$ V. Notice the different scales between both rows.

strain at the interface induces some additional doping. The averaged effective SO coupling profile $\alpha_{\text{eff}}^{(\text{EV})}(\vec{r})$, that is proportional to the gradient of this electrostatic potential, is shown in Fig. 3.9(b). It is mainly radial, as we predicted, and its maximum $(60\,\text{meV}\cdot\text{nm})$ is located at the interface due to the strain there. The mobile charge density of the wire $\rho_{\text{mobile}}(\vec{r})$ depicted in Fig. 3.9(c) exhibits a high localization close to the interface since the band-bottom is bent towards this interface.

If the gate voltage is turned on, the electrostatic potential is increased even more towards the InAs-InP interface [see Fig. 3.9(d)]. This increases the radial asymmetry, leading to a higher SO coupling, see Fig. 3.9(e) [note the change of scale with respect to (b)]. Moreover, the charge density [Fig. 3.9(f)] localizes even closer to the InAs-InP interface, specially at the wire's corners where the SO coupling is maximum. This localization further enhances the effective SO coupling experienced by the electrons inside the wire.

3.5 Conclusions

In this chapter, we have used the multiband k·p effective model to describe the bands of some SMs, and particularly their SO coupling. Since they can be computationally demanding in low-dimensional heterostructures of current interest, in this chapter we have performed a single-band approximation and introduced a heuristic analytical expression that accurately describes the Rashba SO coupling for the CB of III-V SM nanowires. This equation takes into account not only the dependence of α_R with the spatially-dependent electrostatic potential, which accounts for possible

structural inversion asymmetries, but also with the transverse subband energy. It further depends on two SM parameters, the band gap and the split-off gap between valence bands. Additionally, it approximately takes into account the crystal structure of the compound SM, partially lost in the usual the zeroth-order conduction band approximation, through one improved effective parameter that we call P_{fit}. This parameter substitutes the original Kane parameter P in order to account, in a simple and manageable way, for sizable SO coupling contributions originating from transverse subbands in finite-width nanowires.

We find that the magnitude of the SO coupling of nanowires based on zinc-blende InAs is roughly four times stronger than on wurtzite InAs, whereas the SO coupling of InSb nanowires is three times larger than that of InAs ones. We compare the results provided by the effective model with those obtained with other approximations and with exact 8B model calculations. Our improved equation works well regardless of the transverse mode, the particular electrostatic environment surrounding the wire and its chemical composition, considering its specific P_{fit} value given in Table 3.1. It also works well for wire widths ranging form $\sim 50\,$nm to $\sim 200\,$nm, which are the typical experimental values. In particular, for this range, we find that the usual zeroth-order approximation for the SO coupling underestimates its magnitude for zinc-blende nanowires and overestimates it for wurtzite ones, by as much as $\sim 50\%$. As a final proof of the validity of our approach, we simulate the experimental conditions of five magnetoconductance experiments on InAs and InSb nanowires realized in recent years. We find that the Rashba SO coupling of the effective model is in excellent agreement with the experimental data over wide ranges of external gate potentials. We believe that our work may be useful for reducing the computational cost of accurate Rashba SO coupling computations in realistic low-dimensional semiconductors of current interest, where confinement effects turn out to be essential for the correct prediction of α_R. It may also help to understand and design better devices where the Rashba SO coupling is key, e.g., by tuning appropriately the wire's diameter and, in this way, maximizing the SO interaction.

Alongside with this, we have also studied the effect of the strain on the properties of these wires. Its main effect is to renormalize the band gaps of the SM. Therefore, the SO coupling and effective mass of the CB get also renormalized, as the coupling between valence and conduction bands is affected. As a result, the SO coupling is greatly modified by the strain, being enhanced when the strain is compressive towards the nanowire facets. We have compared our theoretical approach with one experiment on InAs-InP core-shell nanowires, finding a good agreement. These heterostructures exhibit a giant SO coupling as a result of the strain at the InAs-InP interface, due to the lattice mismatch between both materials. We believe this strain is also present, with a similar strength, at the interface of InAs-Al hybrid nanowires. This would be beneficial for the formation of topological states as it enhances the topological protection.

SEMICONDUCTOR-SUPERCONDUCTOR NANOWIRES: THE PROXIMITY EFFECT

In this chapter we derive the Hamiltonian that describes, on an equal footing, the SM-SC heterostructure. We show how the conduction band profile inside the SM in a partial-shell nanowire is affected by the inclusion of the SC layer. We unravel the interplay between the gate potential, the wavefunction position and the superconducting proximity effect, in realistic partial-shell devices. In addition to this, we provide and justify a simplified model in which the SC is effectively integrated out and the proximity effect is included directly in the SM nanowire.

The contents of this chapter were pointed out by other authors before, but the simplified model justified at the end is derived and used in our published works in Phys. Rev. B **100**, 045301 (2019) [178]; and Phys. Rev. B **104**, L041404 (2021) [209].

4.1 Full model and InAs-Al heterostructures

Hybrid SM-SC heterostructures offer the possibility to combine the superconducting properties of the SC with the tunable doping and SO coupling of the SM. As we explained in Chapter 1, these ingredients (together with a magnetic field) are necessary to develop a superconducting topological phase, and thus, they are suitable platforms to this end. Here, we primarily focus on the study of partial-shell hybrid nanowires, although our results are general for any other heterostructure with the same choice of materials. Partial-shell nanowires constitute the *standard*, widely studied platform to create MBSs, and thus, the performance of any other platform should be compared to this one. We plot a sketch of this system in Fig. 4.1(a): a SM nanowire (green), usually InAs or InSb, is partially covered with a SC layer (gray) onto two or three facets of the wire. This covering is epitaxial in the experiments, meaning that the SC is assembled with atomic-scale precision. Hence, the lattice mismatch between both materials at the interface is almost zero, at least along the facet direction. This leads to a transparent interface with low disorder that enhances the hybridization between both materials. In order to achieve this epitaxy, the lattice constant of both, the SC and the SM (InAs or InSb in our case), should be similar[1]. This includes several SCs such as Al, Pb, Nb, Ta, V, Sn or NbTiN [52, 81, 210–213]; all of them already achieved experimentally in

---

[1]Apart form the small lattice mismatch, it is foreseeable that the chosen SC also exhibits a large and a hard gap together with a high critical magnetic field. The former increases the robustness of the topological phase, while the later allows for a wider topological phase diagram.
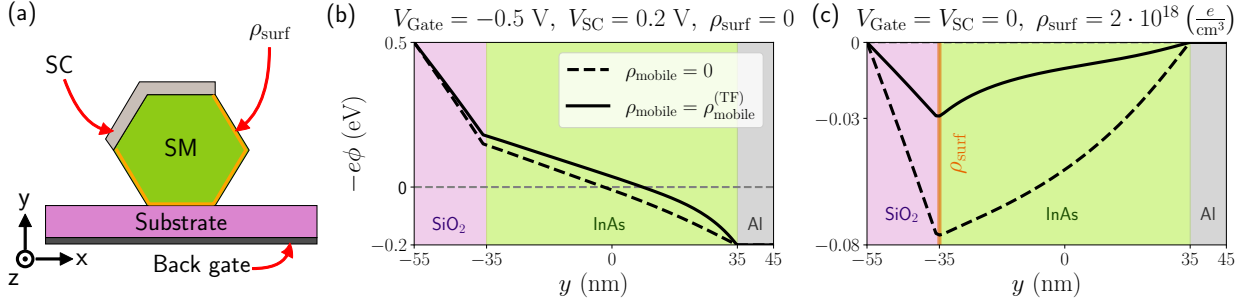
Figure 4.1: (a) Sketch of a hybrid partial-shell SM-SC nanowire: a hexagonal cross-section SM nanowire (green) is partially covered by a SC thin layer (gray), and deposited on top of an insulating substrate (pink), to isolate the wire from the back-gate (black). (b, c) Representative examples of the electrostatic potential profile for the device shown in (a) along the y direction. In (b), for $V_{\text{Gate}} = -0.5$ V, $V_{\text{SC}} = 0.2$ V and $\rho_{\text{surf}} = 0$; and in (c), for $\rho_{\text{acc}} = 2 \cdot 10^{18}$ e/cm^3 and $V_{\text{Gate}} = V_{\text{SC}} = 0$. The screening effect of the mobile charges inside the wire, ρ_{mobile}, is ignored in the dashed line solution, whereas it is taken into account in the solid one in the TF approximation. For these simulations, we choose InAs for the SM, Al for the SC, and SiO$_2$ for the substrate; and the geometric parameters are $W_{\text{Al}} = 10$ nm, $W_{\text{SiO}_2} = 20$ nm, and $W_{\text{wire}} = 80$ nm.

nanostructures.

In this thesis, we use the parameters for Al to describe the SC. It is a well-known material and most of the experimental Majorana nanowires realizations have been performed (so far) using this material as a SC. Our results, nevertheless, are completely independent of the SC material choice as long as (i) the SC has negligible SO coupling, exhibits a hard gap and its band-bottom lies well below the Fermi level, (ii) the interface with the SM is transparent with a Schoktty barrier in the SM due to the work function difference, and (iii) the outer facet of the SC layer is disordered. If these criteria is satisfied for different SCs, then they give rise to the same phenomenology explained here, although the quantitative results may differ.

We model the Al layer as a metal whose CB bottom is well below the Fermi level, -11.8 eV in our simulations, following some estimations [214]. Al has negligible SO coupling, and below the critical temperature, it is a conventional s-wave SC that exhibits a superconducting (parent) gap of $\Delta_0 \sim 0.2$ meV. It can be described through the Hamiltonian

$$H_{\text{SC}} = \left(\frac{\hbar^2 k^2}{2m_e} - E_{\text{F}} \right) \tau_z + \Delta_0 \sigma_y \tau_y. \tag{4.1}$$

Notice that we are treating the superconducting pairing at a mean-field level, ignoring, moreover, its dependence with energy. This is reasonable as long as we aim at the description of subgap states, whose energy $E \to 0$, for which $\Delta(E \to 0) \to \Delta_0$. For simplicity, we also set the phase of the superconducting pairing to zero, and we do not attempt to solve the self-consistent gap equation as it out of the scope of this work.

When the SC is in contact with the SM nanowire, we assume that its properties and parameters remain unaltered inside the the SC layer. And in the same way, we assume that the CB Hamiltonian for a III-V SM nanowire derived in Chapter 3 still applies inside the wire. These assumptions are justified by the fact that the crystal structure of both materials seems to remain unperturbed when the Al covers the wire, so must do their properties. We have nevertheless discussed in Sec. 3.4 that because of the small lattice mismatch in the radial direction, some strain can emerge at the interface in heterostructures that renormalizes the crystal structure. As a result, the strain changes the wire parameters, namely the effective mass or the SO coupling. High-resolution TEM of InAs-Al wires indicates that there is some strain at the interface [80], but a proper characterization is still needed. Therefore, as a first approach to the description of the problem, we neglect this strain.

With the above assumption, the Hamiltonian for the entire heterostructure can be written[2] as a tensor sum of the Hamiltonians of each material

$$H = \left[\vec{k}^T \frac{\hbar^2}{2m^*(\vec{r})} \vec{k} - E_{\rm F}(\vec{r}) + e\phi(\vec{r}) \right] \tau_z + \frac{1}{2} \left[\vec{\alpha}(\vec{r}) \cdot \left(\vec{\sigma} \times \vec{k} \right) + \left(\vec{\sigma} \times \vec{k} \right) \cdot \vec{\alpha}(\vec{r}) \right] \tau_z + \Delta(\vec{r}) \sigma_y \tau_y, \quad (4.2)$$

where $\vec{r}$ applies to both materials (the whole heterostructure); and $m^*(\vec{r})$, $E_{\rm F}(\vec{r})$ and $\Delta(\vec{r})$ are the effective mass, (ungated) band-bottom and superconducting pairing amplitude, respectively, across the heterostructure. All these parameters take a constant value inside each material, but they are different in the SM than in the SC. This is why they are described through spatial varying functions. More explicitly,

$$m^*(\vec{r}) = \begin{cases} m_e & \text{if} \quad \vec{r} \in {\rm SC} \\ m_{\rm SM} & \text{if} \quad \vec{r} \in {\rm SM}, \end{cases} \quad (4.3)$$

$$E_{\rm F}(\vec{r}) = \begin{cases} E_{\rm F,SC} & \text{if} \quad \vec{r} \in {\rm SC} \\ E_{\rm F,SM} & \text{if} \quad \vec{r} \in {\rm SM}, \end{cases} \quad (4.4)$$

$$\Delta(\vec{r}) = \begin{cases} \Delta_0 & \text{if} \quad \vec{r} \in {\rm SC} \\ 0 & \text{if} \quad \vec{r} \in {\rm SM}. \end{cases} \quad (4.5)$$

Apart from that, $\vec{\alpha}$ is a spatial dependent quantity inside the SM, given by Eq. (3.43), and constant (zero) inside the SC; while the electrostatic potential, $\phi(\vec{r})$, is allowed to vary all across the heterostructure. However, in practice, the electrostatic potential inside the SC is constant as the SC behaves as a metal from the electrostatic point of view. Notice that, at the interface, all these parameters change sharply, since the interface is epitaxially growth.

---

[2]This Hamiltonian can be written in this compact form because we are assuming no phase variations of the superconducting pairing phase across the heterostructure. In partial-shell nanowires, this can be done if the magnetic field inside the SC is completely ignored. Otherwise, the phase should change along the SC surface as a result of the supercurrent distribution [115]. However, this assumption does not change the conclusions of our work.

When two different materials are contacted together, the work function difference between both materials can create a bending of the band-bottom towards the interface. Depending on the work function difference, this band-bending could be either positive or negative, leading to an accumulation of holes or electrons at the interface, respectively. In InAs-Al junctions, the band-bending is negative in the InAs towards the Al, so that an electron accumulation layer is formed at this interface. On the other hand, the Al is grounded in most of the experiments to allow some kind of measurements[3], so it does not exhibit a (net) accumulation of charge. We include the InAs band-bending profile in our simulations through a boundary condition $V_{\mathrm{SC}} > 0$ at the SC facets[4]. As we show in the next section, this positive potential attracts the electrons inside the SM wire towards the SC. Consequently, when solving self-consistently the SP equations, this gives rise to an equivalent accumulation of charge and band-bending profile at this interface. Several experiments have accessed to this quantity in InAs-Al heterostructures, providing values ranging from 0.2 to $0.4\,\mathrm{eV}$ [177].

As explained in Chapter 3.2, the wire-vacuum is another interface that leads to a band-bending profile of the wire CB towards the bare facets of the wire. Several experiments [175, 176] have reported the existence of a charge accumulation layers ρ_{acc} at bare InAs nanowire facets, with values of the order of $5 \cdot 10^{18}$ cm^{-3}. We model this band-bending by including a surface layer (one-site-thick in our simulations) of positive charge, ρ_{surf}, at the bare nanowire facets. This is an additional source term to be included in the Poisson equation (2.2)

$$\rho_{\mathrm{T}}(\vec{r}) = \rho_{\mathrm{mobile}}(\vec{r}) + \rho_{\mathrm{surf}}(\vec{r}), \tag{4.6}$$

where $\rho_{\mathrm{mobile}}(\vec{r})$ corresponds to the mobile charges inside the wire (discussed in Chapter 3). Since ρ_{surf} is positive, it attracts the electrons towards this interface, naturally leading to a band-bending and giving rise to the accumulation layer ρ_{acc} at the interface. No free charges inside the SC are considered as it is grounded.

Another ingredient to be included in our simulations is the fact that the outer facet of the Al layer is unavoidably oxidized in experiments. This oxidation layer is usually 1 or 2 nm thick. The effect of the oxidation is to induce disorder on this region. Hence, we model it as an on-site random chemical potential with a Gaussian (quenched) distribution. The strength of the disorder (variance of the distribution) is chosen so that the mean-free path in the SC is of the order of the thickness of the SC (i.e., an electron experiences on average one scattering event when reflected from the vacuum interface), as explained in Ref. [115]. For our simulations, this corresponds roughly to 1 eV. As it

---

[3]In most of the cases, the SC is grounded to perform spectroscopic measurements. This allows to perform transport experiments from one end of the wire to the SC as a function of the bias voltage in the end. With this kind of experiments, one can access to end states as a function of energy, which should provide a (necessary but not sufficient) proof of the existence of MBSs. Moreover, three-terminal measurements, in which the other end is used as well, provide correlations between both ends and information about the charge of subgap quasiparticles.

[4]Nonetheless, we note that the electrostatic potential inside the SC should be zero as it is grounded. We artificially fix it to zero inside the SC once the electrostatic potential is solved. Even though, this has no impact in our simulations since the boundary condition, 0.4 eV, is much smaller than the band-bottom of the SC, 11.7 eV.

has been pointed out in previous works [114, 115, 215], this disorder is beneficial because it breaks the parallel momentum conservation between the SM and the SC, enhancing the hybridization between both.

We note that, when we will look for the bulk properties of the hybrid wire, we will assume that the system is translational invariant along the wire direction (z direction), so does the disorder. This is an artifact as disorder should also vary along this direction. But a 3D simulation would be nevertheless computationally challenging since the huge band-bottom of Al (-11.7 eV) imposes a small FDM's grid spacing (~ 0.1 nm) in order to accommodate the Fermi wavelength inside the Al (~ 0.5 nm) [see Chapter 2 for a deeper discussion]. Even though, we believe our qualitative results are not affected by this artifact.

The last ingredient to take into account in our simulations is the magnetic field $\vec{B}$ used to drive the system to the topological phase in SM-SC heterostructures. We include it in a minimal way in our simulations, since its full description gives rise to a rich phenomenology already explored in other works [123, 124] that do not change the main conclusions of this thesis. In the SC, the magnetic field is basically constant as the thickness of the SC layer in realistic hybrid nanowires is much smaller than the London penetration length. Hence, the magnetic field induces a Zeeman field inside the SC that we nevertheless ignore as it is small for the magnetic field ranges studied in this work. On the other hand, the supercurrent at the SC layer that tries to screen the magnetic field induces a phase winding across the layer and suppresses the superconducting gap. This effect is ignored as it sole effect (although dramatic) is to reduce the topological minigap and phase diagram. We also neglect other possible depairing effects on Δ due to the magnetic field. On the contrary, in the SM, the effect of a magnetic field is to add a Zeeman splitting. One can actually follow the same procedure as explained in Chapter 3 but in the presence of a magnetic field [159], and obtain an additional term

$$V_Z = -\frac{1}{2} g \mu_B \vec{B} \cdot \vec{\sigma} \equiv \vec{h}_Z \cdot \vec{\sigma} \tag{4.7}$$

usually called Zeeman interaction in the literature (and $\vec{h}_Z$ the Zeeman field), where μ_B is the Bohr magneton and

$$g = \frac{m_e}{\hbar^2} \frac{P^2}{3} \left[\frac{1}{\Delta_g} - \frac{1}{\Delta_g + \Delta_{soff}} \right] \tag{4.8}$$

is the effective g-factor for III-V compound SMs. This is found in the simplified approximation [see Sec. 3.1.1], and it provides $g = 14.9$ for InAs and $g = 51$ for InSb, very similar to experimental measurements. This g-factor is also affected by orbital effects, electrostatic potentials and strain; but we neglect this intricate dependence as it is out of the scope of this thesis.

Assuming the magnetic field is oriented parallel to the wire's direction (z direction), we can write the Hamiltonian of the heterostructure including a magnetic field as

$$H = \left[\vec{k}^T \frac{\hbar^2}{2m^*(\vec{r})} \vec{k} - E_F(\vec{r}) + e\phi(\vec{r}) + h_Z(\vec{r})\sigma_z \right] \tau_z$$
$$+ \frac{1}{2} \left[\vec{\alpha}(\vec{r}) \cdot \left(\vec{\sigma} \times \vec{k} \right) + \left(\vec{\sigma} \times \vec{k} \right) \cdot \vec{\alpha}(\vec{r}) \right] \tau_z + \Delta(\vec{r})\sigma_y \tau_y, \tag{4.9}$$

where

$$h_{\rm Z}(\vec{r}) = \begin{cases} 0 & \text{if} \quad \vec{r} \in {\rm SC} \\[2mm] -\frac{1}{2}g\mu_{\rm B}B_z & \text{if} \quad \vec{r} \in {\rm SM}. \end{cases} \tag{4.10}$$

All the parameters used in our simulations in this chapter are summarized in Appendix C.1.

4.2 Electrostatic potential

We start by analyzing the role of the electrostatic potential on hybrid partial-shell SM-SC nanowires. A sketch of this kind of devices is shown in Fig. 4.1(a). It consists on a SM wire (InAs for our parameters choice) that is covered by a SC layer (Al). The wire is usually deposited on an insulating substrate (SiO$_2$), that isolates the wire from the back-gate (black). We fix some potential $V_{\rm Gate}$ to the back-gate to tune the chemical potential inside the wire. Together with this condition, the band-bending $V_{\rm SC}$, the surface charge $\rho_{\rm surf}$, the mobile charges inside the wire $\rho_{\rm mobile}$ and, to a lesser extend, the dielectric constants of the different materials $\epsilon(\vec{r})$, establish the unique solution to the Poisson equation.

To understand the contribution of the different parameters to the electrostatic potential, we show in Fig. 4.1(b,c) different profiles along the y direction for some particular values. We show the results in the presence (absence) of mobile charges inside the wire $\rho_{\rm mobile}$ with a solid (dashed) line. In Fig. 4.1(b), we show the electrostatic energy $-e\phi$ in the absence of $\rho_{\rm surf}$ for some particular values of $V_{\rm Gate}$ and $V_{\rm SC}$. This energy provides the CB bottom in the SM. It is negative close to the Al layer, because of the boundary condition imposed by the InAs-Al work function difference $V_{\rm SC} = 0.2$ V; while it is positive close to the substrate due to the boundary condition imposed by the (tunable) back-gate potential $V_{\rm Gate} = -0.5$ V. Hence, the electrons tend to accumulate close to the InAs-Al interface, where the CB bottom lies below zero. Notice that this happen even if the gate potential is fixed to deplete the wire (i.e., it is negative).

In Fig. 4.1(c), we show the effect of the surface charge layer for zero $V_{\rm Gate}$ and $V_{\rm SC}$. This surface charge also creates a bending of the CB bottom, but towards the facet not covered by the SC. This also creates an electron accumulation layer $\rho_{\rm acc}$, whose electrostatic energy is smaller than the one of the InAs-Al interface [see Fig. 4.1(b)]. This difference in the electrostatic properties of the interfaces has been reported in experiments [177]. In this case, the effect of the non self-consistent solution ($\rho_{\rm mobile} = 0$, dashed line) overestimates the band-bottom displacement with respect to the Fermi level. This happens because the repulsive interaction between electrons in the self-consistent solution (with $\rho_{\rm mobile}$) pushes the band bottom upwards to reduce the wire's average doping. This is, in general terms, the main effect of $\rho_{\rm mobile}$. In Fig. 4.1(b), this effect is small since the effective chemical potential is close to the CB bottom (i.e., $\rho_{\rm mobile} \simeq 0$ because the gate potential is depleting the wire).

Therefore, the effect of the electrostatic potential is two-fold: it sets the doping of the wire by modifying the CB bottom and it changes the charge localization inside the wire, since it is

inhomogeneous. To provide a clear insight into this interplay, we compute the electrostatic and wavefunction profiles as a function of the back-gate voltage for a bulk nanowire in Fig. 4.2. In (a), we show the lowest-energy spectrum as a function of the gate potential at $k_z = 0$. With colors, we show the weight of the wavefunction in the SC layer, where black means that the wavefunction is completely localized in the Al layer and yellow in the InAs wire. At very negative back gate voltages ($V_{\rm bg} \lesssim -1$ V) all the lowest-energy states correspond to states only localized in the Al layer (represented by black color). Moreover, these states barely change with the electrostatic potential. The reason behind is that the Al is grounded and thus the electrostatic potential is screened inside the layer. In Fig. 4.2(b), we show precisely the electrostatic potential profile in this regime, particularly at $V_{\rm Gate} = -2$ V [at the cyan arrow in (a)]. The electrostatic potential is negative all-across the SM nanowire, and it is only positive inside the SC layer, where the band-bending boundary condition fixes it to $\phi = 0.2$ V. The probability density of the lowest-energy state at this gate voltage is shown in Fig. 4.2(f). As expected, the wavefunction is only localized in the SC layer. Hence, for this negative gate voltages, the SM wire is completely empty, in the so-called pinch-off regime.

If the gate voltage is increased towards zero voltage, some mixed states (represented with purple-orange colors) emerge in the lowest-energy spectrum in Fig. 4.2(a) that correspond to different subbands. These states are delocalized in both, the SM wire and the SC layer, and thus, they must acquire the properties of both materials. When the SC is in the non-superconducting state, these states cross the Fermi level (not shown), meaning that they become populated. But in the superconducting state, these states exhibit a superconducting gap as a result of their interaction with the SC. However, their gap is smaller than the parent gap ($\Delta_0 = 0.23$ meV) as they are not completely localized in the SC. In Fig. 4.2(c,d), we show two electrostatic potential profiles when the nanowire starts being populated (close to pinch-off). Now, the electrostatic potential is slightly positive inside the wire, and more particularly, close to the SC layer. The probability density of the lowest-energy states for these gate potentials is shown in Fig. 4.2(g,h). They show that the wavefunction accommodates in this area of positive electrostatic potential.

Increasing even more the electrostatic potential increases the number of states being populated that are more localized in the wire (depicted with a more yellowed color). Moreover, these states exhibit a smaller induced gap as a result of their smaller localization in the SC. The wavefunction profile for positive gate voltages [see Fig. 4.2(e)] actually shows that the potential profile is more positive in the opposite facet of the SM-SC interface. Hence, the wavefunction [see Fig. 4.2(i)] tends to localize there, where its hybridization with the SC is suppressed. Therefore, we conclude that the best gate-voltage regime in order to develop a superconducting topological phase is the one close to pinch-off, as those states are gate-tunable states with a large hybridization with the SC.

4.3   Proximity-induced superconductivity

Figure 4.2(a) seems to indicate that the superconducting pairing correlations diminishes as the gate voltage is increased, since the energy gap (at $k_z = 0$) decreases. As mentioned, this decreasing is in
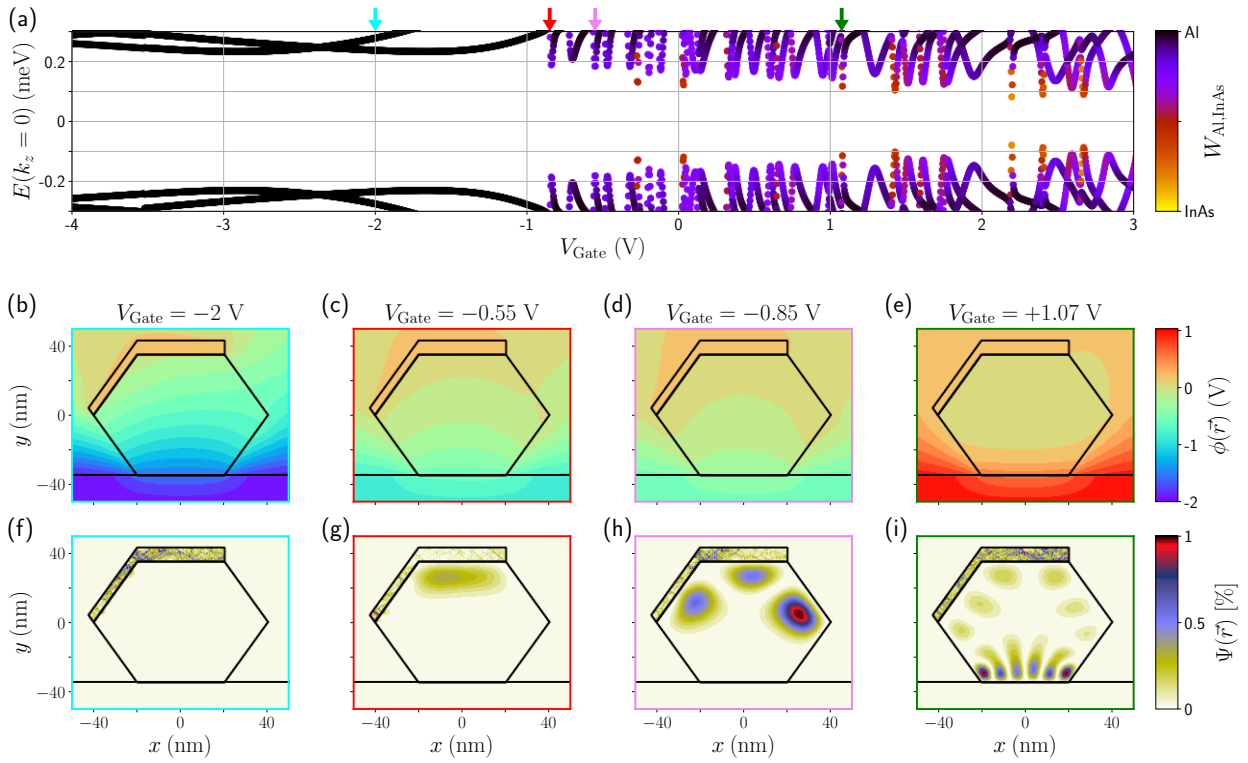
Figure 4.2: (a) Energy spectrum at $k_z = 0$ vs the back-gate potential V_{Gate} for the device shown in Fig. 4.1(a). We show with colors, we show the weight of each state across the heterostructure, from a state completely localized in the Al layer (black) to a state localized only in the wire (yellow). (b-e) Electrostatic potential profiles for the four gate potentials pointed with arrows in (a). With black lines, we show the contours of different interfaces [see sketch of the device in Fig. 4.1(a)]. (f-i) Probability density of the lowest-energy states for the same gate potentials as in (b-e). Same geometrical parameters as in Fig. 4.1. The rest of the parameters can be found in Appendix C.1.

turn a result of the reduction of the SM-SC hybridization. Hence, the superconducting properties induced on the wire are gate-tunable. To better characterize this phenomenon, we show in Fig. 4.3(b) the gap $\Delta_{\mathrm{ind}} = \min\{E(k_z)\}$ of the heterostructure as a function of the gate voltage[5] (with red dots). This quantity is interesting for several reasons. Firstly, it is literally the minimum gap in the spectrum, which can be associated with the induced gap on the hybrid nanowire. Secondly, it is an experimentally accessible parameter, as it can also be obtained from the DOS of the hybrid wire. And thirdly, it is, by definition for this simple theory, the topological minigap of the system when the system is in the non-trivial topological phase[6].

For very negative gate values ($V_{\mathrm{Gate}} \lesssim -1$ V), the gap of the hybrid system is the same than the parent gap, $\Delta_0 = 0.23$ meV. As explained in the previous section, for this gate voltage range the SM wire is in the pinch-off regime, and thus, the gap of the hybrid wire corresponds to the gap of the SC layer. In Fig. 4.3(c), we show the energy bands, $E(k_z)$, for $V_{\mathrm{Gate}} = -1$ V. With colors, we show the weight of each state in the SC (black) or SM (yellow). As expected, all the states are states only localized in the SC layer and they all exhibit the same gap. This is why the DOS in this case [see Fig. 4.3(f)] exhibits a hard gap of $2\Delta_0$.

When the gate is increased to the near pinch-off regime ($V_{\mathrm{Gate}} \sim -1$ V), the superconducting gap slightly decreases, although it is still close to the parent gap. As shown in Fig. 4.2(a), in this gate-voltage regime the SM wire starts being populated with a few electrons whose wavefunctions are strongly hybridized with the SC (as a result of their strong localization close to the SM-SC interface). The energy bands in this case, shown in Fig. 4.3(d) for $V_{\mathrm{Gate}} = -0.25$ V, shows some hybrid states with minima at different momenta. They correspond to different subbands that are already populated, and they exhibit different induced gaps. The induced gap of the hybrid system is just the minimum gap among all of them, and it is the same than the DOS exhibits in Fig. 4.3(g) for the same gate voltage. Notice that the coherence peaks are slightly broadened.

If the gate voltage is increased even more, there is a narrow gate voltage range ($V_{\mathrm{Gate}} = [-0.5, 0.5]$ V) for which the superconducting gap of the hybrid wire decreases close to zero sharply. This transition occurs when the electrostatic potential is (suddenly) more positive at the bottom part of the wire than in the SM-SC interface. This results in a fast transition from a situation where it is more favorable for the electron's wavefunction to localize at the SM-SC interface, to the case where it is more favorable the opposite facet [e.g., compare wavefunction probability density profiles of Fig. 4.2(h) and Fig. 4.2(i)]. As a consequence, the hybridization is quickly suppressed and the hybrid wire losses dramatically its superconducting properties.

In Fig. 4.3(e), we show one example of the energy bands just after this transition (at $V_{\mathrm{Gate}} = 0.5$ V). Now, there are dozens of hybrid states already populated. Some of them exhibit a large localization

---

[5]For each gate voltage, we compute the energy bands (E vs k_z) and we extract the minimum gap from there.

[6]This is only true if the topological minigap is smaller than the induced gap of any other subband. Different subbands could experience different superconducting correlations, and it may happen that subbands already occupied have a smaller superconducting gap than a new one that becomes topologically non-trivial. Hence, the smallest gap would not correspond to the topological minigap in this situation.
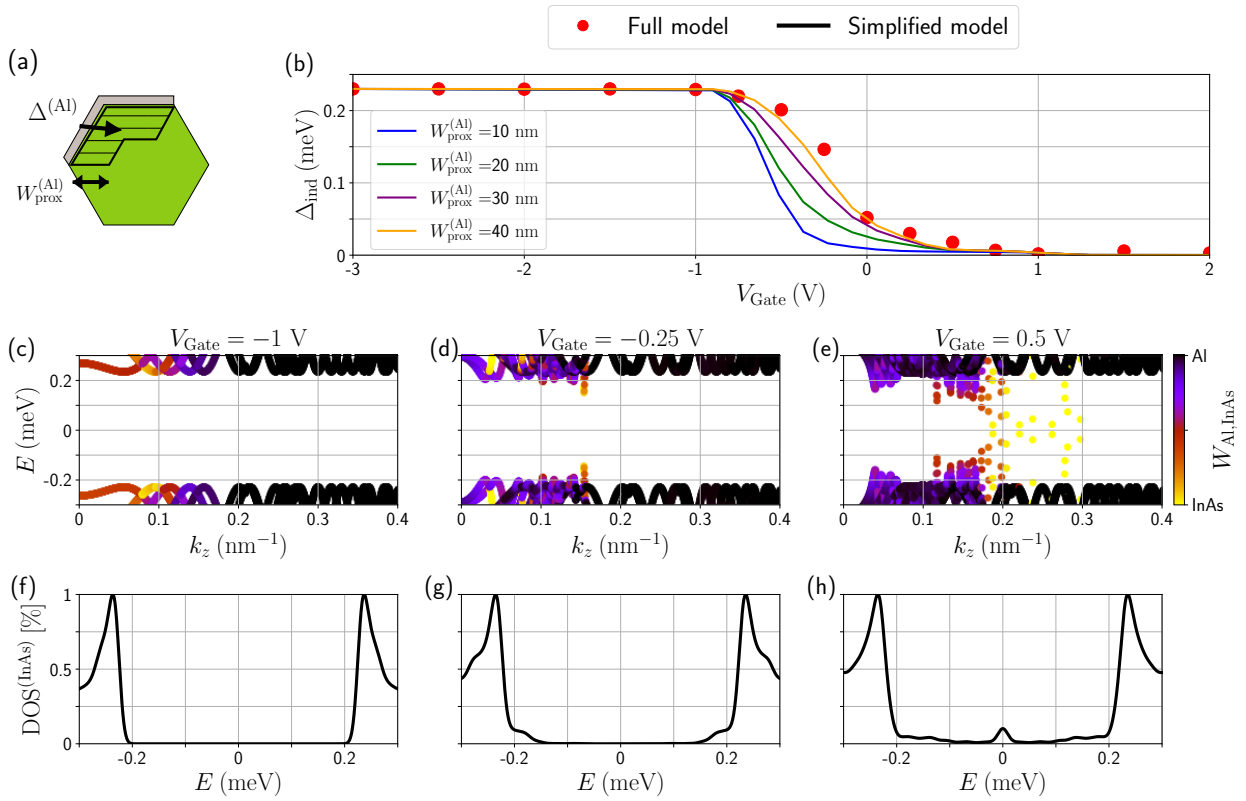
Figure 4.3: Comparison between the full and simplified models. (a) In the full model, we include the SC layer in the Hamiltonian at the same level as the nanowire. In the simplified model, the Al layer is integrated out and the superconducting proximity effect on the wire is included in the Hamiltonian as a proximitized region of width $W_{\text{prox}}^{(\text{Al})}$ with pairing amplitude $\Delta^{(\text{Al})}$ (marked as a streaked region in the schematics). (b) Induced superconducting gap $\Delta_{\text{ind}} = \min\{E(k_z)\}$ vs the back-gate potential V_{Gate} computed with the full model (dots) and the simplified model (lines). For the simplified model, we fix $\Delta^{(\text{Al})} = \Delta_0 = 0.23$ meV, and we consider different proximitized region thicknesses $W_{\text{prox}}^{(\text{Al})}$ (shown with different colors). (c-e) Energy spectrum of the full model for (c) $V_{\text{Gate}} = -1$ V, (d) $V_{\text{Gate}} = -0.25$ V, and (e) $V_{\text{Gate}} = 0.5$ V. (f-h) Corresponding DOS (in the SM wire) for the same energy spectrum. For (f-h), we have fixed $T = 100$ mK.

in the SM wire (shown with yellow color), specially those states with larger momentum. As a result of the smaller hybridization, these states exhibit a smaller superconducting gap. The DOS in this case [see Fig. 4.3(h)] shows no gap since the superconducting pairing correlations are (overall) being suppressed. This illustrates again that the best regime for hosting a topological phase is the near-pinch-off regime, where the induced gap is hard and larger.

It is interesting to note that this sharp transition from a large and hard induced gap to a small and soft gap happens roughly[7] when the gate voltage at the bottom of the wire is similar to the band-bending at the SM-SC. Hence, by characterizing this behavior, one would be able to provide an estimation of the SM-SC band-bending in experiments.

4.4 Simplified model for the superconducting proximity effect

The above simulations are computationally demanding since it is necessary to use a small grid discretization to accommodate the small Fermi wavelength in the SC layer, that is heavily doped. This is inconvenient if one desires to find the spectrum as a function of several parameters. This is the case, for instance, of the topological phase diagram, that requires to compute the eigenspectra vs the gate voltage and magnetic field. One way to surpass this issue is by integrating out the SC and including its effect in the SM through a self-energy. This implies to use the Green's function formalism. But this formalism does not provide the wavefunction profiles of the eigenmodes, or at least not in a direct and low computationally-demanding way. And since we are focusing in this thesis on the interplay between the wavefunction position and the geometry of the heterostructure, then this method is not suitable.

For this reason, we derive a *heuristic* model in which the SC is somehow "integrated out" but without using the Green's function formalism. In this *simplified* model, we only consider the SM wire in the Hamiltonian, and we include directly the superconducting proximity effect by introducing a region close to the SM-SC interface with a finite pairing amplitude $\Delta^{(Al)}$ [see sketch of Fig. 4.3(a)]. The parameter $\Delta^{(Al)}$ and the width of this proximitized region, $W_{prox}^{(Al)}$ are chosen such that this simplified model reproduces (approximately) the same behavior for the induced superconducting gap as the full model. In Fig. 4.3(b), we show with solid lines the induced gap obtained with this simplified model. Different colors correspond to different $W_{prox}^{(Al)}$ with the same $\Delta^{(Al)} = \Delta_0$. We find that $W_{prox}^{(Al)} = 40$ nm (for a 80 nm–thick wire) is a good fit to the full model results.

We note that $\Delta^{(Al)}$ must not be mistaken with a sort of induced superconducting gap in the wire. Strictly speaking, the superconducting pairing amplitude in the wire must be zero[8] as there is no electron-phonon interactions there giving rise to superconducting correlations[9]. Nevertheless,

---

[7]The reason why it is not *exactly* is because the electron-electron interactions contribute to the electrostatic potential as well, shifting this value proportionally to the wire's doping.

[8]It could be non-zero in a very narrow region close to the interface, but negligible in any case.

[9]As we study in Ref. [99], electrostatic electron-electron interactions might also contribute to the pairing amplitude, but we neglect this effect here as it is small.

the SC does induce superconducting pairing correlations in the wire as the wavefunction is spread across the the SC and the SM. And we attempt to reproduce the same correlations in the wire by introducing an (artificial) amplitude $\Delta^{(\text{Al})}$. Notice that, as opposed to a conventional SC self-energy term, $\Delta^{(\text{Al})}$ is fixed to a constant Δ_0 (the parent gap) that does not depend on the energy. However, it has an extension of $W_{\text{prox}}^{(\text{Al})}$ (instead just one site at the interface) that allows to reproduce the full-model results by adjusting it.

# SEMICONDUCTOR-SUPERCONDUCTOR NANOWIRES: SUPERLATTICES

In this chapter we study the spectral properties of superlattice SM-SC nanowires. In these devices, the homogeneous covering (along the wire's length) of SM-SC partial-shell nanowires is substituted by a periodic array of SC fingers. As we illustrate, this superlattice would allow to perform STM measurements or directly use the fingers as local probes. We show how the superlattice affects the induced superconductivity, gating and SO coupling of the hybrid wire; and we provide the optimal geometrical parameters (width and separation of the fingers) that gives the most robust topological phase. Moreover, we perform 3D finite-length simulations of these superlattice devices and we compare them with a homogeneously-coated partial-shell nanowire. We find that, in general, the superlattice is detrimental for the formation of a topological phase as compared to a conventional partial-shell nanowire. For this reason, we propose and study an alternative geometry at the end of the chapter that combines a homogeneous SC coating with a superlattice of normal probes.

The contents of this chapter are published in Phys. Rev. B **100**, 045301 (2019) [178].

5.1 Introduction

Partial-shell nanowires have been investigated in several experiments over the last decade. In most of them, zero bias peaks have been observed at one end of the wire in tunneling conductance measurements, which is a necessary (but not sufficient) condition to claim the existence of MBSs. However, due to the possibility of alternative explanations for the observed zero bias peak, the actual nature of these low-energy states has been brought into question [96, 100, 216–219]. A complementary measurement that could disperse the doubts would be to measure the actual zero mode probability density along the wire, which should show for Majoranas an exponential decay from the edge towards its center with the Majorana localization length [51]. The zero mode probability profile could in principle be accessed with the help of a STM that explores the local density of states at a certain energy along the wire [220]. It is nevertheless difficult to perform STM measurements in conventional partial-shell SM-SC nanowire setups as the top facet of the wire is always covered by the SC and the substrate is a thick insulator.

There are several ways to overcome this issue. One of them is by creating superlattices along the wire, as shown in Fig. 5.1, that would allow to perform STM measurements while tuning the chemical potential with the aid of a potential gate. We consider in this chapter two types of generic
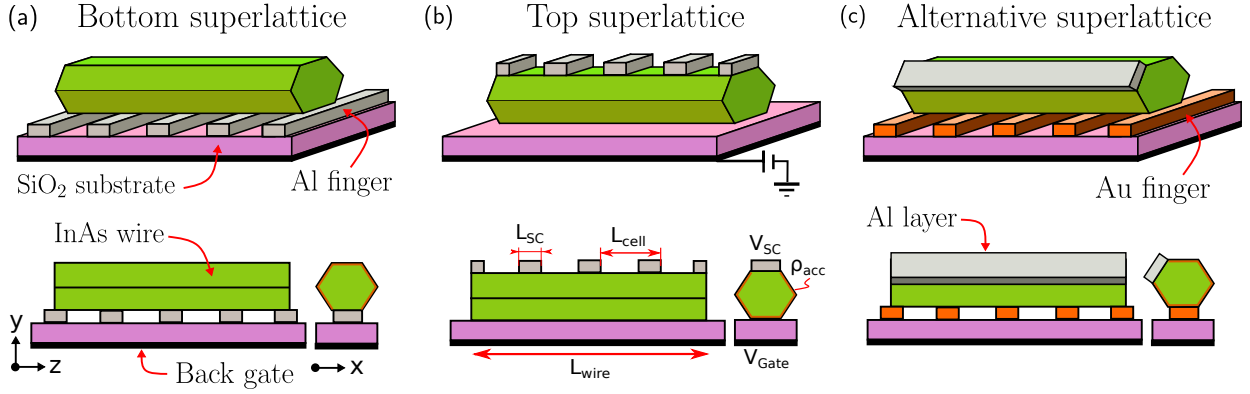
Figure 5.1: Schematic 3D (top) and lateral view (bottom) representations of the three types of superlattice Majorana nanowires analyzed in the text: (a) the bottom-superlattice where the SC fingers are below, (b) the top-superlattice where they are on top of the nanowire, and (c) an alternative proposal where the wire is homogeneously covered by a SC layer but is deposited on top of a superlattice of (non-superconducting) Au fingers. The nanowire is depicted in green, the SC superlattice in gray, the dielectric substrate in pink, the normal fingers in orange and the back gate in black. Different materials have different dielectric constants and dimensions. V_{SC} is the wire's conduction band offset to the metal Fermi level at the interface with the SC fingers, ρ_{surf} is the positive surface charge at the rest of the wire's facets and V_{Gate} is the back gate's voltage. In all our simulations of this chapter, we fix the thickness of the substrate to $d_{SiO_2} = 20$ nm and the SC fingers to $d_{Al} = 10$ nm, and the width of the wire to 80 nm. Rest of parameters can be found in Appendices B.4 and C.1.

superlattice SM-SC nanowires. One with the SC fingers at the bottom, between the nanowire and the back gate, see Fig. 5.1(a), that allows to access the top facet of the wire with a STM tip, and therefore to access the wire's states by driving a current between the tip and each of the SC fingers. Contrary to this device, the other device that we study has the fingers on top, further away from the back gate, see Fig. 5.1(b). In this case, the fingers themselves can play the role of local probes along the wire [86, 221], by driving directly a current between different fingers.

Levine *et al.* [222] considered a minimal 1D model for this nanowire superstructure, in a similar fashion to other previous studies [223–226] with related periodic structures. However, as we show in this thesis, the electrostatic environment and the three-dimensionality of these wires play an important role in all aspects concerning the trivial/topological phases and the appearance of MBSs. Because of the superlattice, the potential is no longer homogeneous along the wire, creating in turn a position-dependent chemical potential that has consequences for the charge density distribution [91, 94, 96, 97, 216, 217] which is not distributed uniformly along the wire. All this gives rise to a rich phenomenology that has consequences for the topological phase diagram and the spectral properties of the wires. Fundamental parameters characterizing this phenomenology are the superlattice cell length L_{cell} and the SC coverage ratio $r_{SC} = L_{SC}/L_{cell}$, where L_{SC} is the size along the wire of the SC fingers. Since the geometry and the resulting 3D electrostatic profile in

each setup are different, we find notable differences between both of them with advantages and disadvantages.

The bottom superlattice setup can be easily accessed from the top, for example with an STM tip as mentioned before, while its charge density is still controllable with the back gate thanks to the metal-free regions between the SC fingers. Nevertheless, the screening effect of the fingers is strong due to their vicinity to the gate, which produces sizable potential oscillations for the electrons inside the wire. This in turn has negative consequences for the stability of the topological phase due to the appearance of localized states on top of the SC fingers that interact with the MBSs when they are present. Furthermore, the SO coupling changes sign along the wire with the periodicity of the superlattice, averaging to a small value. In contrast, in the top-superlattice device the charge density is more easily varied without the need of large back gate potentials and the topological phase is more readily accessible. The potential oscillations are thus softer and the spin-orbit coupling doesn't change sign and averages to a larger value. In turn, there is less nanowire surface exposed to open air and it is in principle more difficult to access.

In both setups the SC does not cover continuously the wire and consequently there is less induced superconductivity than in a uniformly covered one. We find that this leads to a reduced topological protection, manifested in a smaller topological minigap and in a larger overlap between Majoranas at opposite ends of the wire (as measured by the Majorana charge [220]). Interestingly, the Majorana localization length is not only dependent on the SC coherence length, Fermi wavelength and spin-orbit length, as in the uniform hybrid wire, but also on the superlattice length.

To enhance the topological protection, we propose at the end of the chapter (Sec. 5.7) an alternative configuration that combines a conventional hybrid Majorana nanowire (with one of its facets covered uniformly by a thin SC layer) and a superlattice of non-superconducting fingers, as shown in Fig. 5.1(c). This setup benefits from the advantages of the superlattice configuration while displaying a topological minigap and Majorana charge comparable to the uniform wire.

It is important to note that in these systems there are many parameters as well as many length scales playing a role. Hence, we analyze different aspects separately in the following sections (Sec. 5.3 to Sec. 5.5); and we consider all ingredients together and compare the behavior of both setups with realistic nanowire parameters (together with a conventional nanowire) in the last one (Sec. 5.6).

5.2   Methods

Our aim is to study the spectral properties of the superlattice Majorana nanowires of Figs. 5.1(a,b) taking into account their electrostatic environment. To this end, we perform the same SP simulations as before, but now we have to take into account that there is unit cell that is translationally invariant (the one of the superlattice) along the wire's direction (see Ref. [222] for the methods). A fully realistic calculation of the 3D device would require to include the SC superlattice in the Hamiltonian at the same level as the nanowire itself. However, this is an computationally expensive problem that is not affordable with standard numerical resources. For this reason, and due to the complexity

already introduced by the superlattice, we will treat the SC as a rigid boundary in the Hamiltonian and we include the effect of the induced superconductivity using the effective model described in Chapter 4.4: inside the wire, the induced superconductivity is described as a constant pairing amplitude Δ_0, comparable to that of the SC bulk gap, at the sites close to the SC fingers (determined by the superlattice parameters L_{cell} and L_{SC}). Nonetheless, the thickness of the SC fingers and its infinite dielectric constant will be taken into account when solving the electrostatic problem. With this approximation, we are neglecting the fact that the SC metalizes the wire. Since the SC is a (heavily doped) metal, there is a shifting of the SM energy subbands due to the hybridization with the SC. This may be important in superlattices as the chemical potential cannot be shifted homogeneously along the wire. Hence, we will study different dopings of the wire to ascertain the impact of this chemical potential renormalization, which may also be caused by other phenomena, e.g., impurities or strain.

Regarding the boundary conditions used to solve the electrostatic problem, we show in the bottom-right panel of Fig. 5.1(b) a schematic of our simulations. A voltage V_{Gate} is applied to the back gate that is at a distance from the SC fingers/nanowire structure given by the width of the substrate (which we take as SiO$_2$). We use this back gate to tune the average chemical potential inside the wire. Conversely, we assume the SCs are grounded, so we fix the gate potential at the SC boundaries to zero. We note that this SC fingers could be used also for transport measurements, and therefore the gate potential would be the one given by the bias voltage. We also assume that ρ_{surf} covers all the wire's facets except for those in direct contact to the SC fingers because we assume that the SC is grown epitaxially.

5.3 Electrostatic potential profile

First, we want to analyze the shape of the electrostatic potential profile along the 3D wire. This is important as the electrostatic potential sets most of the chemical potential of the wire along with the SO coupling. In this section, we ignore the screening effect of the mobile charges inside the wire, ρ_{mobile}, because we want to isolate the impact of the electrostatic environment on the wire's potential profile. Nevertheless, they are included in the full results of the following sections.

In Fig. 5.2, we plot the potential profile $\phi(\vec{r})$ created by the bottom gate normalized to V_{Gate}, both for the bottom-superlattice device to the left and for the top-superlattice one to the right. In this case we ignore the presence of the SM-SC band offset and the surface charge layer to study the tunable part of the electrostatic potential, so we take $V_{\mathrm{SC}} = 0$ and $\rho_{\mathrm{surf}} = 0$. The potential oscillates along the wire with the periodicity of the superlattice, but the oscillations are very different for each setup, see white dotted guidelines in Figs. 5.2(c,d) that highlight some isopotentials. In the bottom-superlattice device, the potential maximum oscillates between the top and the bottom of the wire depending on whether the wire's section is between or on top of the SC fingers. Conversely, in the top-superlattice setup, the maximum is always at the bottom of the wire, leading to smaller oscillations along the z direction. This can be better appreciated in the bottom panels of Figs. 5.2(c,d), where the potential profile across the wire's section is depicted both for
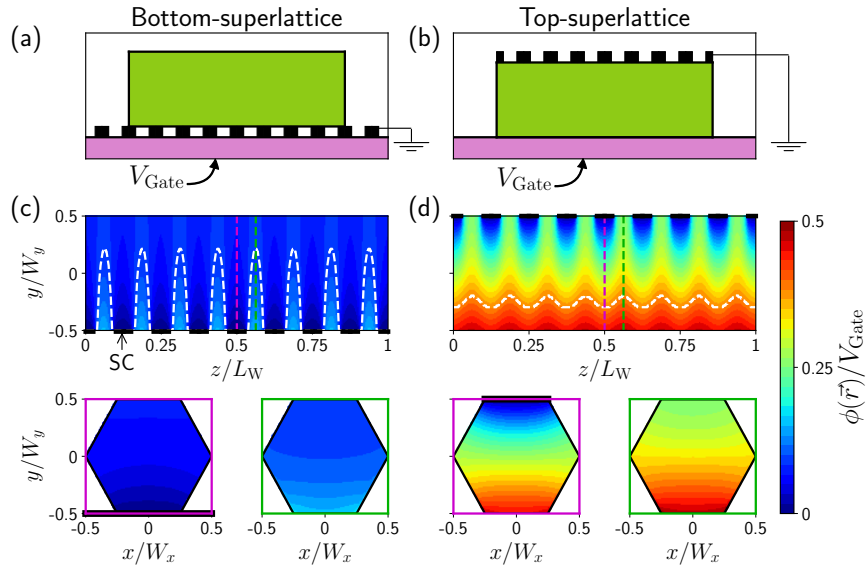
Figure 5.2: Electrostatic potential profile $\phi(\vec{r})$ created inside an InAs wire in contact to Al SC fingers due to the voltage applied to the back gate. Here $V_{SC} = 0$, $\rho_{surf} = 0$ and ρ_{mobile} is neglected. Two setups are considered, bottom-superlattice to the left and top-superlattice to the right, with $L_{cell} = 150$ nm and $r_{SC} = 0.5$. (a,b) Sketches of both systems. (c,d) Electrostatic profile normalized to V_{Gate} along the wire (top), and across the wire's section (bottom), both for sections with SC finger (enclosed by a purple square) and between SC fingers (enclosed by a green square). A white dotted line is used in (c,d) to highlight the shape of the potential oscillations in each setup for one particular isopotential.

sections with a SC finger (purple squared) and between SC fingers (green squared). The oscillations thus produce stronger potential wells in the first setup and subsequent bound states localized over the SCs. When present, these states are detrimental for the stability of the topological phase as we will analyze in Sec. 5.5.

Another difference between the two setups is the ability of the gate to control the potential inside the wire (and, therefore, to produce a certain doping) in the presence of the electrostatic environment. Gating is more difficult in the bottom-superlattice device because the metallic fingers are closer to the gate and thus they screen its potential more strongly. This is why ϕ/V_{Gate} is closer to zero (blue color) in Fig. 5.2(c) whereas in Fig. 5.2(d) the potential better approaches V_{Gate} (red color) at the bottom of the wire, away from the SC fingers.

Now we explore the electrostatic potential profile created by the surface charge density ρ_{surf} and the potential boundary condition at the interface with the SC fingers ($V_{SC} = 0.2$ V), i.e., part of the intrinsic doping of the wire. As illustrated in Fig. 5.3, we perform this study setting the back gate potential to zero. As before, the potential oscillates along the wire with the periodicity of the superlattice and across the wire's section it varies depending on whether that section is on or between the SC fingers. Since the potential profile times the electron charge $-e$ represents the wire's conduction band bottom, the wire's doping is proportional to the electrostatic potential.

The main effect of the wire's band-offset with respect to the Fermi level at the SC interface and the surface charge at the other interfaces is to increase the effective intrinsic wire's doping by a quantity that we call μ_{int}, which is the spatial average of the potential energy profile created by V_{SC} and ρ_{surf}. This is more pronounced for the case with a larger ρ_{surf}. We note that for realistic parameters μ_{int} is always positive. On the other hand, the total doping of the wire μ coming both from the intrinsic charge and the gate voltage can be positive or negative depending on the sign and magnitude of V_{Gate}.

5.4 Inhomogeneous Rashba SO coupling

The inhomogeneous electrostatic potential calculated in the previous section creates an inhomogeneous electric field that, in turn, generates an inhomogeneous Rashba SO coupling across the wire, as shown in Chapter 3. Because of the superlattice, the SO coupling will be also inhomogeneous along the wire, with a periodicity given by the superlattice cell. There are three Rashba couplings, $\alpha_{x,y,z}$, giving rise to six terms in the Hamiltonian of Eq. 1.6. Considering that the magnetic field in our model points in the z direction (the wire's direction), only two of those terms contribute to the opening of a topological minigap. These are proportional to $\alpha_x \sigma_y k_z$ and $\alpha_y \sigma_x k_z$. The effect of the other four Rashba terms is basically to produce hybridization of the transverse subbands and the subsequent even-odd effect for the appearance of Majoranas [227]. It turns out that α_x is negligible in these wire setups (due to the back gate-superlattice parallel disposition). Thus, we focus here on analyzing the spatial behavior of the transverse α_y coupling, shown in Figs. 5.4 and 5.5. Following the rationale of the previous section, in the first figure we explore the Rashba coupling behavior against the back gate potential (normalized to V_{Gate}) setting $V_{\text{SC}} = 0$ and $\rho_{\text{surf}} = 0$; and in the second one we study the intrinsic Rashba SO coupling due to the contribution of the SM-SC band offset and surface charge density (by setting $V_{\text{Gate}} = 0$).

For the top-superlattice setup, we can see in Fig. 5.4(d) that α_y exhibits some oscillations along the wire with the periodicity of the lattice, specially close to the SC fingers, but it is on average large and positive. This is beneficial for the formation of a robust topological minigap. On the contrary, for the bottom-superlattice device α_y oscillates between positive and negative values along the x direction, see Fig. 5.4(d), averaging to a smaller number, which is detrimental for the protection of MBSs.

The Rashba coupling produced by the back gate electric field has to be supplemented with the one created by the SM-SC band offset and surface charge layer, shown in Fig. 5.5. On average this is proportional to the magnitude of ρ_{surf}, see the different color bar ranges in (c,d) and (e,f). For the bottom-superlattice device shown in Figs. 5.5(c,e), α_y oscillates along z as before but with the same sign, giving a finite contribution to the topological gap (specially close to the SC fingers). This is also true for the top-superlattice device in the case of the smaller ρ_{surf}, Fig. 5.5(f), but it changes sign along and across the wire for the larger one, Fig. 5.5(d).

According to these results, the Rashba SO coupling relevant for Majoranas in the bottom-superlattice
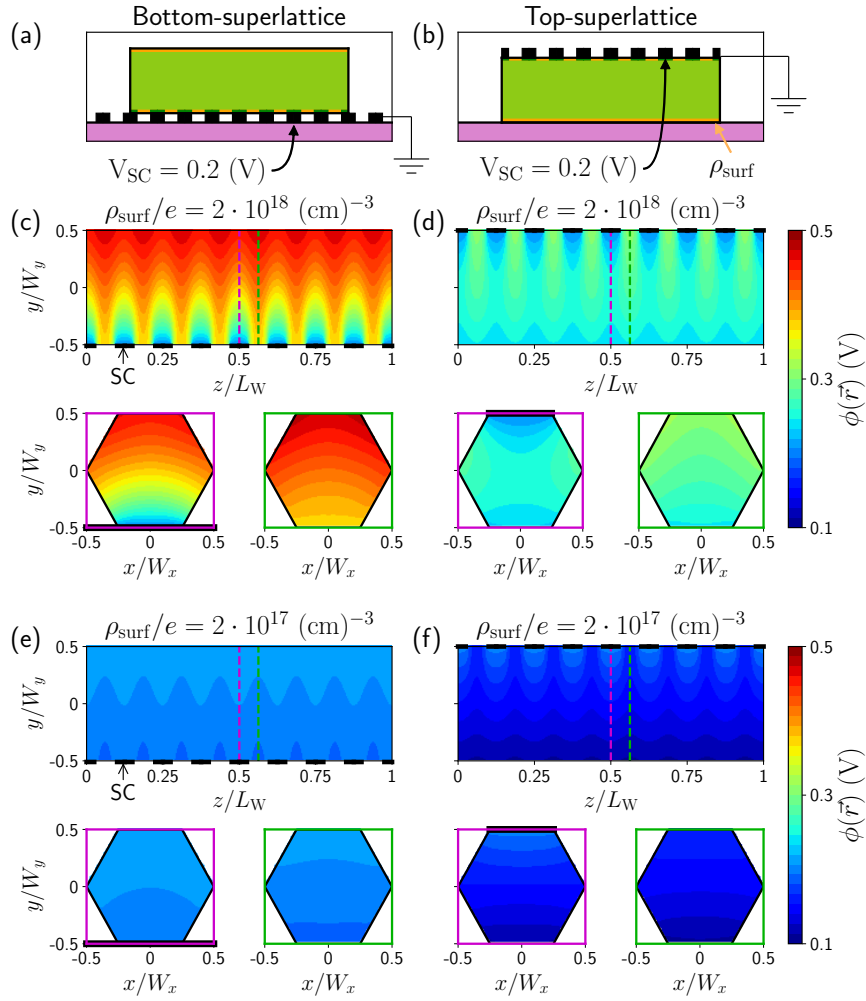
Figure 5.3: Electrostatic potential profile created inside an InAs wire in contact to Al SC fingers due to the wire's band offset with respect to the Fermi level at the interface with the SC ($V_{\mathrm{SC}} = 0.2$ V) and the surface charge layer at the rest of the facets. Here $V_{\mathrm{Gate}} = 0$ and ρ_{mobile} is neglected. Two setups are considered, bottom-superlattice to the left and top-superlattice to the right, with $L_{\mathrm{cell}} = 150$ nm and $r_{\mathrm{SC}} = 0.5$. (a,b) Sketches of both systems. (c,d) Electrostatic profile along the wire (top), and across the wire's section (bottom) for a surface charge density of $\rho_{\mathrm{surf}} = 2 \cdot 10^{18}$ (e/cm^3). (e,f) Same for $\rho_{\mathrm{surf}} = 2 \cdot 10^{17}$ (e/cm^3).
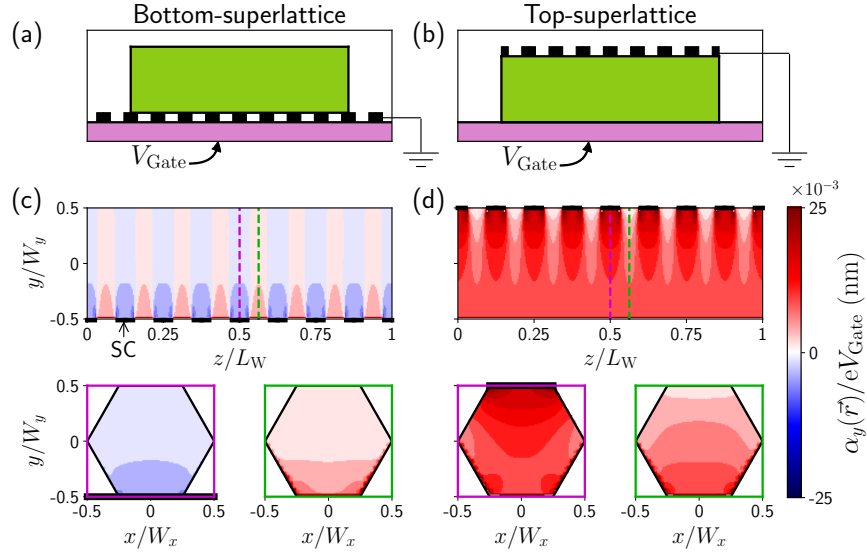
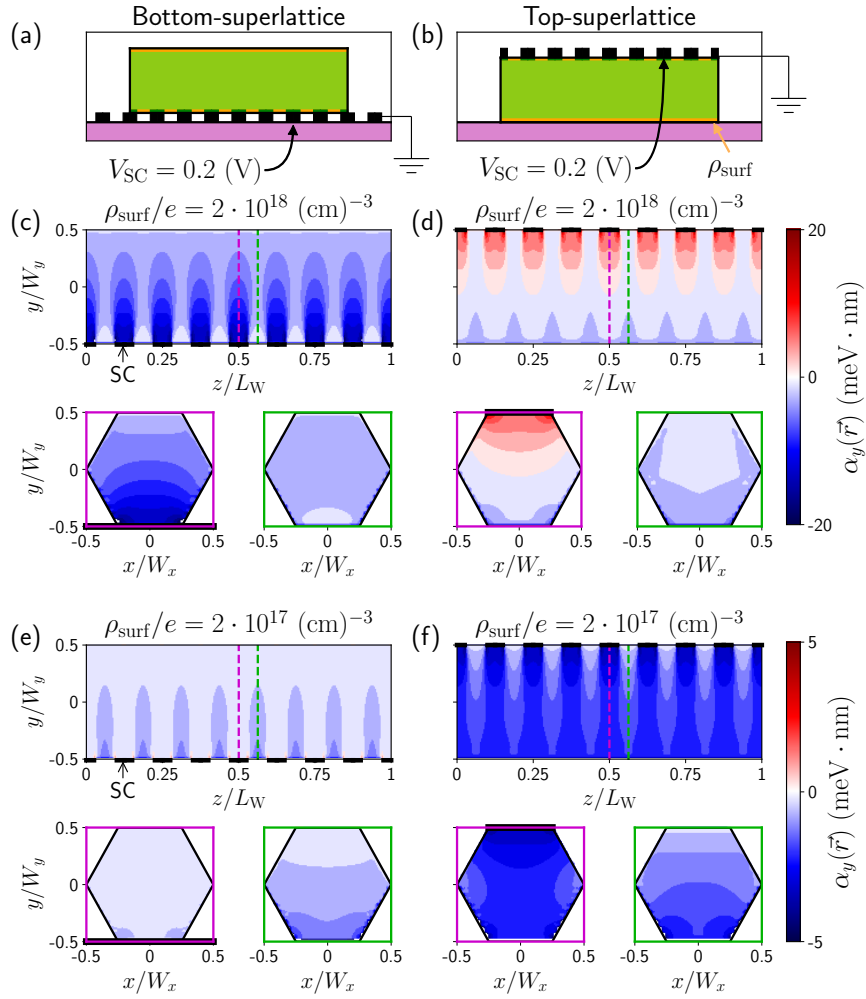**Figure 5.4:** Contribution of the back gate potential to the local longitudinal Rashba coupling inside the wire. V_{SC} and ρ_{surf} are fixed to zero, and ρ_{mobile} is neglected. Two setups are considered, bottom-superlattice to the left and top-superlattice to the right, with $L_{cell} = 150$ nm and $r_{SC} = 0.5$. (a,b) Sketches of the two setups. (c,d) $\alpha_y(\vec{r})$ along the wire (top) and across the wire's section (bottom), both for sections on with SC finger (inside a purple square) and between SC fingers (inside a green square).

setup is going to be dominated by boundary conditions, i.e., the intrinsic Rashba SO coupling, rather than by the voltage applied to the back gate. On the contrary, for the top-superlattice device α_y is going to be dominated by the back gate except for small values of V_{Gate}, in which case its qualitative behavior is strongly dependent on the magnitude of ρ_{surf}. We have nevertheless ignored two other contributions to the SO coupling. One is the metalization induced by the SC, and the other one is the strain's contribution. However, both will have the same effect on both superlattices, being the former detrimental and the later beneficial, possibly canceling out each other.

5.5   Effect of the superlattice on the spectral properties of Majorana nanowires

We focus now on the impact of the superlattice on the spectral properties of a finite-length nanowires. In the calculations of this section we consider that there is only one subband populated, far from the others, and whose charge density is located at the wire's symmetry axis, so that we effectively solve a 1D problem. We do this for two reasons. One is that it is computationally less expensive and still useful to understand the impact of the superlattice on the formation of MBSs. Moreover, it is also a way to isolate the effect of the longitudinal subbands created by the superlattice, which is what we seek here, from the transverse subbands, that introduce further phenomenology [227–229] unrelated to the superlattice. Nonetheless, in the final section, we will solve the complete 3D problem.

Figure 5.5: Contribution of the Al-InAs band offset ($V_{\mathrm{SC}} = 0.2$ V) and surface charge layer to the to the local longitudinal Rashba coupling inside the wire. Here $V_{\mathrm{Gate}} = 0$ V and ρ_{mobile} is neglected. Two setups are considered, bottom-superlattice to the left and top-superlattice to the right, with $L_{\mathrm{cell}} = 150$ nm and $r_{\mathrm{SC}} = 0.5$. (a,b) Sketches of the two setups. (c,d) $\alpha_y(\vec{r})$ along the wire (top), and across the wire's section (bottom) for a surface charge density of $\rho_{\mathrm{surf}} = 2 \cdot 10^{18}$ (e/cm^3). (e,f) Same for $\rho_{\mathrm{surf}} = 2 \cdot 10^{17}$ (e/cm^3).

5.5.1 Impact of the inhomogeneous electrochemical potential

We start by analyzing the effect on the wire's spectrum of the superlattice chemical potential. To understand the sole impact of the inhomogeneous chemical potential, we take constant values for the induced pairing and Rashba coupling ($\Delta_0 = 0.2$ meV and $\alpha_z = 40$ meV·nm), while taking a similar potential profile as the ones of Figs. 5.2(c,d). For the moment, we ignore the inhomogeneous intrinsic doping of the wire (i.e., we set $V_{SC} = 0$ and $\rho_{mobile} = 0$).

Due to the superlattice structure, the real space unit cell is larger than for a homogeneous potential wire, leading to the formation of longitudinal subbands in the dispersion relation, see Figs. 5.6(a,d) for two values of L_{cell}. The number of these longitudinal subbands per unit energy increases with L_{cell}. As stated in Ref. [222], only when the Fermi energy crosses an odd number of Fermi pair points, the system is topologically non-trivial (light blue regions). Otherwise it is trivial (light pink regions). The electrostatic potential can open a gap between longitudinal subbands, whose size depends on the strength of the potential oscillations, leading to energy ranges where the Fermi energy crosses no band [224] [see Fig. 5.6(d)]. This causes the wire to exit the topological phase.

In Figs. 5.6(b,e), we plot the wire's phase diagram versus Zeeman field V_Z and chemical potential, given by the space average of the electrostatic potential times the electric charge $e\langle\phi(z)\rangle$. The green dots mark the values of these parameters for which the dispersion relations in (a,d) are plotted. This phase diagram is certainly more complex than the one of an homogeneous 1D Majorana nanowire, characterized by a single solid hyperbolic topological zone corresponding to one topological band (whose boundary is given by the condition $\mu = \pm\sqrt{V_Z^2 - \Delta^2}$). Here, since there are several longitudinal subbands, there are several more or less contiguous topological zones (with shapes that only slightly resemble the single-band hyperbolic one) separated by trivial regions whenever the Fermi energy crosses an even number of Fermi pair points, see Fig. 5.6(b). Moreover, whenever the Fermi energy lies at the gaps between longitudinal subbands, the phase diagram develops trivial *holes* within the topological phase, see for instance the light pink region at the bottom-right corner in Fig. 5.6(e). At the boundaries of this trivial holes we have the condition $\lambda_F = L_{cell}$, as pointed out in Refs. [224, 226]. Additionally, we note that a change in the back gate potential will not only move the subbands upwards or downwards in a rigid way, but it will also change the hybridization between the longitudinal subbands, leading to a change in the trivial hole sizes.

It is known that, for a finite-length nanowire, Majorana zero modes appear in the wire's spectrum in the topological phase. These states are localized at the edges of the wire and decay exponentially towards its center with the so called Majorana localization length, that is proportional to the SC coherence length [51]. When the wire's length is not much greater than the Majorana localization length, left and right MBSs overlap and their energy lifts from zero producing characteristic Majorana oscillations as a function of V_Z and μ. The lowest level energy of a finite-length nanowire ($L_{wire} = 1.2\,\mu m$) is shown in Figs. 5.6(c,f), where we see the impact of the electrostatic potential superlattice on the Majorana oscillations. As it can be observed, the regions where the lowest-energy modes approach zero energy in Figs. 5.6(c,f), coincide (roughly) with the non-trivial regions in the
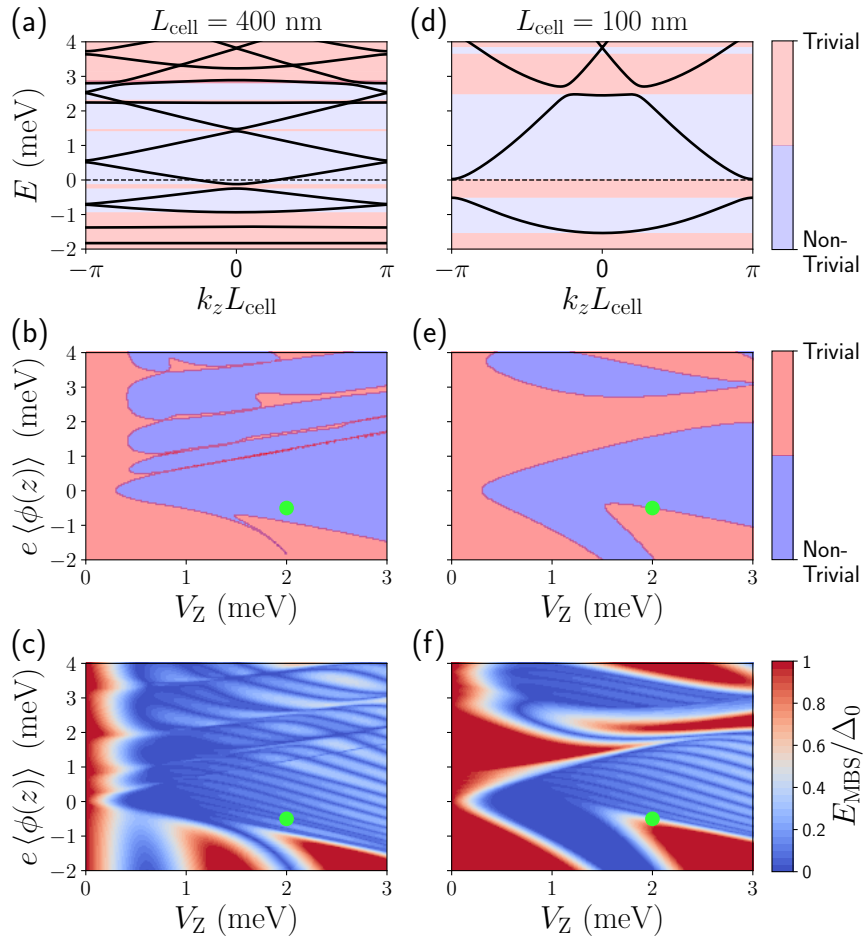
Figure 5.6: (a) Dispersion relation for a 1D superlattice nanowire with superlattice parameters $L_{cell} = 400$ nm and $r_{SC} = 0.5$. The electrostatic potential profile oscillates along the wire's axis following a similar profile as the one shown in Fig. 5.2 but evaluated at $(x, y) = (0, 0)$. Here we take homogeneous in z values for the induced SC pairing, Rashba coupling and intrinsic doping: $\Delta_0 = 0.2$ meV, $\alpha_y = 40$ meV·nm, and $\mu_{int} = 5$ meV. (b) Corresponding topological phase diagram for the bulk system. (c) Lowest level energy for a finite-length nanowire of $L_W = 1.2\,\mu$m. (d-f) The same but for $L_{cell} = 100$ nm. The green dots mark the values of V_Z and $\mu = e\langle\phi(z)\rangle$ for which the top figures are plotted.
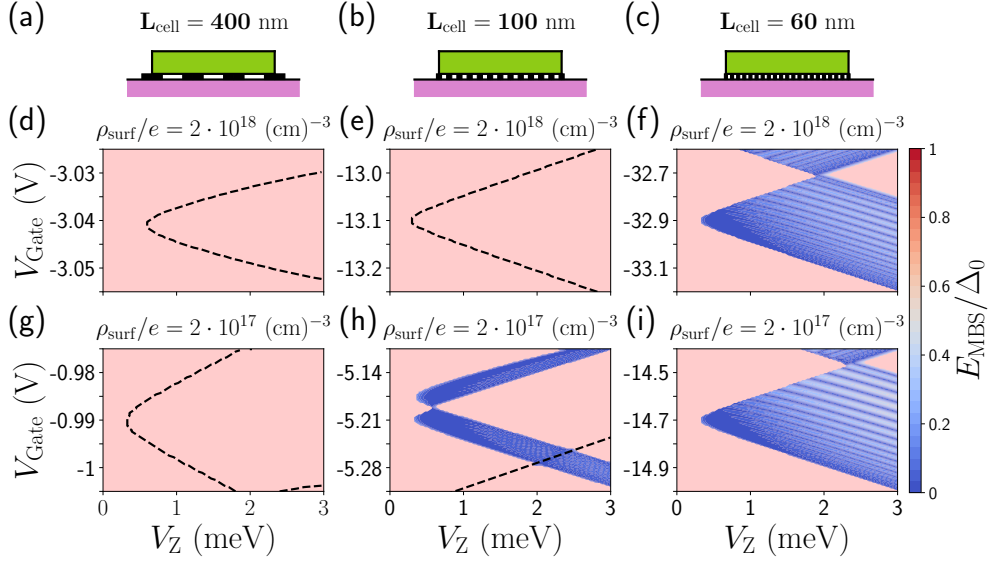
Figure 5.7: Lowest level energy as a function of applied gate voltage and Zeeman field for a finite-length 1D bottom-superlattice nanowire in the presence of an inhomogeneous potential profile. This potential is taken from a 3D calculation with Al-InAs band offset $V_{SC} = 0.2$ V and different surface charge density values, evaluated at $(x, y) = (0, 0)$. Different superlattice cell sizes (with $r_{SC} = 0.5$) are considered. Topologically trivial regions are colored in light pink, non-trivial regions are plotted in blue-red scale given by the colorbar (where the MBS energy is normalized to Δ_0), and the black dashed lines mark localized trivial zero energy modes. The Rashba coupling and induced pairing in the Hamiltonian are fixed to the homogeneous quantities $\alpha_R = 30$ meV·nm and $\Delta_0 = 0.2$ meV. The length of the wire is $L_{wire} = 1.2\,\mu$m.

phase diagrams of Figs. 5.6(b,e).

5.5.2 Role of the intrinsic doping

We now proceed to include in the simulations the effect of the inhomogeneous doping created by the SC-SM band-offset and the surface charge density. Fig. 5.7 and Fig. 5.8 show, for the bottom- and top-superlattice devices, the lowest level energy as a function of the Zeeman field and the back gate voltage for different superlattice cell sizes (with $r_{SC} = 0.5$) and for different surface charge densities. Note that trivial regions are colored in light pink, as in the phase diagrams of Fig. 5.6.

The different columns in Fig. 5.7 and Fig. 5.8 correspond to different sizes of L_{cell}. Notice that the size of the topological regions increases as the superlattice cell decreases. Actually, for a large enough L_{cell} the topological phase is nonexistent, see Figs. 5.7(d,g) and 5.8(d,g). For large superlattice cell sizes, topologically trivial localized states are present (black dashed lines), which may interfere with the MBSs. This effect is more pronounced in the bottom-superlattice setup because the back gate voltages needed to enter the topological phase are larger due to the screening of the SC fingers. This in turn produces stronger potential oscillations and subsequent localized states, as explained in Sec. 5.3. At smaller L_{cell} sizes, the localized states disappear.
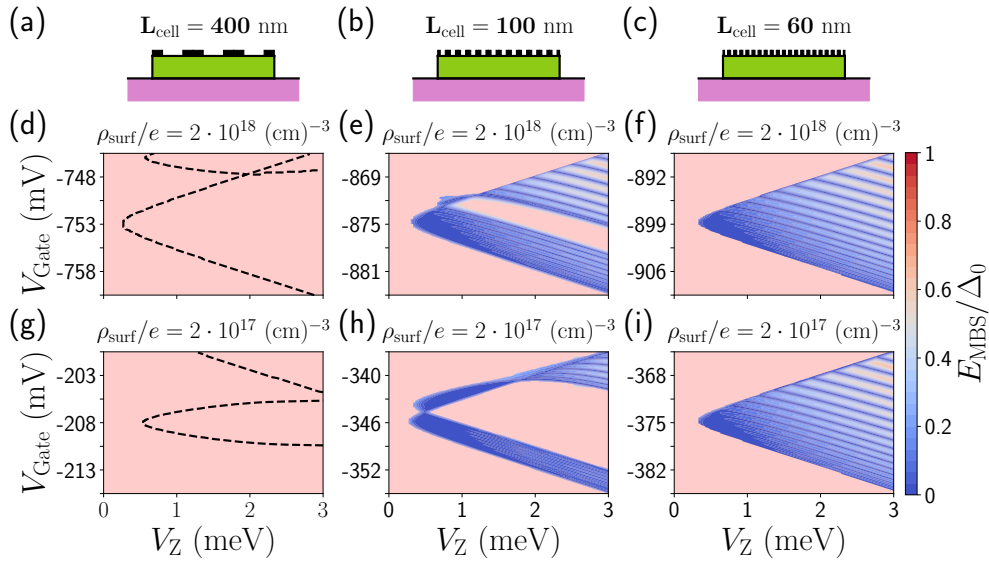
**Figure 5.8:** Same as Fig. 5.7 but for a top-superlattice setup.

For medium cell sizes L_{cell}, which are probably more appropriate for experimental realization, we typically encounter the condition $\lambda_F = L_{\text{cell}}$ explained in the previous subsection and trivial holes appear in the topological phase, both in the bottom and top-superlattice setups. However, the top-superlattice setup develops larger topological regions and they are present for the two values of ρ_{surf} considered, see Figs. 5.8(e,h). In the bottom-superlattice case, no topological region is found for the larger ρ_{surf}, see Fig. 5.7(e).

For small L_{cell} sizes the topological phase is more stable, meaning that there are no trivial holes. This is so because for small and short potential oscillations the electrons in the wire experience an effective homogeneous potential [222]. Moreover, the performance of both setups (top and bottom) is comparable, although the back gate voltages needed for the bottom one are much larger.

5.5.3 Impact of inhomogeneous induced pairing

We lastly consider the impact of the inhomogeneous superconductivity. For this purpose, we solve a 1D wire where we fix the chemical potential and Rashba coupling to constant values. The superconducting pairing amplitude is taken as a telegraph function that oscillates between $\Delta_0 = 0.2$ meV and zero with a period given by L_{cell} and r_{SC}. As done in the previous sections, this is a simplified model to understand qualitatively the effect of inhomogeneous superconductivity. When we consider the realistic 3D model later on, the induced pairing will be only present at the surface of the wire in the regions where it is close to the SC fingers.

Fig. 5.9 shows the energy gap (energy of the lowest-energy state at $k_z = 0$) normalized to Δ_0 for an infinite 1D wire against the superlattice parameters L_{cell} and $r_{\text{SC}} = L_{\text{SC}}/L_{\text{cell}}$. For small coverage, $r_{\text{SC}} < 0.5$, the induced superconductivity is poor and it improves as r_{SC} increases. For
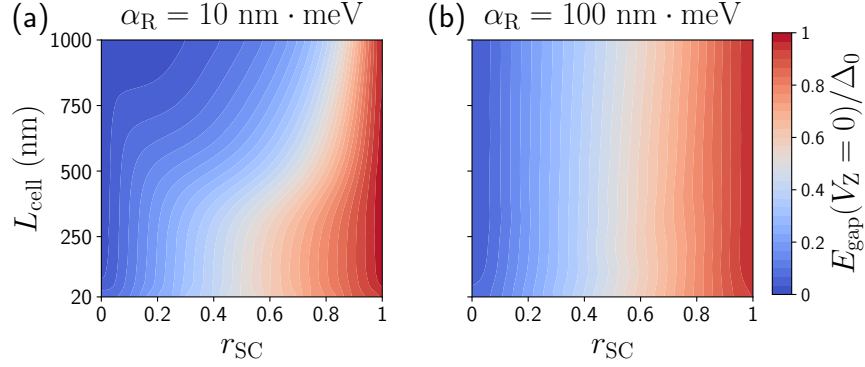
Figure 5.9: Energy gap (at $V_Z = 0$ and $k_z = 0$) versus L_{cell} and $r_{SC} = L_{SC}/L_{cell}$ for a 1D nanowire with a telegraph superconducting pairing that oscillates between $\Delta_0 = 0.2$ meV and zero along z. The chemical potential and Rashba coupling are fixed to homogeneous values $\mu = 0$ and (a) $\alpha_R = 10$ meV·nm, and (b) $\alpha_R = 100$ meV·nm.

$r_{SC} \to 1$, we recover a perfect induced gap Δ_0 corresponding to a wire covered by an uniform SC at $V_Z = 0$. Interestingly, for strong SO coupling the gap energy basically does not depend on L_{cell}, see Fig. 5.9(b). However, for small α_R the induced gap worsens considerably with L_{cell}, as shown in Fig. 5.9(a).

5.5.4   Superlattice features in parameter space

We can summarize our previous findings by plotting a diagram in parameter space that illustrates the different features caused by the superlattice and that interfere with the topological phase. This is done in Fig. 5.10 versus L_{cell} and r_{SC} for $V_Z = 0.6$ meV and $\Delta_0 = 0.2$ meV, and taking the following (realistic) spatial average values for other parameters: $\langle \mu_{int} \rangle = 200$ meV, $\langle \mu_{V_{Gate}} \rangle \in [0, 3]$ meV and $\langle \alpha_z \rangle \in [5, 50]$ meV·nm.

In the brown area, we have values of L_{cell} and r_{SC} for which the Fermi energy crosses an even number of Fermi pair points in the nanowire dispersion relation. This happens when the level spacing between longitudinal subbands is smaller than the (energy) size of the topological phase $(\frac{\pi^2 \hbar^2}{2m L_{cell}^2} \leq \sqrt{V_Z^2 - \Delta^2})$. In this case the topological regions of contiguous longitudinal subbands interfere and the system exits the topological phase (there is an annihilation of an even number of Majoranas at each wire's edge). See, for instance, the upper subbands plotted in Figs. 5.6(a,b).

In the red area, we have values of L_{cell} and r_{SC} for which there appear gaps between (the lowest) longitudinal subbands in the nanowire's dispersion relation. As we explained in Sec. 5.5.2, when the Fermi energy is within these gaps, trivial holes emerge in the topological regions of the phase diagram. See for example the bottom-right corner of Fig. 5.6(e). This happens when there is a resonance between the Fermi wavelength λ_F and the superlattice length L_{cell}. The red area is somewhat larger for the bottom-superlattice than for the top one. This is because the appearance and size of the longitudinal subbands gaps depends on the strength of the potential oscillations,
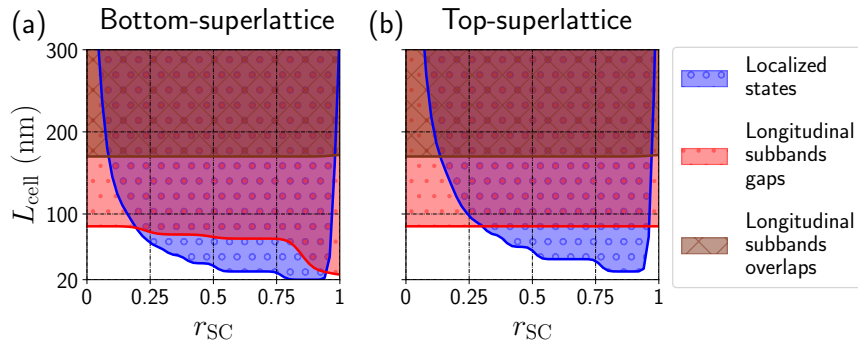
Figure 5.10: Approximate regions in superlattice parameter space L_{cell} and r_{SC} where different mechanisms that spoil the topological phase appear, such as the formation of longitudinal subband overlaps, longitudinal subband gaps and localized states; marked in brown, red and blue, respectively. We have taken $V_Z = 0.6$ meV, $\langle \mu_{int} \rangle = 200$ meV, $\langle \mu_{V_{Gate}} \rangle \in [0, 3]$ meV, and $\langle \alpha_y \rangle \in [5, 50]$ meV·nm. Panel (a) is for the bottom-superlattice device, and (b) for the top one.

which is larger for the bottom-superlattice due to the back gate's screening by the metallic fingers.

Finally, in the blue area localized states are formed. As we saw in Sec. 5.5.2, the superlattice of fingers creates potential oscillations along the wire. When the height of these oscillations is large enough ($\frac{\pi^2 \hbar^2}{2m L_{SC}^2} \leq \frac{\sigma_\phi}{\langle \phi \rangle} \langle \mu_{int} \rangle$), there appear potential wells for the electrons that create localized states. These states interfere with the MBSs detaching them from zero energy. Moreover, when the potential oscillations are very strong, they divide effectively the nanowire into regions of smaller length, destroying the Majoranas. Again, the blue area is slightly larger for the bottom-superlattice than for the top-one.

This diagram gives us an idea of different detrimental mechanisms for a robust topological phase that may appear as a function of superlattice parameters. This does not mean that we cannot find topological regions for those L_{cell} and r_{SC} values, but that those regions will be interrupted at some points instead of extending more widely as a function of nanowire parameters. To complete this study we should also consider the size of the topological minigap. As we saw in Sec. 5.5.3 (see Fig. 5.9), it decreases when the SC partial coverage r_{SC} does, which is additionally Rashba coupling dependent. Moreover, we have to bear in mind that the qualitative analysis of Fig. 5.10 is performed for a 1D model of the nanowire. When a 3D wire is considered, several transverse modes can be occupied. In this case there will be an interplay between longitudinal and transverse subbands that will introduce further complexity to the determination of the optimal superlattice parameters.

5.6 3D results

In this section we consider together all the different ingredients that have been analyzed separately in the previous sections and for a realistic 3D nanowire. In particular, we take representative
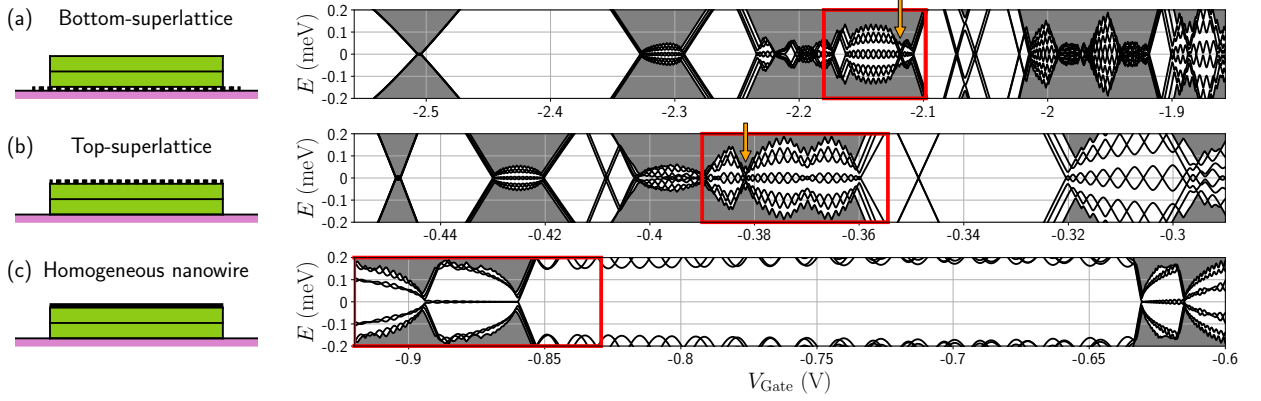
Figure 5.11: Low energy spectrum versus back gate voltage for a $2\,\mu$m long 3D (a) top-superlattice nanowire, (b) bottom-superlattice nanowire, and (c) homogeneous nanowire. Superlattice parameters are $L_{\mathrm{cell}} = 100$ nm and $r_{\mathrm{SC}} = 0.5$. Wire parameters are $V_Z = 0.6$ meV, $\Delta_0 = 0.2$ meV, $V_{\mathrm{SC}} = 0.2$ V and $\rho_{\mathrm{surf}}/e = 2 \cdot 10^{17}$ (cm)$^{-3}$. The red rectangles represent the V_{Gate} values for which Fig. 5.12 is plotted.

superlattice parameters $L_{\mathrm{cell}} = 100$ nm and $r_{\mathrm{SC}} = 0.5$. We find the wire states for a $2\,\mu$m long wire. We model the induced pairing as a telegraph function with $\Delta_0 = 0.2$ meV in the regions of the wire close to the SC fingers and zero otherwise. In particular, for these 3D calculations we consider $\Delta_0 \neq 0$ for a certain depth ($\sim 25\%$ of the wire's width) close to the SC fingers in the transverse direction, as justified in Sec. 4.4.

In Fig. 5.11, we show the low-energy spectrum as a function of back gate voltage for a particular value of Zeeman splitting, $V_Z = 0.6$ meV, both for the bottom-superlattice in (a) and the top-superlattice setup in (b). We explore a wide range of V_{Gate} values that corresponds to the first transverse occupied subband that develops topological states (seen as quasi-zero energy states whose energies split from zero in an oscillating manner). As explained in Sec. 5.5, this subband appears for larger negative values of V_{Gate} in the bottom-superlattice case due to the screening effects of the SC fingers. We note that, strictly speaking, in these systems one cannot really label subbands as purely transverse or longitudinal because the spin-orbit term in the Hamiltonian mixes the two momenta. However, and due to the small cross section of the wires, groups of subbands have still a dominant weight on a particular quasi-transverse subband.

In these spectra, we can observe all the phenomenology that we have been discussing in previous sections. For the most negative values of V_{Gate}, left part of Figs. 5.11(a,b), the wire is almost empty except for very flat bands that appear at the quantum wells of the electrostatic potential oscillations. As a function of V_{Gate}, these create quick gap closings and reopenings and the topological phase cannot be developed. As V_{Gate} is increased, middle part of Figs. 5.11(a,b), different dispersing longitudinal subbands become populated. When the topological conditions are satisfied, we find extended V_{Gate} regions with oscillating low energy modes separated by a minigap from the quasicontinuum of states (dark gray). These are the regions of interest because

those oscillating states correspond to (more or less overlapping) MBSs localized at the left and right edges of the finite-length wire. The size of the oscillations and the minigap depends on the longitudinal subband. Sometimes, these topological regions are crossed by a localized state that closes the minigap at a certain V_{Gate} point [see arrows in Figs. 5.11(a,b)]. The localized states disperse linearly with V_{Gate} and cross zero energy displaying an x shape. Other times we find trivial regions (without Majorana oscillations) between two topological ones due to topological subbands gaps or to topological subbands overlaps, as explained in Sec. 5.5.2. Finally, at the right-most values of V_{Gate} an additional transverse subband crosses below the Fermi level and the spectrum becomes more intricate, with the even-odd effect playing a role (not shown).

For comparison, we also show in Fig. 5.11(c) the case of a nanowire homogeneously covered by a SC at the top of the wire. The range of V_{Gate} values displayed in this case is chosen so that no hole states appear in the system. For more negative voltages the lower part of the nanowire becomes populated by hole quasiparticles from the valence band and a proper description of the system would require to consider an extended version of the model Hamiltonian of Eq. (1.6) where electrons and holes coexist. To avoid this complication, we analyze higher voltages for which several transverse subbands are already populated. Note that here there are no longitudinal subbands. At the left and right parts of panel (c), we observe the well known even-odd effect between overlapping topological regions of different subbands. In the middle part, however, and for a pretty wide range of gate voltages, we have a region with no subgap states that corresponds to the trivial phase developed between two well separated transverse subbands.

Now we focus more specifically on one of the topological regions and analyze the location and shape of its MBSs. In Fig. 5.12 we show with more detail the low-energy spectrum as a function of back gate voltage for the regions marked by a red rectangle in Fig. 5.11. The topological minigap is somewhat larger for the top-superlattice setup than for the bottom one. In the top-superlattice device it reaches approximately $\Delta_0/2$, which corresponds to the maximum possible induced gap for a superlattice with $r_{\text{SC}} = 0.5$, see analysis of Fig. 5.9. This is because α_z has a pretty homogeneous finite value all over the wire and it gets specially sizable (~ -30 meV·nm, not shown) below the SC fingers, precisely where most of the charge density is located. However, the minigap in the bottom-superlattice is smaller than in the top's one. In this case, α_z strongly oscillates between positive and negative values along the wire's axis, resulting in a smaller average Rashba coupling. In the homogeneous case, the minigap is the largest, close to Δ_0 in the middle region of panel Fig. 5.12(j). Here the induced effective gap has to be necessarily better since the SC covers the whole length of the wire. Moreover, there is a homogeneous and large Rashba coupling along the wire (~ -30 meV·nm) close to the SC where the charge density concentrates (not shown here). Concerning the Majorana oscillations, they are pretty comparable for the two types of superlattices and definitively bigger than for the homogeneous case.

In Figs. 5.12(c,g,k), we plot the Majorana probability density of the different setups along and across the wire for the values of V_{Gate} marked by the blue lines in (b,f,j), respectively. We find that in all cases the MBSs are localized at the edges of the wire, but with different longitudinal and
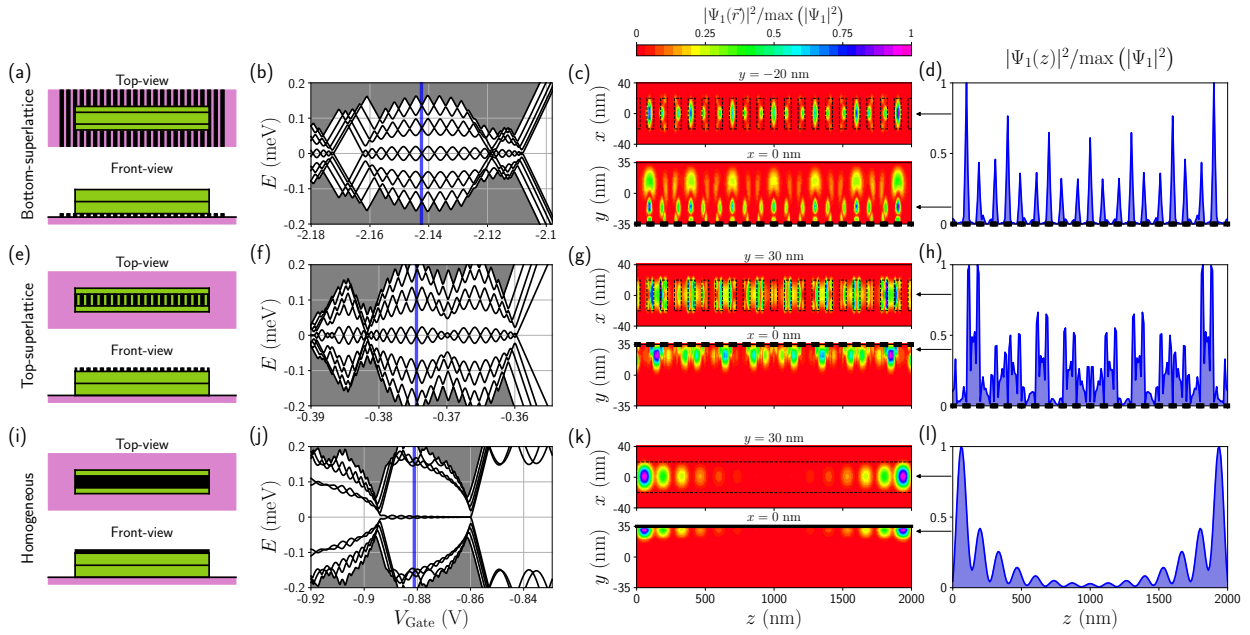
Figure 5.12: Low energy spectrum and Majorana wave function for the same devices of Fig. 5.11 at the region of the red rectangles. (a,e) Top and front view of the two setups considered throughout this work: bottom- and top-superlattice of SC fingers. (b,f) Low-energy spectrum versus back gate voltage. (c,g) Probability density of the lowest-energy eigenstate at the voltage marked with a blue line in (b,f). (d,h) Longitudinal cut of the probability density of (c,g) at the (x,y) cross-section values marked by arrows. For comparison, we show equivalent results for an homogeneous nanowire in (i-l).

transverse profiles. Across the wire's section the wave function tends to be close to the SC fingers in the top-superlattice setup. On the other hand, the probability density oscillates from top to bottom in the bottom-superlattice one, see lower panel of Fig. 5.12(c). As we noticed in Sec. 5.3, this is related to the shape of the potential profile due to the strong gate voltages needed to deplete the wire in this setup. The probability density accommodates to the isopotential curves, which for the bottom-superlattice device oscillate from top to bottom in the z direction for a particular ϕ value.

Figures 5.12(d,h,l) show longitudinal cuts of the probability density at the (x,y) cross-section values marked by arrows in Figs. 5.12(c,g,k). As expected, in the homogeneous case the wave function decays exponentially towards the wire's center with the Majorana localization length ξ_{M} [51]. For the parameters of this case we obtain $\xi_{\mathrm{M}} = 350$ nm, which is consistent with panel (l). On the other hand, for the superlattice nanowires the decay length is characterized by the interplay between two scales, the Majorana length and the superlattice length L_{cell}. The decay length in the homogeneous case is shorter and the probability density is pretty localized at the wire edges and almost zero at its center. This is not the case for the superlattices since their wave functions decay more slowly. To quantify this, we compute the absolute value of the Majorana charge Q_{M} that measures the wave function overlap between the right and the left Majoranas [98, 99, 220]

$$|Q_{\mathrm{M}}| = e \left| \int u_{\mathrm{L}}(\vec{r}) u_{\mathrm{R}}(\vec{r}) dr^3 \right|, \tag{5.1}$$

where $u_{\mathrm{L,R}}$ are the electron components of the left and right Majorana wavefunctions, given by $\gamma_{\mathrm{L}} = \Psi_{+1} + \Psi_{-1}$ and $\gamma_{\mathrm{R}} = -i(\Psi_{+1} - \Psi_{-1})$, being $\Psi_{\pm 1}$ the even/odd lowest-energy eigenstates. We get the values $\left|Q_{\mathrm{M}}^{\mathrm{BS}}\right|/e = 0.93$, $\left|Q_{\mathrm{M}}^{\mathrm{TS}}\right|/e = 0.88$ and $\left|Q_{\mathrm{M}}^{\mathrm{h}}\right|/e = 0.63$ for the bottom-superlattice, top-superlattice and homogeneous cases, respectively. As expected, the Majorana charge is larger for both superlattice devices compared to the homogeneous case.

5.7   Alternative superlattice configuration

We have seen that the main inconvenience of the superlattice Majorana nanowires comes from the partial SC coverage produced by the SC superlattice (specially as r_{SC} diminishes). This leads to a reduced induced SC gap that, in turn, produces a smaller topological minigap and a larger Majorana charge. We could improve this scenario by covering one of the wire's facets continuously with a thin SC layer, like in a conventional epitaxial Majorana nanowire, while still placing the hybrid structure on a superlattice. We analyze this alternative configuration in Fig. 5.13 for the case of a bottom-superlattice setup [see Fig. 5.1(c) for a sketch of the device]. Now the superlattice can be either superconducting or normal (since the induced superconductivity is already provided by the SC layer). We choose here a set of normal metal fingers, such as gold, that could be used as tunneling local probes along the wire by driving a current between each finger and the SC homogeneous layer. The tunneling coupling in this case is advantageous because it leads to a smaller wire's intrinsic doping and to a larger localization of the MBS wavefunctions close to the Al SC layer, where the electrostatic potential and induced pairing are larger.
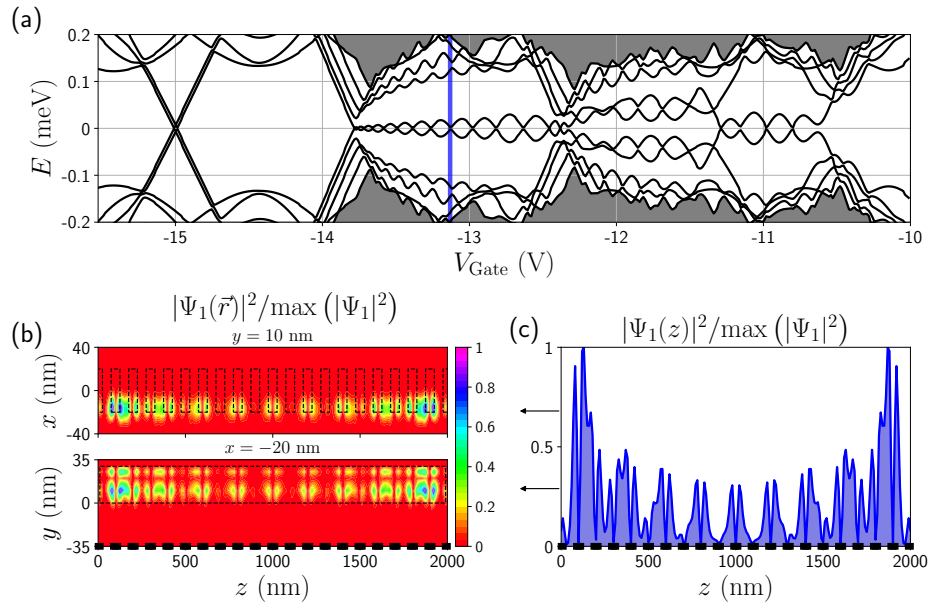
Figure 5.13: (a) Low-energy spectrum versus back gate voltage for the alternative superlattice device shown in Fig. 5.1(c). (b) Probability density of the lowest-energy eigenstate at the voltage marked with a blue line in (a). (b) Longitudinal cut of the probability density of (c) at the (y,z) cross-section values marked by arrows. Parameters are the same as in Fig. 5.12: $L_{\text{wire}} = 2\,\mu\text{m}$, $L_{\text{cell}} = 100$ nm, $W_{\text{Au}} = W_{\text{Al}} = 10$ nm, $r_{\text{SC}} = 0.5$, $V_Z = 0.6$ meV, $\Delta_0 = 0.2$ meV, $V_{\text{SC}} = 0.2$ V and $\rho_{\text{surf}}/e = 2 \cdot 10^{17}$ (cm)$^{-3}$. We take $V_N = 0$ V as the boundary condition for the fingers.

In Fig. 5.13(a), we show the low-energy spectrum of this setup for the same parameters of Fig. 5.12 except for the boundary condition between the (normal) bottom superlattice and the wire, which we take as $V_N \simeq 0$ V. The values of V_{Gate} for which we find the first topological subbands are pretty negative since the continuous Al layer induces a large intrinsic doping in the wire. The structure of this spectrum is a combination of the homogeneous and superlattice ones. From $V_{\text{Gate}} \simeq -13.7$ V to $\simeq -12.3$ V one transverse topological subband is occupied. At that point a different transverse subband populates the wire and the even-odd effect destroys the topological phase (as it occurs in the homogeneous wire). However, at $V_{\text{Gate}} \simeq -11.3$ V a zero energy mode appears again but without a (prominent) gap closing. This is the signature of a gap between different longitudinal subbands, which allows one of the last two transverse subbands to re-enter into the topological phase. The interplay between longitudinal and transverse subbands gives rise to a wider $V_{\text{Gate}} - V_Z$ space where topological states emerge, in comparison to a homogeneous nanowire, as it was previously stated in Ref. [222].

Now, as was our intention, in the topological regions we get a topological minigap that is comparable to the one of the homogeneous case, see Fig. 5.12(j). The probability density of the lowest energy mode at the V_{gate} value marked with a blue line in (a) can be seen in (b). As expected, it is located close to the Al thin layer in the transverse direction. A longitudinal cut at the (x,y) values marked by arrows is shown in (c). The MBSs, that still display a doubling of the oscillating peaks

characteristic of the superlattice, decay exponentially from the edges towards the wire's center faster than for the top- and bottom-superlattices analyzed before. The Majorana charge is now $|Q_{\mathrm{M}}|/e = 0.71$, considerably smaller than for the bottom superlattice alone (0.93) and closer to that of the homogeneous case (0.61). The sizable minigap in this case protects the system from quasiparticle excitations, separating the Majorana modes from the quasi-continuum of states and preventing transitions into it due to, e.g., temperature or out of equilibrium perturbations.

5.8 Conclusions

We have analyzed in detail the superlattice SM-SC partial-shell nanowires, in which the induced superconductivity is achieved by proximity to a superlattice of SC fingers (instead of having the SC cover continuously the length of the SM wire). This configuration can have practical benefits to manipulate the Majorana wave function and to measure it. For instance, one could use an STM tip to drive a current between the tip and each of the SC fingers to measure the local density of states along the wire. The fingers could also work as local probes themselves.

Specifically, we have studied the impact of the three-dimensionality and the electrostatic environment on the spectral properties of two types of experimental setups: one in which the SC superlattice is on top of the nanowire and the other where it is below with respect to the back gate. We find that an accurate description of the nanowire boundary conditions and the surrounding media are crucial for a proper understanding of the system's properties. In particular, the interface of the nanowire with the SC, vacuum or substrate, creates an accumulation of electrons around the wire's cross section. Its main effect is to contribute to the average intrinsic doping of the wire (that has to be compensated with an external gate when looking for the first populated subbands). On the other hand, the extrinsic doping produced by the applied gate voltage is dominated by the SC superlattice structure, giving rise to an inhomogeneous (oscillating) electrostatic potential.

Depending on the location of the SC superlattice and the number and width of the SC fingers, we find a rich phenomenology that includes the emergence of trivial holes in the topological phase diagram and the formation of localized states near the SC fingers that may interfere with the topological states. Moreover, since the Rashba coupling is proportional to the electric field, the spin-orbit coupling also becomes an inhomogeneous quantity in this system. This results in a reduction of the topological minigap, specially in the bottom-superlattice device, owing to a lower spatial average Rashba value. In the same vein, the induced superconducting gap is smaller than in a conventional homogeneous Majorana nanowire due to the smaller SC coverage of the nanowire.

In contrast, the system develops a wider topological phase as a function of magnetic field and average chemical potential as a consequence of the emergence of additional (longitudinal) subbands. In the topological regions, MBSs do appear at the edges of the superlattice nanowire. Their probability density across the wire's section is concentrated close to the SC fingers in the top-superlattice setup. They extend further into the wire's bulk in the bottom-superlattice one due to the stronger potential oscillations created in this case by the back gate. Along the wire, the MBSs decay exponentially

towards its center with a decay length characterized by the interplay between the superconducting coherence length and the superlattice length.

In general, we find that the performance of the two types of setups considered here is quite similar, although the bottom-superlattice nanowire is slightly worse because of the larger potential oscillations that appear in this case. In both cases, the main disadvantage is the poor topological protection of the MBSs. This manifests in a small topological minigap and a large Majorana charge, arising essentially from the low SC coverage. This could be solved by covering one of the lateral wire's facets with a continuous SC layer while still placing it on a superlattice of fingers (that could be superconducting or not). This kind of device benefits from the superlattice structure (with a wider topological phase in $V_{\text{Gate}} - V_{\text{Z}}$ space and the possibility to use the fingers as probes), and furthermore displays a sizable topological minigap and small Majorana charge comparable to those of a conventional homogeneous Majorana nanowire. We thus believe that the use of mixed setups of this type is probably the best route towards creating Majorana states in such superlattice devices.

CHAPTER 6

SEMICONDUCTOR-FERROMAGNETIC INSULATOR-SUPERCONDUCTOR HETEROSTRUCTURES: HYBRID NANOWIRES AND 2DEGS

In this chapter we characterize the properties of SM-FI-SC heterostructures, i.e., SM-SC heterostructures with an additional layer of a ferromagnetic insulator (FI). We show that this FI layer can induce, also by proximity effect, a Zeeman field in the heterostructure; and thus, there is no need to apply a magnetic field to obtain a topological phase in this device. We first derive the full Hamiltonian that includes, on an equal footing, the conduction bands of the three materials. We then analyze the induced superconductivity, effective chemical potential, SO coupling and Zeeman field of the heterostructure as a function of external gate voltages and for different devices. We first study setups based on SM nanowires. We find that, in order to obtain a topological phase, the wavefunction needs to be pushed *at the same time* to both, the SC and FI layer, with the aid of external potential gates. We show that this tuning can be facilitated with an advantageous layer's disposition design. Apart from this device, we also study a setup based on a SM 2DEG. In this case, the heterostructure is arranged in a planar SM-FI-SC stacking geometry, where the SM and SC are not directly in contact. We find the optimal FI layer thicknesses for which the system can undergo a topological phase transition. We compare this 2DEG-based device with the nanowire ones, finding that it provides more robust and sizable topological phases.

The contents of this chapter are published in Phys. Rev. B **104**, L041404 (2021) [209]; and in Npj Quantum Materials **7**, 81 (2022) [132].

6.1 Introduction

The SM-SC hybrid nanowires proposals studied in the previous chapters rely on external magnetic fields to create superconducting topological states. In Chapter 5, we have shown that when one tunes appropriate the gate potentials, it is possible to find MBSs at the end of the hybrid nanowires if the magnetic field is large enough. However, this magnetic field introduces further complexity into the problem that makes these proposals unappealing.

First, we have completely ignored orbital effects in this problem as it is beyond the current analysis

performed in this thesis. This phenomenon emerges due to the inclusion of the magnetic potential vector $\vec{A}$ in the canonical momentum, i.e., $\vec{k} \to \vec{k} - \frac{e}{\hbar}\vec{A}$, that introduces some extra terms in the Oreg-Lutchyn Hamiltonian that depends on the magnetic field. These extra-terms renormalizes the effective mass, the g-factor and the chemical potential; being these last two parameters crucial for the formation of topological states. As a result, the resulting phase diagrams may turn from regular separated parabolic regions into messy and (apparently) unpredictable regions which may include trivial holes [115, 123, 124]. And this complexity introduces an unwanted uncertainly in the experimental demonstration of MBSs.

Alongside with the effect in the SM, magnetic field is also detrimental for the superconducting state because the (s-wave) superconducting pairing amplitude diminishes with the magnetic field[1] [79], so does the superconducting gap. Since the topological protection of the MBSs depends on the superconducting gap, this is also harmful for the formation of the superconducting topological state. In fact, since the gap is completely closed above the so-called critical magnetic field, the topological phase diagram dramatically shrinks, so the magnetic field must be smaller than this threshold but larger than the critical (topological) magnetic field. It may actually occur that the critical magnetic field is smaller than the topological one for some subband, and thus, this subband cannot support a topological state in a realistic scenario.

In addition, an external magnetic field sets strict constraints on the device geometry of multiwire devices. In order to demonstrate the topological properties of these wires [23] or to build a hypothetical topologically-protected quantum computer [24], one needs to arrange and connect several of these wires, so that one can perform braiding operations. But in the above proposals, all the wires must be aligned with the magnetic field. Hence, all the wires in a multiwire device must be parallel, and thus the possible connections among wires is limited by this geometry.

In this context, ferromagnetic insulators (FIs) could offer a way to solve the above problems. This kind of materials can be combined with the hybrid nanowires to induce a local exchange field on the SM nanowire by proximity effect, eliminating the need for external magnetic fields. Moreover, since this material is an insulator, it does not introduce additional (unwanted) states in the wire. However, while the idea of replacing the external magnetic field by the ferromagnetic insulating layer appears as rather straightforward in simplified (Majorana) models [36], there are open questions when applied to realistic systems. Microscopic calculations are required to demonstrate whether or not the topological regime could be reached for the actual geometrical and material parameters, as well as gating conditions. Furthermore, understanding the interplay of magnetic and superconducting proximity effects in such devices is of relevance in the broader field of superconducting spintronics [230, 231] and quantum thermodevices [232, 233].

Several experiments have shown that it is actually possible to have coexisting superconducting and

---

[1]We do not include this effect in our theory as it has a trivial impact in the simulations (a reduction of the superconducting gap with an increasing magnetic field) that complicates the understanding of the phenomena arising in the heterostructures.

ferromagnetic phases in FI-SC and SM-FI-SC heterostructures. Recent experiments in hexagonal nanowires partially covered by overlapping SC and FI shells showed the appearance of zero-bias conductance peaks [127], spin-polarized subgap states [128], and supercurrent reversal [234]; which are necessary conditions to create superconducting topological states in this heterostructure. Strikingly, some devices, depending on the layer disposition across the heterostructure, show no induced magnetization, indicating that the magnetic proximity effect strongly depends on the relative position between the electron's wavefunction and the proximitizing layers.

To address this problem, we perform the same comprehensive numerical simulations including in the hybrid nanowire a FI layer in Sec. 6.3. In Sec. 6.2, we first describe the FI following the spirit of our theoretical approach, including its CB in the Hamiltonian, and using relevant experimental parameters and geometries. We then show that there are different mechanisms that can give rise to a proximity-induced magnetic effect in this tripartite system: either the spin polarization is directly induced by the ferromagnet in the SM nanowire, or indirectly through a more elaborate process where it is first induced on the SC layer (at the regions where the SC and FI shells overlap) and then in the wire. A third mechanism whereby electrons tunnel from the SC to the SM through the spin-polarized FI barrier is also possible for sufficiently thin FI layers (in configurations where the SC and the SM are separated by the FI layer). We note nevertheless that in devices where the three materials are in direct contact, a sharp distinction between the three mechanisms is artificial and the overall induced exchange field is due to a combination of all of them. We find that, in general, fine-tuning from back and side gates is necessary in order to push the SM electron wavefunction close to both the SC and FI layers, maximizing magnetic and superconducting correlations at the same time. Hence, we prove that topological superconductivity can indeed arise in these systems provided when certain geometrical and electrostatic conditions are met.

To avoid this fine-tuning, we propose in Sec. 6.4 a planar SM/FI/SC heterostructure based on a SM 2DEG that gives rise to wider and more regular (in parameter space) topological phases. We associate this behavior with the stronger vertical confinement achieved in 2DEGs compared to hexagonal nanowires. Therefore, our work establishes 2D ferromagnetic heterostructures as a promising platform for topological superconductivity, opening the possibility of defining complex topological multiwire structures easy to scale.

We note that several theoretical works on the same subject have been published concurrently or recently [177, 235–240] to ours [209, 241]. All the results presented in this thesis are in agreement with these works.

6.2 Ferromagnetic insulators and InAs-EuS-Al heterostructures

Ferromagnets are materials with a large magnetic permeability, i.e., materials that strongly respond to external magnetic fields, acquiring a magnetization, and remaining magnetized even after the external magnetic field is switched off. These materials are typically metals, specially those which are pure elements. But there are some compounds that are (electronic) insulators, the so-called

ferromagnetic insulators (FI). The origin of these two joint properties depend on the material where it is present.

One family of FIs are the Europium monochalcogenides, which are compounds made of Eu and any element of the group VI of the periodic table. Most common forms are EuO and EuS, although EuTe and EuSe are also possible. The origin of the ferromagnetic insulating properties of these materials is the strong exchange interaction present in their highly-localized $4f$-orbitals[2] [242, 244]. Several experiments have measured the ferromagnetic and insulating properties of their crystal forms [245–247], generally cubic rock salt structure. In addition, several theoretical works have tried to describe the bands using *ab initio* methods to give a detailed description of these materials. Fig. 6.1(a) shows an schematics of the energy bands based on calculations of Refs. [248], which seems to be in agreement with several experiments [242, 244, 249–251]. The Fermi level lies in an insulating gap Δ_{EuX} that ranges from 1 to 2 eV. The first valence bands are composed by the $4f$ atomic orbitals, and they are (almost) completely flat and with the same spin-orientation. This indicates that these spin-polarized bands correspond to strongly localized orbitals. The other $4f$ bands (with the other spin orientation) fall far above the CBs, pointing to a large magnetic exchange interaction. The first CB in contrast is a dispersive state with d-symmetry, and its minimum is not at the Γ-point but in the X-one instead. These bands are also spin-polarized as a result of their interaction with the large spin-polarized $4f$-states. Their Zeeman splitting is nevertheless much smaller, of the order of 0.1 eV.

Several experiments on Europium chalcogenides heterostructures have been carried out during the last decade to demonstrate that it is possible to induce the magnetic properties of these materials on others by proximity effect. Examples of them are hybrid devices of EuS with Pb 2DEG [252], graphene nanosheets [253], Bi_2Se_3 crystals [254], and Al layers [255–257]. In the last years, hybrid InAs nanowires partially covered with EuS layers [126] and both, EuS and Al layers [125], have been achieved too. Experiments have demonstrated that magnetism and superconductivity can coexist inside the SM nanowire [127, 128, 234]. Therefore these hybrid nanowires contain all the ingredients needed to develop a superconducting topological phase.

The band alignment is nonetheless another key ingredient for the experimental realization of such phase, as the three materials should keep their electronic properties when they are joint together. This has been accessed in several experiments [125, 126, 240], and a scheme can be found in Fig. 6.1(b). The Fermi level is barely affected by the inclusion of the EuS layer. It lies roughly at the bottom of the InAs CB, and therefore the Al layer keeps it metallic properties, being the bottom of its CB at roughly -11 eV [79]. On the other hand, the EuS CB is located at 0.7 eV above the Fermi level (and InAs CB), while the $4f$-states (the EuS valence band) falls 1 eV below. Together with this alignment, the work function difference between the different materials impose a band-bending. For both interfaces, InAs-EuS and InAs-Al, it is created an electron pocket inside the SM nanowire and close to the interface, that creates in turn a Schottky barrier. This can be understood as a

---

[2]Concretely, the dominant exchange magnetism is the so-called Kramers antiferromagnetic superexchange mechanism [242, 243].
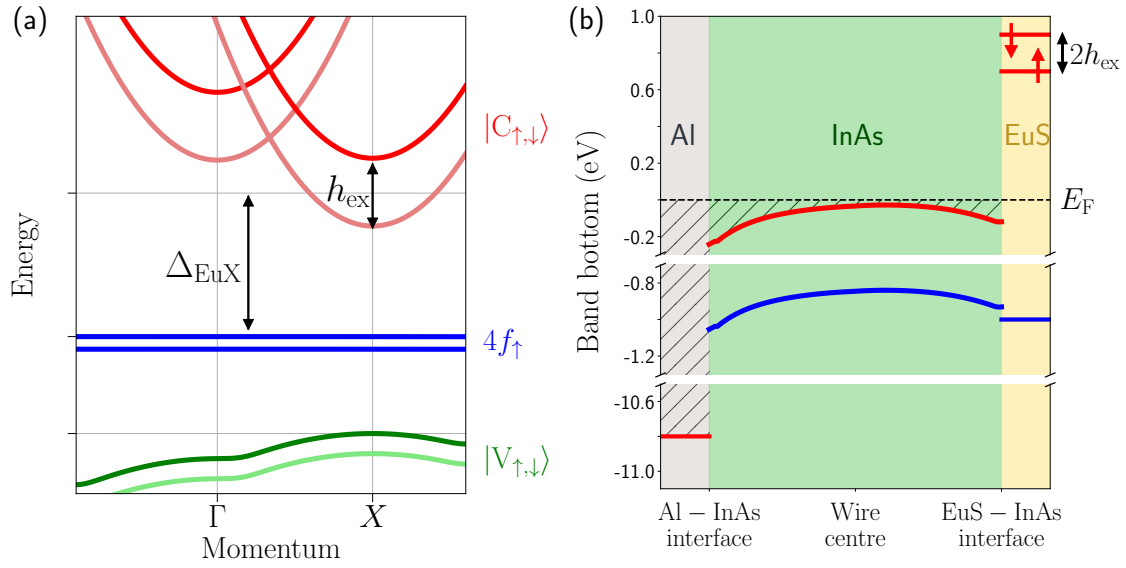
Figure 6.1: (a) Schematic band diagram of bulk Europium monochalcogenides. The low-energy spectrum is concentrated around the X-point, where the crystal exhibits a band-gap Δ_{EuX} (being X here any group VI element). The CB (in red) is spin-splitted (by a quantity h_{ex}) as a result of its coupling with the $4f$ valence bands (in blue), which are completely spin-polarized. Another gap separates the $4f$ bands with the next valence bands (in green). See Refs. [242, 248] for further details. (b) Schematic diagram of the conduction and valence-band edge positions (in red and blue, respectively) across the SC-SM-FI heterostructure, spanning the three different materials. In the Al and InAs, the Fermi energy is located in the CB (close to the band bottom in InAs), whereas in the EuS it is inside its insulating gap. The EuS conduction band is spin-splitted.

band bending towards these interfaces inside the wire, that distorts the CB band-bottom. For the InAs-Al, it has been shown that in these heterostructures ranges from $0.2\,\mathrm{eV}$ to $0.4\,\mathrm{eV}$ [177], while for the InAs-EuS interface is the half, quite similar to the InAs-vacuum interface. As we will discuss, this fact is crucial for the development of the topological state, as the electrons will naturally be pushed towards the InAs-Al interface, acquiring robustly a superconducting phase, but in detrimental to acquire a magnetic phase. All these band alignments are further distorted by the electric fields defined by the gate electrodes. However, for sufficiently small fields one can assume that only the InAs CB moves and can neglect its hybridization with the EuS valence bands.

The quality of the interface and the growing conditions are another aspects that must be taken into account in the simulations. Both, EuS can be grown epitaxially on the InAs nanowire [126], and the Al on the resulting hybrid EuS-InAs wire[3] [125]. This can be done since all the materials have similar lattice constants (for some crystallographic direction). This is beneficial as it leads to high-quality interfaces among the three materials. We note that the EuS-Al interface is not completely flat, as the EuS grows in domains (like Al). This roughness is characterized by a corrugation thickness of $\sim 1\,\mathrm{nm}$. Moreover, the outer facet of the Al is incidentally oxidized in the experiments[4]. Both have the same effect in our simulations: they break parallel-momentum conservation increasing the hybridization between the materials involved in the interface. We actually find that the corrugation of the EuS-Al does not change the results of our simulations as long as the effect of the disordered outer facet of the Al is already included.

6.3 Wire-based devices

6.3.1 Model

Following closely the experiments of Ref. [127], we consider the two types of device geometries depicted in Fig. 6.2(a) and (b). In both cases a hexagonal cross-section InAs nanowire (in green) is partially covered by two different thin layers. Both are grown epitaxially over certain facets of the wire. The highly transparent epitaxial interfaces improve the hybridization between the nanowire and the layers. One of these layers is SC shell made of Al (light gray), whose outer surface is oxidized. The other layer is a FI made of EuS (yellow), whose interface with the Al is also grown epitaxially in the experiments, although it is not completely flat. The main difference between both setups of Fig. 6.2 is that in the *overlapping* device [Fig. 6.2(a)], the Al and EuS layers partially overlap on one facet, while in the *non-overlapping* one [Fig. 6.2(b)] they lie on adjacent facets.

This hybrid system is surrounded by three gates (dark gray), one at the bottom and two at the left and right sides, which allow to tune the wire doping level and the charge distribution inside the heterostructure simultaneously. The side gates are placed symmetrically from the center of the wire

---

[3]Apparently, EuS must be grown first on InAs before the Al, as its melting point is above the Al one. However, it could be different for other Europium chalcogenides or FIs.

[4]The outer facet of EuS must be covered with another insulator (like AlO_2/Al_2O_3) to prevent this oxidation. Otherwise, it may lose its magnetic properties.
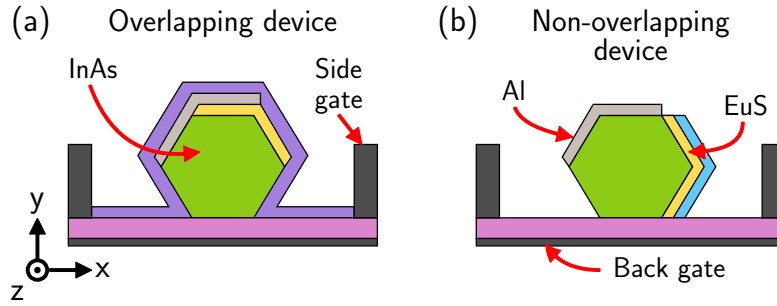
Figure 6.2: (a,b) Sketches of the tripartite SM-FI-SC nanowires studied in this thesis: a hexagonal cross section InAs nanowire (green) is simultaneously proximitized by an Al superconductor layer (light gray) and an EuS magnetic insulator layer (yellow). Two side gates and one back gate (dark gray) allow to tune the chemical potential and control the position of the wavefunction inside the heterostructure. Different dielectrics are used in the experiments [127] to allow gating (SiO$_2$, in pink) and to avoid the oxidation of the EuS layer (HfO$_2$ and AlO$_2$, in purple and blue, respectively). In the *overlapping* device, (a), the Al and EuS layers overlap on one facet, while in the *non-overlapping* device, (b), they are grown on different facets.

at some distance from the outer corners of the wire, and their height is half the wire's width. On the other hand, the wire is placed on top of a SiO$_2$ dielectric substrate (pink). This substrate fixes the distance between the back gate and the bottom of the wire.

There are other dielectrics in the devices that are necessary to avoid the unwanted oxidation of the EuS layer. This includes a layer of HfO$_2$ (purple) surrounding the whole heterostructure in the overlapping device, and a layer of AlO$_2$ (blue) covering the EuS layer in the non-overlapping one. We include them in our electrostatic simulations to obtain a better qualitative agreement with the experiment of Ref. [127] although they play a minor role in our results. Finally, we assume that the rest of the environment (white) is vacuum. All the geometrical parameters are summarized in Appendix D.3.

6.3.2 Electrostatic potential

As we show for the SM-SC, the wavefunction position inside the SM cross section, which is governed by the electrostatic potential, determines the strength of superconducting proximity effect. The same will apply for the hybrid SM-FI-SC nanowires, with the difference that now there are two proximity phenomena, and therefore the wavefunction needs to be pushed towards both interfaces at the same time. To understand how realistic is this scenario, we show in Fig. 6.3 the electrostatic potential in the overlapping (a) and the non-overlapping (b) devices. In these simulations, the back-gate voltage is set to a negative value, particularly $V_{\mathrm{bg}} = -1$ V. This is a typical situation in our simulations and in the experiments, as one needs to deplete the wire in order to populate it with just a few bands. Hence, the electrostatic potential is negative at the bottom of the wire, while it is positive and maximum close to the SM-SC interface due to the SM-SC band bending. This is translated into an accumulation of (mobile) charges ρ_{mobile} in this interface, quantity that
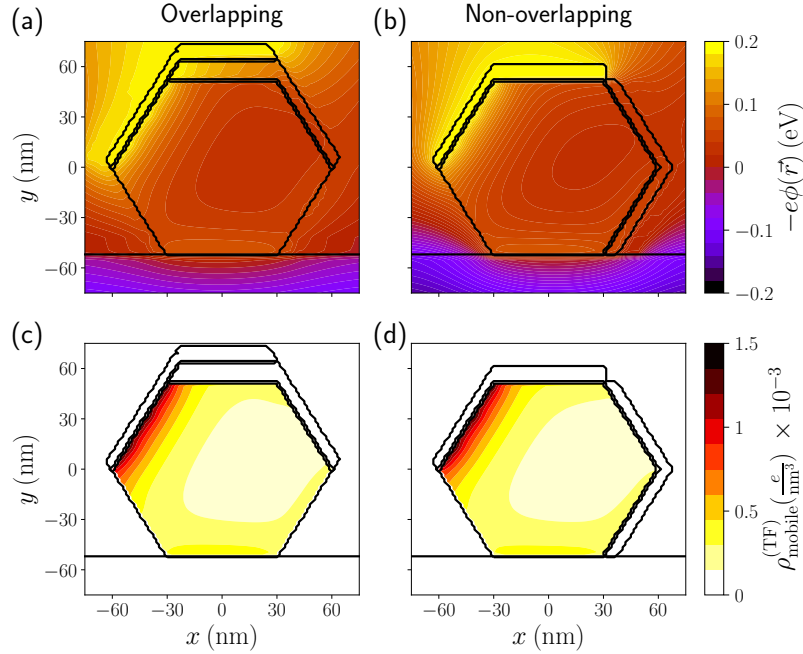
Figure 6.3: Electrostatic potential across the heterostructure section in the overlapping device (a) and in the non-overlapping one (b). (c,d) Mobile charge density in the wire computed within the Thomas-Fermi approximation using the upper electrostatic potentials. The back-gate voltage is fixed to $V_{\mathrm{bg}} = -1$ V, and the other two gate potentials to zero, $V_{\mathrm{sg}}^{(\mathrm{L,R})} = 0$.

we show in Fig. 6.3(c) and (d) for the same devices in the TF approximation. Even if both devices exhibit a similar electrostatic and charge density distributions, notice that, while in the overlapping device [Fig. 6.3(c)] the charge is also accumulated in the left corner of the SM-FI interface, in the non-overlapping device [Fig. 6.3(d)] is far apart from this interface. This (apparently minor) difference may enhance the hybridization with the FI in the overlapping device, and suppress the same hybridization in the non-overlapping one.

6.3.3 Rashba spin-orbit coupling

The FI barely introduces any change to the SO coupling because (i) it is an insulator layer and thus electrons do not tunnel into this region with no SO coupling, and (ii) the band-bending towards the SM-FI is similar to that of the SM-vacuum interface and therefore the electric field barely changes between both interfaces. To better illustrate this fact, in Fig. 6.4. we show calculations of the SO coupling for (a) the overlapping and (b) non-overlapping devices. Both devices exhibit the same profile as the electrostatic potential [Fig. 6.3(a,b)] is the same for both. The maximum is located at the SM-SC interface, precisely where the charge density is maximum [see Fig. 6.3(c,d)], what will benefit the (possible) topological protection of the states populating the wire. Notice that the SO coupling at the SM-SC and SM-FI interfaces is larger than 10 meV·nm, which is large enough to have a (robust) topological phase.
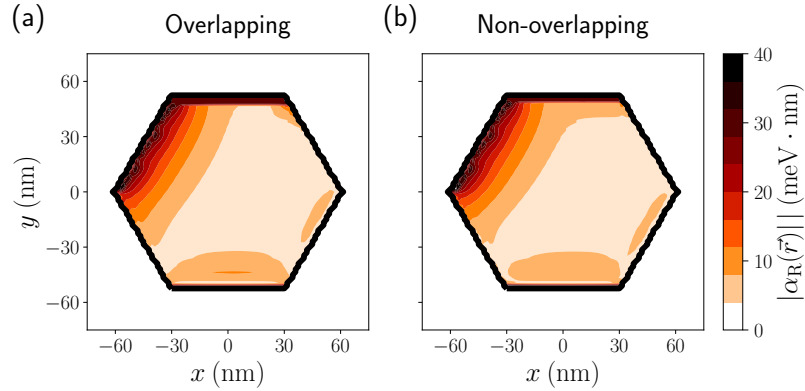
Figure 6.4: Rashba SO coupling across the wire section for the same devices as in Fig. 6.3.

This SO coupling has been computed for (111) zinc-blende InAs wires. In Ref. [209], we also compute the same profile for (0001) wurtzite InAs wires, and we find that the SO coupling is halved in this crystal, as we predicted in Chapter 3. It is nevertheless larger than 10 meV·nm close to the interfaces, so wires with this crystallography will also support (robust) topological phases, if the other (topological) conditions are met.

6.3.4 Spectrum and topological phase

We want to study now whether these devices can undergo a topological phase transition or not. To this end, we compute the bulk properties (energy spectrum and DOS) of both systems, assuming to this end that they are translationally invariant along the wire's direction.

Overlapping device

We first focus on the DOS and dispersion relation of the overlapping geometry (see Fig. 6.5) fixing the side-gate voltages to zero and the back-gate to ~ -1 V. In order to identify the separate effect of the magnetic and superconducting terms, we perform three different calculations: in the first one we switch off the exchange field in the EuS and the Rashba SOC in the InAs [Fig. 6.5(a)]; then we switch on h_{ex} [Fig. 6.5(b)] and finally we also connect α_R [Fig. 6.5(c)].

In the top panel of Fig. 6.5(a), we show the partial DOS integrated over the InAs volume. It exhibits a well-defined induced superconducting gap, although halved with respect to the ~ 0.2 meV gap observed in the DOS integrated over the Al shell volume, Fig. 6.5(a) bottom panel. This is in accordance with what one expects from a conventional superconducting proximity effect [81, 115, 258].

When $h_{ex} \neq 0$ (but $\alpha_R = 0$) we observe two main features in the spin-resolved partial DOS. First, an energy splitting of the superconducting coherence peak appears in the Al [Fig. 6.5(b) bottom panel], which is of the order of ~ 0.06 meV, in agreement with recent theoretical and experimental results on Al/EuS junctions [255–257, 259]. This agreement without any fine tuning of the parameters in
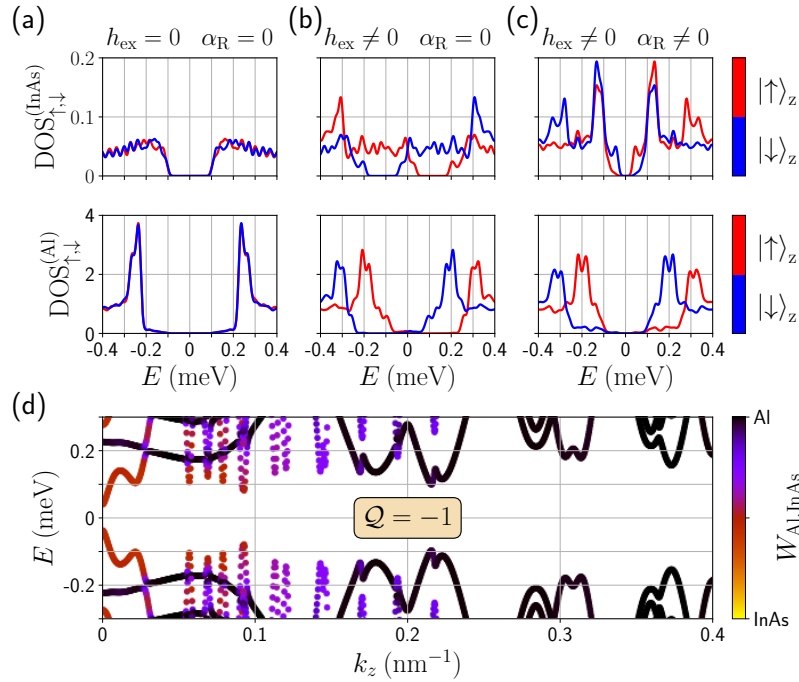
Figure 6.5: (a-c) Spin-resolved partial density of states (DOS) for the overlapping device integrated over the InAs wire volume (top row) and the Al layer volume (bottom row) when (a) the exchange field h_{ex} in the EuS layer and the Rashba SOC α_{R} in the InAs wire are set to zero, (b) only the exchange field is turned on, and (c) both are present. Red and blue correspond to the DOS for different spin orientations along the z axis (wire's direction). (d) Low-energy band structure versus k_z for the hybrid-wire parameters in (c). The colorbar represents the relative weight W of a given state in the Al layer (black) and in the InAs wire (yellow). The wavefunction weight in the EuS layer is negligible since it is an insulating material. The $\mathbb{Z}_2$ topological invariant is $\mathcal{Q} = -1$, signaling a topological phase. We take here $V_{\text{bg}} = -0.95$ V and $V_{\text{sg}}^{(\text{L,R})} = 0$ V. Other parameters can be found in Appendix D.3.

our model is encouraging about its validity. Second, there is a complete closing of the induced gap in the InAs [Fig. 6.5(b) top panel]. This points to an induced exchange field larger than ~ 0.1 meV, the induced gap in the semiconductor, and therefore, larger than in the Al layer. In contrast to previous proposals [125, 127] our results suggest that in the current case topological superconductivity is achieved below the Chandrasekar-Clogston limit [260, 261] for the Al ($h_{\mathrm{ex}}^{(\mathrm{Al})} < \Delta/\sqrt{2}$).

Finally, in Fig. 6.5(c) top panel we observe that a gap is opened again in the presence of SO coupling. This sequence of gap closing and reopening at a high-symmetry k_z-point is a signature of a topological phase transition. The band structure shown in Fig. 6.5(d) further illustrates the spatial distribution of the low-energy states in this last case (i.e., with $h_{\mathrm{ex}} \neq 0$ and $\alpha_{\mathrm{R}} \neq 0$). The weight $W_{\mathrm{Al,InAs}}$ of each state in the SC/SM is represented with colors, from a state completely located in the Al layer (black) to one completely located in the InAs wire (yellow). The lowest-energy states close to $k_z = 0$ have significant weight both in the Al and in the InAs, as expected for a topological superconducting phase [115]. We prove that the system in Figs. 6.5(c) and 6.5(d) is indeed in the topological regime by calculating the $\mathbb{Z}_2$ topological invariant $\mathcal{Q}$ (see Chapter 2 for the calculation method). We find $\mathcal{Q} = -1$, which actually corresponds to the nontrivial case.

Figure 6.5 corresponds to a specific gate voltage that could be fine tuned. To gain more insight into this, we compute in Fig. 6.6(a) the energy spectrum versus the gate voltage at $k_z = 0$. For the voltage range shown there, we observe low energy pairs of states that cross zero energy at (roughly) $V_{\mathrm{bg}} = -4.5$ V, $V_{\mathrm{bg}} = -4$ V and $V_{\mathrm{bg}} = -1$ V. These zero-energy crossings of the bulk states are related to topological phase transitions. This is demonstrated by the calculation of the topological invariant shown with white-gray colors. The topological phase of these states extend for hundred of volts, revealing a measurable robustness against chemical potential perturbations. In Fig. 6.6(b-d), we show the dispersion relation versus the momentum along the wire's direction k_z for three specific V_{bg} values: (b) at $V_{\mathrm{bg}} = -1$ V, i.e., before the last topological region; (c) at $V_{\mathrm{bg}} = -0.95$ V, inside the topological region [this is the one shown in Fig. 6.5(d)]; and (d) at $V_{\mathrm{bg}} = -0.6$ V, after this region. In the top panel of these three figures, we show with colors the weight of the states in the different materials, from a state completely located in the Al layer (black) to completely located in the InAs wire (yellow). The states that cross zero energy in this topological region correspond to mixed states with half of the wavefunction located in the Al and the other half in the InAs. For completeness, we also show in Fig. 6.6(e-f) the spin-polarized DOS for the bandstructures shown in Fig. 6.6(b-d).

Non-overlapping device

Strikingly, the same analysis for the non-overlapping geometry [see Fig. 6.7(a)] reveals that the magnetic proximity effect in the whole non-overlapping heterostructure is not strong enough to close and reopen the superconducting gap in the wire at any gate voltage. The reason for this behavior can be traced to the limited spin polarization induced on the nanowire [i.e., the total spin-polarized DOS shown in Fig. 6.7(e-g) is not spin-polarized].

To further understand the lack of magnetization of this geometry, we compute in Fig. 6.8 the same
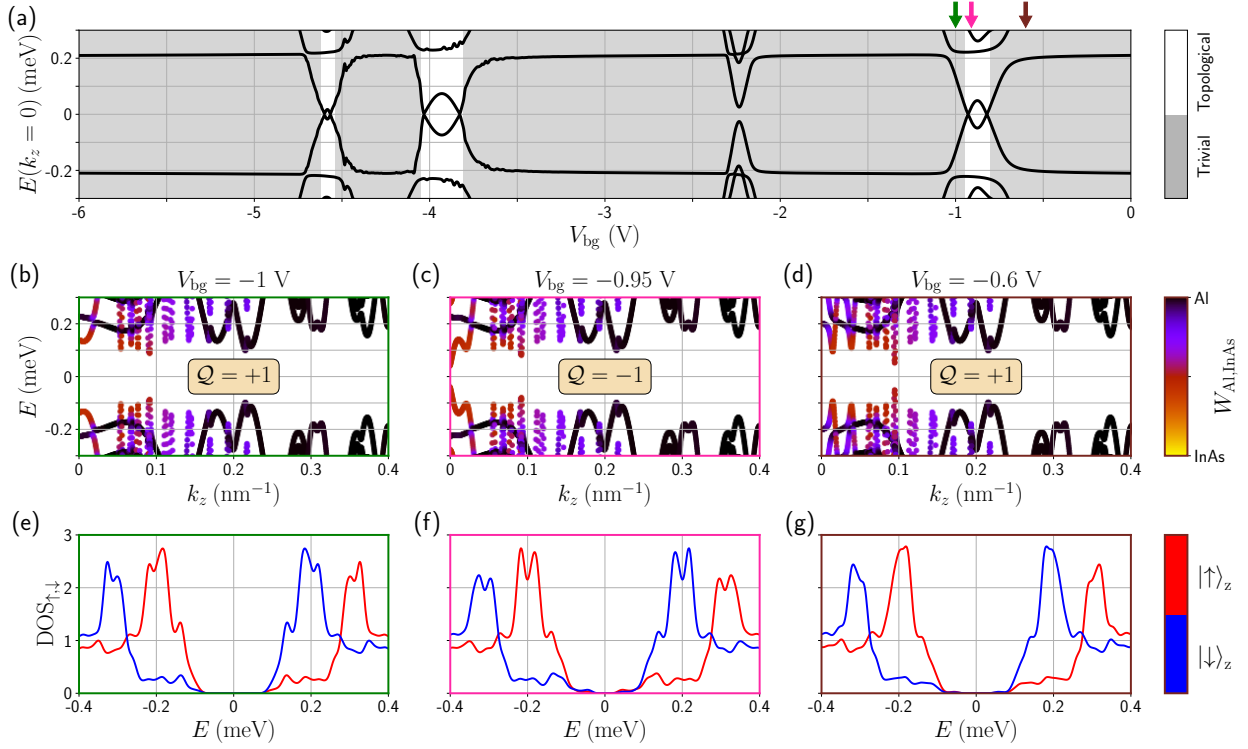
Figure 6.6: (a) Energy spectrum at $k_z = 0$ versus the back-gate voltage V_{bg} using the full model for the overlapping device. gray (white) color corresponds to a trivial (non-trivial) topological phase. This can be established by computing the topological invariant $\mathcal{Q}$, as explained in the text. (b-d) Band structure versus k_z for different gate voltages around the last topological region (see arrows): (b) before, (c) inside, and (d) after the topological region. With colored bars we show the weight of the eigenstate in the Al layer (black) and in the InAs wire (yellow). In (e-f) we show the spin-polarized DOS for the same back-gate voltages indicated with arrows in (a). We set $V_{sg}^{(L,R)} = 0$.
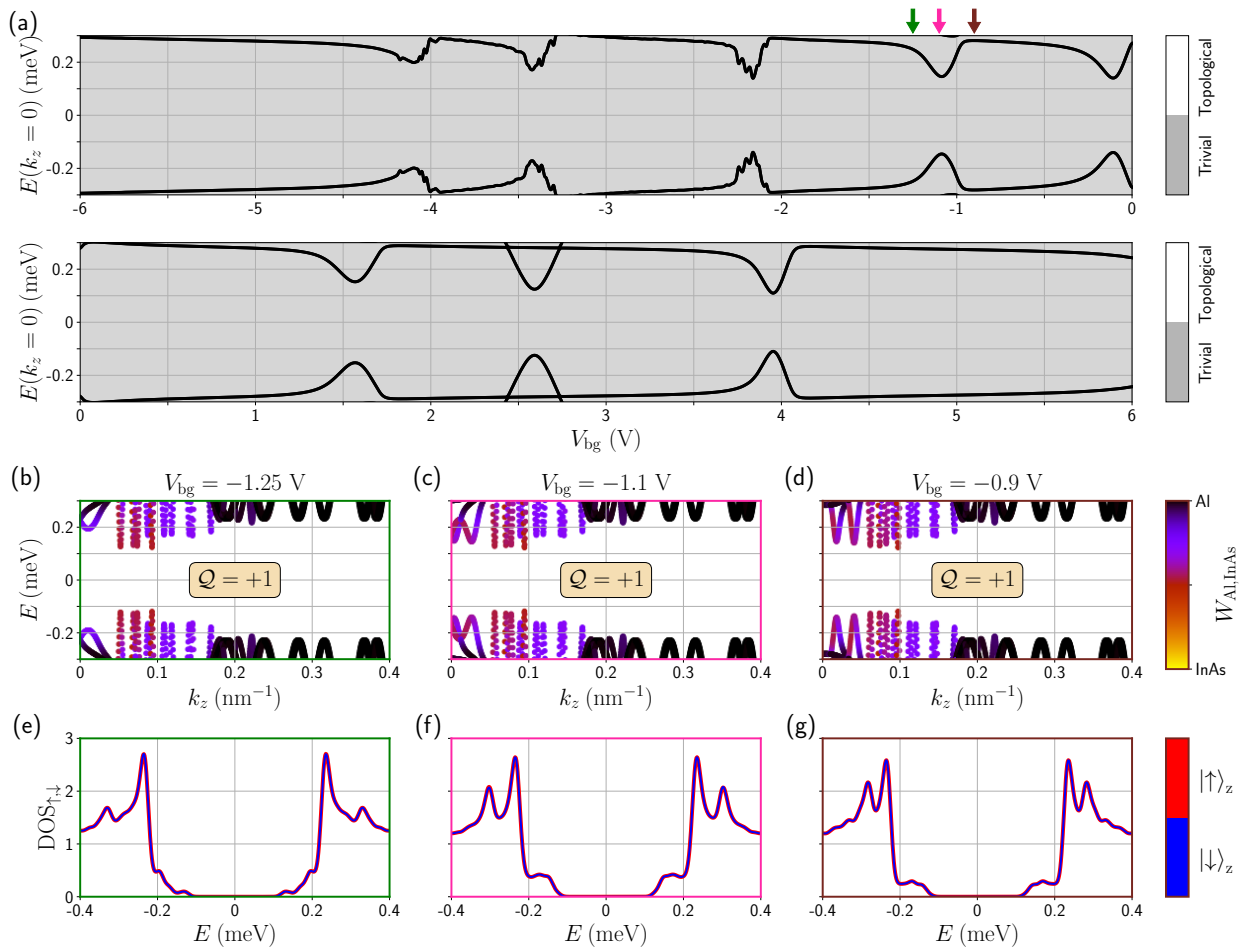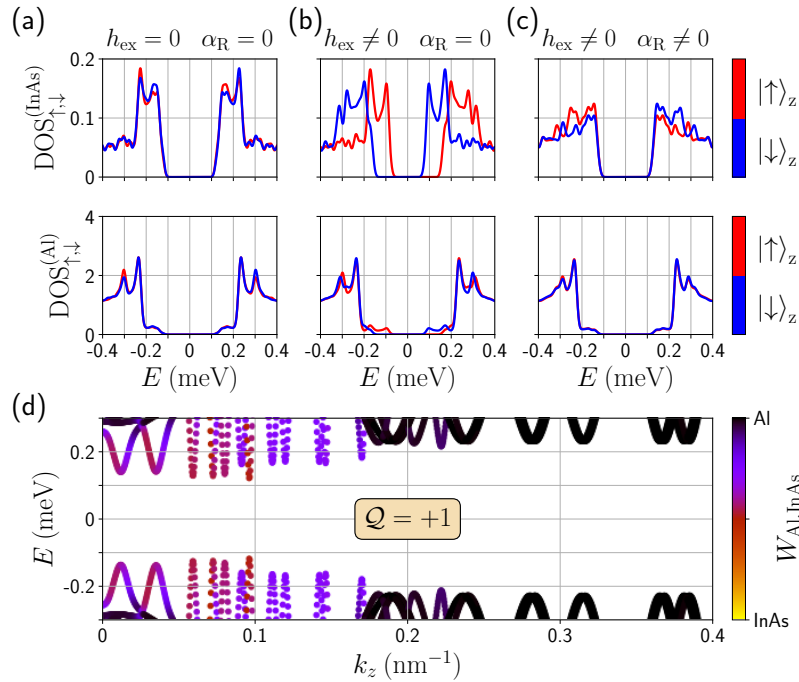
Figure 6.7: Same as in Fig. 6.6 but for the non-overlapping device.

Figure 6.8: Same as in Fig. 6.5 but for the non-overlapping device. The $\mathbb{Z}_2$ topological invariant in (d) is now $\mathcal{Q} = 1$, signaling a trivial phase.

simulations as in Fig. 6.5 but for the non-overlapping device and for an specific gate voltage (at $V_{\text{bg}} = -1.1$ V). In Fig. 6.8(a), we show the partial DOS integrated over the InAs and Al volume when the exchange field in the FI and the SO coupling in the SM are set to zero. This plot exhibits the same superconducting coherence peaks as in the overlapping device, pointing a good hybridization between the SM and the SC. When the magnetization in the FI is turned on, see Fig. 6.8(b), then a gap is still opened, as opposed to the overlapping device. On the one hand, the InAs does exhibit an induced magnetization since the DOS is spin-splitted [see top panel of Fig. 6.8(b)]. But it is twice smaller than in the overlapping device, and it is not enough to close the gap. This can be understood by looking at the charge density distributions discussed in Fig. 6.3(d). It shows that, for this configuration, the charge is mainly localized close to the SM-SC interface, far from the SM-FI one; diminishing the induced exchange field. On the other hand, the possible additional contribution coming form the Al is negligible, as the SC is barely magnetized [the DOS in the Al layer shown in the bottom panel in Fig. 6.8(b) is not spin-polarized]. This is precisely because the SC and FI are not in contact in the non-overlapping device, and thus, the hybridization between both materials is weak. Hence, the induced exchange field in the SM seems not to be large enough to close the induce gap, and to create a topological phase in turn in the non-overlapping device.

6.3.5 Simplified model and topological phase diagram

In the previous simulations, we fixed the exchange field inside the FI to $h_{ex} = 100$ meV. However, departures from our idealized full-model might reduce the value of the induced magnetic exchange. For instance, the mismatch between the minima of the InAs conduction band [at the Γ-point; see sketch in Fig. 3.1] and the EuS one [at the X-point; see sketch in Fig. 6.1(a)] could suppress their hybridization depending on material growth directions or other details, leading to a smaller h_{ex} value. In addition, different materials of the same family exhibit different exchange field values. So, in order to understand the robustness of our the previous findings for different exchange fields, we would need to compute the phase diagrams (vs exchange field and gate potential) for both devices. Nonetheless, this is not affordable with our full-model and computational resources, since the diagonalization of the Hamiltonian is a computationally demanding task because of the small grid spacing imposed by the large Fermi momentum of the Al layer.

We overcome this problem by using (again) a simplified model in which the SC, and now the FI too, are somehow integrated out. To this end, we consider the same Oreg-Lutchyn Hamiltonian but restricted only to the InAs wire. We include the proximity effects with both layers by including an effective pairing amplitude $\Delta^{(Al)}$ and an exchange field $h_{ex}^{(EuS)}$ of the same magnitude than the parent ones, on the cross-section regions closer to the Al and the EuS shells, respectively, as schematically depicted in Figs. 6.9(a) and (b). We also include a smaller exchange coupling $h_{ex}^{(Al)} = 0.06$ meV in the Al-proximitized region of the overlapping device. The extension of the corresponding regions are extracted by adjusting to the behavior of the full model results, as explain in Sec. 4.3 for the induced superconductivity and in Appendix D.1 for the exchange field.

In Fig. 6.9(c), we present the topological phase diagram of the overlapping device as a function of the back-gate voltage and the exchange field of the EuS (or an arbitrary FI). With colors, we show in the left panel of Fig. 6.9(c) the effective exchange coupling, $h_{eff} = \langle h_{ex}(\vec{r}) \rangle$, for the energy state closest to the Fermi energy. As we show in Appendix 4.4, each subband of the heterostructure can be effectively described through a 1D Oreg-Lutchyn Hamiltonian [Eq. (1.2)], and this effective parameter corresponds to the exchange field entering in this equation. Alongside with this, we show in the middle panel the minigap, $\Delta_{min} = |E(k_z = k_F)|$, for the energy state closest to the Fermi energy. In these plots, white means trivial (i.e., $\mathcal{Q} = 1$), while the colored regions correspond to the topological phase. There are several topological regions against V_{bg} corresponding to different transverse subbands. In those regions, the condition that h_{eff} is larger than the square root of the induced gap squared plus the chemical potential squared is fulfilled, as expected [20, 21] (see also Appendix 4.4 for further details). To the right in Fig. 6.9(c), we show the probability density of the transverse subband closer to the Fermi level at $k_z = 0$ across the wire section for the parameters indicated with arrows. In the three cases exhibited, the wavefunction concentrates both around the left-upper facet covered by Al, and the top facet where the Al and EuS layers overlap. This is consistent with the requirement of maximizing simultaneously the superconducting and magnetic proximity effects.

The phase diagram for the non-overlapping device is shown in Fig. 6.9(d). The extension of the
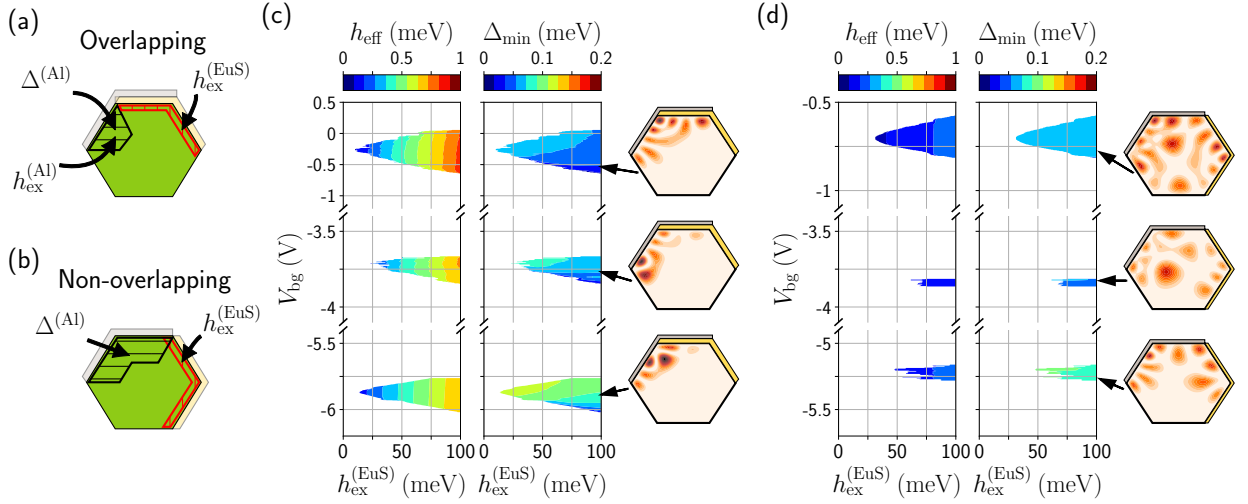
Figure 6.9: The Al and EuS layers are integrated out and their respective effective induced pairing amplitude and exchange field on the InAs wire are included within the streaked regions shown in the sketches of (a) the overlapping device and (b) the non-overlapping one. We take $\Delta^{(\mathrm{Al})} = 0.23$ meV and $h_{\mathrm{ex}}^{(\mathrm{Al})} = 0.06$ meV over a wide region of 45 nm near the Al interface. $h_{\mathrm{ex}}^{(\mathrm{Al})}$ is only present in (a) where the Al and the EuS are in contact. We include $h_{\mathrm{ex}}^{(\mathrm{EuS})}$ over a thin region of 1 nm close to the EuS layer. (c) Topological phase diagram of the overlapping device versus back-gate potential, V_{bg}, and exchange field at the EuS-InAs interface, $h_{\mathrm{ex}}^{(\mathrm{EuS})}$, for $V_{\mathrm{sg}}^{(\mathrm{L,R})} = 0$. In the topological regions, we show with colors the effective exchange field (left panel), the topological minigap (middle panel), and the wavefunction profile (right panel), all of them for the transverse subband closest to the Fermi energy. The parameters for which the wavefunctions are plotted are indicated with arrows. (d) Same as (c) but for the non-overlapping device and fixing $V_{\mathrm{sg}}^{(\mathrm{R})} = 2$ V and $V_{\mathrm{sg}}^{(\mathrm{L})} = 0$. The values of $V_{\mathrm{sg}}^{(\mathrm{L,R})}$ in (c) and (d) are taken to maximize the topological regions in each case. The extension of the topological phase is very much reduced with respect to (c) (almost negligible for some subbands) both in the V_{bg} and $h_{\mathrm{ex}}^{(\mathrm{EuS})}$ axes. Moreover, in the regions where it is present, the topological gap is small. In contrast, large topological regions with stronger minigaps are found for the overlapping device. The reason is twofold: (i) the wavefunction can be pushed simultaneously close to the Al and EuS layers due to the electrostatics of the overlapped shells, which increases the superconducting and magnetic proximity effects; (ii) the induced exchange field feeds both from the direct and indirect contributions in this case.
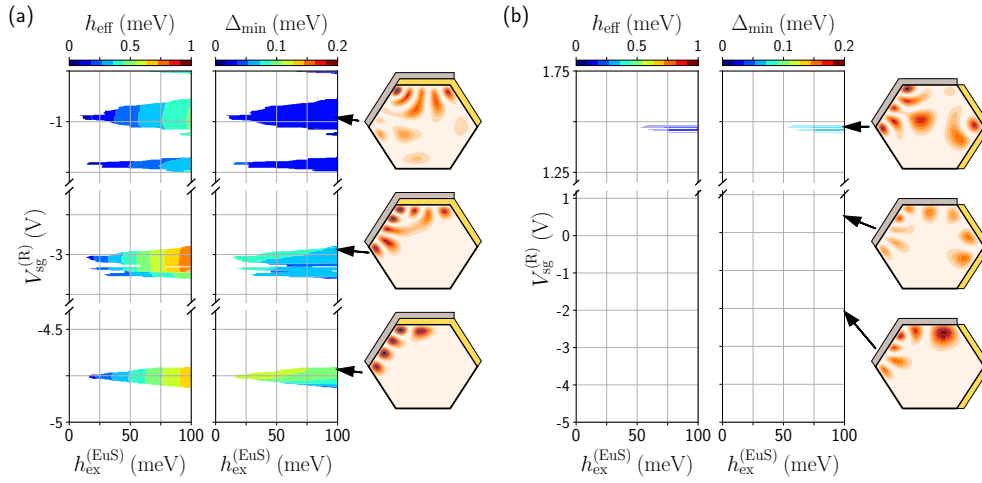
Figure 6.10: Same as in Fig. 6.9 but vs the right side-gate potential $V_{\text{sd}}^{(\text{R})}$ instead the back one.

topological phase is very much reduced, almost negligible for some subbands. It is interesting to observe that, for realistic gate potential values, the wavefunction needs to be very spread across the wire section in order to acquire the superconducting and magnetic correlations for the topological phase to develop. This in turn translates into narrow back-gate voltage ranges for which this is possible and small topological minigaps.

Notice that in both devices, as one increases the back-gate potential, not only the chemical potential inside the wire is tuned, but also the wavefunction is pushed towards the back-gate. This explains in turn why the minigap is reduced as one increases this gate: as the wavefunction is moved away from the SC and FI interfaces, it loses the proximity induced properties. In the same way, the side gates play a similar role, but they change the position of the wavefunction along the perpendicular axis (the x axis). Just by looking at the geometries of both devices (see Fig. 6.2) one can infer that if the side gates push the wavefunction towards the right part, the hybridization with the FI will be increased while the hybridization with the SC will be suppressed.

To show this fact and to prove that the systems exhibit similar features in their topological phase diagrams regardless of whether the back gate or the side gates are tuned, we compute the same topological phase diagram as in Fig. 6.9 but vs the right side-gate[5]. We show the results in Fig. 6.10(a) for the overlapping device, and in Fig. 6.10(b) for the non-overlapping one.

Let us discuss first the results for the overlapping device shown in Fig. 6.10(a). This geometry exhibits several topological regions that span across potential ranges of the order of 250 mV. Increasing the right-side gate voltage for a fixed $h_{\text{ex}}^{(\text{EuS})}$ (see left panel) keeps the effective exchange field almost constant, while it decreases the minigap (see right panel). This is precisely because the

---

[5]Note that, because right and left side gates are placed parallel to each other and symmetric with respect to the wire, they provide comparable phase diagrams.

lowest-energy wavefunction is being pushed towards the EuS layer, moving away from the Al layer (see charge density plots on the right).

In the non-overlapping device [see Fig. 6.10(b)], we observe that there is no topological phase for negative right-side gate potential values. However, there are some small topological regions for positive gate potentials. This happens because the wavefunction is located close to the EuS layer for these gate potentials (see charge density plots on the right), acquiring a non-negligible effective exchange field. But due to the large doping of the wire, these states have a large kinetic energy, what implies that they spread all across the wire. Hence, both quantities, the effective exchange field and the minigap, are small or even negligible for these states.

6.4 Planar-based devices

Notice that in the previous wire proposal, it is necessary, in general, to do fine-tuning from back and side-gates to push the SM electron wavefunction close to both the SC and FI layers. This gives rise to a diverse phase diagram in which the different subbands have very different topological minigap and extension (in parameter space), if they do develop a topological phase. This scenario is not experimentally advantageous, as the performance of the device will change considerably with gate voltages and among different devices.

This can be solved with a planar SM/FI/SC heterostructure like the one depicted in Fig. 6.11(a). In this setup, a thin FI layer is grown between the SC and the SM[6]. Due to the band alignment properties between materials, a charge accumulation layer appears at the SM/FI interface [177], hosting a 2DEG. In addition, the SC stripe on top of the FI layer defines a quasi-1D geometry beneath where superconductivity is induced.

Using specifically an InAs/EuS/Al heterostructure, we show that a robust topological phase appears when the FI thickness is between $\sim 1.5\,\mathrm{nm}$ and $\sim 3\,\mathrm{nm}$, equivalent to 2–5 EuS monolayers. It approximately corresponds to the wavefunction penetration length into the FI. When comparing this device with the hexagonal cross-section nanowire geometry, we find that our 2D proposal provides larger and more regular topological regions as the external gate is varied, which moreover display larger and harder gaps. This is associated with a stronger vertical confinement achieved in 2DEGs compared to hexagonal nanowires.

6.4.1 Model

We simulate the device shown in Fig. 6.11(a), where the FI layer is grown between the SC and the SM. Due to the band alignment properties between materials, see Fig. 6.11(b), a charge accumulation layer appears at the SM/FI interface [177], hosting a 2DEG. Notice that the role of the FI layer here is two-fold: to induce an exchange field in the 2DEG (direct induced exchange field) and the SC

---

[6]We note that, in principle, a planar SC/SM/FI heterostructure can also exhibit topological properties. However, we do not consider such an arrangement of materials because the growing conditions would lead to a highly disordered heterostructure.
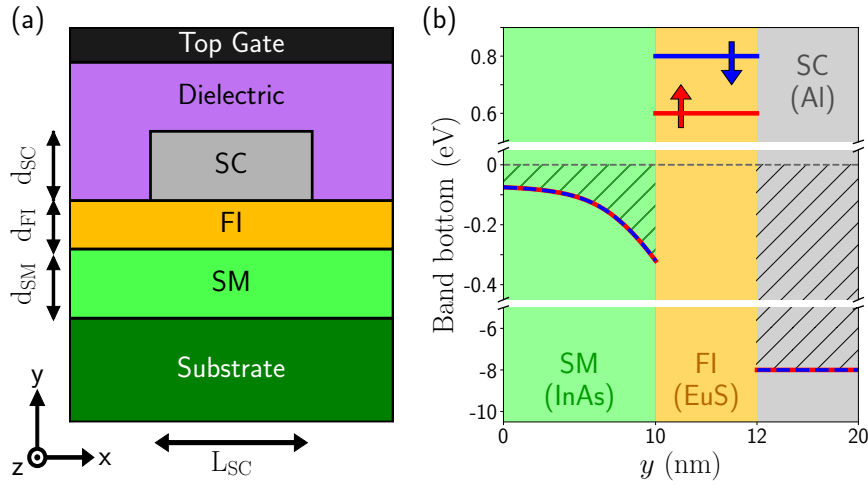
Figure 6.11: (a) Sketch of the device studied in this work: 2D semiconductor (SM)/ferromagnetic insulator (FI)/superconductor (SC) heterostructure stacked in the y direction and translationally invariant in the z direction. The substrate is insulating and typically composed of several stacked SM layers. The top gate can be used to confine the wavefunction below the grounded SC. The thickness of the ferromagnetic insulator layer d_{FI} is varied to optimize the topological properties. (b) Schematics of the conduction-band bottom along the heterostructure stacking direction for a specific choice of materials (InAs/EuS/Al) and representative geometrical parameters ($d_{SM} = 10$ nm, $d_{FI} = 2$ nm, $d_{SC} = 8$ nm and $L_{SC} = 100$ nm; these geometrical parameters are the ones that we use in this section). Red and blue colors represent different spin directions, and the gray dashed line depicts the Fermi level.

(indirect induced exchange field), and to act as a spin-polarized barrier for electrons. State-of-the-art 2DEG platforms are usually grown on top of rather thick substrates, making it hard to gate them from the bottom. For this reason, we include a top gate in our design, used to manipulate the wavefunction profile in the SM region and drive the system in and out of the topological phase. Since the SC screens the top-gate one can then define a quasi-1D system by means of an electrostatic lateral confinement. This is achieved by applying a negative potential to the top gate that depletes the 2DEG everywhere except underneath the grounded SC stripe. This allows to control the lateral extension (in the x direction) of the SM 1D channels. Moreover, the top gate allows for partial control of the local chemical potential in the effective wire. Our design is independent of the choice of the specific materials as long as they fulfill some requirements: the SM should feature a surface 2DEG, whereas the FI should have a moderate bandgap to allow electron tunneling, and a sufficiently large spin-splitting to induce the topological transition (but small enough not to suppress superconductivity in the SC).

We note that our setup could tolerate in principle an arbitrary misalignment of the exchange field in the z direction since this would still be perpendicular to the spin-orbit term. This is an advantage with respect to schemes relying on magnetic fields, where relatively small perpendicular magnetic fields to the SC layer suppress superconductivity due to orbital effects.
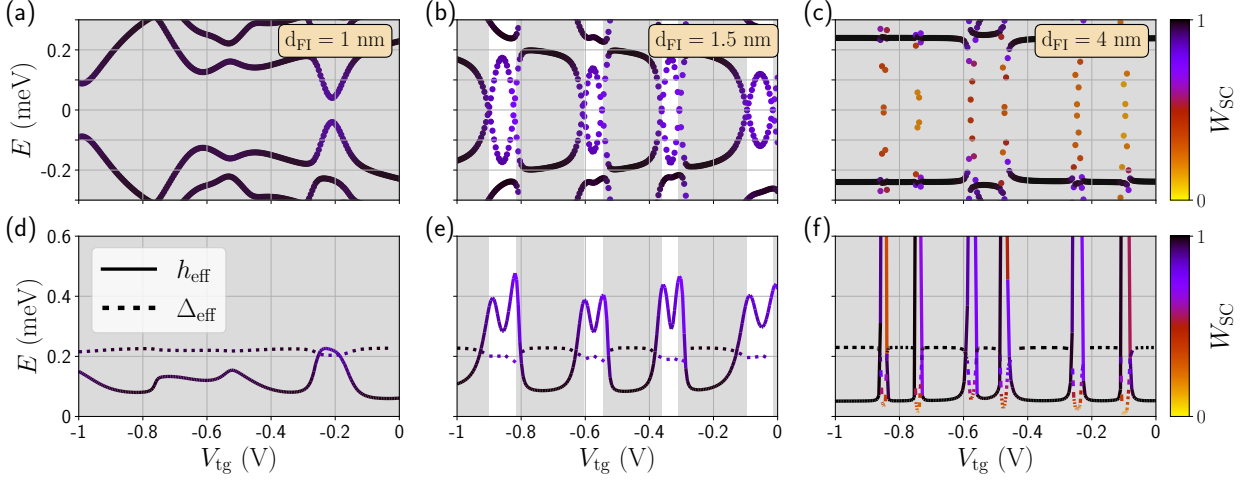
Figure 6.12: Top row: energy spectrum at $k_z = 0$ as a function of the top-gate voltage V_{tg} for a FI thickness of (a) $d_{FI} = 1$ nm, (b) $d_{FI} = 1.5$ nm and (c) $d_{FI} = 4$ nm. colors represent the weight W_{SC} of each state in the SC Al layer. Shaded V_{tg} regions are those characterized by a trivial phase, i.e., $\mathcal{Q} = +1$; while white regions correspond to a topological phase, $\mathcal{Q} = -1$. Bottom row (d,e,f): effective exchange coupling h_{eff} (solid lines) and superconducting pairing amplitude Δ_{eff} (dotted lines) for the lowest-energy state in (a), (b), (c), respectively.

6.4.2 Results

The low-energy wavefunctions decay exponentially in the FI layer on a length scale approximately given by $\xi_{FI} = \sqrt{2E_{F,FI} m_{FI}^* / \hbar^2}$, where $E_{F,FI}$ is the conduction band minimum in the FI with respect to the Fermi level. For our materials choice $\xi_{FI} \approx 2.3$ nm. As a consequence, the thickness of the FI layer determines the tunneling amplitude between the 2DEG and the SC: thicker FI layers decouple the 2DEG from the SC resulting in a reduction of the superconducting proximity effect, while thinner ones exhibit a reduced induced magnetization in the 2DEG. Hence, there is an optimal barrier thickness that allows for a sufficiently large induced exchange field and pairing potential in the 2DEG to drive the system into the topological regime.

The topological phase transition of the system occurs at a gap closing and reopening when the lowest energy subband crosses zero energy at the $k_z = 0$ high symmetry point, as explained in Chapter 1. For this reason, in Fig. 6.12 we show the energy spectrum of the system at $k_z = 0$ as a function of the top-gate voltage for three different values of the FI thickness, $d_{FI} = [1, 1.5, 4]$ nm (in Appendix D.2 we show the same figure for seven different d_{FI} values ranging from 1 to 4 nm). The white (gray) background denotes the topological (trivial) phase, determined by the corresponding topological invariant.

Left panels in Fig. 6.12 show the regime where the FI is too thin to induce a topological phase transition. The energy spectrum shows low-energy bands localized mainly in the SC, represented by the black color in Fig. 6.12(a). In this case, superconductivity dominates the properties of the low-energy modes. In Fig. 6.12(d), we show the effective superconducting pairing amplitude (dotted
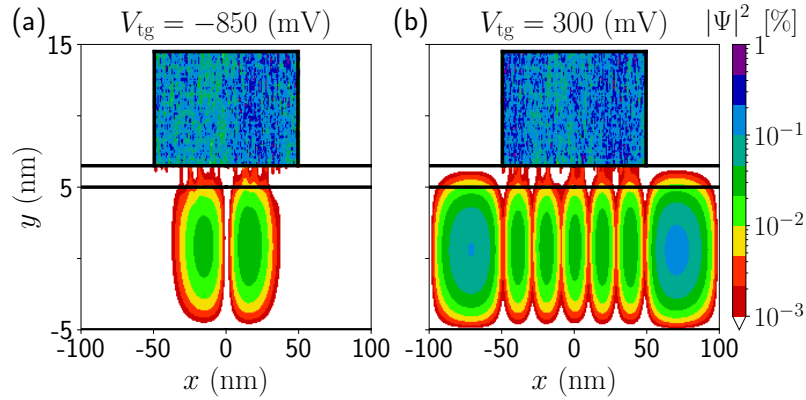
Figure 6.13: (a) Transverse probability density at $k_z = 0$ for the lowest-energy state in a topological regime ($V_{\text{tg}} = -850$ mV). For comparison, we also show in (b) the case in a topologically trivial regime ($V_{\text{tg}} = 300$ mV). Parameters are the same as in Fig. 6.12, corresponding to $d_{\text{FI}} = 1.5$ nm.

line) and exchange coupling (solid line). As explained before (see Appendix A for more details), each subband can be effectively described by the 1D Oreg-Lutchyn Hamiltonian [Eq. (1.2)]. And the effective parameters that describe each subband (and enters into the effective 1D Hamiltonian) can be obtained from the full calculations by performing the expectation values as justified in Appendix A. For this thickness, we observe that h_{eff} is mostly below Δ_{eff}, consistent with the system being in the trivial regime as the topological condition $|h_{\text{eff}}| \gtrsim \sqrt{\Delta_{\text{eff}}^2 + \mu_{\text{eff}}^2}$ cannot be fulfilled.

The situation becomes more favorable for FI layers of intermediate thickness, middle panels in Fig. 6.12. As a function of V_{tg}, the system shows several topological transitions when consecutive subbands cross zero energy. The topological regions are characterized by a non-trivial topological invariant and are marked by a white background in Figs. 6.12(b) and (e). In these regions, the lowest-energy wavefunction has a significant weight in both the SC and the SM, as illustrated by the purple line color. The topological transition is associated with an increase of h_{eff}, overcoming the value of Δ_{eff}, see Fig. 6.12(e), and roughly fulfilling the single-band topological criterion. The small deviations (between the criterion ant the topological invariant) are due to the approximated character of the effective parameters. We note that, for the optimal range of d_{FI}, every subband can be tuned to the topological regime as V_{tg} is varied, in contrast to the hexagonal wire case where some subbands do not show a topological crossing. This is due to the effective hard-wall confinement of the wavefunction in the thin SM layer in the y direction [see wavefunction profiles in Fig. 6.13(a)], which keeps the wavefunction close to the FI/SC layers for every subband. As a consequence, the device shows a regular alternation of trivial and topological regions against V_{tg} with comparable minigaps. The topological regions thus occupy a larger area in parameters space compared to the hexagonal wire case (see Appendix D.2 for the wire vs planar devices comparison), where the appearance of the topological regions is more erratic, since the wavefunction can spread throughout the wide hexagonal section, sometimes avoiding a good proximity effect with the SC/FI layers.
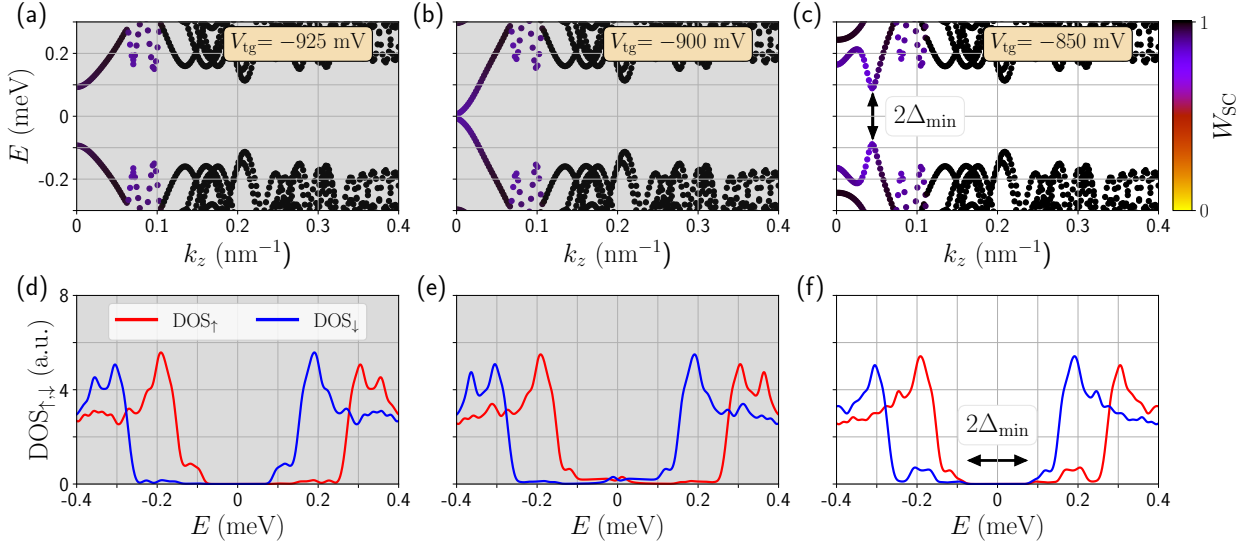
Figure 6.14: Dispersion relation for a device with EuS layer thickness $d_{\text{FI}} = 1.5$ nm, and for (a) $V_{\text{tg}} = -925$ mV (before the topological transition), (b) $V_{\text{tg}} = -900$ mV (at the topological transition), and (c) $V_{\text{tg}} = -850$ V (in the middle of the topological phase). In (d-f) we show the spin-resolved integrated DOS of the corresponding plot on the top. Only the (c,f) case is topological, with Δ_{min} being the topological minigap, i.e., the lowest-state energy at $k_z = k_{\text{F}}$.

The situation of a too-thick FI barrier is illustrated in the right panels of Fig. 6.12. A thick barrier hinders tunneling through the FI, preventing the hybridization of SC and 2DEG states. The reduced hybridization between the two materials can be seen from the shape of the spectrum in Fig. 6.12(c), where the system shows an almost horizontal black line at the SC gap ($E \sim 0.23\,\text{meV}$) and a series of almost vertical lines (orange dots) crossing the gap. This also manifests in the abrupt transitions of effective parameters in Fig. 6.12(f). When $\Delta_{\text{eff}} > h_{\text{eff}}$ the ground-state wavefunction is localized mostly in the SC and it is essentially independent of the gate voltage, whereas when $\Delta_{\text{eff}} < h_{\text{eff}}$ it is localized mostly in the SM. We note that the regions with a large effective exchange field also exhibit a suppressed superconducting pairing, consistent with normal gapless states in the SM.

The properties of a topological superconductor are highly dependent on the value and quality of the topological minigap, which we examine now. In Fig. 6.14, we consider a device with $d_{\text{FI}} = 1.5$ nm as we sweep V_{tg}. We show the energy subbands versus momentum k_z and the spin-resolved density of states (DOS) in three representative situations: before (left column), at (middle column), and after (right column) the topological transition. Before the transition, Fig. 6.14(a), the heterostructure features a trivial gap and the above-gap states are mostly localized in the SC (black color curves). The DOS displays a hard gap around zero energy and the characteristic spin-split superconducting coherence peaks, see red and blue curves in Fig. 6.14(d). From this plot we infer that the induced exchange field in the SC is around $100\,\mu\text{eV}$ ($\sim 50\%$ of the Al gap), consistent with the value found in experiments [255–257]. A similar peak splitting is found in Figs. 6.14(e,f), i.e., it is independent of the value of the gate potential.

At the topological transition, one subband crosses zero energy at $k_z = 0$, Fig. 6.14(b). It results in a finite DOS inside the superconducting gap, see Fig. 6.14(e). As we increase V_{tg}, the superconducting gap reopens in the topological phase, Fig. 6.14(c), accompanied by the onset of Majorana bound states at the ends of a finite-length quasi-1D wire defined by the SC stripe (not shown). The hard gap found in Fig. 6.14(f), Δ_{min}, has a typical value of tens to a hundred µeV. We associate the large topological gaps found in these devices with the electrostatic confinement in the vertical direction. The thin SM layer, together with the top gate tuned to negative values, makes it possible to concentrate the weight of the wavefunction in the region where superconductivity, magnetism, and spin-orbit coupling coexist. This is signaled by the purple color of the lowest-energy subband in Fig. 6.14(c). As discussed in Appendix D.2, this is not the case of wire-based devices, that exhibit softer gaps as a result of the larger delocalization of the wavefunction across the cross section of the wire.

The importance of the wavefunction localization is illustrated in Fig. 6.13, which shows the lowest-energy wavefunction probability density across the device. In the topological regime, Fig. 6.13(a), the ground state wavefunction is concentrated below the SC, maximizing the proximity effects of the SC and FI layers on top. The vertical confinement (in the y direction) is determined by the SM width, d_{SM}, and the fact that there is an insulating substrate below. The lateral confinement (in the x direction) is achieved by a negative top-gate voltage that depletes the SM everywhere except below the SC. We note that the SM wavefunction penetrates the FI layer all the way to the SC due to its moderate gap and thickness. In the trivial regime shown in Fig. 6.13(b), the wavefunction spreads laterally through all the device cross section (due to a V_{tg} value comparable to or larger than the band bending at the SM/FI interface), reducing the proximity effects.

Finally, we vary the FI thickness to extract the optimal range for topological superconductivity, Fig. 6.15. The effective exchange coupling is shown in Fig. 6.15(a) and the effective superconducting pairing in Fig. 6.15(b). The transverse modes considered (depicted with different colors) are the first four lowest-energy subbands that get populated starting from a depleted SM as we increase V_{tg}. For each calculated point, we tune V_{tg} to the value where the subband is closer to the Fermi level ($E = 0$), where h_{eff} is maximum, see Fig. 6.12(e,f). Therefore, each point corresponds to a different V_{tg} value. We observe that in general h_{eff} increases with d_{FI} because of the growing weight of the wavefunction inside the FI. In contrast, the effective superconducting pairing decreases with the FI thickness as the weight of the wavefunction in the SC diminishes.

The topological minigap is shown in Fig. 6.15(c). It is calculated for the value of V_{tg} that maximizes E_{min} for each subband, i.e., well within the topological region. Depending on the transverse mode, its value ranges from tens to a hundred µeV. Note that we have used the bulk SC gap for the Al layer, $\Delta_0 = 230\,\text{µeV}$. Nevertheless, SCs with larger gaps such as Pb, Nb, Ta, V, or Sn, which can also be grown epitaxially over InAs [210–213], could help to increase the topological minigap. Interestingly, for the small SM thickness considered here (10 nm), E_{min} is essentially constant with d_{FI} for every transverse mode. This is again a consequence of the vertical confinement that tends to produce regular topological patterns. This regularity gets lost as the SM layer is made thicker, as
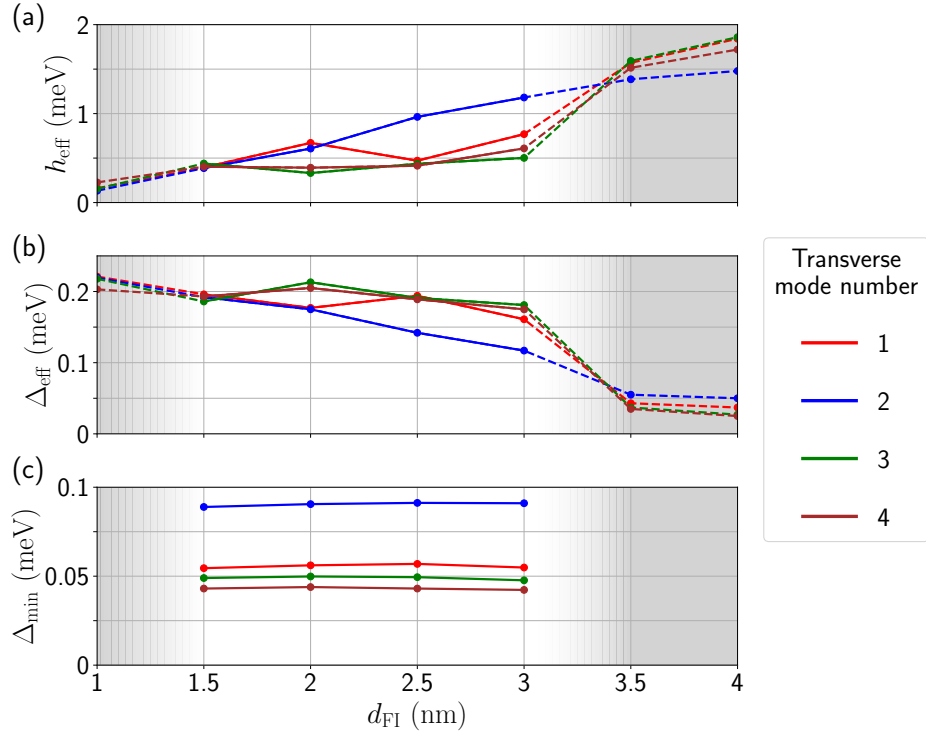
Figure 6.15: (a) Effective ferromagnetic exchange coupling h_{eff}, (b) effective superconducting pairing amplitude Δ_{eff}, and (c) topological minigap $\Delta_{\text{min}} = |E(k_z = k_F)|$ for the first four occupied transverse subbands (in different colors) versus the EuS thickness d_{FI}. We extract these effective parameters when the subband is close to the Fermi level ($E = 0$), and therefore different points necessarily correspond to different V_{tg} values. Shaded regions and dashed lines represent that the system is characterized by a topologically trivial phase (and therefore there is no minigap). The suitable FI thickness d_{FI} for topological superconductivity in the 2D stacking device proposed in this work ranges from $\sim$1.5 to $\sim$3 nm.

we show in Ref. [241]. There, we also investigate the role of the SC thickness, finding similar results for thicknesses between $4\,\text{nm}$ and $12\,\text{nm}$. For a SC with surface disorder, as the one considered here, the induced gap remains essentially unchanged and the main effect of the SC thickness is the renormalization of the SM chemical potential, shifting the picture described in Fig. 6.12(b,e) to lower/higher V_{tg} values. Thus, the main properties of the topological phase, i.e., regularity, extension, and robustness, do not significantly change, just the value of the top-gate voltage one needs to apply to populate the different subbands.

6.5 Conclusions

From calculations of the DOS, band structure, topological invariant and the phase diagram, we conclude that the hybrid InAs/Al/EuS nanowires studied in this chapter can exhibit topological superconductivity under certain geometrical and gating conditions. For a topological phase to exist, the electron wavefunction must acquire both superconducting and magnetic correlations such that the induced exchange field exceeds the induced pairing. Since the proximity effects occur only in wire cross-section regions close to the Al and EuS layers, the wavefunction needs to be pushed simultaneously close to both materials by means of nearby gates.

Our numerical simulations demonstrate that this is electrostatically favorable in device geometries where the Al and EuS shells overlap over some wire facet. This configuration is further advantageous in that, apart from a direct magnetization from the EuS layer in contact to the wire, there is an indirect one through the Al layer, which favors reaching the topological condition.

We have studied several proposals based on wires and planar heterostructures along this chapter. We find that the devices with the best performance are those based on planar heterostructures. More particularly, we find that the stacking SM-FI-SC geometry, where the thin FI acts as a spin-filter barrier for electrons tunneling through, provides a regular phase diagram with robust and sizable minigaps. For illustration, we have considered an experimentally tested material combination: InAs (SM), EuS (FI), and Al (SC) [127]. We have found topological regions for FI thicknesses between 1.5 and $3\,\text{nm}$. Outside this range, the FI is either too thick to allow tunneling between the SC and the SM, or too thin to have a significant influence on the SM electrons. The topological phase features a hard superconducting gap in a range between tens to a $100\,\mu\text{eV}$.

This constitutes a significant improvement with respect to previous hexagonal nanowire geometries [127, 177, 209], where these gaps were only possible by fine-tuning side gates to push the wavefunction sufficiently close to the FI/SC layers. We have compared also our results for the proposed 2D planar heterostructure with a similar stacking in hexagonal nanowires in Ref. [241]. The hexagonal nanowire can also be tuned to the topological regime using an electrostatic gate. However, the topological phase appears for reduced and irregular gate-voltage ranges compared to the planar structure. In addition, the topological gap in hexagonal nanowires is typically soft, exhibiting low-energy trivial states. These states are prone to creating quasiparticle excitations poisoning, undermining coherence in the device and being an obstacle to topological superconductivity.

We associate this behavior to the vertical confinement of the wavefunction for thin SM layers. Most importantly, this vertical confinement also helps to create a rather regular phase diagram, with topological and trivial phases appearing at controlled values of the top-gate potential. The topological regions produced by the subsequent inverted subbands have moreover a similar V_{tg}-range and comparable topological minigaps. This is an experimentally advantageous property since it permits to search for the topological phase in a predictable manner rather than by randomly scanning parameters, as it is typically the case with hexagonal nanowires.

Our proposed stacking allows to define and control complex wire networks of topological superconductors. The presented planar structure requires no magnetic field to reach the topological phase, allowing for different orientations of the effective wires. This opens the door to experimentally access a new set of problems, including multi-terminal junctions for braiding experiments and unconventional Josephson junctions.

Concerning the experimental detection of Majorana states in this system, the stacking platform offers the possibility to perform local tunneling spectroscopy to detect the presence of low-energy states bound to the wire's end. Examples of such experiments in a planar geometry (in the absence of the FI) can be found in Refs. [59, 262]. Moreover, several experiments devices [89, 90] have recently shown that correlations between two or more local probes along the quasi-1D wire and non-local transport spectroscopy can be realized in these planar devices (without the FI layer). We thus believe that they can be also performed in our SM-FI-SC stacking device as well. Another common tool to try to detect the presence of Majoranas is the anomalous behavior of the Josephson effect. Actually, phase-dependent zero-bias conductance peaks measured by tunneling spectroscopy at the end of Josephson junctions, as well as phase-dependent critical currents, have been studied recently in planar SM-SC heterostructures [61, 263, 264] (again, in the absence of the FI but with applied magnetic field).

CHAPTER 7

CONCLUSIONS AND OUTLOOK

Throughout this thesis, we have made progress towards an accurate and realistic theoretical description of hybrid heterostructures. We have derived analytical expressions for the Hamiltonians that describe the different materials of the heterostructure, the SM wire (or 2DEG), and the SC and FI layers, as well as their band alignments. Moreover, we have included the effect of the electrostatic interactions in our model and simulated several experimental setups. Our model provides a single-band description for the hybrid system that successfully predicts some experimental features.

As compared to more microscopic models, like the 8B k·p model or *ab initio* calculations, our description presents an advantageous reduced computational cost since only one band (the CB) is involved. However, the tiny Fermi wavelength that SCs typically exhibit imposes a small discretization of the tight-binding Hamiltonians employed to describe them (because the grid must accommodate the wavefunction oscillations along the heterostructure). This makes the simulations challenging and, thus, we have looked for an efficient numerical implementation to the solutions of the SP equation. Our method is published as an open-source package called `Majorana Nanowires: Quantum Simulation Package` [133]. With this package, it is only possible to (efficiently) access to the low-energy spectrum of the heterostructures. Despite of that, we show in this thesis that one can obtain from these states the effective parameters of the heterostructure, and more remarkably, the topological invariant. However, our numerical methods are limited to bulk systems, i.e., we have restricted our simulations to the 2D cross section of the hybrid wires (and 2DEGs) assuming that they are translationally invariant along the perpendicular direction. Finite 3D simulations are computationally demanding and out of the reach of the majority of computer clusters.

In Chapter 3, we have derived a single-band Hamiltonian from an 8B model that can reproduce the conduction band (CB) of III-V compound SM nanowires in the presence of an electrostatic potential. We have found that the equation that describes the Rashba SO coupling in its simplest approximation (widely used in the literature) does not accurately capture the SO coupling of nanowires due to their finite cross section. To overcome this problem, we have proposed a heuristic equation that retains the simplicity of the lowest-order approximation, but that provides an excellent approximation to the SO coupling calculated with the (more sophisticated) 8B model. We have modeled several experimental setups based on III-V compound SM nanowires (such as InAs, InSb, GaAs and GaSb) and we have compared the values our model provides for the SO coupling with the experimental ones. We find a remarkable agreement, indicating that our model can predict the

realistic values of the SO coupling in nanostructures. This is important as the SO coupling strength influences the robustness of a possible topological phase (in SM-SC and SM-FI-SC heterostructures). Particularly, we have found that the SO coupling ranges from 5 to $20 \, \text{meV} \cdot \text{nm}$ for the typical experimental devices and parameters, large enough to support a sizable topological phase[1]. The precise value depends on several factors, such as the specific device geometry and the gate potentials, as the SO coupling depends on the electrostatic potential and, remarkably, on the wire thickness. We have discovered that for diameters around $100–150 \, \text{nm}$ the SO coupling of zinc-blende wires is maximized, being ~ 1.2 times larger than for wires either half thinner or twice thicker (for the same electric field). Actually, we have shown that for typical wire diameters in experiments ($50–150 \, \text{nm}$), the SO coupling for zinc-blende crystals in nanowires is ~ 1.8 times larger than for bulk systems due to cross-section confinement effects. Strikingly, this phenomenon seems to be the opposite in wurtzite crystals: confinement effects are detrimental in this case and the SO coupling is roughly halved for the same wire diameters.

Additionally, we have examined the effect of the strain in the wire. This mechanism has been overlooked in previous attempts to give a microscopic description of the wire. We have discovered that the strain renormalizes the SM gaps and interband couplings. This in turn leads to changes in the parameters that describe the CB of the SM wire; namely, the chemical potential, the effective mass and the SO coupling. In this thesis, we have focused on the effect on the SO coupling, finding that a compressive strain (i.e., a shrinkage of the lattice cell) enhances the SO coupling. We have analyzed the specific case of an InAs-InP core-shell nanowire that presents strain between both materials as a result of the lattice mismatch. We have found that the (compressive) strain enhances by a factor of more than 10 the SO coupling at the wire surface in comparison to the wire's core. This in turn increases the total effective SO coupling of the InAs-InP wire by a factor of 3.

There are several aspects that have not been addressed in this part of the thesis and that could be explored in the future. On the one hand, we believe that the same kind of strain analyzed in core-shell nanowires could be present at the SM-SC interface in InAs-Al nanowires. If this is true, it could also be beneficial for the topological protection of the MBSs. We nevertheless highlight that a deeper study is needed in this respect. On the other hand, the fact that the strain changes the chemical potential of the wire at the interface could explain some unexpected experimental features in hybrid nanowires. Notice that Al grows in nucleation islands along the InAs facets [80], that grow until they connect and give rise to the homogeneous coating. Although they grow expitaxially, different islands could have different crystallographic orientations. These are characterized by different lattice constant and, therefore, they can produce different a disordered strain pattern at the interface. As a result, the chemical potential may vary along the wire even if the covering is homogeneous. This in turn could generate localized states or could be detrimental for the topological phase.

---

[1]We mean by "sizable topological phase" that the minigap is large enough so that current experimental techniques can resolve it. More particularly, spectroscopic measurements at $25 \, \text{mK}$ can perfectly resolve $\sim 50 \, \mu\text{eV}$ gaps with zero-bias peaks inside them.

In addition to this, we have not included the effect of a magnetic field in our theoretical derivation of the SM bands. Several works have followed the same approach to derive a CB Hamiltonian but in the presence of an external magnetic field in bulk systems [159, 172]. They find that the magnetic field gives rise to a Zeeman splitting that is proportional to the external magnetic field through the g-factor. Although not included in this manuscript, we have found that this g-factor is also affected by confinement effects in nanowires [265] as well as strain, so that the typical bulk values found in the literature (e.g., $g_{\mathrm{InAs}} = 14.9$ or $g_{\mathrm{InSb}} = 51$) are different for nanowires and hybrid heterostructures. However, we have not included this study here as we wanted to focus on the description of SM-FI-SC heterostructures, where the g-factor is irrelevant.

In Chapter 4, we have analyzed the properties of SM-SC nanowires, focusing on InAs-Al materials for concreteness. We have used a effective model Hamiltonian that can describe the heterostructure treating on an equal footing the SM wire and the SC layer, and studied how superconducting properties are induced on the SM wire. We have shown that the proximity effect depends strongly on the gate potential since the electrostatic potential profile determines the wavefunction position inside the wire. We find that, in order to have a good proximity effect, the wavefunction inside the wire needs to be localized close to the SC shell. We show that this is actually the favorable situation as in realistic devices there is a charge accumulation at the interface due to the ohmic SM conduction band-bending at the SM-SC interface resulting from the InAs-Al work-function difference. In any case, this can also be achieved by depleting the wire from the opposite facet by means of an external electrostatic potential (created, e.g., with a potential gate). We actually find that the SM wire undergoes a sharp transition from having a strong proximity-induced superconducting gap to a soft and suppressed gap when the electrostatic potential at the bottom of the wire (roughly) equals the band-bending. We thus believe that the value of the SM band bending, which is in principle unknown in nanowires, could be accessed simply by performing conventional transport measurements as a function of the back-gate voltage.

In future works, we intend to study the effect of the SC on the SO coupling of the wire. Notice that, apart from inducing superconducting correlations in the SM wire, the SC also induces a metalization that it is detrimental for the SM SO coupling because the Al metal lacks of it. This phenomenon, although included in our simulations, is not explicitly discussed in this manuscript. This could be analyzed together with the strain effects at the SM-SC interface. Besides, a new generation of hybrid SM-SC nanowires are being fabricated with different SC materials such as Pb, Nb, Ta, V or Sn [210–213]. These materials may exhibit different properties as compared to Al, the SC that we use in our simulations, that could be beneficial or detrimental for the topological phase.

The development of devices that could support topological superconductivity should be accompanied with the design of measurement protocols that could unequivocally identify this phase. We have proposed in Chapter 5 a device that allows to perform local transport spectroscopy along the wire, in such a way that one could probe the MBS wavefunction localization at the ends of the wire. We have explored three setups in which the hybrid nanowire is embedded in a superlattice structure in different ways. One option is to deposit the SM wire onto an array of SC fingers (a superlattice).

This would allow to perform STM measurements at the top facet of the wire by driving a current between the STM tip and each finger through the SM. Another option is to grow epitaxially an array of SC fingers on top of the wire. One could use the fingers themselves to perform spectroscopic transport measurements between them and obtain information about the wavefunction probability density. Notice that both designs share the same disadvantage: the SC covering is not homogeneous along the wire. As a result, the induced superconductivity is proportionally reduced with the SC coverage. Moreover, since the SC fingers screen the electrostatic potential created by the gates, the chemical potential induced by the gates is not homogeneous. We have found that, depending on the (intrinsic) doping of the wire, the inhomogeneous gating is prone to the creation of QD states and/or just detrimental for the creation of a topological phase. We have identified the geometrical parameters (size of the fingers and distance between them) that provide the most robust and extended topological phases. Specifically, experimentally-feasible 30 nm–wide SC fingers separated by also 30 nm provide a measurable topological gap of $\sim 100\,\mu eV$ without the presence of topologically trivial states. Larger widths or separations make these trivial states to emerge, while smaller widths result in smaller topological gaps.

We have also analyzed the spatial profile of the MBSs in this system and compared it with the homogeneous covering case. The MBSs in the superlattice device have additional oscillations due to the superlattice periodicity and, as a consequence of the reduced covering, they have a larger decay length (smaller minigap) than the homogeneous device. Unfortunately, this could hinder their detection. To overcome this problem, we have proposed a third setup in which the partial-shell nanowire is still homogeneously covered by the SC, but it is deposited on top of an array of *normal* metallic fingers. If the top facet of the wire is uncovered, i.e., the capped facets are on one side of the wire, then STM measurements are still possible. The advantage of this system is that the SC covering is homogeneous and, thus, the minigap is comparable to a conventional partial-shell nanowire (100–200 μeV). We believe that this setup is promising for detecting the exponential decay of MBSs in nanowires. Actually, several experiments are currently being performed in a similar setup. They are based on effective wires in planar SM 2DEGs instead of nanowires, where an array of probes is built on top of the device. With this disposition, they can perform tunneling spectroscopy at different points of the wire. We believe our results may be useful to interpret their experimental findings.

Finally, in Chapter 6, we have analyzed a proposal to develop topological superconductivity in hybrid heterostructures without the need of applying a magnetic field. The idea is to cover a SM-SC heterostructure with an additional layer of a ferromagnetic insulator (FI) that induces, also by proximity effect, a Zeeman field inside the wire. We have performed numerical simulations based specifically on InAs-Al-EuS tripartite systems. We have shown that the wavefunction inside the SM needs to be pushed simultaneously close to the SC and the FI layers, in order to acquire both proximity effects and achieve the topological phase. This can be done using back and lateral gates, so that one can control, in a more precise manner, the electrostatic profile inside the wire. We have also found that a configuration in which the SC and the FI layers overlap is beneficial. This is because a Zeeman field of 0.07 meV is induced from the EuS layer into the Al one when they are

in contact. And this is in turn induced into the InAs nanowire through the SM-SC interface. For realistic devices, we have obtained topological minigaps ranging from 25 to 100 μeV for overlapping devices, in agreement with experimental measurements [127], and large enough to support a sizable topological phase. On the other hand, minigaps for non-overlapping devices are hardly measurable as they range from 0 to 25 μeV.

This proposal requires in general fine tuning of two potential gates to develop a sizable topological phase. To avoid this inconvenience, we have proposed a different setup based on a planar stacking geometry. The idea is to use a 2DEG inside a SM heterostructure instead of a nanowire, which is further advantageous as 2DEGs exhibit longer mean-free paths. The 2DEG is embedded in a planar SM stacking geometry in which the top surface is covered by a thin FI layer. On top of the FI, a SC stripe is further grown. If the system is gated (depleted) from the top, then a quasi-1D channel is created beneath the SC by means of electrostatic confinement. We use again InAs-Al-EuS heterostructures, as these are the materials explored experimentally at the moment. We show that this system can support topological superconductivity if the FI is thin enough to allow electrons for tunnel between the SM and the SC. On the other hand, the FI acts moreover as a spin-polarized tunneling barrier that induces spin-polarization in the SM when the electrons pass through. Hence, the FI needs to be thick enough to induce a strong Zeeman field and drive the system into the topological phase. We have identified that the suitable thickness for the EuS in InAs-EuS-Al heterostructures is $1.5 - 3$ nm. In this range, the penetration length of the electrons inside the FI is comparable to the thickness of the FI. The resulting topological phase diagram is more regular (vs the gate potential) than in the nanowire counterpart due to the strong confinement achieved in stacking geometries: the wavefunction in nanowires spreads more across the wire section, and thus the achieved proximity effects are weaker than in planar geometries. This happens because the wavefunction is completely confined in the 2DEG and below the SC finger within the planar device.

Notice that, differently from hexagonal nanowires, the 2DEG-based structures proposed here require no magnetic field to reach the topological phase, allowing for different orientations of the effective wires and the design and control of complex wire networks of topological superconductors. This opens the door to more sophisticated and reliable Majorana detection schemes based on the spatial exchange or fusion of the Majorana bound states [48, 266–274]. Moreover, and as an outlook for future works, these platforms offer in principle the possibility to create 2D topological superconductivity by using a SC island instead of a finger. If the exchange field points in the stacking direction, then chiral Majorana modes may emerge at the edge of the island (if some other conditions are met).

In summary, our work establishes the importance of taking into account the effect of electrostatic interactions in realistic SM-SC and SM-FI-SC heterostructures. They influence most of the relevant parameters and, thus, understanding them deeply is necessary to design better devices or protocols to achieve and enhance a superconducting topological phase in these systems. We believe that this knowledge is crucial to develop a functional qubit based in hybrid nanowires and 2D platforms. In

fact, state of art simulations like the ones presented in this thesis are currently used in Microsoft to guide their quest for a Majorana qubit [26].

CHAPTER 8

CONCLUSIONES Y PERSPECTIVAS

A lo largo de esta tesis hemos contribuido al desarrollo de una descripción teórica, precisa y realista de las heteroestructuras híbridas semiconductoras-superconductoras. Hemos derivado expresiones analíticas del Hamiltoniano que describe los diferentes materiales de la heteroestructura así como el alineamiento de sus bandas. Además, hemos incluido el efecto de las interacciones electrostáticas en nuestro modelo y simulado varias experimentos. Nuestro modelo provee una descripción teórica de una única banda del sistema híbrido que puede predecir de forma exitosa algunas de las observaciones experimentales.

Comparado con modelos más microscópicos, como el modelo k·p de 8 bandas o cálculos *ab initio*, nuestra descripción presenta un coste computacional reducido ya que sólo involucra una única banda (la banda de conducción). Sin embargo, la diminuta longitud de onda de Fermi que exhiben típicamente los superconductores, impone una discretización pequeña del Hamiltoniano de *tight-binding* que utilizamos para describirlos (debido a que la red debe acomodar las oscilaciones de la función de onda a través de la heteroestructura). Esto hace que nuestras simulaciones sean exigentes y, por tanto, hemos tenido que desarrollar una implementación numérica eficiente para obtener las soluciones a la ecuación de Schrödinger-Poisson. Nuestro método está publicado como un paquete de código abierto llamado `Majorana Nanowires: Quantum Simulation Package` [133]. Con este paquete sólo es posible obtener, eficientemente, el espectro de baja energía de la heteroestructura. A pesar de ello, mostramos en esta tesis que es posible obtener a partir de estos estados los parámetros efectivos de la heteroestructura, y lo que es más, el invariante topológico. Sin embargo, nuestros métodos numéricos se limitan a sistemas *bulk*, i.e., nuestras simulaciones se restringen a la sección transversal 2D de los hilos híbridos (y 2DEGs) de modo que asumimos invariancia traslacional a lo largo de la dirección perpendicular. Las simulaciones finitas en 3D son computacionalmente exigentes y están fuera de las capacidades de la mayoría de los clústeres de computación modernos.

En el Capítulo 3 hemos derivado un Hamiltoniano de una única banda a partir de un modelo de 8 bandas que puede reproducir la banda de conducción (CB, por sus siglas en inglés) de los nanohilos semiconductores hechos de compuestos III-V y bajo la presencia de un potencial electrostático. Hemos encontrado que la ecuación que describe el acoplo Rashba espín-órbita (SO, por sus siglas en inglés) no captura de forma correcta el acoplo SO de los nanohilos debido a su sección finita. Para solucionar este problema, hemos propuesto una ecuación heurística que mantiene la simplicidad de la aproximación de más baja energía pero que provee una excelente aproximación al acoplo SO calculado con el modelo de 8 bandas. Hemos modelizado varios experimentos basados en nanohilos

semiconductores de tipo III-V (como InAs, InSb, GaAs y GaSb) y hemos comparado los valores que nuestro modelo da para el acoplo SO con los encontrados experimentalmente. Encontramos un acuerdo notable, lo que indica que nuestro modelo puede predecir los valores reales del acoplo SO en nanoestructuras. Esto es importante debido a que el valor del acoplo SO influye en la robustez de la posible fase topológica (en heteroestructuras semiconductor-superconductor y semiconductor-ferromagnético-superconductor). Particularmente, hemos encontrado que el acoplo SO varía entre 5 y $20 \, \text{meV} \cdot \text{nm}$ para los típicos dispositivos y parámetros experimentales, suficientemente grande como para albergar una fase topológica. El valor concreto depende de varios factores, como la geometría concreta del dispositivo y las puertas de potencial, ya que el acoplo SO depende del potencial electrostático y, notablemente, de la anchura del hilo. Hemos descubierto que para diámetros del hilo entre 100–150 nm, el acoplo SO de los hilos de zinc-blende se ve maximizado, siendo ~ 1.2 veces mayor que para un hilo tanto la mitad de fino como el doble de grueso (para el mismo capo eléctrico). De hecho, hemos mostrado que para los típicos diámetros del hilo experimentales (50–150 nm), el acoplo SO de cristales zinc-blende para nanohilos es ~ 1.8 veces mayor que para el *bulk* debido a los efectos de confinamiento impuestos por la sección del hilo. Sorprendentemente, este fenómeno es el opuesto para cristales de tipo wurtzita: los efectos de confinamiento son perjudiciales para el acoplo SO y se ve reducido a la mitad para el mismo rango de diámetros.

Por otra parte, hemos examinado el efecto de la tensión entre los átomo del hilo. Este mecanismo ha sido pasado por alto en anterior intentos de dar una descripción microscópica del hilo. Hemos descubierto que la tensión renomaliza el *gap* semiconductor y los acoplos entre las bandas. Esto lleva a su vez a cambios en los parámetros que describen la CB del hilo semiconductor; a saber, el potencial químico, la masa efectiva y el acoplo SO. En esta tesis, nos hemos centrado en el efecto sobre el acoplo SO, encontrando que una tensión compresiva (i.e., que reduce la celda unidad) incrementa el acoplo SO. Hemos analizado el caso específico de un hilo de InAs completamente cubierto por una capa de InP, el cual presenta tensión entre la interfaz de ambos materiales debido al desajuste entre las celdas unidad. Hemos encontrado que la tensión (compresiva) incrementa por un factor de más de 10 el acoplo SO en la interfaz del hilo híbrido en comparación con su núcleo. Esto a su vez incremente el acoplo SO total efectivo del hilo híbrido en un factor 3.

Hay varios aspectos que no hemos analizado en esta parte de la tesis y que podrían ser explorados en trabajos futuros. Por un lado, creemos que el mismo tipo de tensión analizado en los hilos InAs-InP puede estar presente los hilos híbridos semiconductores-superconductores de InAs-Al. Si esto es cierto, este fenómeno podría ser beneficioso para la protección topológica de los MBSs. Sin embargo, sería necesario hacer una estudio más profundo de este tema. Por otro lado, el hecho de que la tensión renormalice el potencial químico del hilo en la interfaz podría explicar algunas de las observaciones experimentales hechas en nanohilos. Hacemos notar que el Al crece en islas de nucleación a lo largo de las caras del hilo de InAs [80], hasta que crecen lo suficiente que se conectan unas con otras y dan lugar al recubrimiento homogéneo. A pesar de que este crecimiento es epitaxial, las diferentes islas podrían tener diferentes direcciones cristalográficas que podrían tener diferentes constates de red y, por tanto, producir un patrón de tensión a lo largo del hilo. Como resultado, el potencial químico podría variar a lo largo del hilo incluso si el recubrimiento es

homogéneo. Esto a su vez podría general estados localizados o ser perjudicial para la formación de la fase topológica.

Sumado a esto, no hemos incluido el efecto de un campo magnético en nuestra derivación teórica de las bandas semiconductoras. Varios trabajos han seguido la misma derivación para obtener el Hamiltoniano de la CB pero en la presencia de un campo magnético externo para sistemas *bulk* [159, 172]. Estos trabajos encuentran que el campo magnético produce un Zeeman *splitting* que es proporcional al campo magnético externo a través del g-factor. Aunque no incluimos esta derivación en este manuscrito, hemos encontrado que este g-factor se ve también afectado por los efectos de confinamiento en nanohilos [265] así como por la tensión, de modo que los típicos valores de *bulk* encontrados en la literatura (e.g., $g_{InAs} = 14.9$ o $g_{InSb} = 51$) son diferentes para nanohilos y heteroestructuras híbridas. Sin embargo, no hemos incluido este estudio aquí ya que queríamos centrarnos en la descripción de heteroestructuras semiconductoras-ferromagnéticas-superconductoras, donde el g-factor es irrelevante.

En el Capítulo 4 hemos analizado las propiedades de los hilos semiconductores-superconductores, centrándonos en los materiales InAs-Al por concreción. Hemos usado un Hamiltoniano efectivo que puede describir la heteroestructura y que trata al mismo nivel el hilo semiconductor y la capa superconductora. Hemos estudiado cómo las propiedades superconductoras se inducen en el hilo, concretamente el efecto proximidad. Hemos mostrado que este depende fuertemente del voltaje de la puerta de potencial ya que el potencial electrostático determina la posición de la función de onda dentro del hilo. Encontramos que para que halla un buen efecto proximidad, la función de onda dentro del hilo debe estar localizada cerca del recubrimiento superconductor. Mostramos además que esta situación es natural en los dispositivos reales ya que existe una acumulación de carga en la interfaz debido al doblamiento (resistivo) de la banda de conducción resultante de la diferencia del trabajo de extracción electrónico entre el InAs y el Al. En cualquier caso, esto también se puede lograr vaciando el hilo desde la cara opuesta por medio de un potencial electrostático externo (creado, por ejemplo, con una puerta de potencial). De hecho, encontramos que el hilo semiconductor atraviesa una transición abrupta desde exhibir un *gap* superconductor fuertemente proximizado a un *gap* suprimido y blando cuando el campo electrostático en el fondo del hilo es igual (aproximadamente) al doblamiento de la banda en la interfaz. Pensamos, por lo tanto, que el valor del doblamiento de la banda, que es en principio desconocido para nanohilos, podría ser obtenido simplemente realizado medidas convencionales de transporte electrónico en función del voltaje de la puerta de potencial.

En futuros trabajos, pretendemos estudiar el efecto que tiene el superconductor sobre el acoplo SO del hilo híbrido. Hacemos notar que, aparte de inducir correlaciones superconductoras en el hilo, el superconductor también induce una metalización que es perjudicial para el acoplo SO del semiconductor debido a que el Al carece del mismo. Este fenómeno, aunque está incluido en nuestras simulaciones, no está explícitamente discutido en este manuscrito; y podría ser discutido conjuntamente con los efectos de la tensión en la interfaz semiconductora-superconductora. A parte, una nueva generación de nanohilos híbridos está siendo fabricada actualmente utilizando diferentes

materiales superconductores como Pb, Nb, Ta, V o Sn [210–213]. Estos materiales podrían exhibir propiedades diferentes a las del Al (el superconductor que usamos en nuestras simulaciones) lo que podría ser beneficioso o perjudicial para la fase topológica.

El desarrollo de dispositivos que puedan albergar una fase topológica superconductora debería estar acompañado de protocolos que puedan unívocamente identificar esta fase. Hemos propuesto en el Capítulo 5 un dispositivo que permitiría realizar medidas espectroscópicas locales de transporte a lo largo del hilo, de modo que uno podría medir la localización de la función de onda de los MBSs al final del hilo. Hemos explorado tres configuraciones en las que el hilo híbrido se integra en una estructura de superred de diferentes formas. Una opción es depositar el hilo semiconductor sobre un conjunto ordenado de franjas superconductoras (que llamamos superred). Esto permitiría realizar medidas STM en la cara superior del hilo conduciendo una corriente entre la punta STM y cada franja superconductora a través del hilo. Otra opción es crecer epitaxialmente las franjas sobre el hilo. En este caso, se podrían usar los superconductores para realizar medidas de transporte entre ellos y obtener así información sobre la distribución de la función de onda. Pero ambas configuraciones tienen la misma desventaja: el recubrimiento superconductor no es homogéneo a lo largo del hilo. Además, como las franjas superconductoras apantallan el potencial electrostático creado por las puertas de potencial, el potencial químico inducido no es homogéneo. Hemos encontrado que, dependiendo del dopaje intrínseco del hilo, el dopaje inhomogéneo es propicio a la creación de estados de tipo QD y/o es perjudicial para la creación de una fase topológica. Hemos identificado los parámetros geométricos (tamaño de las franjas y distancia entre ellas) que proveen las fases topológicas más robustas y extendidas. Específicamente, encontramos que franjas de 30 nm separadas también por 30 nm (lo que es experimentalmente posible) provee un *gap* topológico de $\sim 100\,\mu$eV sin la aparición de estados triviales. Mayores anchuras o separaciones hace que estos estados triviales aparezcan, mientras que menores anchuras dan lugar a *gaps* topológicos más pequeños.

Hemos analizado la distribución espacial de los MBSs en este sistema y la hemos comparado con el caso de un recubrimiento homogéneo. Los MBSs en las superredes poseen oscilaciones adicionales debido a la periodicidad de la superred y, como consecuencia del recubrimiento reducido, poseen una escala de decaimiento mayor que en el caso homogéneo. Desafortunadamente, esto podría dificultar su detección. Para solucionar este problema, hemos propuesto una tercera configuración en la que los hilos parcialmente cubiertos se cubren todavía de forma homogénea con el conductor, pero se depositan sobre un conjunto de franjas de un conductor normal. Si la cara superior del hilo está descubierta, i.e., las caras recubiertas están en un lateral del hilo, entonces las medidas STM son posibles en este sistema. La ventaja de este sistema es que el recubrimiento superconductor es homogéneo y, por tanto, el *minigap* es comprable al de un nanohilo híbrido convencional (100–200 μeV). Creemos que este tipo de dispositivos es prometedor para detectar el esperado decaimiento exponencial de los MBSs en nanohilos. De hecho, varios experimentos están siendo actualmente realizados en geometrías parecidas. Están basados en hilos efectivos creados en 2DEGs en lugar de nanohilos, donde un conjunto de franjas metálicas se depositan encima del dispositivo. Con esta configuración, pueden realizar espectroscopía túnel entre los diferente puntos del hilo. Pensamos

que nuestros resultados podrían ser útiles para interpretar sus resultados experimentales.

Por último, en el Capítulo 6, hemos analizado una propuesta para obtener superconductividad topológica en heteroestructuras híbridas sin necesidad de aplicar un campo magnético. La idea es cubrir la heteroestructura híbrida semiconductora-superconductora con una capa adicional de un aislante ferromagnético que induzca, también por efecto proximidad, un campo Zeeman dentro del hilo. Hemos realizado simulaciones numéricas basadas concretamente en sistemas tripartitos InAs-Al-EuS. Hemos mostrado que la función de onda dentro del semiconductor debe ser empujada simultáneamente cerca de las capas superconductora y ferromagnética, de modo que adquiera ambos efectos proximidad y alcance la fase topológica. Esto se puede realizar usando puertas de potencial laterales y desde abajo, de modo que uno tiene un control más preciso del perfil de potencial dentro del semiconductor. Hemos encontrado además que la configuración en la que las capas superconductoras y ferromagnéticas se superponen es beneficiosa. Esto es debido a un campo Zeeman de $0.07\,\text{meV}$ que es inducido desde la capa de EuS a la de Al cuando están en contacto. Para dispositivos realistas, hemos obtenido que los *gaps* topológicos varían entre 25 y $100\,\mu\text{eV}$ para configuraciones que se superponen, en acuerdo con medidas experimentales [127] y lo suficientemente grande como para albergar una fase topológica medible. Por otro lado, los *minigaps* de las configuraciones que no se superponen varían entre 0 y $25\,\mu\text{eV}$.

En general, esta propuesta requiere de ajuste preciso de dos puertas de potencial para obtener una fase topológica medible. Para evitar este inconveniente, hemos propuesto una configuración diferente basada en una geometría plana donde los diferentes materiales están apilados por capas. La idea es usar un 2DEG dentro de una heteroestructura semiconductora en lugar de un nanohilo, el cual es además ventajoso ya que los 2DEGs exhiben un camino libre medio electrónico mayor. El 2DEG es apilado dentro de una geometría plana en la que su cara superior es cubierta por una capa ferromagnética aislante. Encima de esta capa, se crece además una tira superconductora. Si el sistema se dopa (vaciándola) desde arriba, entonces se crea un canal cuasi-1D bajo el superconductor por medio de un confinamiento electrostático. Usamos de nuevo InAs-Al-EuS en nuestras simulaciones ya que estos son los materiales explorados experimentalmente hasta el momento. Mostramos que este sistema puede albergar una fase topológica superconductora si el aislante ferromagnético es lo suficientemente fino como para permitir a los electrones tunelear entre el semiconductor y el superconductor. Por otro lado, el ferromagneto actúa además como una barrera polarizada de espín que induce una polarización en el semiconductor cuando los electrones tunelean a través. Por tanto, el ferromagneto tiene que ser lo suficientemente grueso como para inducir un campo Zeeman y llevar al sistema a la fase topológica. Hemos identificado que el grosor adecuado del EuS en heteroestructuras InAs-EuS-Al es de $1.5-3\,\text{nm}$. Dentro de este rango, la longitud de penetración de los electrones dentro del ferromegneto es comparable con la anchura del mismo. El diagrama de fase resultante provee fases topológicas de forma más regular (frente al voltaje de la puerta de potencial) que en un nanohilo debido al fuerte confinamiento alcanzado en estas geometrías planas: la función de onda en nanohilos se esparce más a lo largo de sus sección y, por tanto, los efectos de proximidad se logran de forma más débil que en las geometrías planas. Esto ocurre porque la función de onda está completamente confinada en el 2DEG y debajo de la franja superconductora

en los dispositivos planos.

Hacemos notar que, de forma diferente a los hilos hexagonales, las plataformas 2DEG propuestas aquí no requieren de un campo magnético para alcanzar la fase topológica, lo que permite diferentes orientaciones de los hilos efectivos así como diseñar y controlar redes de hilos de superconductores topológicos. Esto abre la puerta a esquemas de detección de MBSs más sofisticados basados en el intercambio o fusión de los mismos [48, 266–274]. Además, y como perspectiva para un futuro trabajo, estas plataformas ofrecen la posibilidad de crear superconductividad topológica en 2D usando islas superconductoras en vez de franjas. Si el campo de intercambio magnético apunta en la dirección del apilamiento de los materiales, entonces debería aparecer estados quirales de Majorana en el borde de la isla (si otras condiciones además se satisfacen).

En resumen, nuestro trabajo establece la importancia de tener en cuenta el efecto de las interacciones electrostáticas en heteroestructuras realistas semiconductoras-superconductoras y semiconductoras-ferromagnéticas-superconductoras. Estas interacciones influyen en la mayoría de los parámetros relevantes y, por tanto, entenderlos en profundidad es necesario para diseñar mejores dispositivos o protocolos para la obtención de una fase topológica. Creemos que este conocimiento es crucial para desarrollar un cúbit funcional basado en estos sistemas híbridos. De hecho, simulaciones punteras como las presentadas en esta tesis están siendo utilizadas actualmente por Microsoft para guiar su búsqueda de un cúbit de Majorana [26].

EFFECTIVE 1D OREG-LUTCHYN HAMILTONIAN

The energy spectrum of the heterostructures studied in this work typically present several subbands as a result of their low-dimensionality that may exhibit very different behaviors. Interestingly, we find that it is possible to (roughly) describe each subband through a 1D Oreg-Lutchyn Hamiltonian [20, 21] using effective parameters. This formulation is advantageous since the 1D Oreg-Lutchyn Hamiltonian describes a simpler model from which one can infer, in a transparent way, the topological properties of the system.

To obtain this single-band Hamiltonian, one assumes the separability of the eigenfunctions into a product of a purely spatial profile $\psi_n(\vec{r})$, and a position-independent Nambu spinor φ_n for the spin and particle-hole subspaces

$$\Psi^{(n)}(\vec{r}) \simeq \psi_n(\vec{r})\varphi_n \,. \tag{A.1}$$

This approximation is valid for any subgap state ($|E_n| < \Delta_0$) when the heterostructure thickness is small compared to the length where the spin and Nambu components change significantly, i.e., the spin-orbit length λ_{SO} and the superconducting coherence length ξ_{SC}. This is, $d_{SM} \ll \lambda_{SO}$ and $d_{SC} \ll \xi_{SC}$. Under this assumption, one can write an effective Oreg-Lutchyn Hamiltonian for each transverse subband n as

$$H_{\text{eff},n} = \left(\frac{\hbar^2 k_z^2}{2m_{\text{eff},n}} - \mu_{\text{eff},n} + h_{\text{eff},n}\sigma_z \right) \tau_z + \alpha_{\text{eff},n} k_z \sigma_y \tau_z + \Delta_{\text{eff},n} \sigma_y \tau_y, \tag{A.2}$$

where the effective parameters are given by

$$\Delta_{\text{eff},n} \equiv \langle \Delta(\vec{r})\sigma_0\tau_0 \rangle_n = \Delta_0 W_{\text{SC},n}, \tag{A.3}$$

$$\mu_{\text{eff},n} \equiv \left\langle \left(\partial_x \frac{\hbar^2}{2m^*(\vec{r})}\partial_x + \partial_y \frac{\hbar^2}{2m^*(\vec{r})}\partial_y + E_{\text{F}}(\vec{r}) - e\phi(\vec{r}) \right)\sigma_0\tau_0 \right\rangle_n, \tag{A.4}$$

$$h_{\text{eff},n} \equiv \langle h_{\text{Z}}(\vec{r})\sigma_0\tau_0 \rangle_n, \tag{A.5}$$

$$\alpha_{\text{eff},n} \equiv \langle \alpha_z(\vec{r})\sigma_0\tau_0 \rangle_n, \tag{A.6}$$

$$m_{\text{eff},n}^{-1} \equiv \left\langle \frac{1}{m^*(\vec{r})}\sigma_0\tau_0 \right\rangle_n, \tag{A.7}$$

being $W_{\beta,n} = \int_{\vec{r}\in\beta} \left| \Psi^{(n)}(\vec{r}) \right|^2 d\vec{r}$ the weight of the wavefunction in the material β. We neglect for simplicity additional effective Zeeman contributions arising from the SO interaction.

Notably, the effective Hamiltonian (A.2) reproduces the spectrum for each subband since its eigenvalues $E^{(n)}$ (i.e., $H_{\text{eff},n}\varphi_n = E^{(n)}\varphi_n$) are the same as the ones of the full Hamiltonian of Eq. (4.9). This allows to understand the behavior of each subband by directly inspecting these effective parameters. Actually, for each subband n that becomes topological when approaching $E = 0$ through a gap closing at $k_z = 0$, it is possible to verify where the 1D topological criterion

$$|h_{\text{eff}}| \gtrsim \sqrt{\mu_{\text{eff}}^2 + \Delta_{\text{eff}}^2} \tag{A.8}$$

is fulfilled as a function of the gate voltage. We find a good agreement between this criterion and the exact calculation of the topological invariant, as we prove in Ref. [241].

APPENDIX B

APPENDICES FOR CHAPTER 3

B.1 Wurtzite 8-band k·p model

The 8B k·p Kane Hamiltonian for wurtzite crystals has been derived and described in previous works [166]. The basis for wurtzite-type semiconductors is given by

$$
\begin{cases}
|C_\uparrow\rangle = i\,|S_\uparrow\rangle\,, & |C_\downarrow\rangle = i\,|S_\downarrow\rangle\,, \\[4pt]
|LH_\uparrow\rangle = \frac{1}{\sqrt{2}}\,|(X-iY)_\uparrow\rangle\,, & |LH_\downarrow\rangle = -\frac{1}{\sqrt{2}}\,|(X+iY)_\downarrow\rangle\,, \\[4pt]
|HH_\uparrow\rangle = -\frac{1}{\sqrt{2}}\,|(X+iY)_\downarrow\rangle\,, & |HH_\downarrow\rangle = \frac{1}{\sqrt{2}}\,|(X-iY)_\uparrow\rangle\,, \\[4pt]
|SO_\uparrow\rangle = |Z_\uparrow\rangle\,, & |SO_\downarrow\rangle = |Z_\downarrow\rangle\,,
\end{cases}
\tag{B.1}
$$

where the z direction is taken along the (0001) crystallographic orientation. Its corresponding Hamiltonian in the $\Psi = (\Psi_{c,\uparrow}, \Psi_{c,\downarrow}, \Psi_{lh,\uparrow}, \Psi_{lh,\downarrow}, \Psi_{hh,\uparrow}, \Psi_{hh,\downarrow}, \Psi_{soff,\uparrow}, \Psi_{soff,\downarrow})$ basis up to first-order in

Löwdin perturbation theory[1] is

$$
H_{\mathrm{kp}} = \left(
\begin{array}{ccccc}
T_{\mathrm{c}} & -i\alpha_5 k_- & P_2 k_+ + \Omega_2 & i\sqrt{2}\Delta_4 - \sqrt{2}P_5 k_z & \ldots \\[4pt]
i\alpha_5 k_+ & T_{\mathrm{c}} & i\sqrt{2}\Delta_4 - \sqrt{2}P_5 k_z & -P_2 k_- + \Omega_2^\dagger & \ldots \\[4pt]
P_2 k_- + \Omega_2^\dagger & -i\sqrt{2}\Delta_4 - \sqrt{2}P_5 k_z & T_{\mathrm{lh}} & 0 & \ldots \\[4pt]
-i\sqrt{2}\Delta_4 - \sqrt{2}P_5 k_z & P_2 k_+ + \Omega_2 & 0 & T_{\mathrm{lh}} & \ldots \\[4pt]
-P_3 k_+ + \Omega_2 & 0 & -\Omega_4 & i\alpha_2 k_+ & \ldots \\[4pt]
0 & P_3 k_- + \Omega_2^\dagger & -i\alpha_2 k_- & -\Omega_4^\dagger & \ldots \\[4pt]
P_1 k_z + \Omega_1^\dagger & -P_4 k_- & -i\left(P_6 + \frac{\alpha_1}{\sqrt{2}}\right)k_+ + \Omega_3^\dagger & \sqrt{2}\Delta_3 + i\sqrt{2}\alpha_1 k_z & \ldots \\[4pt]
P_4 k_+ & P_1 k_z + \Omega_1^\dagger & \sqrt{2}\Delta_3 + i\sqrt{2}\alpha_1 k_z & -i\left(P_6 + \frac{\alpha_1}{\sqrt{2}}\right)k_- - \Omega_3 & \ldots
\end{array}
\right.
$$

$$
\left.
\begin{array}{ccccc}
\ldots & -P_3 k_- + \Omega_2^\dagger & 0 & P_1 k_z + \Omega_1 & P_4 k_- \\[4pt]
\ldots & 0 & P_3 k_+ + \Omega_2 & -P_4 k_+ & P_1 k_z + \Omega_1 \\[4pt]
\ldots & -\Omega_4^\dagger & i\alpha_2 k_+ & i\left(P_6 + \frac{\alpha_1}{\sqrt{2}}\right)k_- + \Omega_3 & \sqrt{2}\Delta_3 - i\sqrt{2}\alpha_1 k_z \\[4pt]
\ldots & -i\alpha_2 k_- & -\Omega_4 & \sqrt{2}\Delta_3 - i\sqrt{2}\alpha_1 k_z & i\left(P_6 + \frac{\alpha_1}{\sqrt{2}}\right)k_+ - \Omega_3^\dagger \\[4pt]
\ldots & T_{\mathrm{hh}} & 0 & -i\left(P_6 - \frac{\alpha_1}{\sqrt{2}}\right)k_+ - \Omega_3^\dagger & 0 \\[4pt]
\ldots & 0 & T_{\mathrm{hh}} & 0 & i\left(P_6 - \frac{\alpha_1}{\sqrt{2}}\right)k_- + \Omega_3 \\[4pt]
\ldots & i\left(P_6 - \frac{\alpha_1}{\sqrt{2}}\right)k_- - \Omega_3 & 0 & T_{\mathrm{soff}} & -i\alpha_3 k_+ \\[4pt]
\ldots & 0 & -i\left(P_6 - \frac{\alpha_1}{\sqrt{2}}\right)k_+ + \Omega_3^\dagger & i\alpha_3 k_- & T_{\mathrm{soff}}
\end{array}
\right) , \quad (\mathrm{B.2})
$$

where the diagonal terms are

$$
T_{\mathrm{c}} = E_{\mathrm{c}} + \Omega_0^{\mathrm{c}} - e\phi(\vec{r}), \ \ \Omega_0^{\mathrm{c}} = \frac{\hbar^2}{2m_e}\left[(k_x^2 + k_y^2)e_2 + k_z^2 e_1\right] \qquad (\mathrm{B.3})
$$

$$
T_{\mathrm{lh}} = E_{\mathrm{h}} + \Delta_1 + \Delta_2 + \Omega_0^{\mathrm{lh}} - e\phi(\vec{r}), \ \ \Omega_0^{\mathrm{lh}} = \frac{\hbar^2}{2m_e}\left[(k_x^2 + k_y^2)(\gamma_2 - \gamma_4) + k_z^2(\gamma_3 + \gamma_1)\right], \qquad (\mathrm{B.4})
$$

$$
T_{\mathrm{hh}} = E_{\mathrm{h}} + \Delta_1 - \Delta_2 + \Omega_0^{\mathrm{hh}} - e\phi(\vec{r}), \ \ \Omega_0^{\mathrm{hh}} = \frac{\hbar^2}{2m_e}\left[(k_x^2 + k_y^2)(\gamma_2 - \gamma_4) + k_z^2(\gamma_3 + \gamma_1)]\right], \qquad (\mathrm{B.5})
$$

$$
T_{\mathrm{soff}} = E_{\mathrm{soff}} + \Omega_0^{\mathrm{soff}} - e\phi(\vec{r}), \ \ \Omega_0^{\mathrm{soff}} = \frac{\hbar^2}{2m_e}\left[(k_x^2 + k_y^2)\gamma_2 + k_z^2\gamma_1\right], \qquad (\mathrm{B.6})
$$

---

[1]Second-order Löwdin perturbative terms are also included for the k·p term to properly account for the quasi-parabolic dispersion relation.

and the off-diagonal ones

$$\Omega_1 = i\left[\tilde{P}_1 k_z^2 + \tilde{P}_2(k_x^2 + k_y^2)\right], \tag{B.7}$$

$$\Omega_2 = i\tilde{P}_3 k_+ k_z, \tag{B.8}$$

$$\Omega_3 = \gamma_6 k_+ k_z, \tag{B.9}$$

$$\Omega_4 = \gamma_5 k_+^2, \tag{B.10}$$

being Δ_i, e_i, α_i, P_i, $\tilde{P}_i$ and γ_i the Kane parameters. The explicit form of these parameters are

$$\Delta_2 = \frac{i\hbar}{4m_e^2 c^2}\langle X|\frac{\partial\phi_0}{\partial x}p_y - \frac{\partial\phi_0}{\partial y}p_x|Y\rangle, \tag{B.11}$$

$$\Delta_3 = \frac{i\hbar}{4m_e^2 c^2}\langle Y|\frac{\partial\phi_0}{\partial y}p_z - \frac{\partial\phi_0}{\partial z}p_y|Z\rangle = \frac{i\hbar}{4m_e^2 c^2}\langle Z|\frac{\partial\phi_0}{\partial z}p_x - \frac{\partial\phi_0}{\partial x}p_z|X\rangle, \tag{B.12}$$

$$\Delta_4 = \frac{i\hbar}{4m_e^2 c^2}\langle Y|\frac{\partial\phi_0}{\partial y}p_z - \frac{\partial\phi_0}{\partial z}p_y|S\rangle = \frac{i\hbar}{4m_e^2 c^2}\langle S|\frac{\partial\phi_0}{\partial z}p_x - \frac{\partial\phi_0}{\partial x}p_z|X\rangle, \tag{B.13}$$

$$\alpha_1 = \frac{\hbar^2}{4m_e^2 c^2}\langle X|\frac{\partial\phi_0}{\partial x}|Z\rangle = \frac{\hbar^2}{4m_e^2 c^2}\langle Y|\frac{\partial\phi_0}{\partial y}|Z\rangle, \tag{B.14}$$

$$\alpha_2 = \frac{\hbar^2}{4m_e^2 c^2}\langle X|\frac{\partial\phi_0}{\partial z}|X\rangle = \frac{\hbar^2}{4m_e^2 c^2}\langle Y|\frac{\partial\phi_0}{\partial z}|Y\rangle, \tag{B.15}$$

$$\alpha_3 = \frac{\hbar^2}{4m_e^2 c^2}\langle Z|\frac{\partial\phi_0}{\partial z}|Z\rangle, \tag{B.16}$$

$$\alpha_5 = \frac{\hbar^2}{4m_e^2 c^2}\langle S|\frac{\partial\phi_0}{\partial z}|S\rangle, \tag{B.17}$$

$$P_1 = \frac{i\hbar}{m_e}\langle Z|p_x|S\rangle, \tag{B.18}$$

$$P_2 = \frac{\hbar}{\sqrt{2}m_e}\langle X|ip_x + \frac{\hbar}{4m_e c^2}\frac{\partial\phi_0}{\partial x}|S\rangle = \frac{\hbar}{\sqrt{2}m_e}\langle Y|ip_y + \frac{\hbar}{4m_e c^2}\frac{\partial\phi_0}{\partial y}|S\rangle, \tag{B.19}$$

$$P_3 = \frac{\hbar}{\sqrt{2}m_e}\langle X|ip_x - \frac{\hbar}{4m_e c^2}\frac{\partial\phi_0}{\partial x}|S\rangle = \frac{\hbar}{\sqrt{2}m_e}\langle Y|ip_y - \frac{\hbar}{4m_e c^2}\frac{\partial\phi_0}{\partial y}|S\rangle, \tag{B.20}$$

$$P_4 = \frac{\hbar^2}{4m_e^2 c^2}\langle Z|\frac{\partial\phi_0}{\partial z}|S\rangle, \tag{B.21}$$

$$P_5 = \frac{\hbar^2}{4m_e^2 c^2}\langle X|\frac{\partial\phi_0}{\partial x}|S\rangle = \frac{\hbar^2}{4m_e^2 c^2}\langle Y|\frac{\partial\phi_0}{\partial y}|S\rangle, \tag{B.22}$$

$$P_6 = \frac{i\hbar}{\sqrt{2}m_e}\langle y|p_y|Z\rangle = \frac{i\hbar}{\sqrt{2}m_e}\langle X|p_x|Z\rangle. \tag{B.23}$$

$$\tag{B.24}$$

The parameters $E_{\rm h}$ and $E_{\rm c}$ are the hole and conduction band edges and Δ_1 provides the crystal field energy (that arises because of the anisotropy between the $x-y$ plane and the z direction in wurtzite crystals). We choose the conduction band edge as the reference energy, fixing $E_{\rm c} = 0$. The

specific values of the Kane parameters that we use are extracted from Ref. [166] and shown in Appendix B.4. They are also valid inside the range $\left|\vec{k}\right| = [-1, 1]$ nm^{-1}.

One can proceed to obtain the effective (zeroth-order) CB Hamiltonian as in the case of zinc-blende but starting from this wurtzite 8B Hamiltonian. However, this derivation would certainly be more involved due to the presence of more coupling parameters. Actually, we expect the effective mass and the SO coupling to be anisotropic as the conduction-to-valence bands couplings involve more than one different parameter P_i. This is a direct manifestation of the unit cell anisotropy of wurtzite crystals. To avoid this complexity, in practice, the zinc-blende zeroth-order results for the effective mass and SO coupling are frequently used in the literature for III-V compound SMs with wurtzite structure as well, but taking the appropriate values of Δ_g and Δ_soff (see Appendix B.4) while keeping the zinc-blende P parameter. In any case, as we discuss in the main text, the zeroth-order SO coupling cannot account for the specific crystal structure, be it zinc-blende or wurtzite, when confinement effects are important, since the neglected terms proportional to γ_i are essential. Hence, we propose to describe the SO coupling in wurtzite crystals using the same improved zeroth-order CB equations derived for zinc-blende but with a different parameter P_fit. Once again, this parameter is chosen so as the improved SO coupling equation fits the result of the wurtzite 8B Hamiltonian of Eq. (B.2).

B.2 Beyond zeroth-order in the conduction-band approximation

We could go to higher orders in the Dyson expansion of the valence bands Green's function of Eq. (3.21). For instance, let us compute the first-order correction to the CB Hamiltonian to understand its importance. It is given by

$$H_\mathrm{CB}^{(1)} = V_\mathrm{cv} G_\mathrm{v}^{(0)} V G_\mathrm{v}^{(0)} H_\mathrm{cv}^{\dagger}. \tag{B.25}$$

Although this correction can be found analytically, it does not provide manageable expressions and it gives rise to new additional terms (that are neither kinetic nor SO terms) that are difficult to interpret. However, if we assume that the off-diagonal terms in V are negligible in comparison to the main diagonal ones, as it happens for III-V compound SMs (we have checked this numerically; not shown), then we obtain a simple first-order correction

$$H_\mathrm{CB}^{(1)} \simeq \left[\vec{k} \frac{\hbar^2}{2\mathbf{m}^{(1)}(\vec{r})} \vec{k} + E_c - e\phi(\vec{r}) \right] \sigma_0 + \vec{\Gamma}^{(1)}(\vec{k}) \cdot \vec{\sigma}. \tag{B.26}$$

The parameter $\mathbf{m}^{(1)}(\vec{r})$ is the first-order correction to the effective mass[2], which is now a tensor with non-zero elements

$$\left(\frac{1}{\mathbf{m}^{(1)}(\vec{r})}\right)_{xx} = \left(\frac{1}{\mathbf{m}^{(1)}(\vec{r})}\right)_{yy} =$$

$$-\frac{2P^2}{3\hbar^2}\left[\frac{1}{E_{\mathrm{h}} - e\phi(\vec{r}) - E}\left((2\gamma_1 + \gamma_3)\frac{\hbar^2}{2m_e}(k_x^2 + k_y^2) + 2\gamma_1\frac{\hbar^2}{2m_e}k_z^2\right)\frac{1}{E_{\mathrm{h}} - e\phi(\vec{r}) - E}\right.$$
$$\left. + \frac{1}{E_{\mathrm{soff}} - e\phi(\vec{r}) - E}\left(\gamma_1\frac{\hbar^2}{2m_e}(k_x^2 + k_y^2 + k_z^2)\right)\frac{1}{E_{\mathrm{soff}} - e\phi(\vec{r}) - E}\right], \text{(B.27)}$$

$$\left(\frac{1}{\mathbf{m}^{(1)}(\vec{r})}\right)_{zz} =$$

$$-\frac{2P^2}{3\hbar^2}\left[\frac{1}{E_{\mathrm{h}} - e\phi(\vec{r}) - E}\left(2(\gamma_1 - \gamma_3)\frac{\hbar^2}{2m_e}(k_x^2 + k_y^2) + 2(2\gamma_3 + \gamma_1)\frac{\hbar^2}{2m_e}k_z^2\right)\frac{1}{E_{\mathrm{h}} - e\phi(\vec{r}) - E}\right.$$
$$\left. + \frac{1}{E_{\mathrm{soff}} - e\phi(\vec{r}) - E}\left(\gamma_1\frac{\hbar^2}{2m_e}(k_x^2 + k_y^2 + k_z^2)\right)\frac{1}{E_{\mathrm{soff}} - e\phi(\vec{r}) - E}\right]. \text{(B.28)}$$

The other parameter, $\vec{\Gamma}^{(1)}$ is the (first-order) SO interaction, which has an intricate tensor structure that can be written as

$$\vec{\Gamma}^{(1)}(\vec{k}) = \frac{1}{2}\left[\begin{pmatrix} 0 & \alpha_z^{(1)} & -\alpha_y^{(1)} \\ -\alpha_z^{(1)} & 0 & \alpha_x^{(1)} \\ \tilde{\alpha}_y^{(1)} & -\tilde{\alpha}_x^{(1)} & 0 \end{pmatrix}\cdot\vec{k}^t + \vec{k}\cdot\begin{pmatrix} 0 & \alpha_z^{(1)} & -\alpha_y^{(1)} \\ -\alpha_z^{(1)} & 0 & \alpha_x^{(1)} \\ \tilde{\alpha}_y^{(1)} & -\tilde{\alpha}_x^{(1)} & 0 \end{pmatrix}^t\right]. \quad \text{(B.29)}$$

Here $\vec{\alpha}^{(1)}$ and $\vec{\tilde{\alpha}}^{(1)}$ are the first-order SO couplings, given by the expressions

$$\vec{\alpha}^{(1)} = -\frac{2P^2}{3}\left[\frac{\gamma_1 - \gamma_3}{E_{\mathrm{h}} - e\phi(\vec{r}) - E}\vec{\nabla}\left\{\frac{1}{E_{\mathrm{h}} - e\phi(\vec{r}) - E}\right\}\right.$$
$$\left. - \frac{\gamma_1}{E_{\mathrm{soff}} - e\phi(\vec{r}) - E}\vec{\nabla}\left\{\frac{1}{E_{\mathrm{soff}} - e\phi(\vec{r}) - E}\right\}\right]\frac{\hbar^2}{2m_e}(k_x^2 + k_y^2)$$
$$-\frac{2P^2}{3}\left[\frac{\gamma_1 + 2\gamma_3}{E_{\mathrm{h}} - e\phi(\vec{r}) - E}\vec{\nabla}\left\{\frac{1}{E_{\mathrm{h}} - e\phi(\vec{r}) - E}\right\}\right.$$
$$\left. - \frac{\gamma_1}{E_{\mathrm{soff}} - e\phi(\vec{r}) - E}\vec{\nabla}\left\{\frac{1}{E_{\mathrm{soff}} - e\phi(\vec{r}) - E}\right\}\right]\frac{\hbar^2}{2m_e}k_z^2, \text{ (B.30)}$$
$$\vec{\tilde{\alpha}}^{(1)} = \vec{\alpha}^{(1)} - P^2\frac{1}{E_{\mathrm{h}} - e\phi(\vec{r}) - E}\vec{\nabla}\left\{\frac{1}{E_{\mathrm{h}} - e\phi(\vec{r}) - E}\right\}\left(\gamma_3\frac{\hbar^2}{2m_e}(k_x^2 + k_y^2) - 2\gamma_1\frac{\hbar^2}{2m_e}k_z^2\right). \text{ (B.31)}$$

In these equations, the nabla operator only apply to the expressions within the brackets.

If we apply these equations to a wire that it is translational invariant along the z direction, we

---

[2]Notice that the effective mass up to first-order is then a (diagonal) tensor and is given by $\mathbf{m}_{\mathrm{eff}}(\vec{r}) = \left(\frac{\mathbf{I}}{m^{(0)}(\vec{r})} + \frac{1}{\mathbf{m}^{(1)}(\vec{r})}\right)^{-1}$.

obtain the first-order corrections to the effective Hamiltonian for each subband j

$$\tilde{H}_{\text{eff}}^{(j)}(k_z) = \left(\frac{\hbar^2 k_z^2}{2m_{\text{eff}}^{(j)}} + E_{\text{T}}^{(j)}\right)\sigma_0 + \left(\alpha_{\text{eff},x}^{(j)}\sigma_y - \alpha_{\text{eff},y}^{(j)}\sigma_x\right)k_z + \left(\beta_{\text{eff},x}^{(j)}\sigma_y - \beta_{\text{eff},y}^{(j)}\sigma_x\right)k_z^3, \qquad \text{(B.32)}$$

where the effective parameters, in the simplified approximation $E_i \gg E + e\phi(\vec{r})$ (that we perform just for simplicity), are given by

$$\frac{1}{m_{\text{eff}}^{(j)}} = -\frac{2P^2}{3\hbar^2}\left[\frac{2(\gamma_1 - \gamma_3)}{\Delta_{\text{g}}^2} + \frac{\gamma_1}{(\Delta_{\text{g}} + \Delta_{\text{soff}})^2}\right]\left\langle\frac{\hbar^2}{2m_e}(\partial_x^2 + \partial_y^2)\right\rangle_j, \qquad \text{(B.33)}$$

$$\vec{\alpha}_{\text{eff}}^{(j)} = 2e\frac{P^2}{3}\left[\frac{\gamma_1 - \gamma_3}{\Delta_{\text{g}}^3} - \frac{\gamma_1}{(\Delta_{\text{g}} + \Delta_{\text{soff}})^3}\right]\left\langle\vec{\nabla}\phi(\vec{r})\frac{\hbar^2}{2m_e}(\partial_x^2 + \partial_y^2)\right\rangle_j, \qquad \text{(B.34)}$$

$$\vec{\beta}_{\text{eff}}^{(j)} = -2e\frac{P^2}{3}\left[\frac{\gamma_1 + 2\gamma_3}{\Delta_{\text{g}}^3} - \frac{\gamma_1}{(\Delta_{\text{g}} + \Delta_{\text{soff}})^3}\right]\left\langle\vec{\nabla}\phi(\vec{r})\right\rangle_j. \qquad \text{(B.35)}$$

Notice that all these terms are one $1/\Delta_i$ order more than their corresponding zeroth-order terms of Eqs. (3.29) and (3.30), and proportional to the Kane parameters γ_i, as one would expect from the first-order expansion. The parameter $\vec{\beta}_{\text{eff}}$ is just the effective *cubic* SO coupling, as the term it belongs to in Eq. (B.32) is proportional to k_z^3. On the other side, the effective mass and linear SO coupling corrections to first-order are also proportional to the transverse energy $\left\langle\frac{\hbar^2}{2m_e}(\partial_x^2 + \partial_y^2)\right\rangle_j$, meaning that confinement effects play a role on them: in finite-width nanowires, this energy goes like $\sim 1/W_{\text{wire}}$, and therefore, for very thick wires (large W_{wire}) these corrections are not relevant, while they might be for thin ones (small W_{wire}). We actually show in the main text that for typical experimental nanowire diameters (50–200 nm) they actually play an important role for the SO coupling, and this is why the SO coupling equation to zeroth-order does not account for the total SO coupling predicted by the 8B model.

To understand the importance of the contribution of this first-order correction, let us consider, for instance, a zinc-blende InAs nanowire subject to a position-independent electric field in the y direction, particularly $\vec{E} = (0, 2, 0)$ meV·nm. We want to compare the SO coupling calculated to different orders in Ω_i/Δ_i. In Fig. B.1(a), we plot the modulus of the SO coupling as a function of the nanowire width W_{wire}. In red we show the result found with the 8B Hamiltonian of Eq. (3.53), which is a computationally demanding calculation, especially as W_{wire} increases. We consider the red curve (the one provided by the 8B model) as the exact or correct result in our work. We see that the SO coupling rapidly increases for small wire widths and then approximately plateaus from $W_{\text{wire}} \approx 25$ nm to $W_{\text{wire}} \approx 175$ nm. From that moment on it decreases. In green we have the zeroth-order conduction band approximation calculated from Eq. (3.30). It also increases for small widths, for approximately the same W_{wire}-range as the 8B model result, but then it remains constant and about half the value of the 8B model. In particular, for $W_{\text{wire}} = 80$ nm, it is a 54% of the exact value. We have also worked out numerically the SO coupling to first order, cyan curve, and to second order, pink curve. At $W_{\text{wire}} = 80$ nm again, the cyan curve provides the 75% of the 8B model result, and the pink one the 85%. We observe that, in order to approach the red value, we
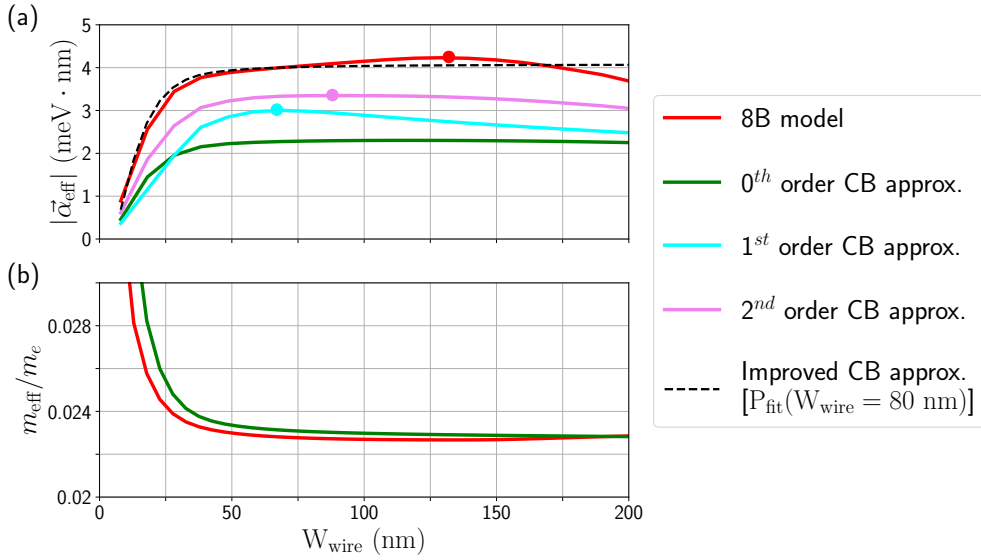
Figure B.1: (a) Modulus of the SO coupling as a function of the wire's width W_{wire} for a zinc-blende InAs nanowire in a homogeneous electric field $\vec{E} = (0, 2, 0)$ meV·nm. Different degrees of approximation are compared in this figure. In red we show the SO coupling found with the 8B model Hamiltonian of Eq. (3.53), considered as the exact result in this work. The result to zeroth-order in the CB approximation is shown in green, to first order in cyan and to second order in pink. Dots mark the maximum of each curve. The dashed black curve corresponds to the improved SO Eq. (3.43), which considers a constant P_{fit} parameter fixed to $W_{\text{wire}} = 80$ nm. (b) Effective electron mass m_{eff} over bare electron mass m_e versus W_{wire}. In red the 8B model result and in green the value of the zeroth-order CB approximation.

need to sum many orders (if not all) in the Dyson expansion for the realistic wire widths presented in this figure, something that is neither easy nor practical.

In Fig. B.1, we only get to wire widths of 200 nm, but as $W_{\text{wire}} \to \infty$, the red curve should approach the green one, the zeroth-order. Note that the first and second orders also decrease with width. This can be understood because, as the width increases, the transverse momenta $k_{x,y} \sim 1/W_{\text{wire}}$ go to zero and so does $\Omega_i = \hbar^2 \vec{k}^2 \gamma_i / (2m_e)$. Hence, for bulk SMs, the zeroth-order SO coupling commonly found in the literature is a very good approximation. Moreover, for $W_{\text{wire}} \to \infty$, the SO coupling of zinc-blende and wurtzite InAs are very similar. Nonetheless, when confinement effects are important, $\alpha_{\text{R}}^{(0)}$ cannot provide the quantitative and the qualitative behavior of the SO coupling, nor distinguish between different crystal structures.

Notice that, in spite of the fact that the 8B model SO coupling has a pretty constant value from $W_{\text{wire}} \approx 25$ nm to 175 nm, as mentioned above, it has a maximum at $W_{\text{wire}} = 130$ nm. This maximum value depends on the band and Kane parameters in an intricate way. The cyan and pink curves have also a maximum, but for smaller W_{wire}. Knowing the wire's width for which the SO coupling is maximum can help design SM nanowires with stronger SO effects.

In Fig. B.1(b), we study the CB effective mass as a function of W_{wire}. As before, the red curve

corresponds to the zinc-blende InAs 8B model result, whereas the green one to the zeroth-order approximation of Eq. (3.29). Strikingly, we observe that $m^{(0)}$ provides an excellent approximation to the exact red result for basically all wire widths, except for the smallest ones, where, in any case, the k·p model is not valid. This means that, while higher corrections in the CB approximation are necessary to correctly account for the SO coupling of SM nanowires, the effective mass can be accurately captured with the common zeroth-order limit. The ultimate reason comes from the relative signs between the $1/\Delta_i$ terms in Eqs. (3.29) and (3.30). For the effective mass these terms are added, while for the SO coupling they are subtracted.

B.3 Dependence of the improved P_{fit} parameter on the electrostatic environment

One of the core assumptions of our work is that the improved Kane parameter P_{fit} depends weakly on the electrostatic potential. This allows us to use the improved SO coupling equation [Eq. (3.43)] regardless of the precise electrostatic environment surrounding the wire. To illustrate further this point, we follow the same procedure as the one explained in Sec. 3.3.1 to extract P_{fit} from four different devices/environments. Their sketches are depicted to the left of each sub-figure in Fig. B.2. To the right, we show the SO coupling of the lowest-energy subband extracted from 8B model simulations (blue dots) versus gate voltage, taking into account the electrostatic environment of its corresponding sketch. We obtain P_{fit} by fitting Eq. (3.43) to these values. The fitting curves are shown with solid red lines, and the resulting P_{fit} values are shown in their respective legends. The geometries considered here are significantly different between them. Simulations for (a) and (c) have two gates (back and top ones), but with different applied voltages and covering different number of wire's facets. In (b) we consider a device with three gates (one back-gate and two side-gates), and we explore the dependence of the SO coupling with one of the side gates, similarly to the device of Ref. [73]. Finally, in (d) we consider only one gate (a back one), but we include the charge density of the wire ρ_{mobile} in the TF approximation, as the device of Ref. [69]. We also consider different charge accumulation layers ρ_{surf} [in (b) is zero], different substrate widths and materials, and a square cross section for the nanowire in (d). Despite all these differences, the discrepancy of P_{fit} between these setups is below 2%. This implies that the corrections of the electrostatic potential to P_{fit} are small (for the range of gate potentials studied in this work) and that, in practice, we can neglect the dependence of P_{fit} with $\phi(\vec{r})$.

B.4 Parameters for Chapter 3

Here, we provide all the parameters that we have used to perform our simulations of Chapter 3. Some of these parameters are also used in Chapter 4 and Chapter 6 to describe the semiconducting part of the heterostructure.

Table B.1: Band and Kane/Luttinger parameters for 8B zinc-blende Hamiltonians, extracted from Ref. [158].

Parameter	InAs	InSb	GaAs	GaSb
Δ_{g} (meV)	417	235	1519	812
Δ_{soff} (meV)	390	810	341	760
P (meV·nm)	919.7	940.2	1047.5	971.3
$\gamma_1^{(L)}$	20.0	34.8	6.98	13.4
$\gamma_2^{(L)}$	8.5	15.5	2.06	4.7
$\gamma_3^{(L)}$	9.2	16.5	2.93	6.0

Table B.2: Band and Kane parameters for the 8B wurtzite InAs Hamiltonian, extracted from Ref. [166]. The parameters Δ_{g} and Δ_{soff} are obtained as a combination of Δ_i, E_{c} and E_{h}.

InAs					
Energy splittings (meV)		Linear parameters (meV·nm)		Second order parameters (in units of $\hbar^2/2m_e$)	
Δ_1	100.3	P_1	838.6	γ_1	1.5726
Δ_2	102.3	P_2	489.26	γ_2	-1.6521
Δ_3	104.1	P_3	499.09	γ_3	-2.6301
Δ_4	38.8	P_4	-21.71	γ_4	0.5126
E_{c}	0	P_5	-6.95	γ_5	0.1172
E_{h}	-664.9	P_6	-49.04	γ_6	1.3103
		α_1	-1.89	$\tilde{P}_1$	-2.3925
Δ_{g}	467	α_2	-28.92	$\tilde{P}_2$	2.3155
Δ_{soff}	325.7	α_3	-51.17	$\tilde{P}_3$	-1.7231
		α_5	53.06	e_1	-3.2005
				e_2	0.6363

Table B.3: Relative dielectric permittivity constants, ϵ_X (where X is each material), in units of ϵ_0. We show the references where they are extracted.

Material	Dielectric constant		Material	Dielectric constant
InAs	15.5 [275]		HfO$_2$	25 [276]
InSb	16.8 [275]		SiO$_2$	3.9 [276]
GaAs	12.9 [275]		AlO$_2$/Al$_2$O$_3$	9 [276]
GaSb	15.7 [275]		PEO+LiClO$_4$	10^4 [277]

Table B.4: Parameters used for Sec. 3.4. Temperature T is fixed to $1.7\,\mathrm{K}$ in all our simulations, like in the experiments. We use a discretization grid spacing of $0.1\,\mathrm{nm}$ for the FDM.

Material	Parameter	Value	Refs.
InAs	diameter W_{wire}	$100\,\mathrm{nm}$ $65\,\mathrm{nm}$ in Fig. 3.8(c,d)	-
	E_{F}	0	-
	P	$919.7\,\mathrm{meV}\cdot\mathrm{nm}$	[158]
	$P_{\mathrm{fit}}(W_{\mathrm{wire}} = 100\ \mathrm{nm})$	$700\,\mathrm{meV}\cdot\mathrm{nm}$	[151]
	$P_{\mathrm{fit}}(W_{\mathrm{wire}} = 65\ \mathrm{nm})$	$850\,\mathrm{meV}\cdot\mathrm{nm}$	[151]
	Δ_{g}	$467\,\mathrm{meV}$	[158]
	Δ_{soff}	$325.7\,\mathrm{meV}$	[158]
	strain thickness	$4\,\mathrm{nm}$	-
	a_c	$5080\,\mathrm{meV}$	[158]
	a_v	$1000\,\mathrm{meV}$	[158]
	b	$1800\,\mathrm{meV}$	[158]
	ϵ_{InAs}	$15.5\epsilon_0$	[275]
	ρ_{surf}	$8\cdot10^{-2}\left(\frac{\mathrm{e}}{\mathrm{nm}^3}\right)$ 0 in Fig. 3.8(c,d)	Fitted from experimental data
InP	thickness	$4\,\mathrm{nm}$	-
	E_{F}	$478\,\mathrm{meV}$	[158, 278]
	P	$902.4\,\mathrm{meV}\cdot\mathrm{nm}$	[158]
	Δ_{g}	$1423\,\mathrm{meV}$	[158]
	Δ_{soff}	$108\,\mathrm{meV}$	[158]
	ϵ_{InP}	$12.5\epsilon_0$	[275]
Al$_2$O$_3$	thickness	$6\,\mathrm{nm}$	-
	$\epsilon_{\mathrm{Al_2O_3}}$	$9.1\epsilon_0$	[275]
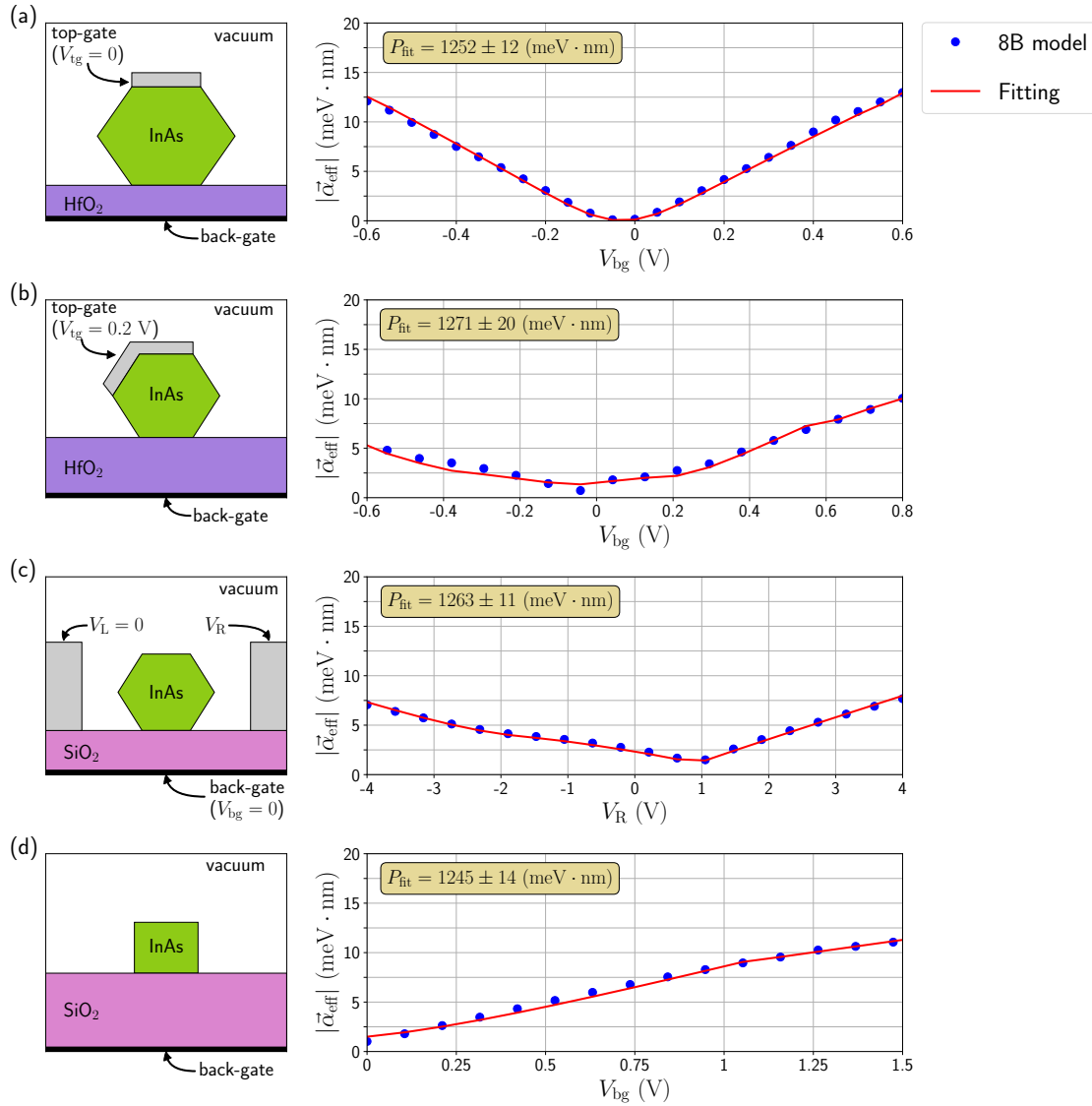
Figure B.2: Effective Rashba SO coupling modulus versus gate voltage for a zinc-blende (111) InAs nanowire with different geometries and located in different electrostatic environments, sketched to the left of each sub-figure. Dots correspond to α_R of the lowest-energy subband obtained from the 8B model Hamiltonian using Eq. (3.42). Solid red curves correspond to the conduction band SO coupling obtained from the improved Eq. (3.43), by fitting P_{fit} in each case to the 8B model result. The resulting P_{fit} values are shown in each sub-figure legend. Parameters: (a) same as in Fig. 3.3; (b) $W_{\mathrm{wire}} = 60$ nm, $W_{\mathrm{substrate}} = 400$ nm, the separation between side gates and the nanowire is 70 nm, $V_{\mathrm{bg}} = 0$ V, $V_L = 0$ V and $\rho_{\mathrm{surf}} = 5 \cdot 10^{-3} \left(\frac{e}{\mathrm{nm}^3}\right)$; (c) $W_{\mathrm{wire}} = 80$ nm, $W_{\mathrm{substrate}} = 50$ nm, $W_{\mathrm{layer}} = 10$ nm, $V_{\mathrm{layer}} = 0.2$ V and $\rho_{\mathrm{surf}} = 0$; (d) $W_{\mathrm{wire}} = 40$ nm, $W_{\mathrm{substrate}} = 40$ nm and $\rho_{\mathrm{surf}} = 5 \cdot 10^{-3} \left(\frac{e}{\mathrm{nm}^3}\right)$. Notice that in this last case the nanowire has a square section instead of hexagonal. The charge density inside the wire ρ_{mobile} has been neglected for simplicity in (a-c), while it has been included in the TF approximation in (d).

C
APPENDIX

APPENDICES FOR CHAPTER 4

C.1 Parameters for Chapter 4

In Table C.1, we provide the parameters that we have used to perform our simulations of Chapter 4. For the parameters used to describe the SO coupling in the SM nanowire, see Appendix B.4.

Table C.1: Parameters used in Chapter 4. Temperature T is fixed to $10\,\mathrm{mK}$ in all our simulations. We use a discretization grid spacing of $0.1\,\mathrm{nm}$ for the FDM.

| Material	Parameter	Value	Refs.
InAs (SM)	m_{eff}	$0.023 m_e$	[158]
	E_{F}	0	[126]
	Δ	0	-
	α_{R}	Eq. (3.43)	-
	ρ_{surf}	$2 \cdot 10^{-3}\left(\frac{\mathrm{e}}{\mathrm{nm}^3}\right)$	[175, 176]
Al (SC)	oxidation width	2 nm	-
	m_{eff}	m_e	[279]
	E_{F}	-11.7 eV	[214]
	Δ	0.23 meV	[81]
	α_{R}	0	[280]
	V_{SC}	0.2 eV	[176, 177]

APPENDIX D

APPENDICES FOR CHAPTER 6

D.1 Simplified model for the induced exchange field

Following the same reasoning as in Sec. 4.4 for the superconducting proximity effect, we can create a simplified model in which we "integrate out" the FI layer and we describe directly the magnetic proximity effect. To do so, as we do in Sec. 4.4, we include an exchange field $h_{\text{ex}}^{(\text{EuS})}$ of the same magnitude than the parent one on the cross-section region closer to the EuS shell, as schematically depicted in Fig. D.1(a). The extension of the corresponding region is extracted by adjusting to the behavior of the full model results. In Fig. D.1(b), we show the effective exchange field computed using the full model (red dots) or using the simplified model with $W_{\text{prox}}^{(\text{EuS})} = 1$ nm (blue line). We find that for $W_{\text{prox}}^{(\text{EuS})} = 1$ nm the agreement of both curves is excellent. The reason of this good agreement is the small penetration length of the electrons inside the FI. For our choice of materials (InAs and EuS), the penetration length inside the FI is typically 1–2 nm. Hence, it is enough to include a proximity region of this size to account for the induced magnetization.

D.2 Comparison between hybrid SM-FI-SC planar and wire devices

The SM/FI/SC stack can also be grown in a hexagonal SM nanowire. Recent experiments have shown that it is possible to grow an epitaxially layer of EuS on selected facets of InAs nanowires, followed by epitaxial Al on top, partially or totally overlapping with EuS [127, 128]. In this Appendix, we analyze the spectrum and topological properties of such a structure to ascertain whether this platform would be better than the planar heterostructure presented in Sec 6.4. We describe the wire device as shown in Fig. 4.1(a) but with a FI layer in between the SC layer and the SM nanowire. The SM wire is an 80 nm-thick InAs nanowire deposited on top of a 200 nm-thick SiO$_2$ dielectric, and gated from below through a back-gate. We highlight that 80 nm is the typical diameter for these nanowires, much larger than the SM thickness in the 2DEG-based devices analyzed in the main text.

The energy spectrum at $k_z = 0$ vs the gate potential is shown, for different thicknesses of the FI layer, in the left panels of Fig. D.2 for the planar device and in Fig. D.3 for the wire one. We show the topological (trivial) phase as a white (gray) background. Comparing both figures, we note that it is possible to tune the wire device in the topological regime for a wider thicknesses of the FI
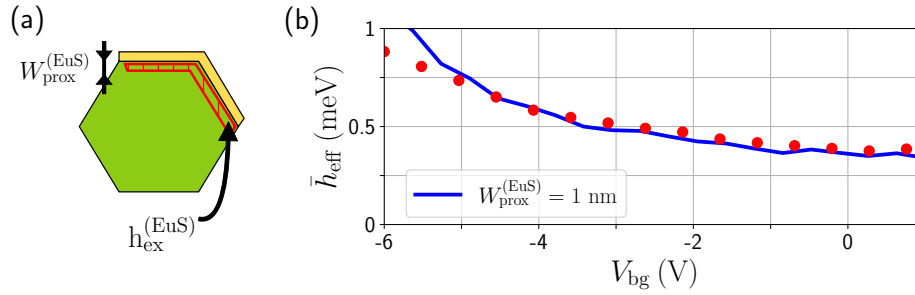
Figure D.1: Comparison between the full and simplified models. (a) In the full model, we include the FI layer in the Hamiltonian at the same level as the nanowire. In the simplified model, the EuS layer is integrated out and the superconducting proximity effect on the wire is included in the Hamiltonian as a proximitized region of width $W_{\mathrm{prox}}^{(\mathrm{EuS})}$ with exchange field $\Delta^{(\mathrm{EuS})}$ (marked as a streaked region in the schematics). (b) Induced exchange field $\bar{h}_{\mathrm{ex}}$ vs the back-gate potential V_{bg} computed with the full model (dots) and the simplified model (lines). For the simplified model, we fix $h_{\mathrm{ex}} = 100$ meV, and we consider different proximitized region thicknesses $W_{\mathrm{prox}}^{(\mathrm{EuS})}$. We show the one that fits the best, $W_{\mathrm{prox}}^{(\mathrm{EuS})} = 1$ nm. The electrostatic environment and parameters are taken as in Fig. 6.2(a) (without the SC layer).

barrier as compared to the planar structure. However, these phases are narrower and appear in a less regular way. This is related to the fact that some bands cannot be tuned to the topological regime as they cannot be confined to the interesting spatial region where superconductivity and exchange field coexists. Therefore, the nanowire exhibits a reduced parameter space where topology exists compared to the planar structure.

This is also illustrated by the effective parameters, shown in the middle panels of Fig. D.2 and Fig. D.3. We note that the exchange field exceeds the superconducting gap for various $V_{\mathrm{tg}}/V_{\mathrm{bg}}$ values. Some of these crossings are correlated to a dip in Δ_{eff}, indicating that the wavefunction is not proximitized by the superconductor and the system remains in the trivial regime.

In the right panels of Fig. D.2 and Fig. D.3, we show the dispersion relation for the same cases. We have chosen parameters deep in a topological regime when present. Notably, the superconducting gap of the wire device is significantly reduced compared to the planar structure: the energy bands of the planar device exhibit a hard gap while the wire device presents several (non-topological) states inside the gap. This is translated, furthermore, in a softer induced gap in the wire device (as compared to the planar one). These ingap states are an obstacle towards applications and the demonstration of Majorana non-Abelian properties. In general, a softening of the gap can be attributed to two main effects: the presence of poorly proximitized subgap states in the SM, and back-action of the SM-FI on the SC that suppresses the pairing. Notice however that, while both effects can be identified in the nanowire case, the softening of the gap in this case can be mainly attributed to states localized in the parent SC. This suggests a stronger back-action of the FI and SM on the SC. This effect appears negligible in the planar case.
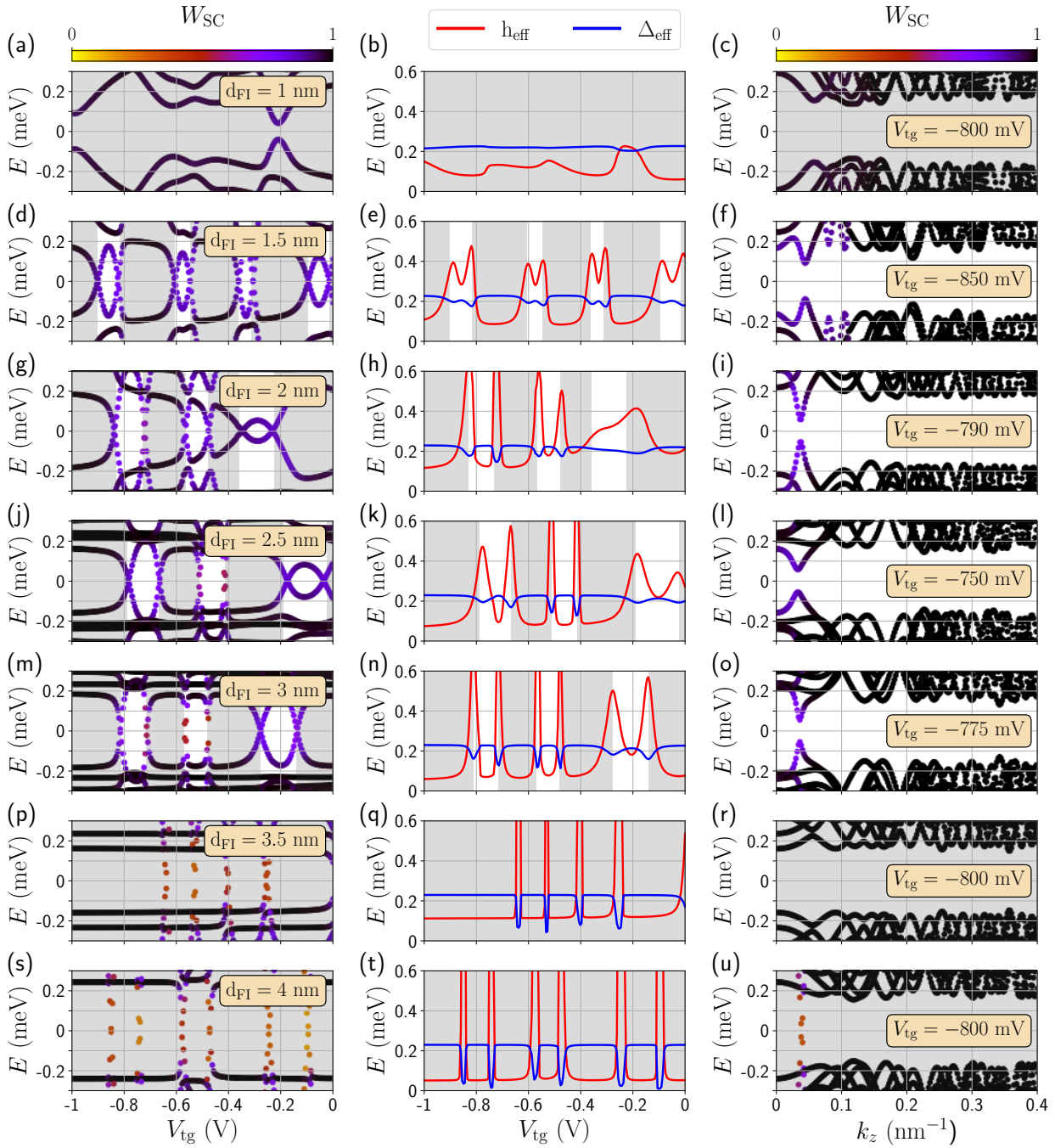
Figure D.2: Left panels: energy spectrum at $k_z = 0$ vs top-gate potential for a device like the one shown in Fig. 6.12. colors represent the weight of each state on the SC. Shaded background V_{tg} regions are characterized by a trivial topological phase, while white background ones correspond to the non-trivial phase. Middle panels: effective exchange coupling h_{eff} and superconducting pairing amplitude Δ_{eff} for the lowest energy state on the left. Right panels: energy bands vs momentum at a certain gate voltage of the left panels. Different rows correspond to different FI layer thicknesses.
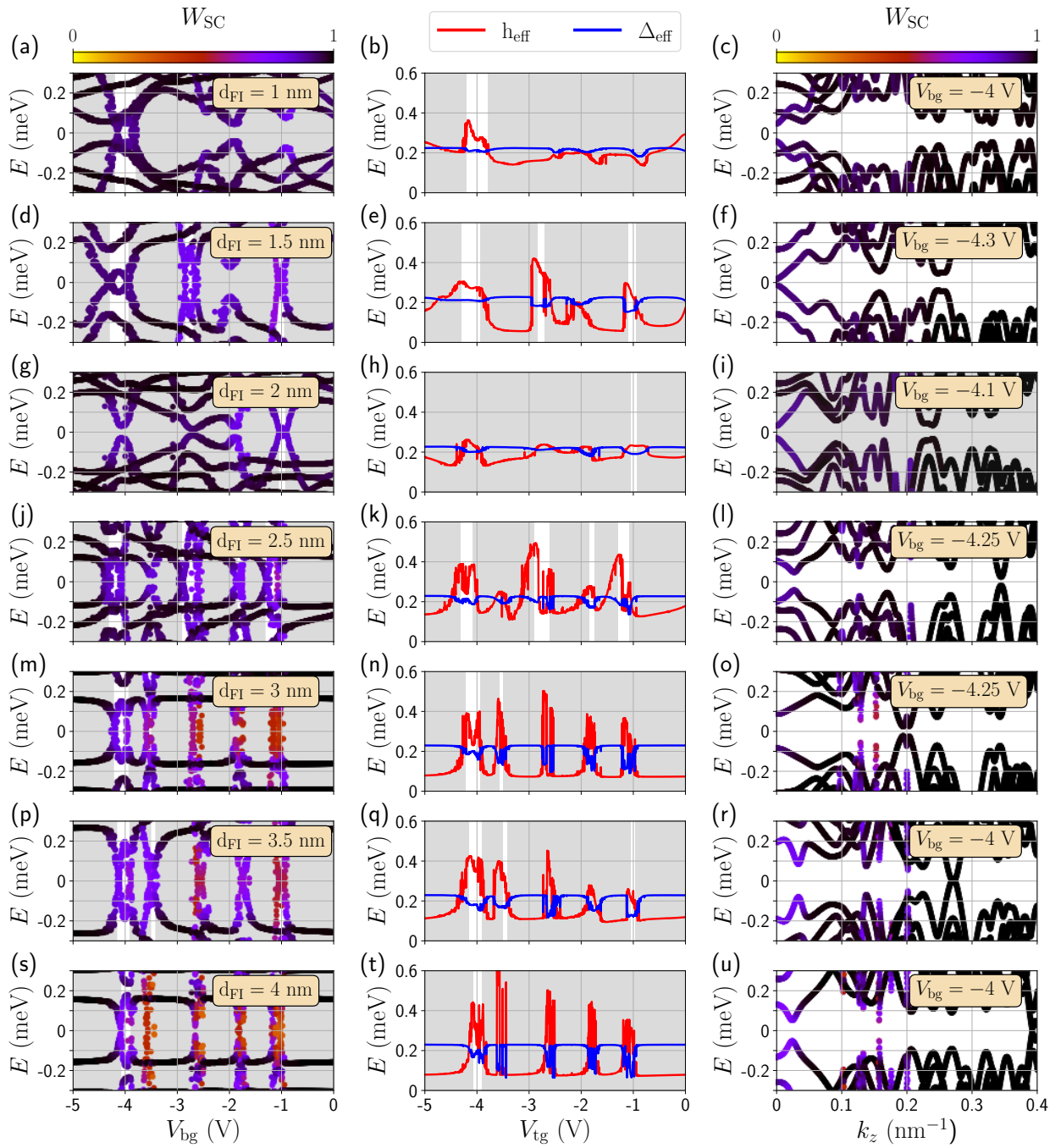
Figure D.3: Same as in Fig. D.2 but for a SM nanowire (like the device shown in Fig. 4.1(a) but with a FI layer in between the SC layer and the SM nanowire).
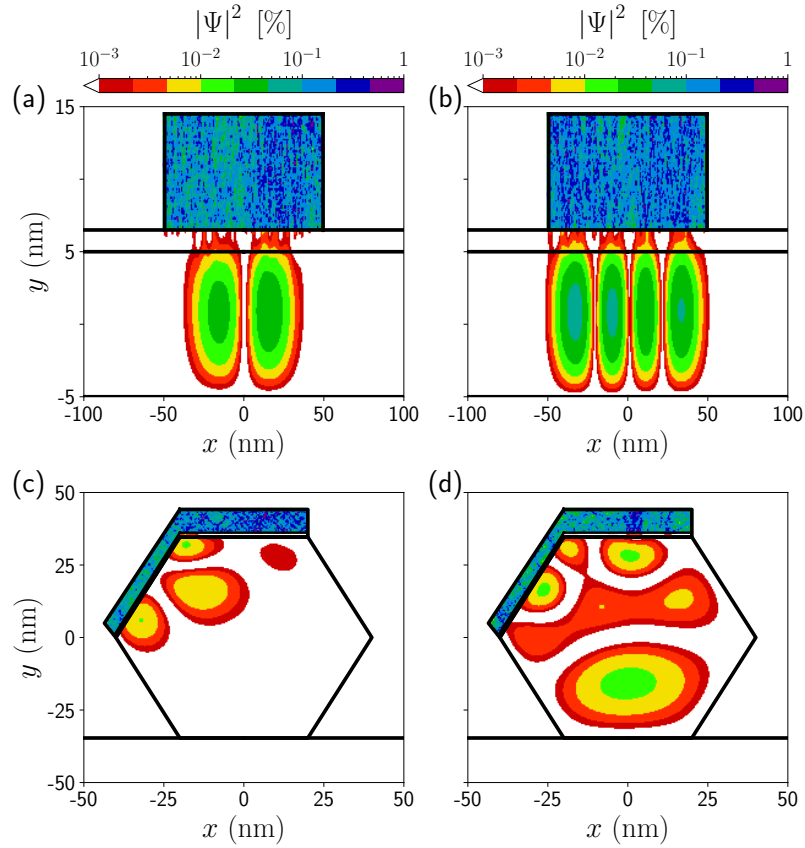
Figure D.4: Wavefunction profile of the lowest-energy state in the planar device (a) in a non-trivial topological phase close to pinch-off, $V_{\text{tg}} = -850$ mV, and (b) in a different non-trivial phase after several subbands are populated in the wire, $V_{\text{tg}} = -350$ mV. We take $d_{\text{FI}} = 1.5$ nm. In (c,d), we show the same profile but for the wire device, also (c) in a non-trivial topological regime close to pinch-off, $V_{\text{bg}} = -4$ V, and (d) in a different non-trivial phase but after several subbands are occupied in the wire, $V_{\text{bg}} = -1$ V. Notice the difference between the FI thickness $d_{\text{FI}} = 10$ nm and the wire's diameter $W_{\text{wire}} = 80$ nm.

This main difference between both devices can be understood by inspecting at their wavefunction profiles. We show two examples of the wavefunction profile in Fig. D.4 for the two geometries considered. The four cases correspond to the lowest-energy state in a topological regime. In the planar geometry (a,b), the wavefunction is well localized below the SC stripe with a regular nodes distribution (top panels in Fig. D.4). This is a consequence of the strong vertical confinement imposed by the thin SM layer. In contrast, the wavefunction in the wire device (bottom panels in Fig. D.4), spreads across the whole cross section of the wire in some cases [Fig. D.4(d)], having a significant weight at positions several nm away from the SM-FI interface. The reduced localization at the interface and the irregular distribution affects the value of the effective superconducting pairing and exchange potential, resulting in the commented reduced topological regions, minigap, and the irregular distribution of the trivial and topological phases in parameter space.

D.3   Parameters for Chapter 6

In Table D.1, we provide the parameters that we have used to perform our simulations of Chapter 6. For the parameters used to describe the SO coupling in the SM part, see Appendix B.4.

Table D.1: Parameters used in Chapter 6. Temperature T is fixed to $10\,\mathrm{mK}$ in all our simulations. We use a discretization grid spacing of $0.1\,\mathrm{nm}$ or $0.2\,\mathrm{nm}$ for the FDM.

Material	Parameter	Value	Refs.
InAs	m^*	$0.023 m_e$	[158]
	E_{F}	0	[126]
	h_{ex}	0	-
	Δ	0	-
	α_{R}	Eq. (3.43)	-
	ρ_{surf}	$2 \cdot 10^{-3} \left(\frac{\mathrm{e}}{\mathrm{nm}^3} \right)$	[175, 176]
Al	oxidation width	$2\,\mathrm{nm}$	-
	m^*	m_e	[279]
	E_{F}	-8 eV	-
	h_{ex}	0	-
	Δ	$0.23\,\mathrm{meV}$	[81]
	α_{R}	0	[280]
	V_{SC}	$0.4\,\mathrm{eV}$	[177]
EuS	m^*	$0.3 m_e$	[244]
	E_{F}	$0.7\,\mathrm{eV}$	[126, 251]
	h_{ex}	$0.1\,\mathrm{eV}$	[242, 251]
	Δ	0	-
	α_{R}	0	-
	ϵ_{EuS}	$10\epsilon_0$	[281]

REFERENCES

[1] E. Noether, Nachrichten von der Gesellschaft der Wissenschaften zu Göttingen, Mathematisch-Physikalische Klasse **1918**, 235 (1918).

[2] L. D. Landau, Zh. Eksp. Teor. Fiz. **7**, 19 (1937).

[3] M. Nakahara, *Geometry, Topology, and Physics (2nd ed.)* (CRC Press, 2003).

[4] A. Altland and M. R. Zirnbauer, Phys. Rev. B **55**, 1142 (1997).

[5] R. B. Laughlin, Phys. Rev. Lett. **50**, 1395 (1983).

[6] D. C. Tsui, H. L. Stormer, and A. C. Gossard, Phys. Rev. Lett. **48**, 1559 (1982).

[7] H. L. Stormer and D. C. Tsui, Science **220**, 1241 (1983).

[8] J. M. Kosterlitz and D. J. Thouless, Journal of Physics C: Solid State Physics **6**, 1181 (1973).

[9] D. J. Thouless, M. Kohmoto, M. P. Nightingale, and M. den Nijs, Phys. Rev. Lett. **49**, 405 (1982).

[10] F. D. M. Haldane, Phys. Rev. Lett. **50**, 1153 (1983).

[11] Press release, "The nobel prize in physics 2016," October, 2016.

[12] C. L. Kane and E. J. Mele, Phys. Rev. Lett. **95**, 146802 (2005).

[13] B. A. Bernevig and S.-C. Zhang, Phys. Rev. Lett. **96**, 106802 (2006).

[14] M. König, S. Wiedmann, C. Brüne, A. Roth, H. Buhmann, L. W. Molenkamp, X.-L. Qi, and S.-C. Zhang, Science **318**, 766 (2007).

[15] M. Z. Hasan and J. E. Moore, Annual Review of Condensed Matter Physics **2**, 55 (2011).

[16] D. Hsieh, D. Qian, L. Wray, Y. Xia, Y. S. Hor, R. J. Cava, and M. Z. Hasan, Nature **452**, 970 (2008).

[17] A. Y. Kitaev, Physics-Uspekhi **44**, 131 (2001).

[18] K. Ishida, H. Mukuda, Y. Kitaoka, K. Asayama, Z. Q. Mao, Y. Mori, and Y. Maeno, Nature **396**, 658 (1998).

[19] L. Fu and C. L. Kane, Phys. Rev. Lett. **100**, 096407 (2008).

[20] Y. Oreg, G. Refael, and F. von Oppen, Phys. Rev. Lett. **105**, 177002 (2010).

[21] R. M. Lutchyn, J. D. Sau, and S. Das Sarma, Phys. Rev. Lett. **105**, 077001 (2010).

[22] R. Aguado, La Rivista del Nuovo Cimento **40**, 523 (2017).

[23] C. W. J. Beenakker, SciPost Phys. Lect. Notes , 15 (2020).

[24] C. Nayak, S. H. Simon, A. Stern, M. Freedman, and S. Das Sarma, Rev. Mod. Phys. **80**, 1083 (2008).

[25] A. Kitaev, Annals of Physics **303**, 2 (2003).

[26] M. Aghaee *et al.*, Preprint at http://arxiv.org/abs/2207.02472 (2022).

[27] E. Prada, P. San-Jose, M. W. A. de Moor, A. Geresdi, E. J. H. Lee, J. Klinovaja, D. Loss, J. Nygård, R. Aguado, and L. P. Kouwenhoven, Nature Reviews Physics **2**, 575 (2020).

[28] E. Majorana, Il Nuovo Cimento (1924-1942) **14**, 171 (1937).

[29] F. T. Avignone, S. R. Elliott, and J. Engel, Rev. Mod. Phys. **80**, 481 (2008).

[30] J. J. Gómez-Cadenas, J. Martin-Albo, M. Mezzetto, F. Monrabal, and M. Sorel, La Rivista del Nuovo Cimento **35**, 29 (2012).

[31] A. B. McDonald, A. Giuliani, and A. Poves, Advances in High Energy Physics **2012**, 857016 (2012).

[32] S. Dell'Oro, S. Marcocci, M. Viel, and F. Vissani, Advances in High Energy Physics **2016**, 2162659 (2016).

[33] S. Fujimoto, Phys. Rev. B **77**, 220501 (2008).

[34] C. Zhang, S. Tewari, R. M. Lutchyn, and S. Das Sarma, Phys. Rev. Lett. **101**, 160401 (2008).

[35] M. Sato, Y. Takahashi, and S. Fujimoto, Phys. Rev. Lett. **103**, 020401 (2009).

[36] J. D. Sau, R. M. Lutchyn, S. Tewari, and S. Das Sarma, Phys. Rev. Lett. **104**, 040502 (2010).

[37] J. Alicea, Reports on Progress in Physics **75**, 076501 (2012).

[38] M. Leijnse and K. Flensberg, Semiconductor Science and Technology **27**, 124003 (2012).

[39] C. Beenakker, Annual Review of Condensed Matter Physics **4**, 113 (2013).

[40] T. D. Stanescu and S. Tewari, Journal of Physics: Condensed Matter **25**, 233201 (2013).

[41] S. D. Sarma, M. Freedman, and C. Nayak, Npj Quantum Information **1**, 15001 (2015).

[42] C. W. J. Beenakker, Rev. Mod. Phys. **87**, 1037 (2015).

[43] M. Sato and S. Fujimoto, Journal of the Physical Society of Japan **85**, 072001 (2016).

[44] R. M. Lutchyn, E. P. A. M. Bakkers, L. P. Kouwenhoven, P. Krogstrup, C. M. Marcus, and Y. Oreg, Nature Reviews Materials **3**, 2058 (2018).

[45] H. Zhang, O. Gül, S. Conesa-Boj, M. Nowak, M. Wimmer, K. Zuo, V. Mourik, F. K. de Vries, J. van Veen, M. W. A. de Moor, J. D. S. Bommer, D. J. van Woerkom, D. Car, S. R. Plissard, E. P. A. M. Bakkers, M. Quintero-Pérez, M. C. Cassidy, S. Koelling, S. Goswami, K. Watanabe, T. Taniguchi, and L. P. Kouwenhoven, Nature Communications **8**, 16025 (2017).

[46] A. Kitaev, AIP Conference Proceedings **1134**, 22 (2009).

[47] M. Sato and S. Fujimoto, Phys. Rev. B **79**, 094504 (2009).

[48] D. Aasen, M. Hell, R. V. Mishmash, A. Higginbotham, J. Danon, M. Leijnse, T. S. Jespersen, J. A. Folk, C. M. Marcus, K. Flensberg, and J. Alicea, Phys. Rev. X **6**, 031016 (2016).

[49] N. Read and D. Green, Phys. Rev. B **61**, 10267 (2000).

[50] G. Moore and N. Read, Nuclear Physics B **360**, 362 (1991).

[51] J. Klinovaja and D. Loss, Phys. Rev. B **86**, 085408 (2012).

[52] V. Mourik, K. Zuo, S. M. Frolov, S. R. Plissard, E. P. A. M. Bakkers, and L. P. Kouwenhoven, Science **336**, 1003 (2012).

[53] A. Das, Y. Ronen, Y. Most, Y. Oreg, M. Heiblum, and H. Shtrikman, Nature Physics **8**, 887 (2012).

[54] M. T. Deng, S. Vaitiekenas, E. B. Hansen, J. Danon, M. Leijnse, K. Flensberg, J. Nygård, P. Krogstrup, and C. M. Marcus, Science **354**, 1557 (2016).

[55] O. Gül, H. Zhang, F. K. de Vries, J. van Veen, K. Zuo, V. Mourik, S. Conesa-Boj, M. P. Nowak, D. J. van Woerkom, M. Quintero-Pérez, M. C. Cassidy, A. Geresdi, S. Koelling, D. Car, S. R. Plissard, E. P. A. M. Bakkers, and L. P. Kouwenhoven, Nano Letters **17**, 2690 (2017).

[56] S. Vaitiekėnas, G. W. Winkler, B. van Heck, T. Karzig, M.-T. Deng, K. Flensberg, L. I. Glazman, C. Nayak, P. Krogstrup, R. M. Lutchyn, and C. M. Marcus, Science **367**, eaav3392 (2020).

[57] S. Vaitiekėnas, P. Krogstrup, and C. M. Marcus, Phys. Rev. B **101**, 060507 (2020).

[58] M. Valentini, F. Peñaranda, A. Hofmann, M. Brauns, R. Hauschild, P. Krogstrup, P. San-Jose, E. Prada, R. Aguado, and G. Katsaros, Science **373**, 82 (2021).

[59] H. J. Suominen, M. Kjaergaard, A. R. Hamilton, J. Shabani, C. J. Palmstrøm, C. M. Marcus, and F. Nichele, Phys. Rev. Lett. **119**, 176805 (2017).

[60] M. Kjaergaard, F. Nichele, H. J. Suominen, M. P. Nowak, M. Wimmer, A. R. Akhmerov, J. A. Folk, K. Flensberg, J. Shabani, C. J. Palmstrøm, and C. M. Marcus, Nature Communications **7**, 12841 (2016).

[61] A. Fornieri, A. M. Whiticar, F. Setiawan, E. Portolés, A. C. C. Drachmann, A. Keselman, S. Gronin, C. Thomas, T. Wang, R. Kallaher, G. C. Gardner, E. Berg, M. J. Manfra, A. Stern, C. M. Marcus, and F. Nichele, Nature **569**, 89 (2019).

[62] J. S. Lee, B. Shojaei, M. Pendharkar, A. P. McFadden, Y. Kim, H. J. Suominen, M. Kjaergaard, F. Nichele, H. Zhang, C. M. Marcus, and C. J. Palmstrøm, Nano Letters **19**, 3083 (2019).

[63] E. P. A. M. Bakkers, M. T. Borgström, and M. A. Verheijen, MRS Bulletin **32**, 117–122 (2007).

[64] K. Tomioka, J. Motohisa, S. Hara, and T. Fukui, Nano Letters **8**, 3475 (2008).

[65] P. Krogstrup, H. I. Jørgensen, E. Johnson, M. H. Madsen, C. B. Sørensen, A. F. i Morral, M. Aagesen, J. Nygård, and F. Glas, Journal of Physics D: Applied Physics **46**, 313001 (2013).

[66] G. Badawy, S. Gazibegovic, F. Borsoi, S. Heedt, C.-A. Wang, S. Koelling, M. A. Verheijen, L. P. Kouwenhoven, and E. P. A. M. Bakkers, Nano Letters **19**, 3575 (2019).

[67] J. Gooth, V. Schaller, S. Wirths, H. Schmid, M. Borg, N. Bologna, S. Karg, and H. Riel, Applied Physics Letters **110**, 083105 (2017).

[68] D. Liang, J. Du, and X. P. Gao, Journal of Materials Science & Technology **31**, 542 (2015), a Special Issue on 1D Nanomaterials.

[69] S. Dhara, H. S. Solanki, V. Singh, A. Narayanan, P. Chaudhari, M. Gokhale, A. Bhattacharya, and M. M. Deshmukh, Phys. Rev. B **79**, 121311 (2009).

[70] D. Liang and X. P. Gao, Nano Letters **12**, 3263 (2012).

[71] I. van Weperen, B. Tarasinski, D. Eeltink, V. S. Pribiag, S. R. Plissard, E. P. A. M. Bakkers, L. P. Kouwenhoven, and M. Wimmer, Phys. Rev. B **91**, 201413 (2015).

[72] K. Takase, Y. Ashikawa, G. Zhang, K. Tateno, and S. Sasaki, Scientific Reports **7**, 2045 (2017).

[73] Z. Scherübl, G. Fülöp, M. H. Madsen, J. Nygård, and S. Csonka, Phys. Rev. B **94**, 035444 (2016).

[74] K. Takase, K. Tateno, and S. Sasaki, Applied Physics Express **12**, 117002 (2019).

[75] C. R. Pidgeon, D. L. Mitchell, and R. N. Brown, Phys. Rev. **154**, 737 (1967).

[76] J. Konopka, Physics Letters A **26**, 29 (1967).

[77] S. M. Albrecht, A. P. Higginbotham, M. Madsen, F. Kuemmeth, T. S. Jespersen, J. Nygård, P. Krogstrup, and C. M. Marcus, Nature **531**, 206 (2016).

[78] S. Vaitiekėnas, M.-T. Deng, J. Nygård, P. Krogstrup, and C. M. Marcus, Phys. Rev. Lett. **121**, 037703 (2018).

[79] M. Tinkham, *Introduction to superconductivity* (Courier Corporation, 2004).

[80] P. Krogstrup, N. L. B. Ziino, W. Chang, S. M. Albrecht, M. H. Madsen, E. Johnson, J. Nygård, C. M. Marcus, and T. S. Jespersen, Nature Materials **14**, 400 (2015).

[81] W. Chang, S. M. Albrecht, T. S. Jespersen, F. Kuemmeth, P. Krogstrup, J. Nygård, and C. M. Marcus, Nature Nanotechnology **10**, 232 (2018).

[82] J.-H. Kang, A. Grivnin, E. Bor, J. Reiner, N. Avraham, Y. Ronen, Y. Cohen, P. Kacman, H. Shtrikman, and H. Beidenkopf, Nano Letters **17**, 7520 (2017).

[83] O. Gül, H. Zhang, J. D. S. Bommer, M. W. A. d. Moor, D. Car, S. R. Plissard, E. P. A. M. Bakkers, A. Geresdi, K. Watanabe, T. Taniguchi, and L. P. Kouwenhoven, Nature News **13**, 192 (2018).

[84] H. Zhang, C.-X. Liu, S. Gazibegovic, D. Xu, J. A. Logan, G. Wang, N. van Loo, J. D. Bommer, M. W. de Moor, D. Car, R. L. M. O. h. Veld, P. J. van Veldhoven, S. Koelling, M. A. Verheijen, M. Pendharkar, D. J. Pennachio, B. Shojaei, J. S. Lee, C. J. Palmstrøm, E. P. Bakkers, S. Das Sarma, and L. P. Kouwenhoven, Nature **556**, 74 (2018).

[85] J. Chen, B. D. Woods, P. Yu, M. Hocevar, D. Car, S. R. Plissard, E. P. A. M. Bakkers, T. D. Stanescu, and S. M. Frolov, Phys. Rev. Lett. **123**, 107703 (2019).

[86] A. Grivnin, E. Bor, M. Heiblum, Y. Oreg, and H. Shtrikman, Nature Communications **10**, 1940 (2019).

[87] J. Danon, A. B. Hellenes, E. B. Hansen, L. Casparis, A. P. Higginbotham, and K. Flensberg, Phys. Rev. Lett. **124**, 036801 (2020).

[88] G. C. Ménard, G. L. R. Anselmetti, E. A. Martinez, D. Puglia, F. K. Malinowski, J. S. Lee, S. Choi, M. Pendharkar, C. J. Palmstrøm, K. Flensberg, C. M. Marcus, L. Casparis, and A. P. Higginbotham, Phys. Rev. Lett. **124**, 036802 (2020).

[89] A. Pöschl, A. Danilenko, D. Sabonis, K. Kristjuhan, T. Lindemann, C. Thomas, M. J. Manfra, and C. M. Marcus, Phys. Rev. B **106**, L161301 (2022).

[90] A. Pöschl, A. Danilenko, D. Sabonis, K. Kristjuhan, T. Lindemann, C. Thomas, M. J. Manfra, and C. M. Marcus, Preprint at https://arxiv.org/abs/2204.02430 (2022).

[91] E. Prada, P. San-Jose, and R. Aguado, Phys. Rev. B **86**, 180503(R) (2012).

[92] L. Fidkowski, J. Alicea, N. H. Lindner, R. M. Lutchyn, and M. P. A. Fisher, Phys. Rev. B **85**, 245121 (2012).

[93] R. M. Lutchyn and J. H. Skrabacz, Phys. Rev. B **88**, 024511 (2013).

[94] G. Kells, D. Meidan, and P. W. Brouwer, Phys. Rev. B **86**, 100503(R) (2012).

[95] T. D. Stanescu and S. Tewari, Phys. Rev. B **89**, 220507 (2014).

[96] C. Moore, C. Zeng, T. D. Stanescu, and S. Tewari, Phys. Rev. B **98**, 155314 (2018).

[97] C.-X. Liu, J. D. Sau, and S. Das Sarma, Phys. Rev. B **97**, 214502 (2018).

[98] F. Peñaranda, R. Aguado, P. San-Jose, and E. Prada, Phys. Rev. B **98**, 235406 (2018).

[99] S. D. Escribano, A. L. Yeyati, and E. Prada, Beilstein Journal of Nanotechnology **9**, 2171 (2018).

[100] C. Reeg, O. Dmytruk, D. Chevallier, D. Loss, and J. Klinovaja, Phys. Rev. B **98**, 245407 (2018).

[101] C.-X. Liu, J. D. Sau, T. D. Stanescu, and S. Das Sarma, Phys. Rev. B **99**, 024510 (2019).

[102] A. Vuik, B. Nijholt, A. R. Akhmerov, and M. Wimmer, SciPost Phys. **7**, 61 (2019).

[103] B. D. Woods, S. Das Sarma, and T. D. Stanescu, Phys. Rev. B **99**, 161118 (2019).

[104] H. Pan and S. Das Sarma, Phys. Rev. Research **2**, 013377 (2020).

[105] H. Pan, C.-X. Liu, M. Wimmer, and S. Das Sarma, Phys. Rev. B **103**, 214502 (2021).

[106] J. Klinovaja and D. Loss, The European Physical Journal B **88**, 62 (2015).

[107] F. Dolcini and F. Rossi, Phys. Rev. B **98**, 045436 (2018).

[108] Z. Cao, H. Zhang, H.-F. Lü, W.-X. He, H.-Z. Lu, and X. C. Xie, Phys. Rev. Lett. **122**, 147701 (2019).

[109] H. Pan, W. S. Cole, J. D. Sau, and S. Das Sarma, Phys. Rev. B **101**, 024506 (2020).

[110] O. Dmytruk, D. Loss, and J. Klinovaja, Phys. Rev. B **102**, 245431 (2020).

[111] C. Reeg, D. Loss, and J. Klinovaja, Phys. Rev. B **97**, 165425 (2018).

[112] C. Reeg, D. Loss, and J. Klinovaja, Beilstein J. Nanotechnol. **9**, 1263 (2018).

[113] A. E. G. Mikkelsen, P. Kotetes, P. Krogstrup, and K. Flensberg, Phys. Rev. X **8**, 031040 (2018).

[114] A. E. Antipov, A. Bargerbos, G. W. Winkler, B. Bauer, E. Rossi, and R. M. Lutchyn, Phys. Rev. X **8**, 031041 (2018).

[115] G. W. Winkler, A. E. Antipov, B. van Heck, A. A. Soluyanov, L. I. Glazman, M. Wimmer, and R. M. Lutchyn, Phys. Rev. B **99**, 245408 (2019).

[116] B. D. Woods, S. Das Sarma, and T. D. Stanescu, Phys. Rev. Applied **16**, 054053 (2021).

[117] S. Ahn, H. Pan, B. Woods, T. D. Stanescu, and S. Das Sarma, Phys. Rev. Mater. **5**, 1 (2021).

[118] D. Bagrets and A. Altland, Phys. Rev. Lett. **109**, 227005 (2012).

[119] D. I. Pikulin, J. P. Dahlhaus, M. Wimmer, H. Schomerus, and C. W. J. Beenakker, New Journal of Physics **14**, 125011 (2012).

[120] S. Das Sarma and H. Pan, Phys. Rev. B **103**, 195158 (2021).

[121] T. D. Stanescu and S. Das Sarma, Phys. Rev. B **106**, 085429 (2022).

[122] H. Pan and S. Das Sarma, Phys. Rev. B **105**, 115432 (2022).

[123] B. Nijholt and A. R. Akhmerov, Phys. Rev. B **93**, 235434 (2016).

[124] O. Dmytruk and J. Klinovaja, Phys. Rev. B **97**, 155409 (2018).

[125] Y. Liu, S. Vaitiekėnas, S. Martí-Sánchez, C. Koch, S. Hart, Z. Cui, T. Kanne, S. A. Khan, R. Tanta, S. Upadhyay, M. E. Cachaza, C. M. Marcus, J. Arbiol, K. A. Moler, and P. Krogstrup, Nano Lett. **20**, 456 (2020).

[126] Y. Liu, A. Luchini, S. Martí-Sánchez, C. Koch, S. Schuwalow, S. A. Khan, T. Stankevič, S. Francoual, J. R. Mardegan, J. A. Krieger, V. N. Strocov, J. Stahn, C. A. Vaz, M. Ramakrishnan, U. Staub, K. Lefmann, G. Aeppli, J. Arbiol, and P. Krogstrup, ACS Appl. Mater. Interfaces **12**, 8780 (2020).

[127] S. Vaitiekėnas, Y. Liu, P. Krogstrup, and C. M. Marcus, Nat. Phys. **17**, 43 (2021).

[128] S. Vaitiekėnas, R. S. Souto, Y. Liu, P. Krogstrup, K. Flensberg, M. Leijnse, and C. M. Marcus, Phys. Rev. B **105**, L041304 (2022).

[129] B. Nijholt, *Towards realistic numerical simulations of Majorana devices* (Delft University of Technology, 2020).

[130] B. D. Woods, *Majorana Nanostructures and Their Electrostatic Environment* (Graduate Theses, Dissertations, and Problem Reports, 2021).

[131] A. Vuik, D. Eeltink, A. R. Akhmerov, and M. Wimmer, New Journal of Physics **18**, 033013 (2016).

[132] S. D. Escribano, A. Levy Yeyati, R. Aguado, E. Prada, and P. San-Jose, Phys. Rev. B **105**, 045418 (2022).

[133] S. D. Escribano, "MajoranaNanowires: Quantum Simulation Package," v1.0 (2020).

[134] C. Grossmann, H.-G. Roos, and M. Stynes, *Numerical Treatment of Partial Differential Equations* (Springer Berlin, Heidelberg, 2007).

[135] C. G. Broyden, Mathematics of Computation **19**, 577 (1965).

[136] D. G. Anderson, J. ACM **12**, 547–560 (1965).

[137] D. D. Johnson, Phys. Rev. B **38**, 12807 (1988).

[138] V. Eyert, Journal of Computational Physics **124**, 271 (1996).

[139] P. Hohenberg and W. Kohn, Phys. Rev. **136**, B864 (1964).

[140] P. Virtanen, R. Gommers, T. E. Oliphant, M. Haberland, T. Reddy, D. Cournapeau, E. Burovski, P. Peterson, W. Weckesser, J. Bright, S. J. van der Walt, M. Brett, J. Wilson, K. J. Millman, N. Mayorov, A. R. J. Nelson, E. Jones, R. Kern, E. Larson, C. J. Carey, İ. Polat, Y. Feng, E. W. Moore, J. VanderPlas, D. Laxalde, J. Perktold, R. Cimrman, I. Henriksen, E. A. Quintero, C. R. Harris, A. M. Archibald, A. H. Ribeiro, F. Pedregosa, P. van Mulbregt, and SciPy 1.0 Contributors, Nature Methods **17**, 261 (2020).

[141] E. Anderson, Z. Bai, C. Bischof, S. Blackford, J. Demmel, J. Dongarra, J. Du Croz, A. Green-baum, S. Hammarling, A. McKenney, and D. Sorensen, *LAPACK Users' Guide*, 3rd ed. (Society for Industrial and Applied Mathematics, Philadelphia, PA, 1999).

[142] A. P. Schnyder, S. Ryu, A. Furusaki, and A. W. W. Ludwig, Phys. Rev. B **78**, 195125 (2008).

[143] T. A. Loring and M. B. Hastings, EPL (Europhysics Letters) **92**, 67004 (2010).

[144] Y.-F. Zhang, Y.-Y. Yang, Y. Ju, L. Sheng, R. Shen, D.-N. Sheng, and D.-Y. Xing, Chinese Physics B **22**, 117312 (2013).

[145] O. Lesser and Y. Oreg, Phys. Rev. Research **2**, 023063 (2020).

[146] R. Yu, X. L. Qi, A. Bernevig, Z. Fang, and X. Dai, Phys. Rev. B **84**, 075119 (2011).

[147] A. Alexandradinata, Z. Wang, and B. A. Bernevig, Phys. Rev. X **6**, 021008 (2016).

[148] B. Bradlyn, Z. Wang, J. Cano, and B. A. Bernevig, Phys. Rev. B **99**, 045140 (2019).

[149] A. Logg and G. N. Wells, ACM Transactions on Mathematical Software **37**, 1 (2010).

[150] A. Logg, K.-A. Mardal, G. N. Wells, *et al.*, *Automated Solution of Differential Equations by the Finite Element Method* (Springer, Berlin, Heidelberg, 2012).

[151] S. D. Escribano, A. L. Yeyati, and E. Prada, Phys. Rev. Research **2**, 033264 (2020).

[152] Manuscript in preparation.

[153] Y. Li, F. Qian, J. Xiang, and C. M. Lieber, Materials Today **9**, 18 (2006).

[154] H. J. Joyce, Q. Gao, H. Hoe Tan, C. Jagadish, Y. Kim, J. Zou, L. M. Smith, H. E. Jackson, J. M. Yarrison-Rice, P. Parkinson, and M. B. Johnston, Progress in Quantum Electronics **35**, 23 (2011).

[155] N. P. Dasgupta, J. Sun, C. Liu, S. Brittman, S. C. Andrews, J. Lim, H. Gao, R. Yan, and P. Yang, Advanced Materials **26**, 2137 (2014).

[156] S. Datta and B. Das, Applied Physics Letters **56**, 665 (1990).

[157] I. Žutić, J. Fabian, and S. Das Sarma, Rev. Mod. Phys. **76**, 323 (2004).

[158] I. Vurgaftman, J. R. Meyer, and L. R. Ram-Mohan, Journal of Applied Physics **89**, 5815 (2001).

[159] R. Winkler, S. Papadakis, E. De Poortere, and M. Shayegan, *Spin-Orbit Coupling in Two-Dimensional Electron and Hole Systems*, Vol. 41 (Springer, Berlin, Heidelberg, 2003).

[160] T. Campos, P. E. Faria Junior, M. Gmitra, G. M. Sipahi, and J. Fabian, Phys. Rev. B **97**, 245402 (2018).

[161] M. Willatzen and L. C. L. Y. Voon, *The k·p Method* (Springer, Berlin, Heidelberg, 2009).

[162] C. M. O. Bastos, F. P. Sabino, P. E. F. Junior, T. Campos, J. L. F. D. Silva, and G. M. Sipahi, Semiconductor Science and Technology **31**, 105002 (2016).

[163] P. Löwdin, The Journal of Chemical Physics **19**, 1396 (1951).

[164] J. M. Luttinger and W. Kohn, Phys. Rev. **97**, 869 (1955).

[165] E. O. Kane, Journal of Physics and Chemistry of Solids **1**, 249 (1957).

[166] P. E. Faria Junior, T. Campos, C. M. O. Bastos, M. Gmitra, J. Fabian, and G. M. Sipahi, Phys. Rev. B **93**, 235204 (2016).

[167] N. Luo, G. Liao, and H. Q. Xu, AIP Advances **6**, 125109 (2016).

[168] Y. M. Niquet, A. Lherbier, N. H. Quang, M. V. Fernández-Serra, X. Blase, and C. Delerue, Phys. Rev. B **73**, 165319 (2006).

[169] V. V. R. Kishore, N. Čukarić, B. Partoens, M. Tadić, and F. M. Peeters, Journal of Physics: Condensed Matter **24**, 135302 (2012).

[170] M. Ehrhardt and T. Koprucki, *Multi-Band Effective Mass Approximations*, Vol. 94 (Springer International Publishing, 2014).

[171] A. A. Soluyanov, D. Gresch, M. Troyer, R. M. Lutchyn, B. Bauer, and C. Nayak, Phys. Rev. B **93**, 115317 (2016).

[172] T. Darnhofer and U. Rössler, Phys. Rev. B **47**, 16020 (1993).

[173] P. Wójcik, A. Bertoni, and G. Goldoni, Phys. Rev. B **97**, 165401 (2018).

[174] L. O. Olsson, C. B. M. Andersson, M. C. Håkansson, J. Kanski, L. Ilver, and U. O. Karlsson, Phys. Rev. Lett. **76**, 3626 (1996).

[175] C. Thelander, K. A. Dick, M. T. Borgström, L. E. Fröberg, P. Caroff, H. A. Nilsson, and L. Samuelson, Nanotechnology **21**, 205703 (2010).

[176] J. Reiner, A. K. Nayak, A. Tulchinsky, A. Steinbok, T. Koren, N. Morali, R. Batabyal, J.-H. Kang, N. Avraham, Y. Oreg, H. Shtrikman, and H. Beidenkopf, Phys. Rev. X **10**, 011002 (2020).

[177] C.-X. Liu, S. Schuwalow, Y. Liu, K. Vilkelis, A. L. R. Manesco, P. Krogstrup, and M. Wimmer, Phys. Rev. B **104**, 014516 (2021).

[178] S. D. Escribano, A. Levy Yeyati, Y. Oreg, and E. Prada, Phys. Rev. B **100**, 045301 (2019).

[179] F. Domínguez, J. Cayao, P. San-Jose, R. Aguado, A. Levy Yeyati, and E. Prada, npj Quantum Materials **2**, 2397 (2017).

[180] M. Gmitra and J. Fabian, Phys. Rev. B **94**, 165202 (2016).

[181] A. E. Hansen, M. T. Björk, C. Fasth, C. Thelander, and L. Samuelson, Phys. Rev. B **71**, 205328 (2005).

[182] A. Iorio, M. Rocci, L. Bours, M. Carrega, V. Zannier, L. Sorba, S. Roddaro, F. Giazotto, and E. Strambini, Nano Letters **19**, 652 (2019).

[183] M. W. A. de Moor, J. D. S. Bommer, D. Xu, G. W. Winkler, A. E. Antipov, A. Bargerbos, G. Wang, and N. van Loo, New J. Phys. **20**, 103049 (2018).

[184] J. D. S. Bommer, H. Zhang, O. Gül, B. Nijholt, M. Wimmer, F. N. Rybakov, J. Garaud, D. Rodic, E. Babaev, M. Troyer, D. Car, S. R. Plissard, E. P. A. M. Bakkers, K. Watanabe, T. Taniguchi, and L. P. Kouwenhoven, Phys. Rev. Lett. **122**, 187702 (2019).

[185] J. Nitta, T. Akazaki, H. Takayanagi, and T. Enoki, Phys. Rev. Lett. **78**, 1335 (1997).

[186] D. M. Zumbühl, J. B. Miller, C. M. Marcus, K. Campman, and A. C. Gossard, Phys. Rev. Lett. **89**, 276803 (2002).

[187] S. A. Studenikin, P. T. Coleridge, N. Ahmed, P. J. Poole, and A. Sachrajda, Phys. Rev. B **68**, 035317 (2003).

[188] T. Schäpers, J. Knobbe, and V. A. Guzenko, Phys. Rev. B **69**, 235323 (2004).

[189] H. C. Koo, J. H. Kwon, J. Eom, J. Chang, S. H. Han, and M. Johnson, Science **325**, 1515 (2009).

[190] R. L. Kallaher, J. J. Heremans, N. Goel, S. J. Chung, and M. B. Santos, Phys. Rev. B **81**, 075303 (2010).

[191] S. Nadj-Perge, V. S. Pribiag, J. W. G. van den Berg, K. Zuo, S. R. Plissard, E. P. A. M. Bakkers, S. M. Frolov, and L. P. Kouwenhoven, Phys. Rev. Lett. **108**, 166801 (2012).

[192] P. Zellekens, N. Demarina, J. Janßen, T. Rieger, M. I. Lepsa, P. Perla, G. Panaitov, H. Lüth, D. Grützmacher, and T. Schäpers, Semiconductor Science and Technology **35**, 085003 (2020).

[193] S. Chakravarty and A. Schmid, Physics Reports **140**, 193 (1986).

[194] C. W. J. Beenakker and H. van Houten, Phys. Rev. B **38**, 3232 (1988).

[195] C. Kurdak, A. M. Chang, A. Chin, and T. Y. Chang, Phys. Rev. B **46**, 6846 (1992).

[196] Y. Gindikin and V. A. Sablikov, The European Physical Journal Special Topics **229**, 503 (2020).

[197] C. P. Kuo, S. K. Vong, R. M. Cohen, and G. B. Stringfellow, Journal of Applied Physics **57**, 5428 (1985).

[198] T. B. Bahder, Phys. Rev. B **41**, 11992 (1990).

[199] C. Pryor, Phys. Rev. B **57**, 7190 (1998).

[200] C. L. dos Santos and P. Piquini, Journal of Applied Physics **111**, 054315 (2012).

[201] A. Çakan, C. Sevik, and C. Bulutay, Journal of Physics D: Applied Physics **49**, 085104 (2016).

[202] P. Razavi and J. C. Greer, Solid-State Electronics **149**, 6 (2018).

[203] M. W. Larsson, J. B. Wagner, M. Wallin, P. Håkansson, L. E. Fröberg, L. Samuelson, and L. R. Wallenberg, Nanotechnology **18**, 015504 (2006).

[204] M.-E. Pistol and C. E. Pryor, Phys. Rev. B **78**, 115319 (2008).

[205] G. Zhang, M. Takiguchi, K. Tateno, T. Tawara, M. Notomi, and H. Gotoh, Science Advances **5**, eaat8896 (2019).

[206] D. Göransson, *Strain and Charge Transport in InAsP-InP and InP-InAs Core-Shell Nanowires*, Ph.D. thesis, Faculty of Engineering, LTH, Solid State Physics (2019).

[207] O. Arif, V. Zannier, A. Li, F. Rossi, D. Ercolani, F. Beltram, and L. Sorba, Crystal Growth & Design **20**, 1088 (2020).

[208] K. Takase, K. Tateno, and S. Sasaki, Applied Physics Letters **119**, 013102 (2021).

[209] S. D. Escribano, E. Prada, Y. Oreg, and A. L. Yeyati, Phys. Rev. B **104**, L041404 (2021).

[210] T. Kanne, M. Marnauza, D. Olsteins, D. J. Carrad, J. E. Sestoft, J. de Bruijckere, L. Zeng, E. Johnson, E. Olsson, K. Grove-Rasmussen, and J. Nygård, Nature Nanotechnology **16**, 776 (2021).

[211] M. Bjergfelt, D. J. Carrad, T. Kanne, M. Aagesen, E. M. Fiordaliso, E. Johnson, B. Shojaei, C. J. Palmstrøm, P. Krogstrup, T. S. Jespersen, and J. Nygård, Nanotechnology **30**, 294005 (2019).

[212] S. A. Khan, C. Lampadaris, A. Cui, L. Stampfer, Y. Liu, S. J. Pauka, M. E. Cachaza, E. M. Fiordaliso, J.-H. Kang, S. Korneychuk, T. Mutas, J. E. Sestoft, F. Krizek, R. Tanta, M. C. Cassidy, T. S. Jespersen, and P. Krogstrup, ACS Nano **14**, 14605 (2020).

[213] D. J. Carrad, M. Bjergfelt, T. Kanne, M. Aagesen, F. Krizek, E. M. Fiordaliso, E. Johnson, J. Nygård, and T. S. Jespersen, Advanced Materials **32**, 1908411 (2020).

[214] N. W. Ashcroft and N. D. Mermin, *Solid State Physics*, Vol. 1 (Saunders College Publishing, Philadelphia, 1976).

[215] T. Kiendl, F. von Oppen, and P. W. Brouwer, Phys. Rev. B **100**, 035426 (2019).

[216] F. Setiawan, C.-X. Liu, J. D. Sau, and S. Das Sarma, Phys. Rev. B **96**, 184520 (2017).

[217] C.-X. Liu, J. D. Sau, T. D. Stanescu, and S. Das Sarma, Phys. Rev. B **96**, 075161 (2017).

[218] J. Avila, F. Peñaranda, E. Prada, P. San-Jose, and R. Aguado, Communications Physics **2**, 133 (2019).

[219] A. Vuik, B. Nijholt, A. R. Akhmerov, and M. Wimmer, SciPost Phys. **7**, 061 (2019).

[220] G. Ben-Shach, A. Haim, I. Appelbaum, Y. Oreg, A. Yacoby, and B. I. Halperin, Phys. Rev. B **91**, 045403 (2015).

[221] Y. Huang, J. D. Sau, T. D. Stanescu, and S. Das Sarma, Phys. Rev. B **98**, 224512 (2018).

[222] Y. Levine, A. Haim, and Y. Oreg, Phys. Rev. B **96**, 165147 (2017).

[223] J. D. Sau, C. H. Lin, H.-Y. Hui, and S. Das Sarma, Phys. Rev. Lett. **108**, 067001 (2012).

[224] M. Malard, G. I. Japaridze, and H. Johannesson, Phys. Rev. B **94**, 115128 (2016).

[225] S. Hoffman, J. Klinovaja, and D. Loss, Phys. Rev. B **93**, 165418 (2016).

[226] Y. Lu, W.-Y. He, D.-H. Xu, N. Lin, and K. T. Law, Phys. Rev. B **94**, 024507 (2016).

[227] J. S. Lim, L. Serra, R. López, and R. Aguado, Phys. Rev. B **86**, 121103(R) (2012).

[228] T. D. Stanescu, R. M. Lutchyn, and S. Das Sarma, Phys. Rev. B **84**, 144522 (2011).

[229] R. M. Lutchyn, T. D. Stanescu, and S. Das Sarma, Phys. Rev. Lett. **106**, 127001 (2011).

[230] S. A. Wolf, D. D. Awschalom, R. A. Buhrman, J. M. Daughton, S. von Molnár, M. L. Roukes, A. Y. Chtchelkanova, and D. M. Treger, Science **294**, 1488 (2001).

[231] J. Linder and J. W. A. Robinson, Nature Physics **11**, 1745 (2015).

[232] F. Giazotto, T. T. Heikkilä, A. Luukanen, A. M. Savin, and J. P. Pekola, Rev. Mod. Phys. **78**, 217 (2006).

[233] P. Machon, M. Eschrig, and W. Belzig, Phys. Rev. Lett. **110**, 047002 (2013).

[234] D. Razmadze, R. S. Souto, L. Galletti, A. Maiani, Y. Liu, P. Krogstrup, C. Schrade, A. Gyenis, C. M. Marcusa, and S. Vaitiekėnas, Preprint at https://arxiv.org/abs/2204.03202 (2022).

[235] B. D. Woods and T. D. Stanescu, Phys. Rev. B **104**, 195433 (2021).

[236] A. Maiani, R. Seoane Souto, M. Leijnse, and K. Flensberg, Phys. Rev. B **103**, 104508 (2021).

[237] A. Khindanov, J. Alicea, P. Lee, W. S. Cole, and A. E. Antipov, Phys. Rev. B **103**, 134506 (2021).

[238] K. Pöyhönen, D. Varjas, M. Wimmer, and A. R. Akhmerov, SciPost Phys. **10**, 108 (2021).

[239] J. Langbehn, S. Acero González, P. W. Brouwer, and F. von Oppen, Phys. Rev. B **103**, 165301 (2021).

[240] C.-X. Liu and M. Wimmer, Phys. Rev. B **105**, 224502 (2022).

[241] S. D. Escribano, A. Maiani, M. Leijnse, K. Flensberg, Y. Oreg, A. L. Yeyati, E. Prada, and R. Seoane Souto, npj Quantum Materials **7**, 81 (2022).

[242] A. Mauger and C. Godart, Phys. Rep. **141**, 51 (1986).

[243] H. Kramers, Physica **1**, 182 (1934).

[244] R. Xavier, Phys. Lett. A **25**, 244 (1967).

[245] T. R. McGuire and M. W. Shafer, Journal of Applied Physics **35**, 984 (1964).

[246] K. Ananth, P. Gielisse, and T. Rockett, Materials Research Bulletin **9**, 1167 (1974).

[247] D. O'Mahony, C. Smith, C. Budtz-Jorgensen, M. Venkatesan, J. Lunney, J. McGilp, and J. Coey, Thin Solid Films **488**, 200 (2005).

[248] S. J. Cho, Phys. Rev. B **1**, 4589 (1970).

[249] A. Yanase and T. Kasuya, Journal of the Physical Society of Japan **25**, 1025 (1968).

[250] P. Wachter, C R C Critical Reviews in Solid State Sciences **3**, 189 (1972).

[251] B. W. Alphenaar, A. D. Mohite, J. S. Moodera, and T. S. Santos, in *Physical Chemistry of Interfaces and Nanomaterials VIII*, Vol. 7396, edited by O. L. A. Monti and O. V. Prezhdo, International Society for Optics and Photonics (SPIE, 2009) pp. 24 – 32.

[252] J. M. Gomez-Perez, X.-P. Zhang, F. Calavalle, M. Ilyn, C. González-Orellana, M. Gobbi, C. Rogero, A. Chuvilin, V. N. Golovach, L. E. Hueso, F. S. Bergeret, and F. Casanova, Nano Letters **20**, 6815 (2020), pMID: 32786952.

[253] P. Wei, S. Lee, F. Lemaitre, L. Pinel, D. Cutaia, W. Cha, F. Katmis, Y. Zhu, D. Heiman, J. Hone, J. S. Moodera, and C. T. Chen, Nature Materials **15**, 711 (2016).

[254] F. Katmis, V. Lauter, F. S. Nogueira, B. A. Assaf, M. E. Jamer, P. Wei, B. Satpati, J. W. Freeland, I. Eremin, D. Heiman, P. Jarillo-Herrero, and J. S. Moodera, Nature **533**, 513 (2016).

[255] X. Hao, J. S. Moodera, and R. Meservey, Phys. Rev. Lett. **67**, 1342 (1991).

[256] E. Strambini, V. N. Golovach, G. De Simoni, J. S. Moodera, F. S. Bergeret, and F. Giazotto, Phys. Rev. Materials **1**, 054402 (2017).

[257] M. Rouco, S. Chakraborty, F. Aikebaier, V. N. Golovach, E. Strambini, J. S. Moodera, F. Giazotto, T. T. Heikkilä, and F. S. Bergeret, Phys. Rev. B **100**, 184501 (2019).

[258] M. W. A. de Moor, J. D. S. Bommer, D. Xu, G. W. Winkler, A. E. Antipov, A. Bargerbos, G. Wang, N. van Loo, R. L. M. O. h. Veld, S. Gazibegovic, D. Car, J. A. Logan, M. Pendharkar, J. S. Lee, E. P. A. M. Bakkers, C. J. Palmstrøm, R. M. Lutchyn, L. P. Kouwenhoven, and H. Zhang, New Journal of Physics **20**, 103049 (2018).

[259] X. P. Zhang, V. N. Golovach, F. Giazotto, and F. S. Bergeret, Phys. Rev. B **101**, 180502 (2020).

[260] B. S. Chandrasekhar, Applied Physics Letters **1**, 7 (1962).

[261] A. M. Clogston, Phys. Rev. Lett. **9**, 266 (1962).

[262] F. Nichele, A. C. C. Drachmann, A. M. Whiticar, E. C. T. O'Farrell, H. J. Suominen,

A. Fornieri, T. Wang, G. C. Gardner, C. Thomas, A. T. Hatke, P. Krogstrup, M. J. Manfra, K. Flensberg, and C. M. Marcus, Phys. Rev. Lett. **119**, 136803 (2017).

[263] A. Banerjee, O. Lesser, M. A. Rahman, H.-R. Wang, M.-R. Li, A. Kringhøj, A. M. Whiticar, A. C. C. Drachmann, C. Thomas, T. Wang, M. J. Manfra, E. Berg, Y. Oreg, A. Stern, and C. M. Marcus, Preprint at http://arxiv.org/abs/2201.03453 (2022).

[264] F. Nichele, E. Portolés, A. Fornieri, A. M. Whiticar, A. C. C. Drachmann, S. Gronin, T. Wang, G. C. Gardner, C. Thomas, A. T. Hatke, M. J. Manfra, and C. M. Marcus, Phys. Rev. Lett. **124**, 226801 (2020).

[265] K. Gawarecki and M. Zieliński, Scientific Reports **10**, 22001 (2020).

[266] P. Bonderson, M. Freedman, and C. Nayak, Phys. Rev. Lett. **101**, 010501 (2008).

[267] J. Alicea, Y. Oreg, G. Refael, F. von Oppen, and M. P. A. Fisher, Nature Physics **7**, 412 (2011).

[268] K. Flensberg, Phys. Rev. Lett. **106**, 090503 (2011).

[269] B. van Heck, A. R. Akhmerov, F. Hassler, M. Burrello, and C. W. J. Beenakker, New Journal of Physics **14**, 035019 (2012).

[270] S. Vijay and L. Fu, Phys. Rev. B **94**, 235446 (2016).

[271] T. Karzig, C. Knapp, R. M. Lutchyn, P. Bonderson, M. B. Hastings, C. Nayak, J. Alicea, K. Flensberg, S. Plugge, Y. Oreg, C. M. Marcus, and M. H. Freedman, Phys. Rev. B **95**, 235305 (2017).

[272] S. Plugge, A. Rasmussen, R. Egger, and K. Flensberg, New Journal of Physics **19**, 012001 (2017).

[273] S. Krøjer, R. Seoane Souto, and K. Flensberg, Phys. Rev. B **105**, 045425 (2022).

[274] R. Seoane Souto and M. Leijnse, SciPost Phys. **12**, 161 (2022).

[275] M. Levinshtein, S. Rumyantsev, and M. Shur, *Handbook series on semiconductor parameters*, Vol. 1 (World Scientific Publishing, 2000).

[276] J. Robertson, Eur. Phys. J. Appl. Phys. **28**, 265 (2004).

[277] S. Das and A. Ghosh, AIP Advances **5**, 027125 (2015).

[278] Z. Zanolli, L. Fröberg, M. Björk, M.-E. Pistol, and L. Samuelson, Thin Solid Films **515**, 793 (2006), proceedings of the Eighth International Conference on Atomically Controlled Surfaces, Interfaces and Nanostructures and the Thirteenth International Congress on Thin Films.

[279] B. Segall, Phys. Rev. **124**, 1797 (1961).

[280] Y. N. Chiang and M. O. Dzyuba, EPL **120**, 17001 (2017).

[281] J. Axe, J. Phys. Chem. Solids **30**, 1403 (1969).

Semiconductor-based heterostructures are suitable platforms to engineer and manipulate exotic quasiparticles that emerge in low dimensions. One example, with promising applications to quantum technologies, is a semiconductor nanowire partially covered by a superconductor layer. These wires support quasi one-dimensional states that acquire superconducting correlations by proximity effect. When applying an external magnetic field, the system may enter a topological superconducting phase giving rise to the so-called Majorana bound states at the ends of the wire. Alternatively, magnetic-free platforms have been proposed in which the hybrid nanowire is additionally covered by a ferromagnetic-insulator layer. Ideally, the ferromagnet induces a proximity-induced spin polarization on the wire that leads to the same kind of topological quasiparticles.

During the last decade, several simplified models have been introduced to predict and explain the features emerging in experimental devices based on these nanostructures. However, the phenomenology arising in these systems seems to be richer and more complex than what these models can capture. In this thesis, we seek to describe this kind of heterostructures in an accurate and realistic way. To this end, we use a microscopic numerical approach in which we consider the three-dimensionality of the heterostructure, the different materials involved, their interaction when they are placed together, as well as the interaction of the hybrid system with the surrounding electrostatic environment.

We apply this formalism to hexagonal nanowires, superlattice nanowires, as well as effective wires in planar stacking geometries. Particularly, we study how the different layers induce their properties into the semiconductor as well as the behavior of the electrostatic potential and the spin-orbit coupling inside the wire. These quantities establish the appearance, extension and robustness of the topological phase and, thus, their understanding is crucial to design topological qubits based on these nanostructures. We find that, in order to acquire topological properties, the wavefunction inside the semiconductor needs to be close to both the superconductor and ferromagnetic insulator layers so that the hybridization among the different materials is enhanced. We show that this can be controlled using external potential gates or by means of a strong confinement if the semiconductor is thin. We furthermore explore the intricate dependence of the spin-orbit coupling on the electrostatic potential profile and strain, showing that it can be strong enough to support a topological phase under certain conditions. We use this knowledge to propose new hybrid wire designs with improved topological performance.

Universidad Autónoma de Madrid
2022